# AN EXPERIMENTAL INVESTIGATION OF THE TURBULENT FLOW STRUCTURE IN ONE-DIMENSIONAL EMERGENT MACROPHYTE PATCHES

A thesis

Presented to the Faculty of the Graduate School

of Cornell University

in Partial Fulfillment of the Requirements for the Degree of

Master of Science

by

Rafael Omar Tinoco Lopez

August 2008

ABSTRACT

The presence of aquatic vegetation in streams becomes an important factor when dealing with water quality assessment, river and wetland restoration, management of fisheries and recreational areas and other environment related issues, yet its effects on flow structure and mass transport are not fully understood. Aquatic vegetation plays an important role in several hydrodynamic processes, regulating the fate and transport of sediments and nutrients, and is a key factor for the foraging and mating habits of many living organisms in rivers, lakes and wetlands.

Several studies have been carried out on flows through aquatic vegetation, primarily focused on characterizing the velocity field and characteristic drag, as well as the transport and dispersion of passive scalars. Most of the previous laboratory studies use different approaches to mimic vegetation, from arrays of rigid cylinders to scaled plastic models of selected species. Such experiments provide a good understanding of the underlying physical processes within the plant canopy and have been a benchmark for numerical models.

To gain a better understanding of the processes involved, a series of experiments was conducted using live, highly flexible, emergent plants in a laboratory flume under low speed flow conditions, typical of lakes and quiescent rivers. Since plant morphology and vegetation density have proven to be determinant factors on flow structure, one of the most common aquatic invasive species in North America is chosen as the primary experimental species to simulate a relevant and common condition in nature. Morphology effects are included by means of an optically obtained detailed description of the frontal area ($a$ $[m^{-1}]$) and volume fraction ($\phi[\ ]$) as functions of flow depth.

Particle image velocimetry (PIV) was used to capture the detailed turbulent velocity field within a one-dimensional plant canopy, as well as just up- and down-

stream of the patch. This technique yields detailed insight into both the temporal and spatial variations over the areas studied.

The experimental results are discussed and comparisons made with predictions based on existing models. Based on those results, a simple model able to predict the velocity field within the plant canopy is developed, by making assumptions that are verified through the experimental data. Particular attention is paid to the near bottom boundary effects and Reynolds number ($Re$) dependence of the drag due to the vegetation, in an attempt to estimate the distinct vegetation density ranges where their contributions must be considered to increase the model's accuracy.

## BIOGRAPHICAL SKETCH

The author was born in Mexico City, Mexico. He graduated from the Universidad Nacional Autonoma de Mexico as a Civil Engineer in 2004. A year later he moved to Ithaca NY, to begin his MS/PhD program in the Environmental Fluid Mechanics group at Cornell University.

## DEDICATORY

To my family

## ACKNOWLEDGMENTS

Sincere thanks go to Todd Cowen, Bob Johnson, Allie King, Evan Variano, Seth Schweitzer and everyone in the EFMH group who contributed to this project.

Acknowledgment must also go to the CONACyT and the graduate school at Cornell University for funding the author's studies at Cornell University. This work was also supported by the National Science Foundation through award CBET-0626164. Any opinions and comments are those of the author and do not necessarily reflect the views of the sponsors.

## TABLE OF CONTENTS

## LIST OF FIGURES

## LIST OF TABLES

## LIST OF ABBREVIATIONS

| | |
|---|---|
| 1D | One-Dimensional |
| 2D | Two-dimensional |
| 3D | Three-dimensional |
| ADV | Acoustic Doppler Velocimetry |
| CR | Current Regulation |
| DS | Downstream Section |
| FOV | Field Of View |
| LDV | Laser Doppler Velocimetry |
| LES | Large Eddy Simulations |
| LIF | Laser Induced Fluorescence |
| LR | Light Regulation |
| MKE | Mean Kinetic Energy |
| MS | Midstream Section |
| PIV | Particle Image Velocimetry |
| PTV | Particle Tracking Velocimetry |
| RANS | Reynolds-Averaged Navier-Stokes |
| RTD | Residence Time Distribution |
| TKE | Turbulent Kinetic Energy |
| US | Upstream Section |

## LIST OF SYMBOLS

| | |
|---|---|
| $a$ | Frontal area ($m^{-1}$) |
| $C_D$ | Drag coefficient |
| $E_{ii}$ | Spectral density |
| $f_x$ | Drag term |
| $h$ | Plant height |
| $UN$ | Nominal velocity |
| $\langle u_i \rangle$ | Spatial averaged velocity |
| $\bar{u}_i$ | Time averaged velocity |
| $\langle \overline{u'w'} \rangle$ | Reynold Stress |
| $\langle \overline{u}''\overline{w}'' \rangle$ | Dissipative fluxes |
| $x$ | Longitudinal coordinate, parallel to the flow |
| $y$ | Spanwise coordinate, perpendicular to the flow |
| $z$ | Vertical coordinate |
| $\phi$ | Volumetric fraction |
| $\tau_W$ | Bottom stress |
| $\nu$ | Kinematic viscosity |
| $\mu$ | Dynamic viscosity |

# Chapter 1

# Introduction

## 1.1 Thesis structure

This thesis is presented in three main chapters, each one dedicated to a specific part of the research process: divided into background, experimental set up and the analysis of the results. Chapter 1 addresses the reasons why this project was conducted and the relevance of these types of studies, covering motivation for this work, the main objectives, and an extensive bibliographic review concerning the subject from the first studies on terrestrial vegetation to the latest laboratory and field experiments developed on submerged vegetation. A general theoretical framework is developed focusing on the main assumptions and simplifications made in previous studies. The assumptions are revisited later in this work and tested with the collected data. Chapter 2 provides a detailed explanation of how the experiments were conducted, from the selection of the materials and the modification of the facilities to the performance of the experimental techniques developed for the studies. It covers the characteristics of the plants selected and their usual distribution in natural environments. Flume set up and instrumentation is explained as well as the components and set up of the particle image velocimetry (PIV) tech-

nique: optics, illumination, and software. Chapter 3 presents the results obtained and the subsequent analysis of the experimental data. It couples the experimental results with the theoretical framework to build a simple general model and provides validation for it, comparing the results with other models proposed for different density and velocity ranges. Finally, the conclusions are presented and the importance of the line of research, as well as proposed further research on the subject.

## 1.2 Motivation

The study of water related issues has been a continual work throughout history, thus a motivation for engineering developments. Modern day measurement techniques allow investigators to obtain more detailed descriptions of the underlying physical processes within flows and water bodies, which allows them to compare with, validate, or adapt the existing theoretical framework.

Of all the water on the planet, merely 3% is fresh water, and of that amount surface water comprises only 0.3% (Gleick 1996), contained within rivers, lakes, and swamps, in which vegetation is often, if not always present (Figure 1.1). This small percentage of the total amount represents the water supply for a considerable part of the world's population and provides habitat to numerous animal and plant species, increasing the importance of the subject of study.

In general, the presence of aquatic vegetation in streams becomes an important factor when dealing with water quality assessment, river and wetland restoration, management of fisheries and recreational areas and other environment related issues, yet its effects on flow structure and mass transport are not fully understood.

Aquatic vegetation plays an important role in several hydrodynamic processes, regulating the fate and transport of sediments and nutrients, and is a key factor

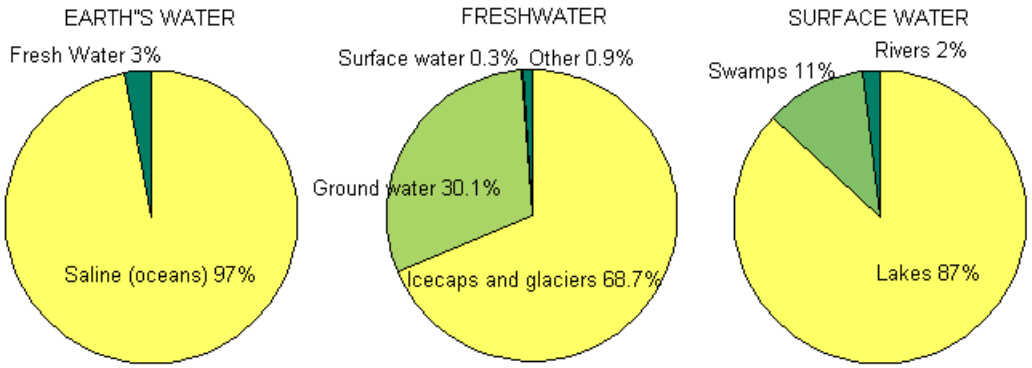


Figure 1.1: Fresh water distribution on Earth.

for the foraging and mating habits of many living organisms in rivers, lakes and wetlands. It is also involved in the distribution of living resources in receiving estuaries, fish spawning, shellfish survival, bird nesting, seed propagation, seasonal activities of fish and wildlife, among others.

From a biological perspective, macrophytes play an important role in pollutant removal, promote pollutant degradation, provide shading to suppress algae growth, offer food and habitat to native wildlife, plus the seasonal variations of plant populations varies the internal loading of phosphorus and nitrogen to the water column (Jadhav and Buchberger 1995).

From a more physical point of view, aquatic vegetation controls mean and turbulent flow structure in channels and coastal regions, the stem drag increases flow resistance, reducing mean flow; also affecting the residence time within the water body (Rueda and Cowen 2005), as well as dispersion and diffusion coefficients (Nepf et. al. 1997a). It generates an impact on sediment transport and redeposition (Schulz et. al. 2003) and changes the carrying capacity of floodplains, becoming an important design parameter for channels, wetlands, floodplains, irrigated lands and several other hydrological aspects (Khublaryan et. al. 2004, Nepf 2000).

Management of aquatic vegetation has thus become a controversial subject, since the interest of recreational users (for boating, swimming or fishing) often comes into conflict with ecosystem conservation and restoration pursuits. Therefore, several studies have been made to find an optimal level of biomass in rivers and lakes such that the best solution from both an ecological and a recreational economic point of view is reached (Van-Nes et. al. 1999). However, there is no general rule to be applied to all water bodies, so the optimal strategy for each particular case might result in keeping some water bodies free of aquatic plants while leaving others densely populated.

Several studies have been carried out on flows through aquatic vegetation, primarily focused on characterizing the velocity field and characteristic drag, as well as the transport and dispersion of passive scalars. Most of the previous laboratory studies use different approaches to mimic vegetation, from arrays of rigid cylinders to scaled plastic models of selected species. Such experiments provide a good understanding of the underlying physical processes within the plant canopy and have been a benchmark for numerical models (Lopez and Garcia 1998).

To gain a better understanding of the processes involved, a series of experiments was conducted using live, highly flexible, emergent plants in a laboratory flume under low speed conditions, typical of lakes and quiescent rivers. Since plant morphology and vegetation density are determinant factors on flow structure, one of the most common aquatic invasive species in North America is chosen as the primary experimental species to simulate a relevant and common condition in nature (Madsen et. al. 1991, Janauer and Dokulil 2006). Morphology effects are included by means of an optically obtained detailed description of the frontal area ($a$ $[m^{-1}]$) and volume fraction ($\phi[\ ]$) as functions of plant or canopy height. Mechanical properties of the plants, such as rigidity and stiffness, are not included in this study. It is convenient at this point to define some of the terms used

hereafter, understanding as a canopy the vegetated layer formed by the branches and leaves of the vegetation, and macrophytes as aquatic plants large enough to be apparent to the naked eye. A distinction is also made between submerged ($H/h > 1$) and emergent ($H/h \leq 1$) aquatic plants, where $H$ $(m)$ is the distance from the bottom of the flume to the free surface and $h$ $(m)$ is the height of the plants. For this study, emergent vegetation $H/h \simeq 1$ is used.

Given the characteristics of the selected plants, the experiments can be considered as full-scale, since the diameter doesn't change significantly between the 0.2m length stems used in the laboratory and the 3 to 4m specimens found in the field. However, these differences in length, particularly in the vertical scale, have to be considered before trying to apply experimentally obtained models to field problems, since the shallower flows recreated in the laboratory could create sharper gradients in the velocity field, and produce a bed stress contribution larger than the observed in deeper flows.

To insure a robust set of data, able to provide detailed insight into both temporal and spatial variations over the areas studied, PIV was used to capture the detailed turbulent velocity field within a one-dimensional plant canopy patch, as well as just up- and downstream of the patch. This technique offers advantages over single-point measurements with either acoustic or laser Doppler velocimetry devices (ADV or LDV) given that it is a non-intrusive approach, and has better spatial resolution, yielding a more synoptic set of data and allowing the measurement of instantaneous spatial velocity gradients and other important turbulence statistics (Cowen and Monismith 1997). It also facilitates the careful study of the near bottom boundary effects and Reynolds number (Re) dependence of the drag due to the height dependent vegetation density, to estimate the distinct vegetation density ranges where their contributions must be considered. By running an extensive series of experiments, covering the most common ranges of vegetation

densities and flow velocities, this work aims at obtaining a comprehensive data set to be used for comparison, calibration, and validation of existing models.

## 1.3 Background

Given its repercussions, several studies have been made to understand the turbulent flow through vegetated regions, in both terrestrial and aquatic vegetation. However, as pointed out by Raupach and Thom (1981), for decades most of these studies were purely empirical and observational, lacking a general theory.

Tracking the first works related to canopy flow, one must refer to the first studies on air flows through terrestrial plants. Motivated by agricultural requirements, the first quantitative studies focused on crop fields and other terrestrial vegetation. The study of canopy flow started with attempts to characterize the exchange of momentum, heat and mass between crops and the atmosphere. Both experimental and numerical approaches were used, such as those by Wright and Brown (1967), who performed measurements of wind speed, air temperature and heat flux at several levels within and above a crop field; and Cionco (1965), who investigated the transfer of momentum within a vegetative canopy, developing a model relating the roughness effects of the surface boundary created at the top of the submerged vegetation in terms of height, density and drag characteristics of the canopy. Cionco (1965) makes the distinction between the commonly used "ideal canopy models" and the real nature conditions, the first being defined as arrays with a uniform leaf area distribution and drag coefficients that are vertically uniform and independent of the local Reynolds number, conditions that are seldom met in nature but that have been, and still are, often used in experiments and numerical simulations to understand the basic characteristics of vegetated flows.

Based on a mixing length approach, this work goes further and implies a relationship between the velocity of the flow and the flexibility of the plants with the value of the drag coefficient, assuming that higher velocities will produce an increased bending of the plants, altering the original estimates for drag. It also proposes further research to investigate the effects of different densities and elasticities in the aerodynamic characteristics of vegetation.

A notable contribution from Wright and Brown (1967) is their finding of differences between the drag coefficients calculated by a momentum balance approach, and those calculated with an energy approach, where the latter showed a dependence on height within the crop. The differences between both approaches were reported to be larger in the low Reynolds number region close to the bottom, suggesting that for Reynolds numbers low enough the assumptions on both methods should be investigated. Similar results were found in the present work, which will be discussed in later sections.

A similar work performed by Barr (1971), paid special attention to the transition regions within the canopy, assuming three different zones: 1) a horizontally uniform zone with parallel mean flow, 2) a leading edge transition zone with two dimensional turbulence structure, and 3) a two dimensional trailing edge zone. It presents a detailed analysis beginning by assuming a momentum loss due to drag forces within the canopy which is described as:

$$\frac{d\tau}{dz} = \rho C F(z) U^2(z) \tag{1.1}$$

where $\tau$=turbulent stress, $\rho$=density of the air, $C$= drag coefficient, $F$=leaf area density, $U$=mean wind speed and $z$=height. This concept is used in most subsequent work with varying notation.

For consistency, the most common notation is adopted herein and equation 1.1 becomes:

$$\frac{d\tau}{dz} = \rho \cdot C_D(z) \cdot a(z) \cdot \overline{u}(z)^2 \tag{1.2}$$

with the local drag coefficient represented as $C_D$ and the frontal area of obstruction per unit volume $a$ ($m^{-1}$) replacing the leaf area density. Using a Reynolds averaging approach, some of the classical assumptions in dealing with vegetated flow are introduced. For a flow in two dimensions (2D flow) the momentum conservation equations can be expressed as (for an incompressible flow):

$$\frac{\partial \overline{u}}{\partial t} + \overline{u}\frac{\partial \overline{u}}{\partial x} + \overline{w}\frac{\partial \overline{u}}{\partial z} = -\frac{1}{\rho}\frac{\partial p}{\partial x} - \frac{\partial}{\partial x}(\overline{u'^2}) - \frac{\partial}{\partial z}(\overline{u'w'}) + \nu\nabla^2\overline{u} \tag{1.3}$$

$$\frac{\partial \overline{w}}{\partial t} + \overline{u}\frac{\partial \overline{w}}{\partial x} + \overline{w}\frac{\partial \overline{w}}{\partial z} = -\frac{1}{\rho}\frac{\partial p}{\partial z} - g - \frac{\partial}{\partial x}(\overline{u'w'}) - \frac{\partial}{\partial z}(\overline{w'^2}) + \nu\nabla^2\overline{w} \tag{1.4}$$

Where the primes denote the instantaneous deviation from the time average quantities indicated by the overbars. Assuming a uniform homogeneous canopy and horizontal, steady, homogeneous flow, the above equations simplify to:

$$0 = -\frac{1}{\rho}\frac{\partial p}{\partial x} - \frac{\partial}{\partial z}(\overline{u'w'}) + \nu\frac{\partial^2}{\partial z^2}\overline{u} \tag{1.5}$$

$$0 = -\frac{1}{\rho}\frac{\partial p}{\partial z} - g - \frac{\partial}{\partial z}(\overline{w'^2}) \tag{1.6}$$

However, it doesn't present a consistent way to incorporate the drag coefficient attributed to the vegetation into the Reynolds averaged equations, suggesting instead a mixing length theory approach to model the velocity in the region above the vegetation.

Significant advances are presented in Raupach and Thom (1981), which also addresses the issue of transport models and the necessity of using second-order closure models, as well as the turbulence field within the canopy and in the region above it.

They consider five hydrodynamic processes occurring between the vegetation and the flow around it: 1) absorption of momentum by both form and skin friction drag on elements, 2) exchange of heat and other scalars (e.g. water vapor, carbon dioxide) between the flow and plants, 3) momentum and scalar properties transported vertically by turbulent diffusion and dispersion, 4) turbulent wakes generated by the canopy elements, transforming mean kinetic energy (MKE) into turbulent kinetic energy (TKE) and 5) a cyclic behavior produced by the plants waving , storing MKE as potential energy, to then releasing it as TKE after half a cycle, known as "monami" in aquatic plants and "honami" in terrestrial vegetation.

They also introduce a spatial averaging, denoted with angular brackets $\langle\,\rangle$ and taken over one, two or three dimensions depending on the kind of flow or the measurements available. In this way, the variables are decomposed into time mean and fluctuations and the spatial average and departures therefrom (as defined in Raupach and Thom (1981) and Ayotte et. al. (1999)) which are represented respectively as (for any flow property $\phi$):

$$\phi_i = \overline{\phi_i} + \phi_i' \tag{1.7}$$

$$\overline{\phi_i} = \langle\overline{\phi_i}\rangle + \overline{\phi_i''} \tag{1.8}$$

The averaging processes are defined as follows. The usual time average:

$$\overline{\phi_i} = \frac{1}{T}\int_0^T \phi_i(x,t)dt \tag{1.9}$$

And for space, depending if it is taken over a specific length ($L$), area ($A$), or volume ($V$), the averaging process is defined as:

$$\langle\overline{\phi_i}\rangle_{1D} = \frac{1}{L}\int_L \phi_i(x+r,t)dr \tag{1.10}$$

$$\langle\overline{\phi_i}\rangle_{2D} = \frac{1}{A}\int\int_A \phi_i(x+r,t)dr \tag{1.11}$$

$$\langle\overline{\phi_i}\rangle_{3D} = \frac{1}{V}\int\int\int_V \phi_i(x+r,t)dr \tag{1.12}$$

By their own definitions it is already established that:

$$\overline{u_i'} = 0 \tag{1.13}$$

$$\langle\overline{u_i''}\rangle = 0 \tag{1.14}$$

Raupach and Thom (1981) built a theoretical framework using conservation equations for mass, momentum and for a passive scalar. Similar approaches have been used in most subsequent works, though some variations have been introduced as in the work of Jadhav and Buchberger (1995). In his studies on wetlands, he splits the vegetation resistance to flow into two main factors: bed friction and stem drag, addressing the inadequacies of considering both of them in a bulk roughness term. He also considers the effects of emergent vegetation on detention time and identifies two opposite effects of vegetation on the flow: a static effect that reduces

the volume of water in the channel due to space occupied by the plants; and a dynamic effect manifested as an increase of volume due to water depth rising in response to resistance induced by stem drag. This severely affects diverse transport time scales such as age, flushing time and residence time, as discussed in Monsen et. al. (2002) and Rueda and Cowen (2005), which are key parameters to understand the complex processes occurring in water bodies.

Jadhav uses a modified form of the Saint-Venant equations, applied to densely populated free water surface wetlands, as:

$$\frac{\partial Q}{\partial x} + \frac{\partial}{\partial x}(\eta A) = 0 \quad (1.15)$$

$$\frac{\partial Q}{\partial t} + \frac{\partial}{\partial x}\left(\frac{Q^2}{\eta A}\right) + \eta A g\left(\frac{\partial y}{\partial x} - S_0 + \frac{C_{db} P_e Q^2}{g(\eta A)^3} + \frac{C_{ds} D m B y Q^2}{2g(\eta A)^3}\right) = 0 \quad (1.16)$$

Where $Q$=flow ($m^3/s$), $A$=cross sectional area, $x$=longitudinal distance along the channel, $y$=water depth, $t$=time, $S_0$=longitudinal slope of the channel bottom, $S_f$=friction slope, $g$=gravitational acceleration ($m/s^2$), $\eta$=porosity ($\eta = 1 - \frac{\pi}{4} m D^2$), $P_e$=effective wetted perimeter, $B$=bottom width of the channel, $D$=average stem diameter, $m$=vegetation density (number of stems per unit area $m^{-2}$), $C_{db}$=drag coefficient associated with bed friction and $C_{ds}$=drag coefficient associated with stem friction. However, the work doesn't go further in the detailed velocity field, focusing only on obtaining estimates for residence time for different porosity values, assuming drag coefficients and other variables constant over the water depth.

Returning to the more common momentum and mass conservation approach, the work presented by Ayotte et. al. (1999) and Finnigan (2000) shows in a detailed manner the analysis and inclusion of vegetation related terms into the equations up to a second order.

The continuity equation becomes:

$$\frac{\partial u_i}{\partial x_i} = \frac{\partial \langle u_i \rangle}{\partial x_i} = \frac{\partial \langle \overline{u_i} \rangle}{\partial x_i} = \frac{\partial \overline{u_i}''}{\partial x_i} \quad = \quad 0 \tag{1.17}$$

and momentum:

$$\frac{\partial \langle \overline{u_i} \rangle}{\partial t} + \langle \overline{u_j} \rangle \frac{\partial \langle \overline{u_i} \rangle}{\partial x_j} \quad = \quad -\frac{\partial \langle \overline{p} \rangle}{\partial x_i} + \frac{\partial \tau_{ij}}{\partial x_j} + f_{Fi} + f_{Vi} \tag{1.18}$$

where:

$$\tau_{ij} \quad = \quad -\langle \overline{u_i' u_j'} \rangle - \langle \overline{u_i}'' \overline{u_j}'' \rangle + \nu \frac{\partial \langle \overline{u_i} \rangle}{\partial x_j} \tag{1.19}$$

$$f_{Fi} \quad = \quad \frac{1}{V} \int \int_{S_I} \overline{p} n_i dS \tag{1.20}$$

$$f_{Vi} \quad = \quad -\frac{\nu}{V} \int \int_{S_I} \frac{\partial \overline{u_i}}{\partial n} dS \tag{1.21}$$

With $S_I$ being the sum of all plant surfaces in the volume considered and $n_i$ the unit vector normal on $S_I$. This is consistent with other authors, such as Shaw and Patton (2003), by decomposing the drag into the two components, form or pressure drag and viscous drag or skin friction. A detailed explanation of each term, as well as the equations for the Reynolds stress tensor and dissipative terms are shown in Ayotte et. al. (1999) while in Finnigan (2000) there is a review of several other works available at the time, both being an excellent source for further reference. This approach groups together the form and viscous drag force terms ($f_{Fi}$ and $f_{Vi}$) into one term as: $f_i = f_{Fi} + f_{Vi} = C_d a(z) U_i |U|$, making the assumption that $f_{Fi} >> f_{Vi}$, which is common in vegetated flows. It starts by assuming a constant

$C_d$ and then fits its value in order to match the results with the experimental data available, using it as a calibration parameter instead of calculating it from the data.

Similar efforts have been made by authors such as Lopez and Garcia (1998,2001), expressing the drag force as commonly used in fluid mechanics by $f_1 = \frac{1}{2} C_D a \langle u_i \rangle^2$, in order to solve for the velocity field using numerical models based on both the $k - \epsilon$ and $k - \omega$ models, adjusting the required coefficients with the model calibration. This work is followed closely by Choi and Kang (2004) doing a Reynolds stress modeling of vegetated open channel flows, adjusting the drag coefficient (from a constant average value of $C_{DA} = 1.13$ to a height dependent coefficient $C_D/C_{DA} = 0.74 + 3.51\left(\frac{z}{h_p}\right) - 6.41\left(\frac{z}{h_p}\right)^2 + 2.72\left(\frac{z}{h_p}\right)^3$) and comparing it's results against the numerical model of Lopez and Garcia (2001) and experimental results from Nepf and Vivoni (2000). Other outstanding modeling efforts are those by Neary (2003) using a Reynolds Averaged Navier-Stokes (RANS) model with isotropic turbulence, simulating successfully the time averaged flow features but still suffering from a lack of generalness, since it requires calibration of drag and model coefficients, and the work of Cui and Neary (2008) using a large eddy simulation (LES) approach for the vegetated case, obtaining a good agreement with experimental data.

Nepf et. al. (1997a) considers how vegetation may have an effect on vertical diffusion and longitudinal dispersion. Experimenting with rigid emergent cylinders, paying special attention to the mechanical dispersion created by the dowels in the flow and the existence of fluid trapped in recirculating zones (trapping dead zones). Main conclusions of this work are: 1) Enhancement of turbulence intensities, which increases vertical diffusivity of both mass and momentum; 2) Reduction of shear-flow dispersion relative to the non-vegetated case; and 3) Diminished longitudinal dispersion within high populated regions.

To obtain a model for this process, Nepf et. al. (1997b) carries out experiments with mock vegetation instead of plain cylinders. Using different plant population densities, the velocity and concentration profiles are measured by using a two-dimensional LDV and laser-induced fluorescence (LIF) technique, respectively. For the plain cylinder cases, with increased vegetation density, vertical velocity profiles become more uniform, indicating a possible enhancement of the vertical eddy viscosity, consistent with the measurements of turbulence intensity in each case. Adding plastic strips to the upper half of the cylinders, she simulates the branches and leaves of a canopy. As a result, the velocity profiles show a decrease in the canopy area compared with the region occupied by the stems, which becomes more evident as the plant population increases. In this case, turbulence intensity also presents a vertical variation with a peak at the canopy-stem interface region of high shear stress.

Since plant morphology is a main factor to obtain the flow characteristics, Nepf (1999) addresses the issue of characterizing the different possible kinds of aquatic vegetation, by using a depth dependent vegetation density parameter $a(z)$, defined as projected plant area per unit volume (units of $L^{-1}$):

$$\begin{aligned} a &= nd \\ n &= \frac{\#\, of\ stems}{m^2} \\ d &= stem\, diameter \end{aligned}$$

Based on this, Lightbody and Nepf (2006) develop a model to predict both velocity and dispersion in flow through vegetated canopies. By a balance between vegetation drag and pressure forcing terms in the momentum equation, and neglecting the drag contribution by the base of the array, so that the velocity profile

depends only on canopy morphology. To describe the rate of growth of spatial variance of a cloud of solute or particles, a longitudinal dispersion constant is defined as $K_x = \frac{1}{2}\frac{d\sigma_x^2}{dt}$. Nevertheless, due to the identified dispersion processes arising from stem-scale and depth-scale velocity heterogeneity, this constant is decomposed into a stem-scale dispersion $K_d$ and depth-scale dispersion $K_h$.

Lightbody and Nepf (2006) develop a model following a similar approach to that of Ayotte et. al. (1999), starting from the classic Navier-Stokes equations, looking at the horizontal component of momentum equation:

$$\begin{aligned} \frac{\partial U}{\partial t} + U\frac{\partial U}{\partial x} + W\frac{\partial U}{\partial z} &= -\frac{1}{\rho}\frac{\partial p}{\partial x} - \frac{\partial}{\partial x} < u'^2 > -\frac{\partial}{\partial z} < u'w' > \\ &\quad +\nu\nabla^2 U + f_{form} + f_{viscous} \end{aligned} \tag{1.22}$$

Assuming steady, uniform, fully developed flow, and hydrostatic pressure:

$$0 = -g\frac{\partial h}{\partial x} - \frac{\partial}{\partial z} < u'w' > +\nu\nabla^2 U + f_{form} + f_{viscous} \tag{1.23}$$

Assuming that the viscous stress and bed stress are negligible compared to vegetative drag, i.e. $f_{form} >> f_{viscous}$ and using the same quadratic form $f_{form} + f_{viscous} = f_i = \frac{1}{2}C_d(z)a(z)U(z)^2$:

$$0 = -g\frac{\partial h}{\partial x} - \frac{\partial}{\partial z} < u'w' > +\frac{1}{2}C_d(z)a(z)U(z)^2 \tag{1.24}$$

Which neglecting the vertical turbulent transport of momentum $< u'w' >$ yields:

$$g\frac{\partial h}{\partial x} = \frac{1}{2}C_d a U^2 \tag{1.25}$$

And since $\frac{\partial h}{\partial x}$ is not a function of depth ($\frac{\partial h}{\partial x}$ =surface slope):

$$\begin{aligned} C_d a U^2 &\neq f(z) \\ U(z) &\propto C_d(z)a(z) \end{aligned} \tag{1.26}$$

So a normalized velocity can be found as:

$$\frac{u(z)}{\tilde{u}} = \sqrt{\frac{\tilde{C}_d \tilde{a}}{C_d(z)a(z)}} \tag{1.27}$$

Where $\tilde{u}$, $\tilde{C}_d$ and $\tilde{a}$ are taken at a reference height $\tilde{z}$.

Going further, if $C_d$ is not a strong function of plant density or $Re_d$:

$$\frac{u(z)}{\tilde{u}} = \sqrt{\frac{\tilde{a}}{a(z)}} \tag{1.28}$$

Which yields a normalized velocity profile in terms of only the frontal area $a(z)$.

The previous statement considers a specific range for both Reynolds number and frontal area, and proves to agree with experimental data for such conditions. However, that is not the only case in nature, where often most of the terms neglected in the derivation of this model cannot be ignored.

Other authors address such conditions, looking for a drag dependence on Reynolds number and relative obstructed area, works such as those of Koch and Ladd (1997), Ghisalberti (2005), Tanino and Nepf (2008a, 2008b). All of these researchers use different approaches, with the common objective to find the drag coefficient or the mean drag per unit length in terms of Reynolds number and either frontal area $a(z)$ $(m^{-1})$ or volume fraction $\phi(z)$. A standard approach is to use the known expression for the drag coefficient for a cylinder and modify it to fit the experimental data through an array of cylinders, allowing one to obtain a relationship between the correspondent drag of an isolated cylinder and a staggered or random array of them. Other alternatives estimate the drag coefficient using a linear or quadratic dependence on the Reynolds number, with empirical coefficients that depend on the volume fraction. Just as mentioned before, each one of the approaches proves to work for the density and velocity ranges considered in their respective experiments, which returns us to the task of finding not only the ranges in which these results apply, but the possibility of determining a general expression to cover all the possible values for such parameters. In order to achieve that, it is also important to define a general way to calculate such parameters, since it has been observed that the methods to calculate the frontal area and volume fraction in an array of rigid cylinders don't apply exactly when dealing with real vegetation, which can lead to differences in the magnitudes of the parameters to be compared due to the approximations made.

# Chapter 2

# Experimental technique

## 2.1 Laboratory Facilities

### 2.1.1 Flume Set-up

All experiments were conducted at the DeFrees Hydraulics Laboratory (Hollister Hall, Cornell University), in a 7.4m long, 45.6cm wide flume, which allows a maximum water depth of about 30cm (Figure 2.1).

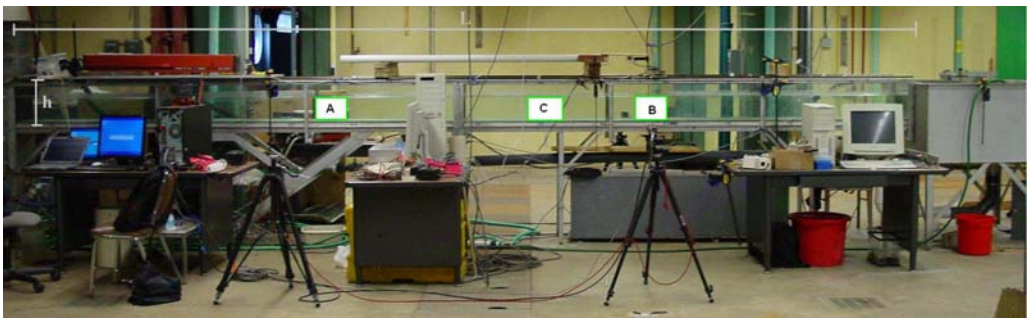


Figure 2.1: Laboratory facilities.

For the series of experiments, two different flow configurations were required. The flume had to work in both recirculating mode (for long PIV experiments) and in a once through mode (for LIF dye experiments) for a pre-established range of

velocities between 0 and 5cm/s. This was achieved by using a constant head tank at the inlet (Figure 2.2), regulating the flow with a valve, using pressure gauges before and after the valve to assure repeatability of the flow rates required. For this purpose, two pressure gauges (7 KPa, 0 to 16.7 mV) were used (Figure 2.3) and data acquired with Easy Data Software (Copyright 2004 Cornell Research Foundation, Inc. Author: Dr. Monroe Weber-Shirk).

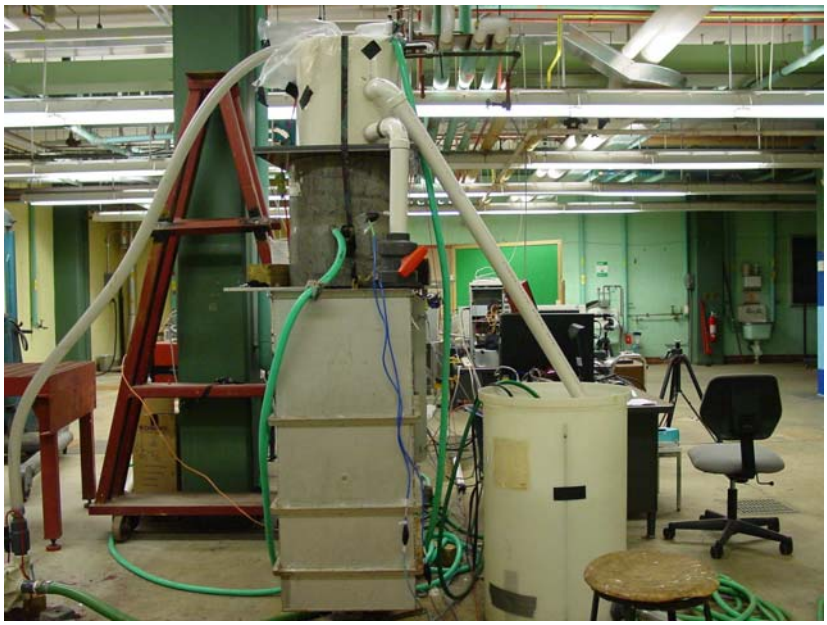

Figure 2.2: Constant head tank.

The flow was driven by a 1.5 HP centrifugal pump (3450 rpm, 50/60 Hz), controlled by a voltage regulator (Magnetek GPD203). The flow rate is regulated by the aperture of the valve, however, with the pump velocity used to insure excess water was being supplied to the constant head tank. This proved to be more accurate than just running the pump without the constant head tank and controlling the flow rate using the voltage regulator (data not included).

Several velocity profiles were taken at different locations along the flume using ADVs (Nortek USA Vectrino and Sontek 10-Mhz Lab ADV) to define the flow rates required to achieve the range of velocities desired. By doing this, the valve aperture

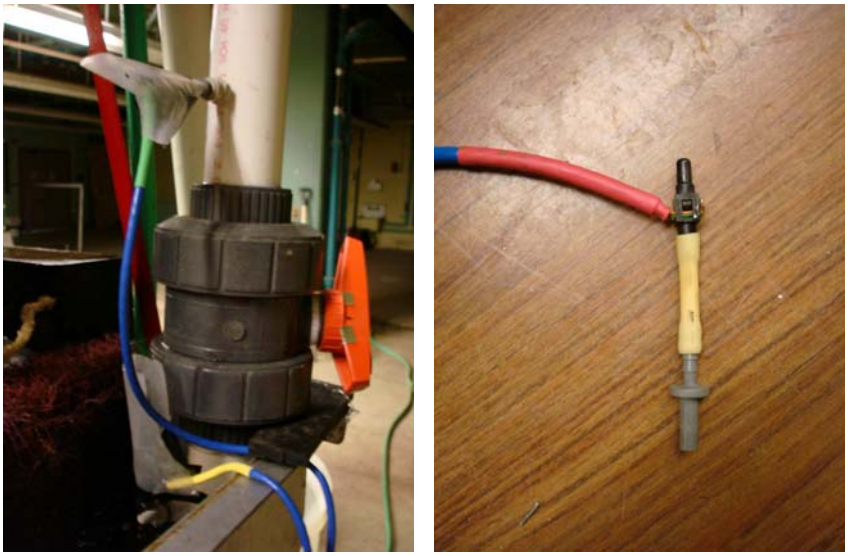

Figure 2.3: Pressure gauges.

(and more specifically the pressure drop across the valve) and pump frequency for the experiments could be set. The measured velocity profiles are shown in Figure 2.4.

Five different flow rates were considered for each experiment, calculating the nominal velocity ($UN$) of each by integrating the longitudinal velocity $u(z)$ over the water depth ($0 < z < h$) and dividing by $h$, which in these series of experiments is $h = H$ =24cm approximately, depending on the flow rate considered.

$$UN = \frac{1}{h}\int_{z=0}^{h} u(z)dz \tag{2.1}$$

Applying equation 2.1 to each of the cases considered yields the results shown in Table 2.1.

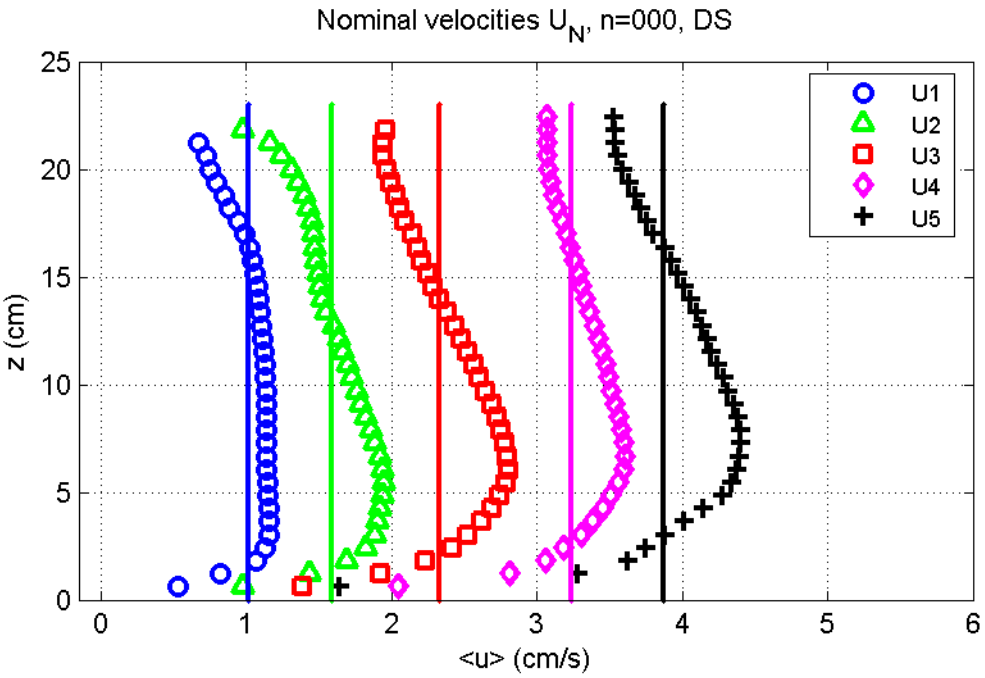


Figure 2.4: Nominal Velocities UN.

Table 2.1: Nominal Velocities.

| Nominal velocity | (cm/s) |
|---|---|
| U1 | 1.02 |
| U2 | 1.59 |
| U3 | 2.33 |
| U4 | 3.24 |
| U5 | 3.87 |

Hereafter, the calculated nominal velocities ($UN$) are used as a reference to compare the results obtained from different experimental conditions.

### 2.1.2 Plant selection and distribution

Previous studies have shown that the flow structure is strongly determined by the plant morphology and canopy density. Thus it was considered important to select a plant that is commonly found in nature, representative of the kind of problems

that this project addresses and satisfies the properties of high flexibility and typical submergence level. These criteria led to the utilization of freshly harvested stems of *Myriophyllum Spicatum*, also known as Eurasian Watermilfoil (Figure 2.5), one of the most important submersed aquatic invasive species in North America.

Figure 2.5: Stem of Eurasian Watermilfoil.

To recreate as accurately as possible the conditions in nature, the individual stems were arranged in clumps of 3 to 7 stems each (Figure 2.6). Such clumps were used to build patches of different densities, varying from 100 to 300 stems per square meter, as was found to be a good representation of natural conditions (Johnson, personal communication). The plants were attached to the glass bottom using natural wax, which allowed for a smooth transition in the bottom and permitted us to work and attach the arrays even in the presence of water, which facilitated the project.

The distribution of the plants over the flume consisted of the following steps: 1) Select the patch density $n(stems/m^2)$, 2) specify the length of the patch to be created ($L_i$), 3) using a normal distribution ($\mu = 5$, $\sigma = 2$), calculate how many

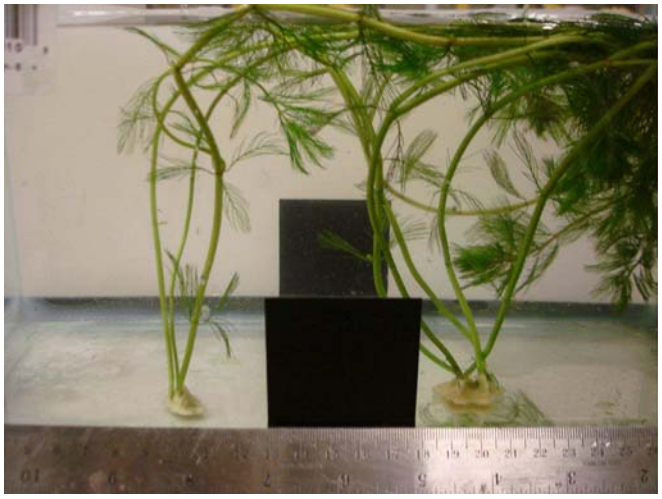

Figure 2.6: Milfoil clumps.

clumps ($N_c$) of how many stems each would be required to reach the density $n$, 4) specify the minimum distance between clumps (grid separation $s_g$) to create a rectangular grid, 5) assign a number to each grid point, 6) create a vector with the grid point numbers (in ascending order), 7) use the random permutation function from MATLAB (randperm) on the vector created in step 6, 7) select the first $N_c$ elements of the resulting vector as the grid points where the clumps will be located.

This method populates the grid as shown in Figure 2.7, for the case considered with $s_g$=5cm and $L_i$=50cm.

This process was repeated, producing a different 50cm long vegetated pattern each time, until the total length of the canopy required was covered. Once all of the grids were created, the clumps were attached to the bottom following such distributions, as shown in Figure 2.8.

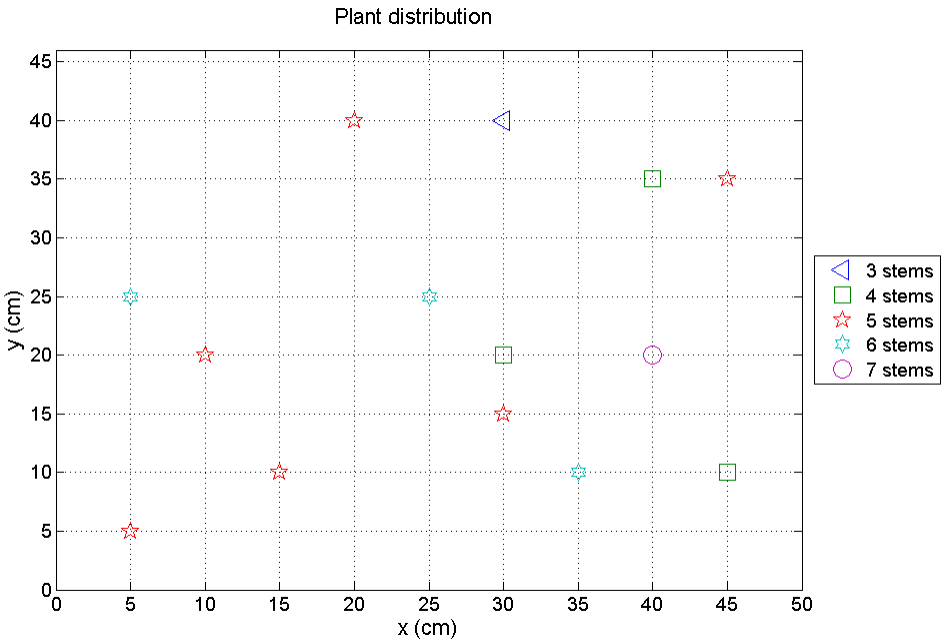


Figure 2.7: Random distribution of stems (Case shown for patch of 50cm length, n=300, minimal separation of 5cm).

Figure 2.8: Stems attached to the bottom. (1) while being attached, (2) once the tank was filled up.

It is noticed that the plants not only reach the free surface, they protrude and bend creating a vegetated bed, a condition commonly observed in the field. The plants kept growing and branching out during the duration of the experiments, starting to lose their leaves by the time of the last series, after 15 to 20 days in the flume.

## 2.2 Illumination and imaging

### 2.2.1 Cameras and lenses

Two digital CCD cameras (UP-680CL/12B, UNIQ Vision, Inc.) were used for both the PIV and LIF techniques. With a maximum frame rate of 60 frames per second, they provided 656×494 pixels, 12-bit images using progressive scanning interline-transfer technology, with the advantage of square pixels which is quite useful for post-processing stages.

Two different lenses were used, to adapt to the specific requirements to get a) a large FOV to capture the total water depth and b) a small FOV to get a more detailed insight of the boundary layer. For the first case a Nikkor-S Auto 1:1.4 f=50mm standard lens (Nikon, Inc.) was used (focal length of 50mm, maximum aperture 1:1.4), whereas for the small FOV there was a Fujinon-TV 1:1.8/75 (Fuji Photo Optical Co.) for high resolution and low distortion in the image acquisition.

An extra camera was used to acquire the frontal area sets. In this case, the same type of camera (UP-680CL/12B, UNIQ Vision, Inc.) was used, incorporating a zoom lens (Fujinon-TV zoom lens H6x12.5R, 1:1.2/12.5-75, Fujinon Co.) to capture the desired images.

For image acquisition, VisionNow software (Boulder Imaging Inc.) was used, with the settings according to the configuration explained in section 2.3.

### 2.2.2 Laser

An Argon-Ion laser was used as the illumination source for both the PIV and LIF measurements performed during this work.

The Argon-Ion laser used in multi-line mode allows for two types of control: Current Regulation (CR) and Light Regulation (LR). Using the first one, the current is fixed and the light intensity varies as the laser efficiency is often a function of operating duration. On LR, a specific intensity (in values of Watts) will be fixed and the current will automatically change to hold it as specified. For all the experiments, the laser was kept on LR mode at 5W.

The shutter used (model LS200, nmLaser Products, Inc) is designed for use as a high speed modulator, providing a short exposure for pulse gating, and fast repetition rates. The shutter was set as close to the laser as possible, to make alignment easier and for safety considerations. Both laser and shutter were attached to the same metal base-plate and moved together as a single piece during mirror positioning and alignment.

To create the light sheet, a scanning mirror (Model 6860 Moving Magnet Capacitive Position Detector Optical Scanner, Cambridge Technology) with full speed of 100 Hz scanning at full range (-10,10)V (absolute speed cannot exceed 2 volts/ms) is attached to a separate mount, allowing an easy switch between the three different sections of study (upstream, midstream and downstream -US, MS, DS).

All electric components were connected to a power conditioner, to avoid failures or irregularities in the current supply.

## 2.3 PIV

### 2.3.1 Hardware communication

To communicate among hardware a Shielded Input-output Connector Block (SCB-68 shielded Input-output connector block with 68 screw terminals for easy signal connection to a National Instruments 68 or 100 pin DAQ device, Figure 2.9) is used, to connect the camera, the mirror, and the shutter following the configuration shown in Table 2.2.

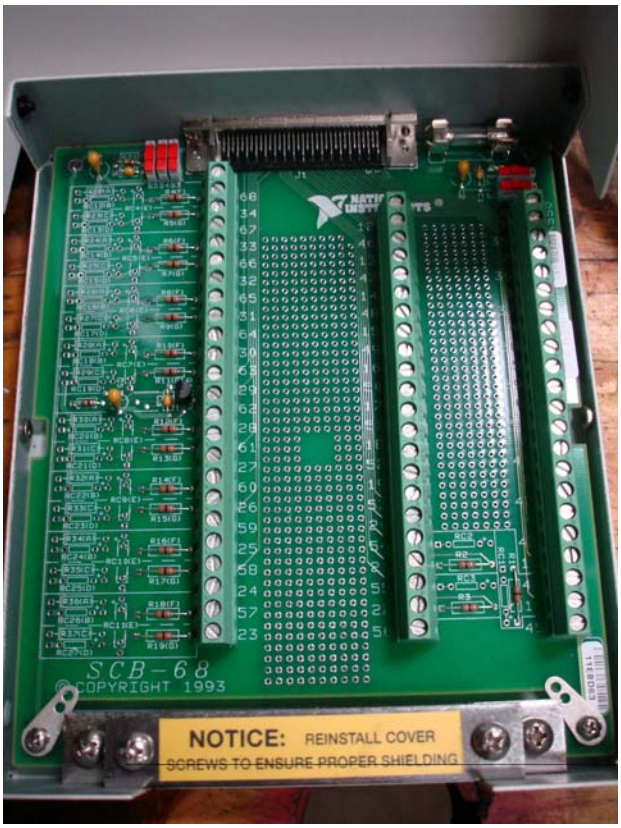


Figure 2.9: Input-Output connector.

Another computer is used to run a MATLAB routine which sends the corresponding signal to the mirror, camera and shutter (Figure 2.10).

Table 2.2: DAQ Connections.

| channel | AO | AO_GND |
|---|---|---|
| 0-mirror | 22 | 56 |
| 1-camera | 21 | 55 |
| 2-shutter | 57 | 23 |

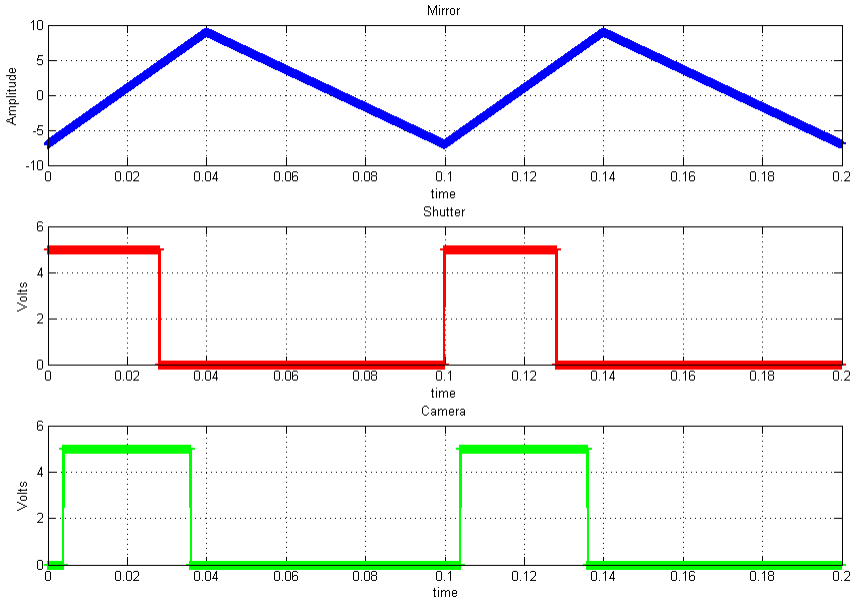


Figure 2.10: Signals for mirror, shutter and camera.

In this way, images are acquired with a rate of 10 to 50 frames per second, according to the rate required for each set of experiments. The signal sent to the shutter is completely dependent on the camera signal, as well as the one for the mirror, in which the speed and angle of rotation are defined based on the frame rate.

### 2.3.2 PIV set up

Three longitudinal sections for study are selected: a section upstream (US) just before the flow reaches the plant canopy, a midstream section (MS) within the patch, and a downstream section (DS), located immediately after the edge of the canopy (Figure 2.11).

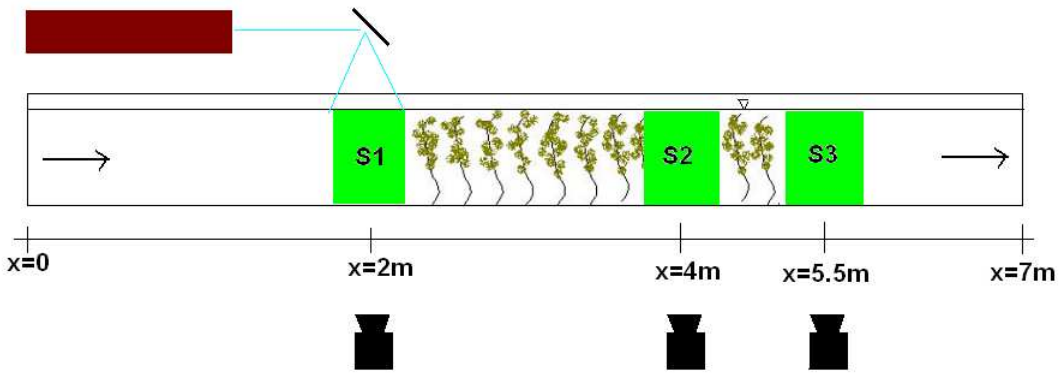


Figure 2.11: Sections considered for PIV analysis.

The pump starts driving the flow for each one of the flow speeds required. The two cameras are set at opposite sides of the flume at one of the locations mentioned. Images of a ruler are taken with both cameras for spatial calibration of the images (Figure 2.12). Once this is done, all lights in the laboratory are turned off and the signals are sent from the MATLAB running PC. The images

are acquired synchronously with both cameras and stored for posterior analysis at the rates shown in Table 2.3. The frame rates in each experiment define the $\Delta t$ between images within an image pair, as $\Delta t = 1/rate$, as presented in Table 2.4. The same process is repeated for all the velocities considered, once the entire range is covered the mirror is moved to another location and the same process is repeated until a set of images for each velocity in each section is obtained, as shown schematically in Figure 2.13.

(a) 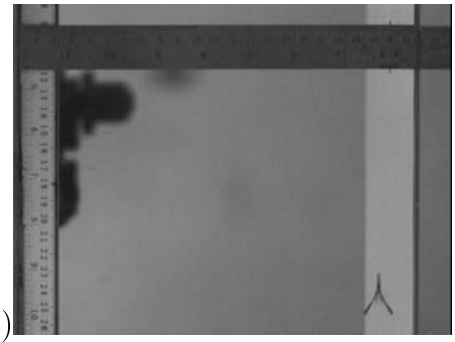 (b) 

Figure 2.12: Calibration images for (a) large FOV, (b) Small FOV.

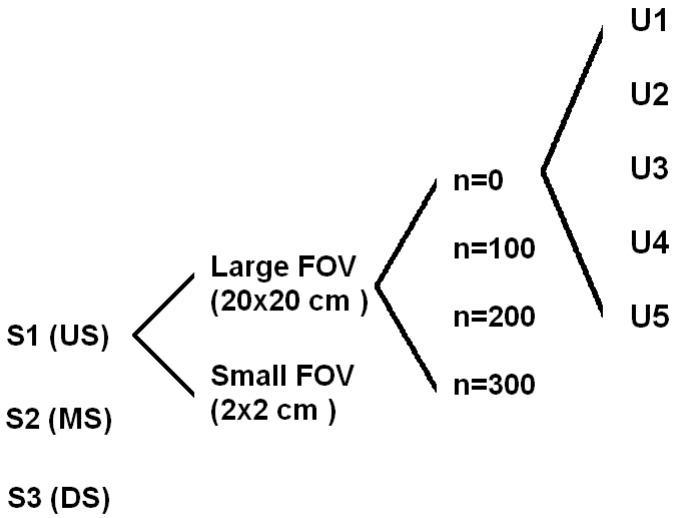


Figure 2.13: Study cases.

Table 2.3: Frame rates for each experiment (fps).

Upstream

| U (cm/s) | n=000 | n=100 | n=200 | n=300 |
|---|---|---|---|---|
| 0.5 | 10 | na | 10 | 10 |
| 1.0 | 20 | na | 20 | 20 |
| 2.0 | 20 | na | 20 | 20 |
| 3.0 | 30 | na | 30 | 30 |
| 4.0 | 30 | na | 30 | 30 |

Midstream

| U (cm/s) | n=000 | n=100 | n=200 | n=300 |
|---|---|---|---|---|
| 0.5 | na | na | 10 | 10 |
| 1.0 | na | na | 20 | 10 |
| 2.0 | na | na | 20 | 20 |
| 3.0 | na | na | 30 | 20 |
| 4.0 | na | na | 30 | 30 |

Downstream

| U (cm/s) | n=000 | n=100 | n=200 | n=300 |
|---|---|---|---|---|
| 0.5 | 10 | 10 | 10 | 10 |
| 1.0 | 20 | 20 | 20 | 20 |
| 2.0 | 20 | 20 | 20 | 30 |
| 3.0 | 30 | 30 | 30 | 30 |
| 4.0 | 30 | 30 | 30 | 30 |

The frequencies are chosen based on different criteria for PIV analysis, such as minimal and maximal particle displacements within an interrogation subwindow. For this analysis, the acquisition frame rate was selected such that the expected displacements were about one quarter of the subwindow's length (thus avoiding biasing), the size of which was decided to get convenient measurements for both large and small FOV.

Images were acquired for periods of 21 minutes for each experiment, yielding sets of 12600, 25200, and 37800 images for the frame rates of 10, 20, and 30fps, respectively. The duration was selected to achieve convergence of the turbulence statistics, as well as to have sets long enough to be divided into subsets for comparison. A more detailed discussion of convergence is presented in Section 3.2.1.3.

Table 2.4: Time between images for each experiment (s).

Upstream

| U (cm/s) | n=000 | n=100 | n=200 | n=300 |
|---|---|---|---|---|
| 0.5 | 0.10 | na | 0.10 | 0.10 |
| 1.0 | 0.05 | na | 0.05 | 0.05 |
| 2.0 | 0.05 | na | 0.05 | 0.05 |
| 3.0 | 0.033 | na | 0.033 | 0.033 |
| 4.0 | 0.033 | na | 0.033 | 0.033 |

Midstream

| U (cm/s) | n=000 | n=100 | n=200 | n=300 |
|---|---|---|---|---|
| 0.5 | na | na | 0.10 | 0.10 |
| 1.0 | na | na | 0.05 | 0.10 |
| 2.0 | na | na | 0.05 | 0.05 |
| 3.0 | na | na | 0.033 | 0.05 |
| 4.0 | na | na | 0.033 | 0.033 |

Downstream

| U (cm/s) | n=000 | n=100 | n=200 | n=300 |
|---|---|---|---|---|
| 0.5 | 0.10 | 0.10 | 0.10 | 0.10 |
| 1.0 | 0.05 | 0.05 | 0.05 | 0.05 |
| 2.0 | 0.05 | 0.05 | 0.05 | 0.033 |
| 3.0 | 0.033 | 0.033 | 0.033 | 0.033 |
| 4.0 | 0.033 | 0.033 | 0.033 | 0.033 |

Following the above procedure, sets of good quality images were obtained providing a wide range to experiment with the analysis parameters. In this way, especially for the large FOV images, it is possible to obtain data using different time separations (lags) and subwindows sizes, as is discussed in section 3.2.

## 2.4 LIF

### 2.4.1 Dye Selection

The dye used in the studies is Rhodamine 6G (Aldrich, Cat. Num. 20,132-4, 95% dye content). An optical filter was used to capture only the fluorescent dye wavelengths avoiding particle reflection of unexcited wavelengths in the images. The

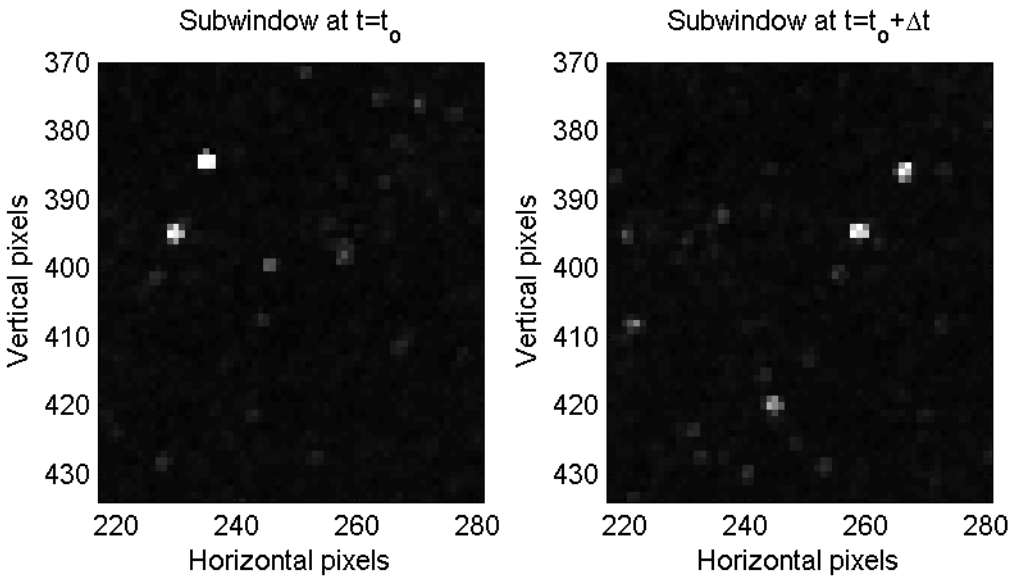


Figure 2.14: Subwindow size and displacement in an image pair.

filter used is a 535-DF-35 X23 Emission filter (Omega Optical Inc.), (Center wavelength of 535nm, Discriminating Filter (DF) with six or more interfering cavities, resulting in a bandpass filter with rectangular shape, very steep edges and very deep blocking up to optical density (OD) 6 outside the passband, Full Width Half Maximum (FWHM) of 35nm, defined as the bandwidth at 50% of the maximum transmission of the filter).

For the selected dye and an Argon-Ion light source (using the same laser as for PIV, at 5W), the excitation and emission spectra are shown in Figure 2.15.

Special attention was paid to the handling of the dye, keeping it away from light sources to avoid photo-bleaching effects.

### 2.4.2 Calibration

The first step was to obtain a set of images for different known concentrations to obtain a calibration curve. This is achieved by adding a volume $V_{Rh}$ with a concentration $C_{Rh} = 57\,PPM$ of Rhodamine 6G to obtain the required concentration

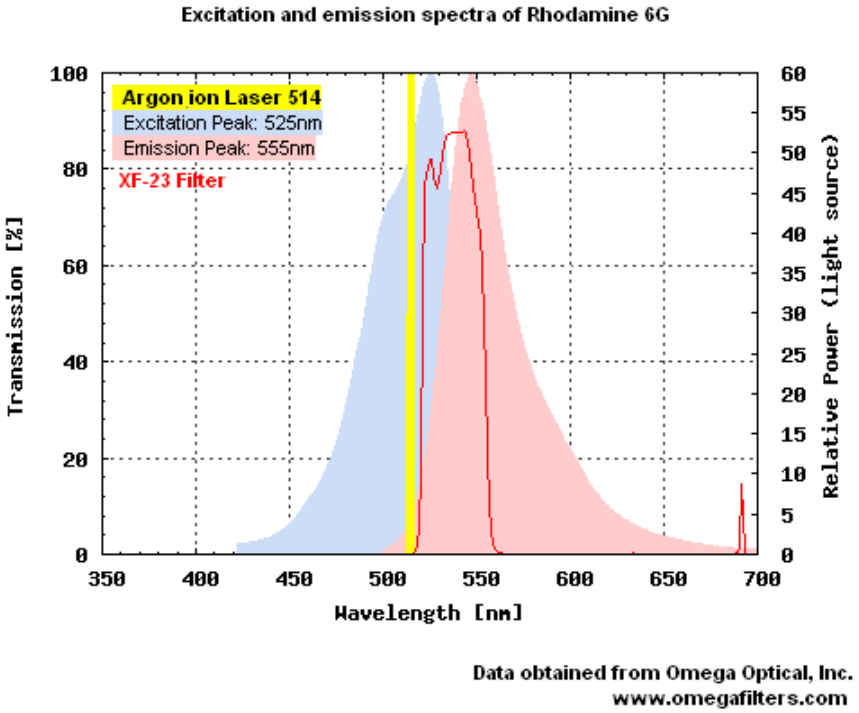


Figure 2.15: Excitation and emission spectra for Rhodamine 6G.

within the flume and running in recirculating mode until homogeneous mixing is observed. Since we can estimate to a good approximation the volume of water in the flume ($V_F$), as seen in Figure 2.16, the resulting concentration $C_F$ is obtained as:

$$C_F = \frac{C_{Rh}V_{Rh}}{V_{Rh} + V_F}$$

Where each term stands for:

$$
\begin{aligned}
C_F &= C\,required\,in\,the\,flume \\
C_{Rh} &= C\,of\,Rhodamine\,6G\,in\,the\,prepared\,solution \\
V_F &= Volume\,of\,water\,in\,the\,flume \\
V_{Rh} &= Volume\,of\,Rhodamine 6G\,solution\,required
\end{aligned}
$$

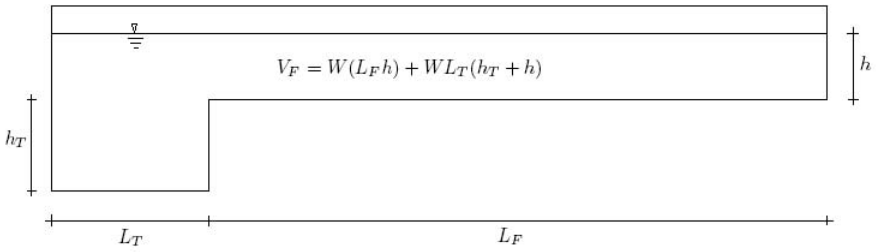


Figure 2.16: Flume dimensions for calibration.

Thus by specifying arbitrary concentrations and adding the respective volume of Rhodamine 6G solution, the concentrations shown in Table 2.5 were obtained.

Table 2.5: Rhodamine 6G concentrations required.

| $C_F$ (PPB) | $V_{Rh}$ (ml) |
|---|---|
| 0 | 0 |
| 10 | 148.5 |
| 20 | 297.0 |
| 40 | 594.3 |

For each concentration, once homogeneous mixing was observed, a set of images was taken for a period of five minutes with an acquisition rate of 10 frames per second using the LIF configuration as explained in section 2.4.3. The mean was taken for each set of images, by taking the intensity value for each pixel and obtaining its mean over the entire set, resulting in one average matrix of intensities for each given concentration.

For each pixel, identified by its row and column location, written as the subindex $(r, c)$, the mean intensity $\overline{I}$ is given as:

$$\overline{I_{(r,c)}} = \sum_{i=1}^{N} I_{(r,c)}^{(i)}$$

Here, the superindex $(i)$ represents the relative number of the frame considered, and $N$ the total number of images in the set.

The area of interest is defined by visual analysis of the mean image obtained, restricting the analysis to the region one pixel below the free surface to one pixel above the bottom, which yields a new area of study of $Nr \times Nc$ pixels (Figure 2.17).

To address the problem of vignetting and the effects of distance from the light source, a pixel by pixel calibration is utilized. As shown in Figure 2.18, each image is divided into sub-cells of $n$ rows by $m$ columns . By doing this, the original area of interest is reduced from $Nr \times Nc$ to $\frac{Nr}{n} \times \frac{Nc}{m}$ (i.e. if $n = m = 1$ the original image is recovered, and if $n = Nr;\ m = Nc$, then we have the simplest case, where all the pixels in the image are averaged to obtain one sole intensity value).

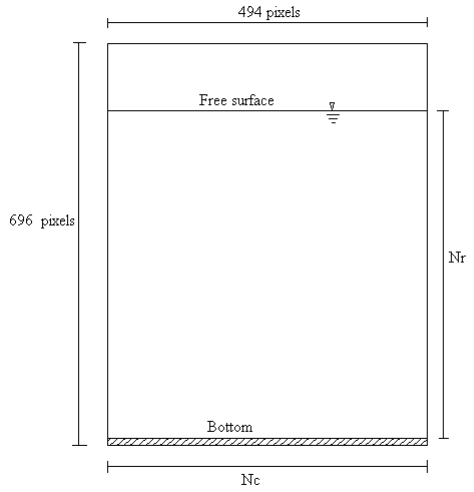


Figure 2.17: Region of interest.

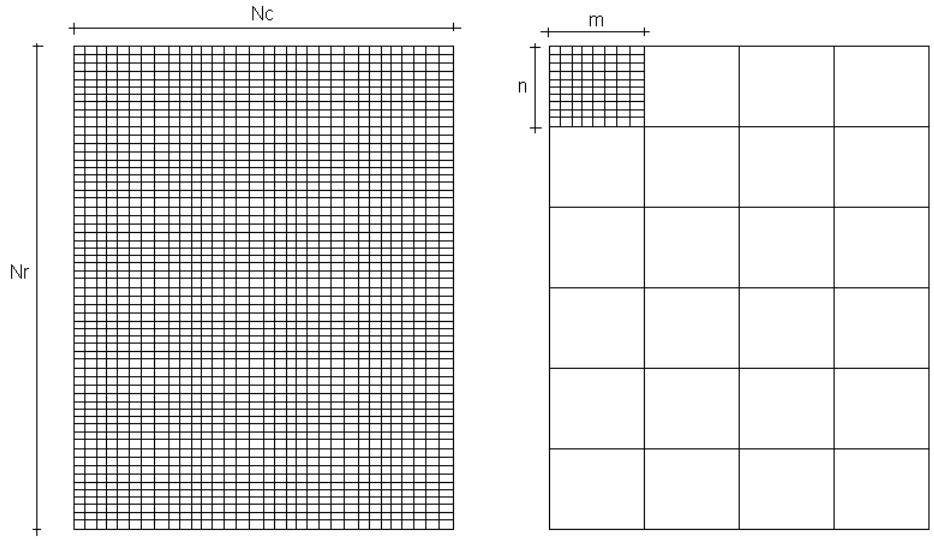


Figure 2.18: Definition of sub-cells.

Once this reduction is achieved, an expression relating intensity $I$ and actual concentration $C$ can be obtained for each sub-cell. For any sub-cell $k$, the relation between I and C is now known, which leads to expressions of the type $C^{(k)} = f^{(k)}(I^{(k)})$. Following the same procedure for each subcell, a total of $\frac{Nr}{n} \times \frac{Nc}{m}$ different functions $C(I)$ are found.

In this way it is possible to divide the region of interest using different patterns for an analysis of vignetting effects, being possible to divide the region in such ways that show the variation in intensity in any direction due to the above mentioned effect. An example of this can be seen if the same process is repeated to divide the images in vertical or horizontal stripes, where the respective variations in intensity by rows (getting away from the free surface) and columns (left to right) are observed. This reinforces the initial selection of a pixel by pixel analysis, which takes into account the possible variations due to location and proximity to the light source.

### 2.4.3 LIF set-up

For each plant density considered, instantaneous (P1) and continuous (P2) dye releases were performed for three different velocities, obtaining the cases shown in Table 2.6 below.

Table 2.6: Velocities and densities considered.

| Density $n$ $(stems/m^2)$ | Nominal velocity $UN$ | | |
|---|---|---|---|
| 0 | $U2$ | $U3$ | $U4$ |
| 100 | $U2$ | $U3$ | $U4$ |
| 200 | $U2$ | $U3$ | $U4$ |
| 300 | $U2$ | $U3$ | $U4$ |

The experimental set-up is shown in Figure 2.19. The dye is released using a peristaltic pump (Cole Parmer Instrument Company, Masterflex Peristaltic Pump 7518-00) with a 1ml/s flow rate. As a diffuser, a porous tube with 6.35mm (0.25") diameter with same length as the flume width is located at mid-depth near the inlet to create a linear source.

Two cameras are located at the sides of the flume in the section located downstream of the vegetated canopy as shown in previous sections. Both cameras start recording once the dye is released and stop once the dye has left the system.

Figure 2.19: Dye injection for LIF.

Once each set of images is captured, each frame is analyzed using a MATLAB routine, converting the intensity value of each pixel into a concentration measure via the calibration explained in section 2.4.2. After this, an average concentration value per frame is obtained, leading to the time series of concentration for each release as shown in section 3.3 .

# Chapter 3

# Results

## 3.1 Plant density imaging

As mentioned in section 2.2.1, a camera (UP-680CL/12B, UNIQ Vision, Inc.) with an incorporated zoom lens (Fujinon-TV zoom lens H6x12.5R, 1:1.2/12.5-75, Fujinon Co.) was used to capture frontal images (perpendicular to the flow direction) in order to obtain the vegetation frontal density. The camera was mounted on the side of the flume, downstream of the canopy, pointing at a mirror set into the water at a 45 degree angle, allowing a good image of the transverse section, as shown in Figure 3.1.

A main concern while processing the images is to determine whether or not the patch can be considered homogeneous. The vegetated patch is divided in slices of 5cm length, both stream- and spanwise, and the number of stems found within each of those slices is plotted for each density considered. This can be seen in Figure 3.2, with the distribution of stems along the x-direction and the spanwise distribution of stems (considering two regions, R1 for the first 100cm of the canopy and region R2 for the last 100cm) in Figure 3.3.

Figure 3.1: Optical acquisition of frontal area (45 degrees mirror).

Even when the density of the canopy varies both stream- and spanwise, the counts along the x-direction fall close to the mean value. The same is not as clear in the y-direction, but still shows a fair spatial distribution, particularly for the $n = 200$ and $n = 300$ cases. Looking at those distributions it is possible to obtain a distance in which the density of the canopy becomes constant, i.e. the length scale at which the cumulative density converges to the nominal density $n$ ($m^{-2}$). Figures 3.4 and 3.5 show the downstream and lateral distance (approximately 0.50 and 0.25cm, respectively) required to reach a quasi-constant vegetation density.

In this way, frontal images can be taken and spatially calibrated by including a ruler within the same images, obtaining sets of pictures as shown in Figure 3.6.

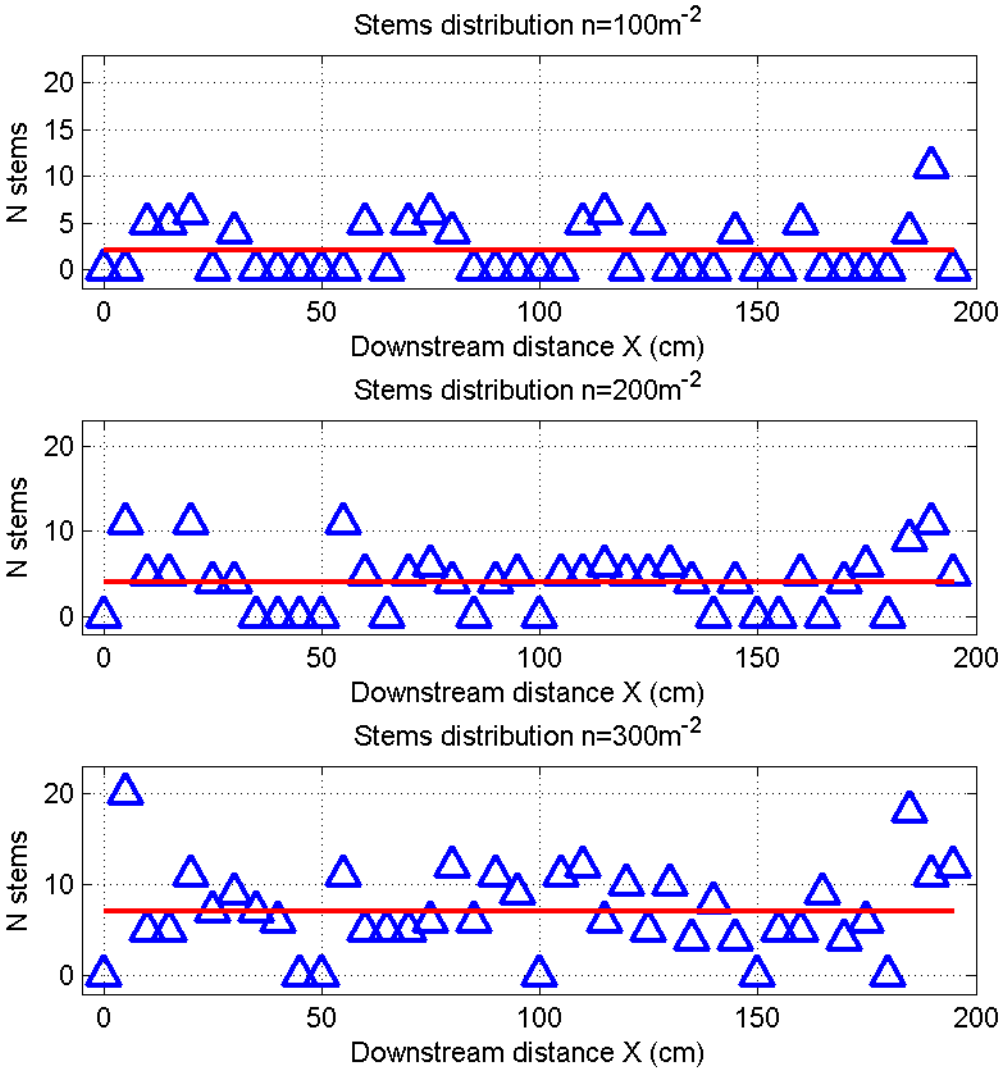


Figure 3.2: Streamwise distribution of stems.

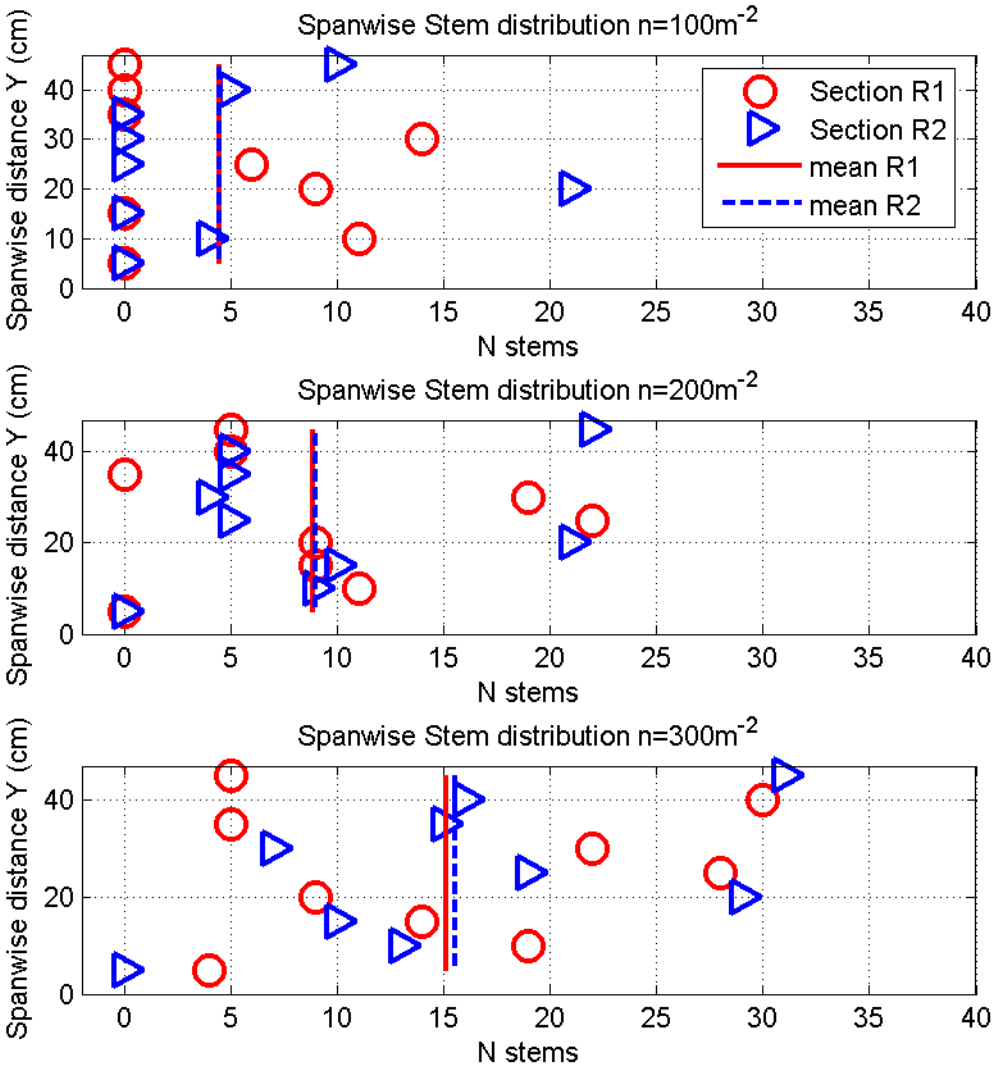


Figure 3.3: Spanwise distribution of stems.

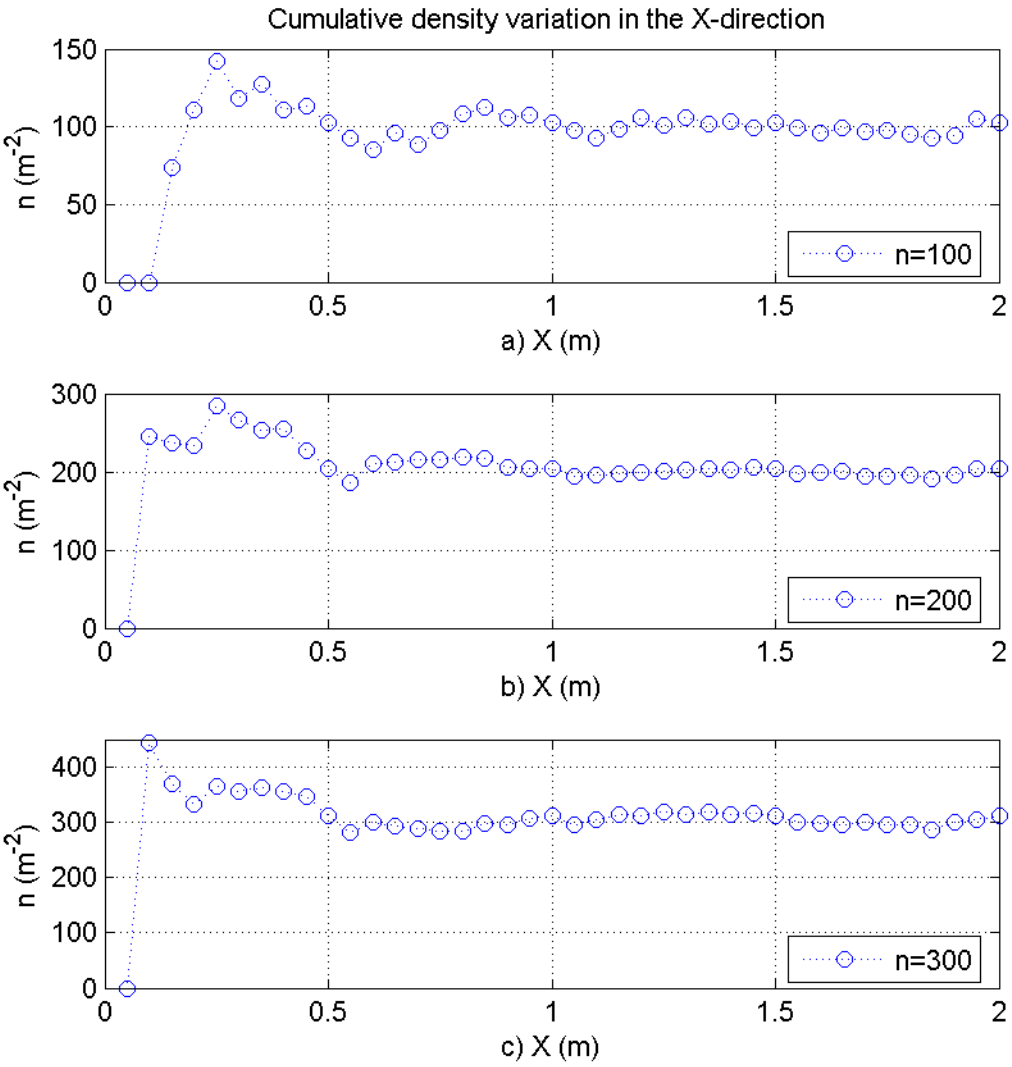


Figure 3.4: Convergence of plant density with downstream distance.

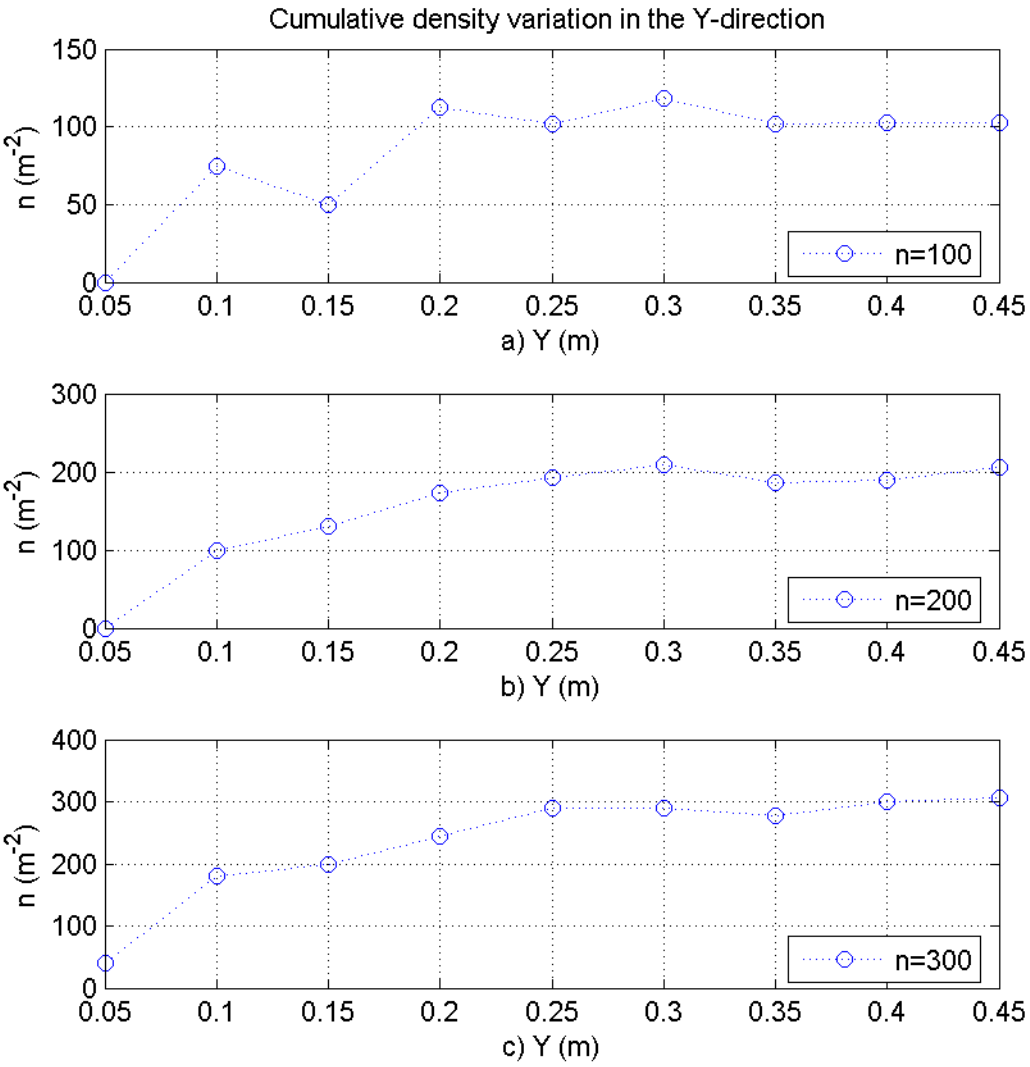


Figure 3.5: Convergence of plant density with lateral distance.

Once the sets of images are acquired, a threshold in intensity is selected manually to separate the vegetated pixels from the background. Using this algorithm, it is possible to pass from the acquired images like Figure 3.6 to a binary image with a clear distinction of the two regions, as shown in Figure 3.7.

To define the appropriate threshold, however, it is necessary to consider other factors, since there is a risk of possible parallax error in the images (the tank side walls showing up at different positions within the image), as well as a non-uniform illumination that could require a spatially dependent threshold, i.e. a different value depending on which region of the images is being considered. To assess this effect, the minimum and maximum intensity values as a function of height for each set of images ($n = 100, 200, 300$) was obtained (Figure 3.8). However, even when the images show a considerable variation of the peak intensity with height, the difference between the values for vegetated and non vegetated pixels remains almost constant, which allows us to use a single value as a threshold for each set.

With that threshold defined, a MATLAB routine is used to count the number of vegetated pixels per line, obtaining the frontal area of the submersed vegetation as a function of depth. This procedure is repeated for different values of $\Delta z$ (i.e. the number of vegetated pixels is counted for $\Delta z = N$ number of rows), as shown in Figure 3.9, for $n = 300$ and $\Delta z = 10$, which is later converted to a percentage of obstructed area, in the process to obtain the parameter of interest $a$ ($m^{-1}$).

This number $N$ clearly depends on the size of the $\Delta z$ considered. To get rid of this dependence it is possible to calculate the percentage of area $PA(\%)$ being covered by vegetation, using the spatial calibration within the same images to get the proper dimensions with respect to the total transversal area of the channel ($TA$). Using the respective $\Delta z$ and the width of the channel ($W$), and considering the total number of stems ($NSs$) that were found for a section of a given length $L$ =0.50m with respect to the number of stems observed in the images ($NSo$) it is

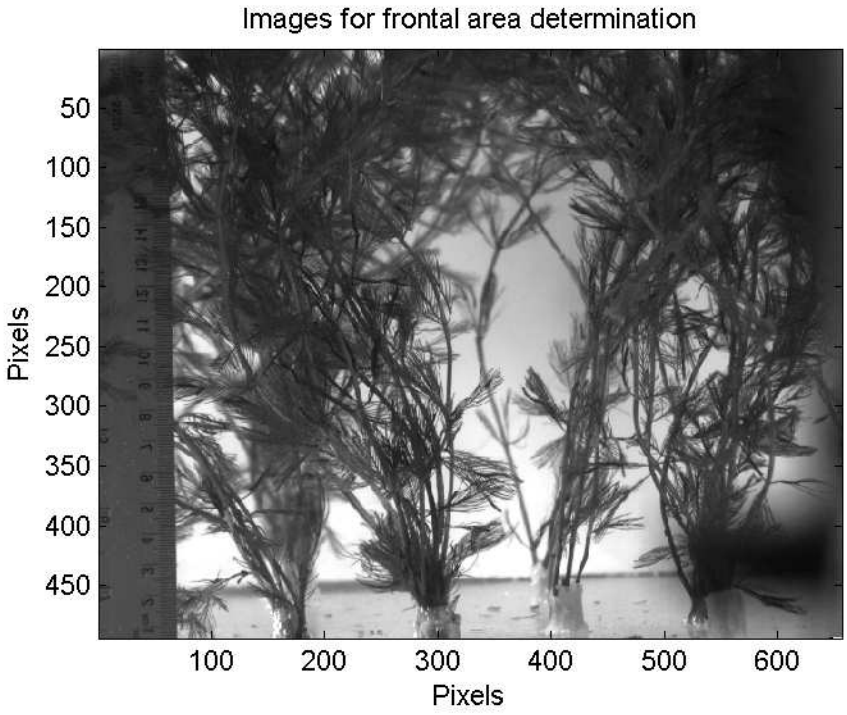


Figure 3.6: Images acquired for determination of frontal area $a(z)$.

possible to calculate the frontal area $a(z)$ as:

$$a(z)(m^{-1}) \quad = \quad (PA)\left(\frac{NSs}{NSo}\right)\left(\frac{(\Delta z)(m)(W)(m)}{(\Delta z)(m)(W)(m)(L)(m)}\right) \tag{3.1}$$

Results are shown in Figure 3.10 for $n = 100, 200, 300$. It is clear the frontal area increases as the vegetation density increases, though it is not as linear as might be expected, which is the way it has been usually considered in studies with mock vegetation.

With the frontal area data available, it is possible to obtain smooth functions by fitting polynomials to the experimental observations, as shown in figure 3.11. This way it's possible to simplify some of the analysis to be presented later.

Furthermore, a similar analysis can be made for different flow velocities. It was assumed that increasing speed would cause the plants to bend, thus changing the

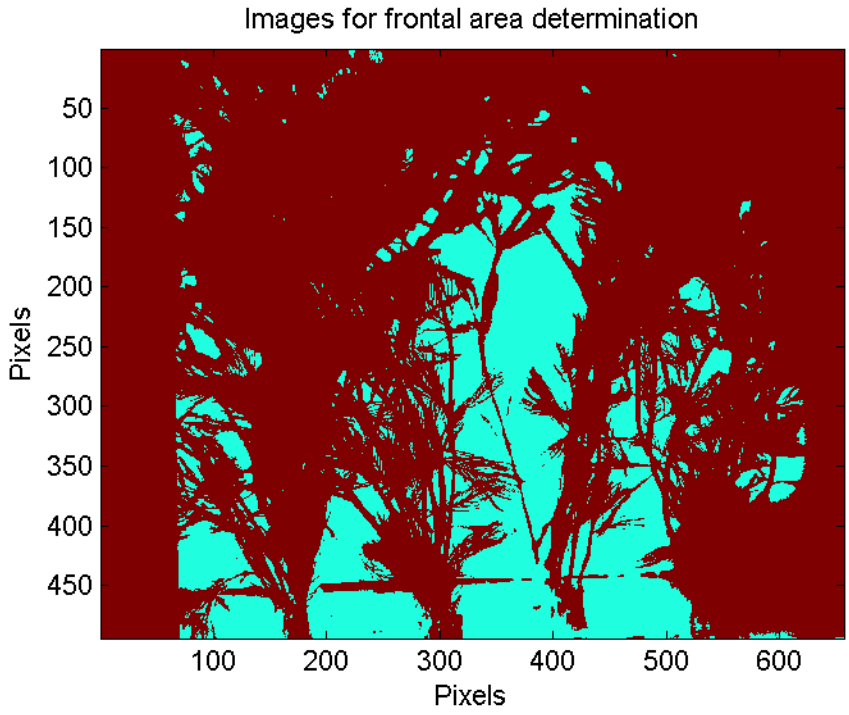


Figure 3.7: Binary images using a constant threshold for vegetated pixels.

values obtained for frontal density from the static case. Taking this into account, different sets of images were acquired for each velocity, yielding the results shown in Figure 3.12. The images were taken looking at the last 50cm of the plant canopy, since it was the region with less visual obstruction for image acquisition. It is observed how by increasing the velocity the frontal area decreases, corresponding to the results expected due to plants bending. The percentage of decrease of frontal area is shown in Figure 3.13.

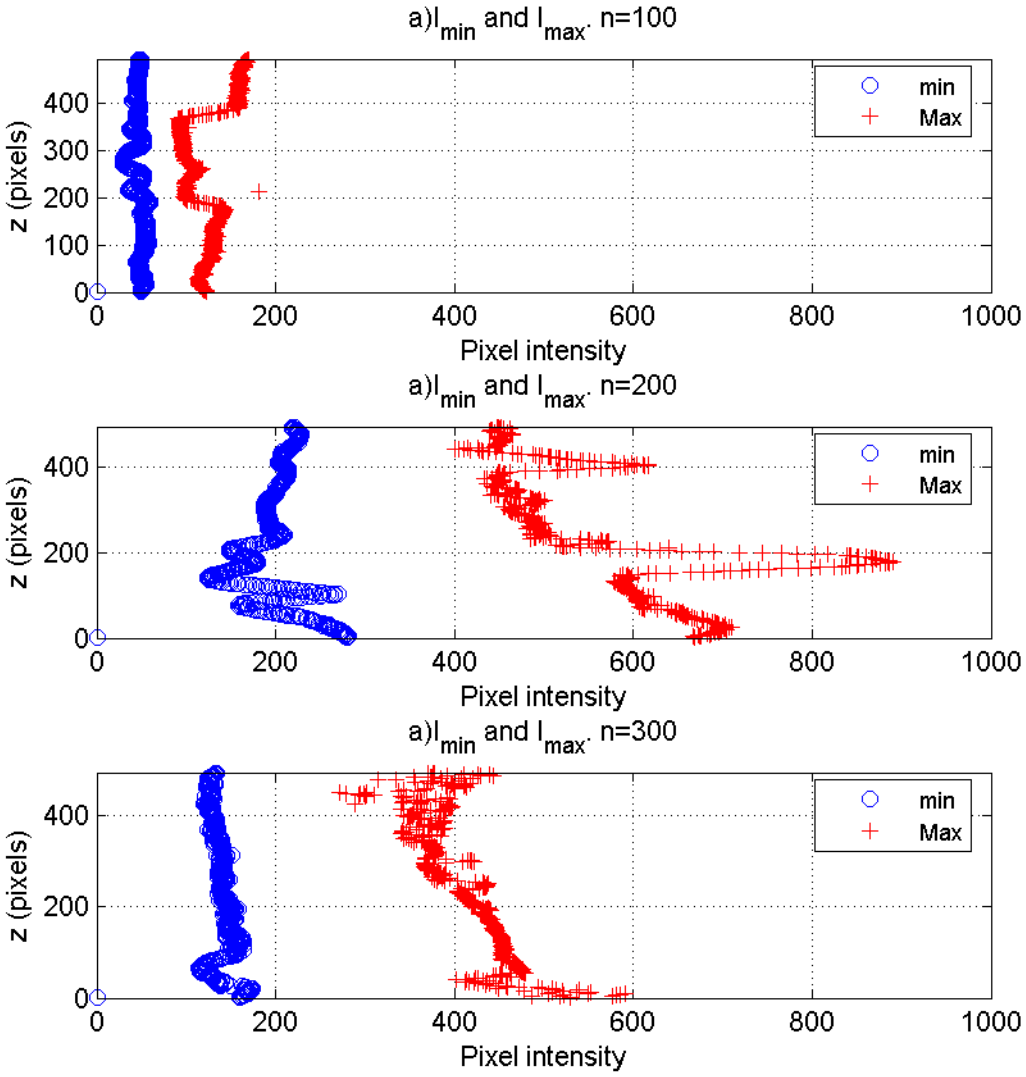


Figure 3.8: Extreme intensity values for each set of images.

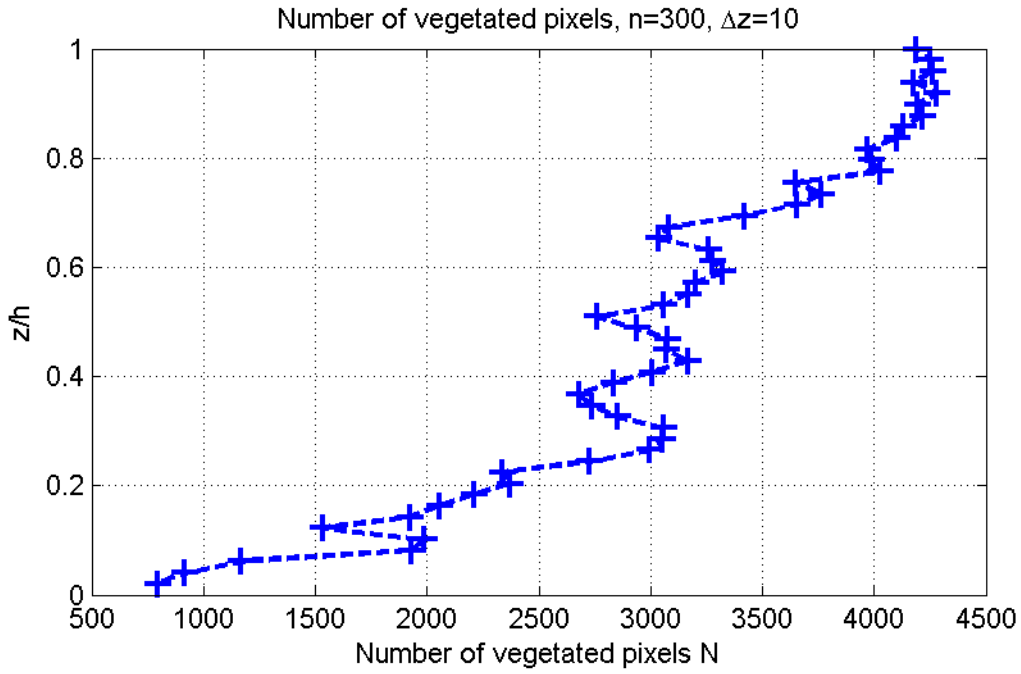


Figure 3.9: Frontal area as a function of depth, for n=300 and $\Delta z = 10$pixels.

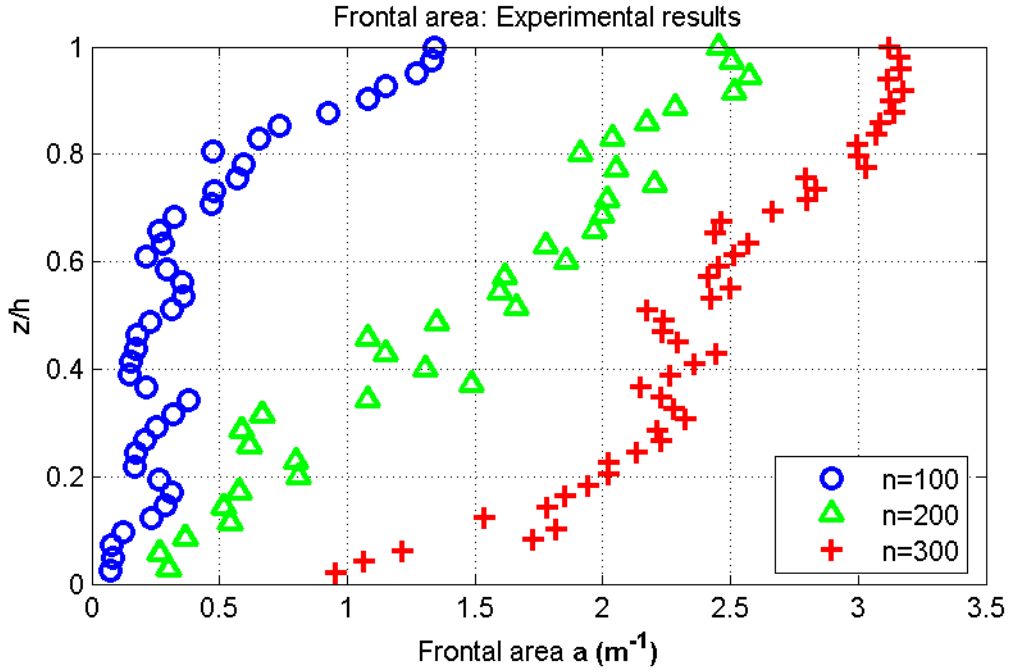


Figure 3.10: Frontal area $a(m^{-1})$ as a function of depth for all the densities considered.

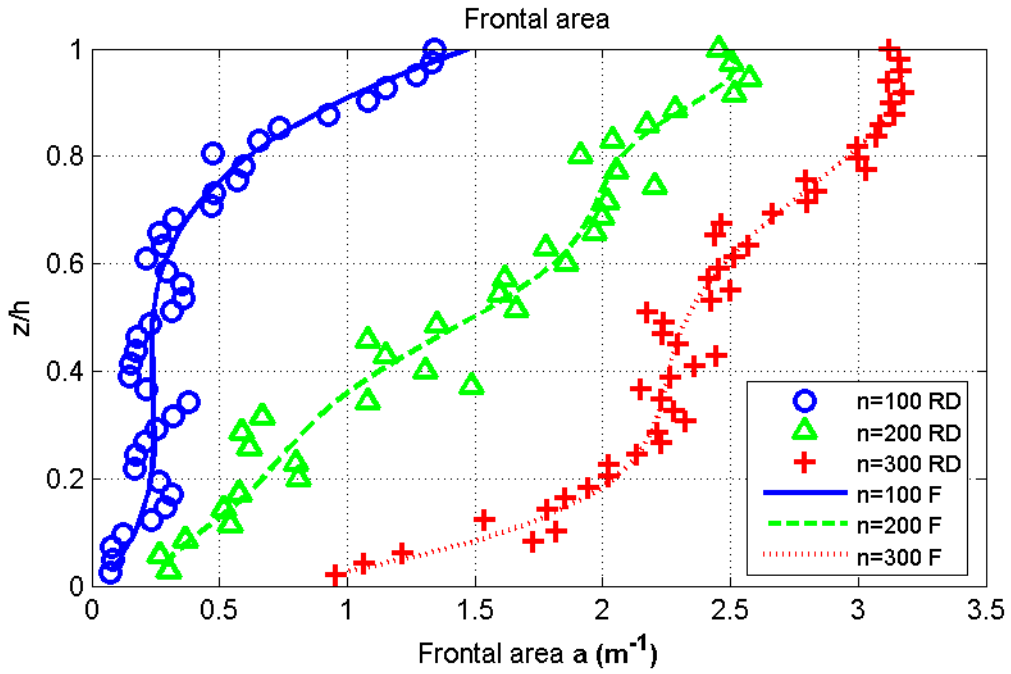


Figure 3.11: Frontal area $a(m^{-1})$ showing the raw data (RD) and the fitted polynomial profiles (F).

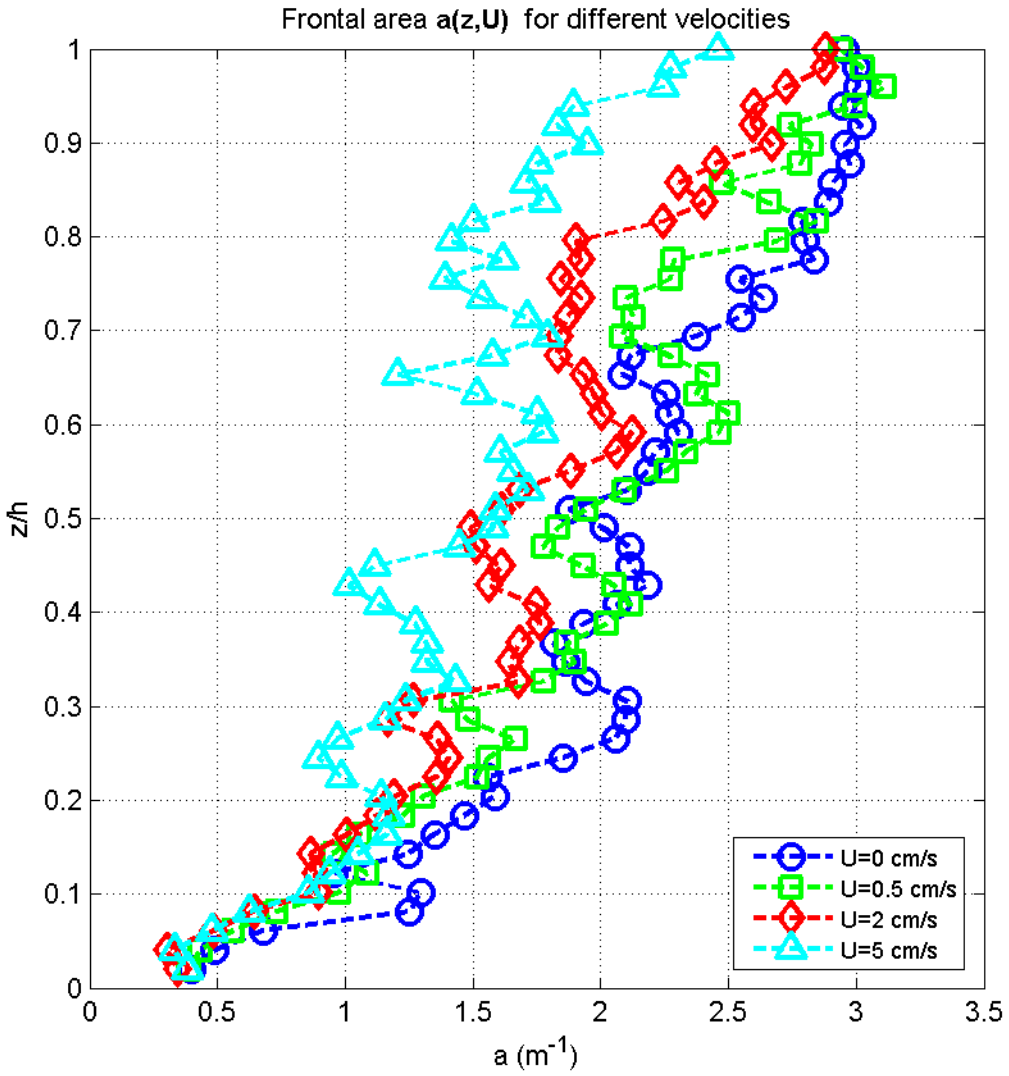


Figure 3.12: Frontal area as a function of depth for different velocities, n=300.

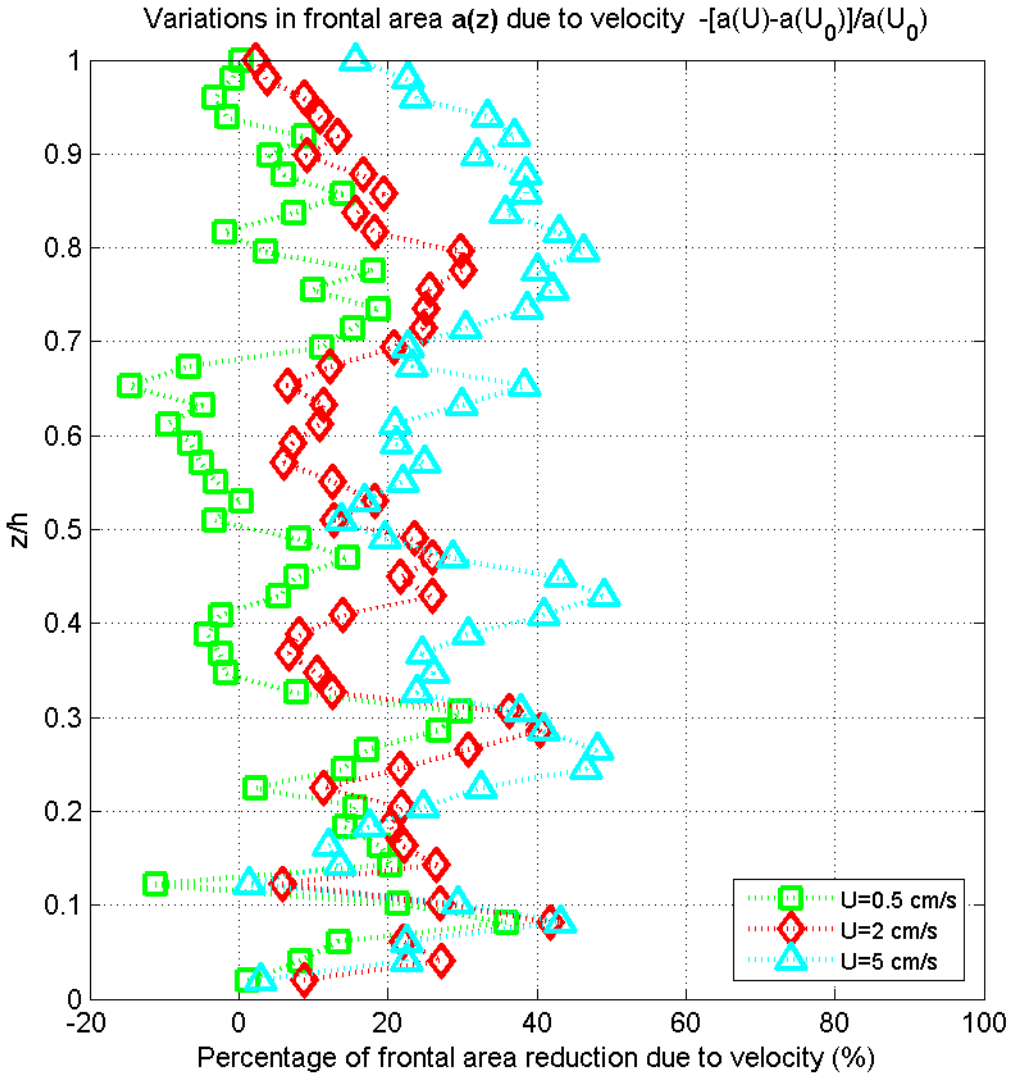


Figure 3.13: Decrease of frontal area $a(z)$ for different velocities, n=300.

Even when the areas change considerably between the slowest and fastest cases studied, there is no simple correlation observed between the increase in velocity and the decrease in frontal area for all the range of velocities $UN$. In order to simplify calculations, for most of the analysis hereafter, the static values (frontal area at $U = 0cm/s$) are used.

## 3.2 PIV Results

### 3.2.1 Base flow: Low Reynolds number channel flow

#### 3.2.1.1 Discussion of Reynolds Number

Channel flow is a well known and broadly studied subject within the field of fluid mechanics. For the purposes of comparison against the classic theoretical benchmarks as well as to the vegetated obstructed flow, it is considered important to analyze the base flows in the experimental facility. Besides, at least to the author's knowledge, there are not many references to studies in channel flow at the velocity range considered for this study, providing an opportunity to apply this technique against a well studied phenomenon but at lower Reynolds number than previous canonical works.

It is convenient to discuss the scales of choice to calculate the Reynolds numbers, $Re = \frac{UL}{\nu}$, where $U$ and $L$ are appropriate velocity and length scales, respectively. Length scales such as the flow depth, length of the plant canopy patch, stem diameter or spacing between plants are the most usual choices, and a detailed analysis must be done to select a Reynolds number representative of the scales of motion within the patch.

For channel flow, a common parameter is the Reynolds number based on the hydraulic radius, $Re_{Rh} = \frac{UR_h}{\nu}$ , where $R_h$ is obtained from the ratio of cross

sectional area of flow over the wetted perimeter, $R_h = \frac{A}{P_w}$. Using $H$=0.24m, and the flume width $B$=0.46m, the hydraulic radius is roughly $R_h$=0.12m. For the range of velocities from $U1$ to $U5$, this yields a range of $Re_{Rh}$=(600-6000), which falls well within the limits of turbulent channel flow.

Previous works have used a streamwise length scale of the element (usually diameter $d$) and a depth averaged streamwise velocity to calculate a stem Reynolds number, $Re_d = \frac{\langle\overline{u}\rangle d}{\nu}$, assumed to control the flow around individual stems (Raupach and Thom 1981, Lightbody and Nepf 2006), and a depth Reynolds number $Re_H = \frac{\langle\overline{u}\rangle H}{\nu}$ (Nepf et. al. 1997a, Lightbody and Nepf 2006). A flow shear Reynolds number using the water depth $H$ and the friction velocity $u_*$, ($Re = \frac{u_* H}{\nu}$), can also be used to account for the turbulent scales (Lopez and Garcia 1997). Other options include a hydraulic radius Reynolds number, $Re_{hr} = \frac{Q}{(2H+b)\nu}$, and a mixing layer Reynolds number based on the thickness of the mixing layer ($t_{ml}$) for submerged vegetation, $Re = \frac{\Delta U t_{ml}}{\nu}$ (Ghisalberti 2005). For the present case, it is possible to calculate a depth Reynolds number $Re_H$ as well as a stem based one $Re_d$, yielding the ranges $Re_H = \{700 - 9000\}$ and $Re_d = \{6 - 70\}$. For comparison to the boundary layer approaches, Reynolds numbers are also calculated using the displacement thickness, $\delta* = \int_0^\infty \left(1 - \frac{\langle\overline{U}\rangle}{U_0}\right) dz$, and the momentum thickness, $\theta = \int_0^\infty \frac{\langle\overline{U}\rangle}{U_0} \left(1 - \frac{\langle\overline{U}\rangle}{U_0}\right) dz$. Since the longitudinal velocity profiles for vegetated flow present a shape similar to a mixing layer in the region with faster increase of vegetation density, it is also possible to evaluate a mixing layer thickness $t_{ml}$, as the vertical distance separating the less vegetated region with higher speed flow and the low speed upper region, and a characteristic velocity difference $\Delta U$ as the difference between the velocities at those regions, to calculate $Re_{t_{ml}} = \frac{\Delta U t_{ml}}{\nu}$. The calculated values are presented in Table 3.1.

Table 3.1: Reynolds numbers.

| | | $Re_H$ | $Re_d$ | $Re_\theta$ | $Re_{\delta^*}$ | $Re_{t_{ml}}$ |
|---|---|---|---|---|---|---|
| n=000 | U1 | 2149 | 15 | 42 | 69 | NA |
| | U2 | 3460 | 24 | 84 | 123 | NA |
| | U3 | 5067 | 35 | 162 | 235 | NA |
| | U4 | 7240 | 48 | 187 | 250 | NA |
| | U5 | 8641 | 58 | 261 | 404 | NA |
| n=100 | U1 | 1817 | 13 | 51 | 80 | 593 |
| | U2 | 2735 | 19 | 59 | 101 | 826 |
| | U3 | 3814 | 26 | 70 | 104 | 1027 |
| | U4 | 5475 | 37 | 98 | 255 | 1093 |
| | U5 | 7126 | 48 | 125 | 208 | 1001 |
| n=200 | U1 | 1262 | 9 | 22 | 28 | 267 |
| | U2 | 2698 | 19 | 68 | 97 | 1586 |
| | U3 | 4283 | 30 | 87 | 112 | 2459 |
| | U4 | 5512 | 37 | 104 | 137 | 3389 |
| | U5 | 6746 | 45 | 119 | 152 | 3294 |
| n=300 | U1 | 1002 | 7 | 36 | 52 | 429 |
| | U2 | 2592 | 18 | 44 | 59 | 1713 |
| | U3 | 4102 | 28 | 77 | 106 | 2643 |
| | U4 | 6064 | 42 | 91 | 134 | 3928 |
| | U5 | 7752 | 52 | 108 | 124 | 2841 |

In general, the Reynolds numbers calculated for this work are lower than the observed by other authors, as seen in Table 3.2.

Table 3.2: Reynolds numbers from other authors.

| Reference | Range of Reynolds numbers considered |
|---|---|
| Spalart (1986) | $Re_\theta = 1410$ |
| Cowen and Monismith (1997) | $Re_\theta = 1300$ |
| Dunn et. al. (1996) | $Re_H = 57000 - 258000$ |
| Lopez and Garcia (2001) | $Re_H = 57000 - 258000$ |
| Stephan and Gutknecht (2002) | $Re_H = 1230000 - 2830000$ |
| Neary (2003) | $Re_H = 6937 - 29433$ |
| Wilson et. al. (2003) | $Re_H = 6000 - 20000$ |
| Jarvela (2004) | $Re_H = 24200 - 178000$ |
| Murphy (2006) | $Re_H = 3000 - 41000$ |
| Koch and Ladd (1997) | $Re_d = 0 - 180$ |
| Nepf et. al. (1997a) | $Re_d = 66 - 1800$ |
| Nepf and Vivoni (2000) | $Re_d = 80 - 4500$ |
| Rowinski and Kubrak (2002) | $Re_d = 800 - 100000$ |
| Ghisalberti and Nepf (2006) | $Re_d = 70 - 240$ |
| Tanino and Nepf (2008) | $Re_d = 25 - 685$ |
| Ghisalberti (2005) | $Re_{t_{ml}} = 3400 - 38000$ |

These differences require us to use different approaches to compare the results with those of other researchers, since some of their assumptions don't apply for the range of Reynolds numbers considered on this work.

#### 3.2.1.2 PIV data process

All the images obtained were analyzed with a set of FORTRAN routines (implemented by Edwin A. Cowen, Cornell University and outlined in Cowen and Monismith, 1997). The input parameters for this analysis depend on the frequency at which the images were taken, the calibration images for each set and the estimated velocity for each case, which determine the size of the subwindows.

The software consists of three main codes. The first one is an image preprocessor to make sure that all the images in the set have been exposed to a light

source. It provides the global minimum intensity images for each pair within the set, which are later subtracted as background from the analysis to improve the signal to noise ratio. Another code performs cross-correlation based PIV to extract the mean displacements from the subwindows. Finally, the last code reads in the raw displacement data, and removes outliers using an adaptive Gaussian filter and a local median filter, and yields the filtered PIV data as well as the PIV statistics.

The analysis was done in three steps. The size of the subwindows is fixed to $32 \times 32$ pixels, with an overlapping of 50%. After running the program once, an estimate of the raw displacement (in pixels per frame) for each subwindow is obtained. With this result as an input, the code runs again estimating each subwindow's location by using the mean displacement from the previous step. Finally, a third step uses the instantaneous displacements obtained from step 2 to estimate the position of the subwindows to calculate a new adjusted displacements.

To address the validity of the results, the percentage of valid vectors obtained from each image pair is calculated and plotted against the pair number, which allows the detection of periods of time in which there is not enough or accurate information to proceed with the calculations (due to problems of illumination or temporary freezing of the mirror or shutter). However, such conditions are rarely found within the data set for periods longer than fractions of a second, as shown in Figure 3.14, for the higher density $n = 300$, in which in general there is an average of 90% or more valid vectors for every set, percentage taken out of a total number of vectors from each pair. The total number corresponds to the number of subwindows within the images, approximately 1000 using square subwindows of 32×32 pixels with a 50% overlapping (e.g., 29 subwindows in the longitudinal direction and 35 in the vertical, giving a total of 1015 possible vectors, yielding more than 900 valid vectors on average per image pair).

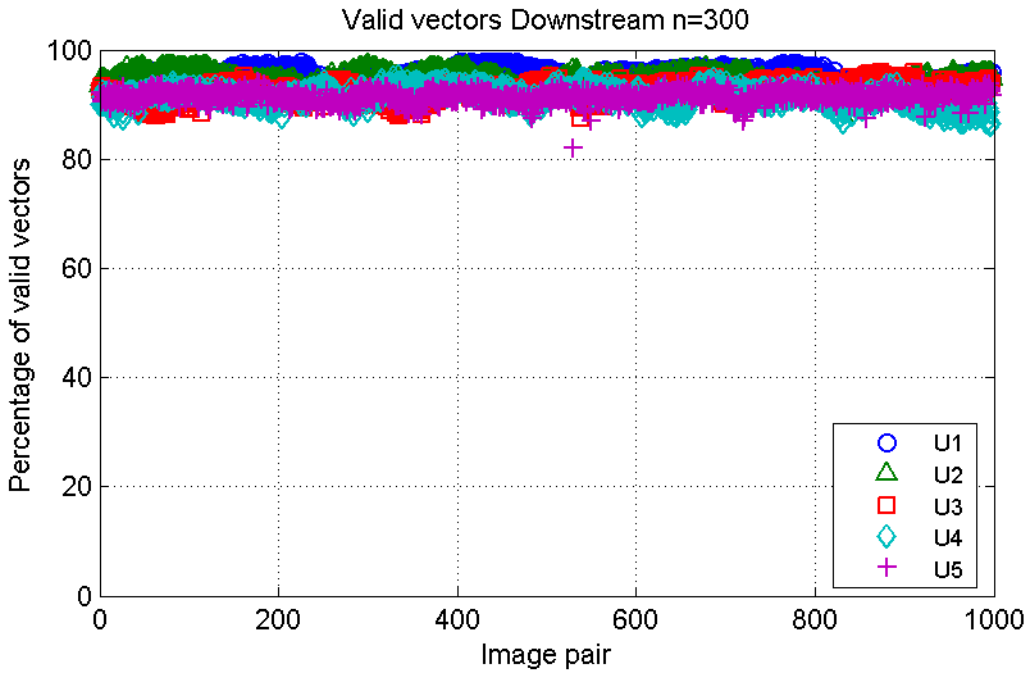


Figure 3.14: Percentage of valid vectors.

The number of valid vectors for particular subwindow locations is also calculated. The time series of longitudinal velocity from the raw displacement data at locations near the free surface (FS), mid-depth (MD), and near the wall (NW), for the flow rates $U1$ and $U5$, $n$=300 case are presented in Figure 3.15, where the most evident outliers are clearly noticed . The number and percentage of valid vectors for the FS, MD, and NW locations at three horizontal transects is presented in Tables 3.3 and 3.4, for the $U1$ and $U5$ flow velocities at $n$=0 and $n$=300.

All the results from the selected locations have more than 90% valid vectors. Similar results (>90%) are found for all the other cases, with some exceptions in subwindows located at the edges of the images, which can be a result of illumination problems.

The program writes as output files the raw and filtered X and Y displacement data, the mean displacement ($\overline{u}_i$) and root mean square values ($u_{RMS_i}$) for both directions, as well as Reynolds stress $\overline{u'v'}$ .

Table 3.3: Number of valid vectors on particular subwindows locations.

| | $n$=0 | | | | | |
|---|---|---|---|---|---|---|
| | $U1$ | | | $U5$ | | |
| | $x_1$ | $x_2$ | $x_3$ | $x_1$ | $x_2$ | $x_3$ |
| FS | 4813 | 4788 | 4795 | 4939 | 4832 | 4773 |
| MD | 4737 | 4585 | 4612 | 4296 | 4917 | 4898 |
| NW | 4907 | 4924 | 4909 | 4909 | 4900 | 4889 |
| | $n$=300 | | | | | |
| | $U1$ | | | $U5$ | | |
| | $x_1$ | $x_2$ | $x_3$ | $x_1$ | $x_2$ | $x_3$ |
| FS | 4815 | 4927 | 4942 | 4927 | 4944 | 4945 |
| MD | 4933 | 4934 | 4914 | 4855 | 4962 | 4941 |
| NW | 4917 | 4834 | 4936 | 4665 | 4601 | 4533 |

Table 3.4: Percentage of valid vectors on particular subwindows locations.

| | $n$=0 | | | | | |
|---|---|---|---|---|---|---|
| | $U1$ | | | $U5$ | | |
| | $x_1$ | $x_2$ | $x_3$ | $x_1$ | $x_2$ | $x_3$ |
| FS | 96.3 | 95.8 | 95.9 | 98.8 | 96.6 | 95.5 |
| MD | 94.8 | 91.7 | 92.2 | 98.5 | 98.3 | 97.9 |
| NW | 98.1 | 98.5 | 98.2 | 98.2 | 98.0 | 97.8 |
| | $n$=300 | | | | | |
| | $U1$ | | | $U5$ | | |
| | $x_1$ | $x_2$ | $x_3$ | $x_1$ | $x_2$ | $x_3$ |
| FS | 96.3 | 98.5 | 98.8 | 98.6 | 98.9 | 98.9 |
| MD | 98.7 | 98.7 | 98.3 | 97.1 | 99.2 | 98.8 |
| NW | 98.3 | 96.7 | 98.7 | 93.3 | 92.0 | 90.7 |

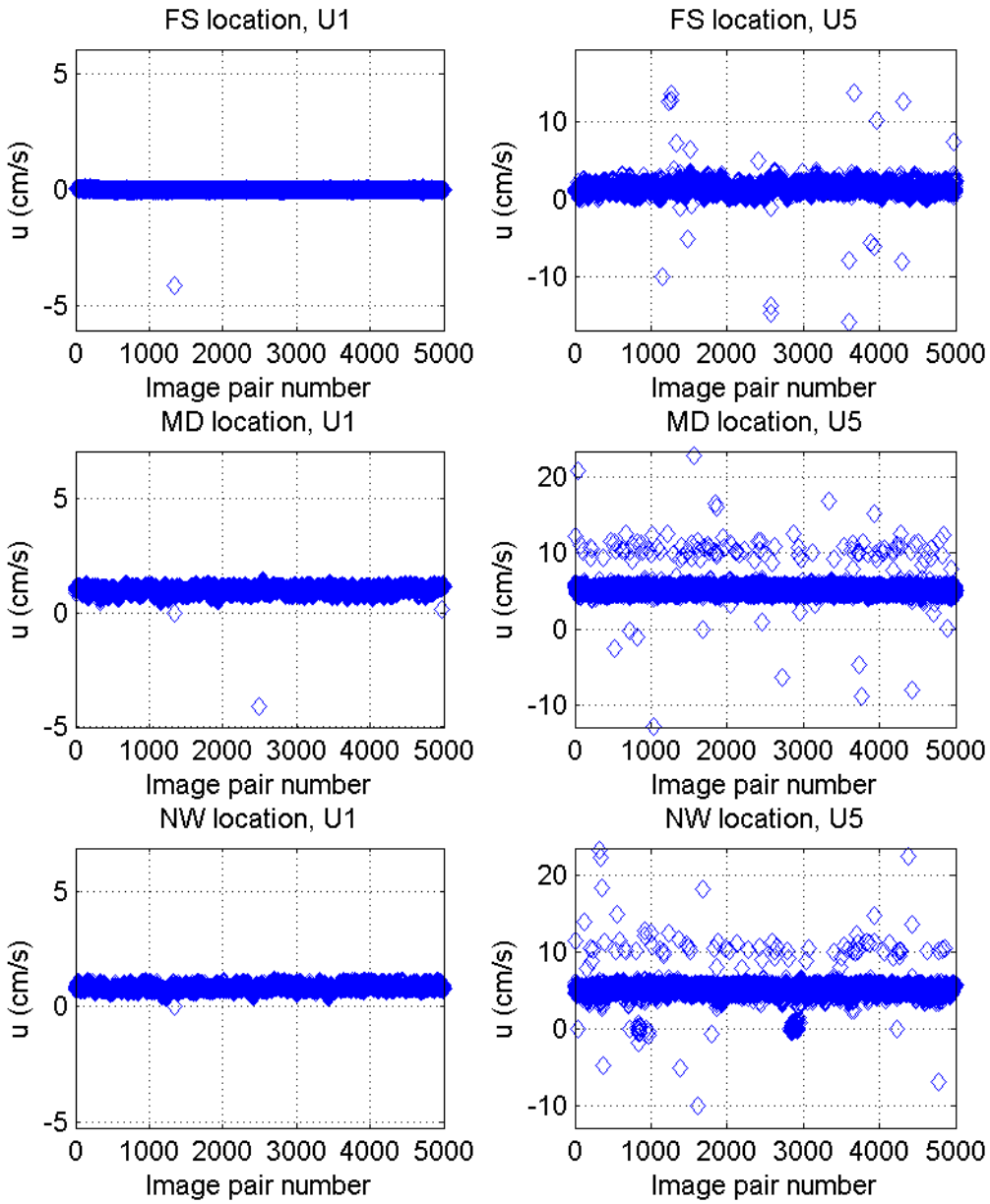


Figure 3.15: Time series of longitudinal velocity $u$ $(cm/s)$, at three vertical locations, n=300.

All displacements obtained by using this software are converted form $pixel/frame$ to $cm/s$ by a simple conversion using the frame rate (same as the scanning rate in this experiment) at which the respective image set was recorded and the ratio $cm/pixels$ obtained from the calibration of such set, i.e.

$$U(cm/s) = U(\frac{pixels}{frame}) \cdot rate(\frac{frame}{second}) \cdot ratio(\frac{cm}{pixels})$$

To analyze the behavior of the flow in the near-bottom region, the small FOV-PIV images (herein SFOV) are analyzed and matched to the large FOV (LFOV) results, as presented in Figure 3.16, for the case of $U3$, $n = 0$.

There is a good match between the mean velocity results from the synchronous large and small FOV images, but some differences are found in the $\langle u_{rms} \rangle$ and $\langle \overline{u'w'} \rangle$ profiles, possibly due to the difference in image resolution for each case.

It is also important to analyze the convergence of the data, as mentioned in section 2.3.2. The quantities $\langle \overline{u} \rangle$, $\langle \overline{w} \rangle$, $\langle \overline{u_{rms}} \rangle$, $\langle \overline{w_{rms}} \rangle$, and $\langle \overline{u'w'} \rangle$, for minimum and maximum velocity ($U1$ and $U5$), for the $n$=0 and $n$=300 cases, were calculated for sets of up to 5000 image pairs analyzed (spanning 1000s and 333s for $U1$ and $U5$ respectively), yielding the results shown in Figures 3.17 to 3.26.

For mean velocities, there is a faster convergence, reaching a range of $\pm 1\%$ of the mean value of the whole set in approximately 500s for $U1$ and less than 100s for $U5$. For turbulence intensities and Reynolds stress, as expected, it takes longer for them to converge to a $\pm 5\%$, but they still do so within the duration of the experiment.

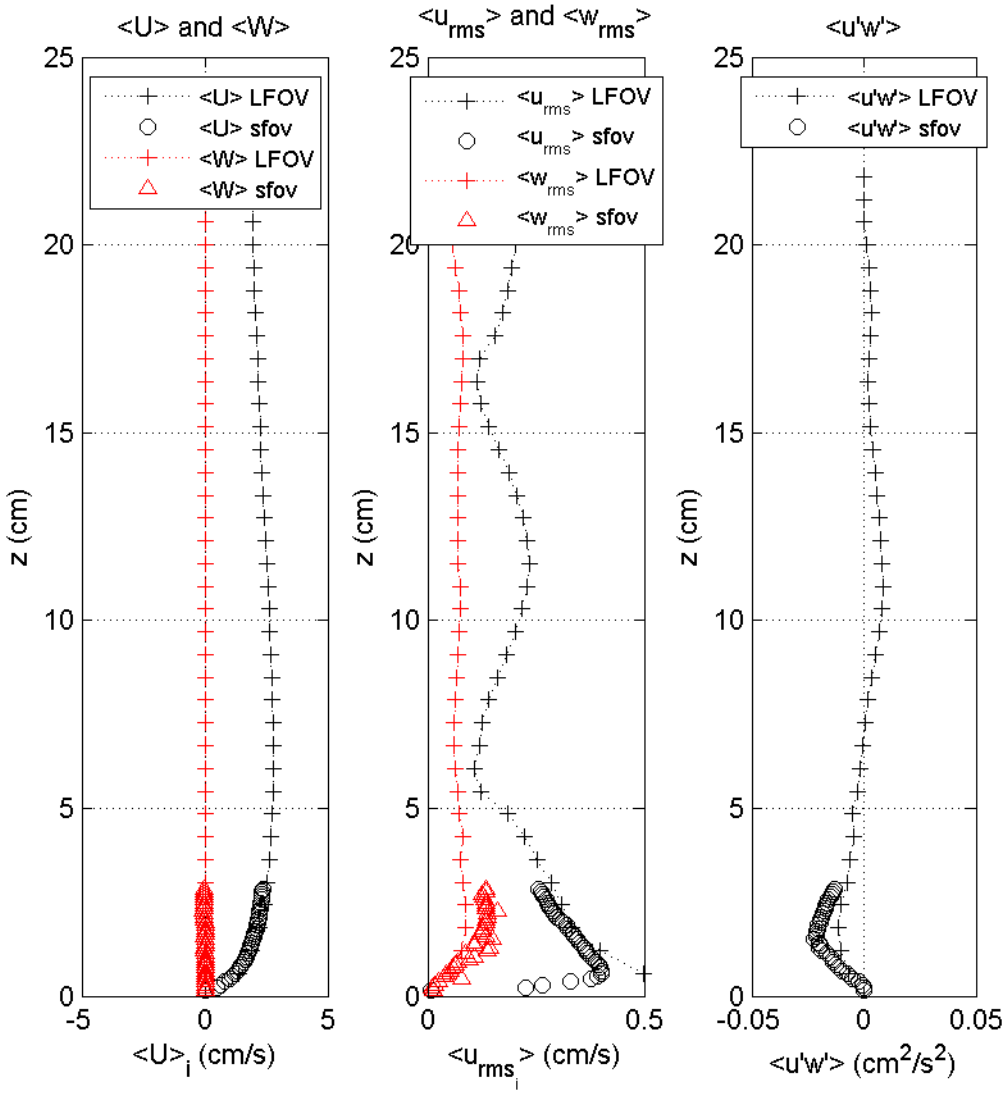


Figure 3.16: Profiles for small and large FOV, U3, n=0.

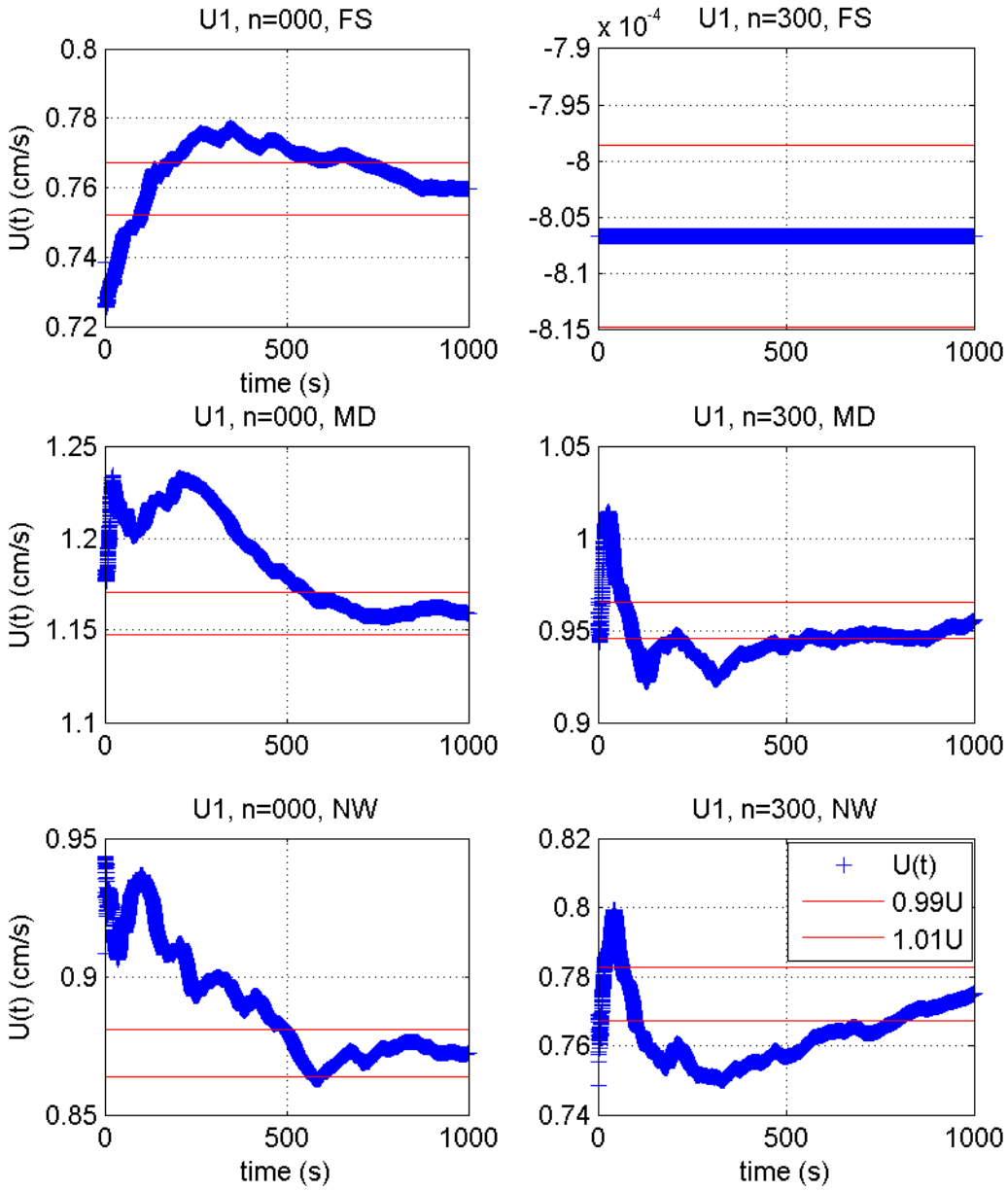


Figure 3.17: Convergence of $\langle \overline{u} \rangle$ $(cm/s)$, for $n$=0 and $n$=300, $U1$.

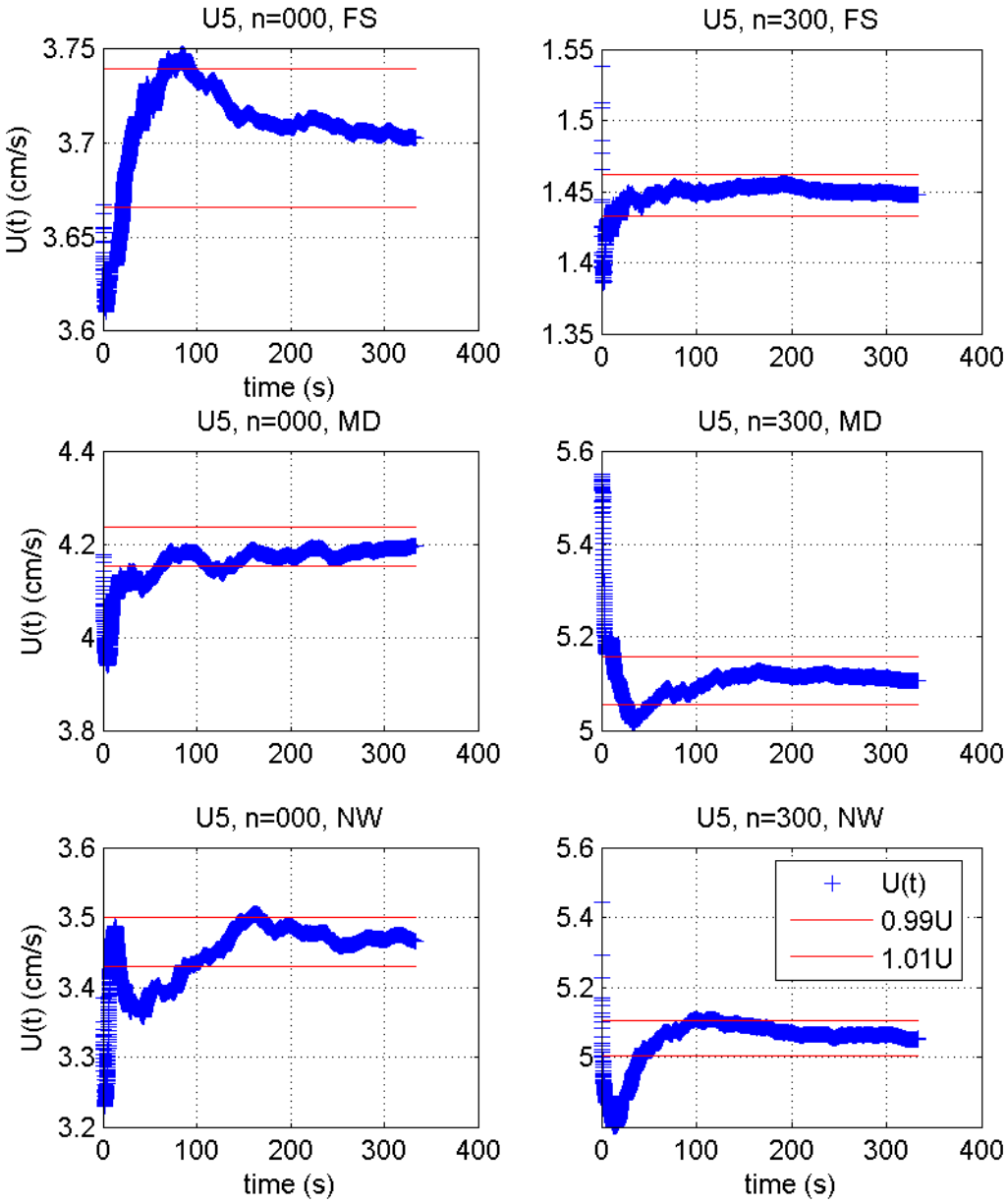


Figure 3.18: Convergence of $\langle \overline{u} \rangle$ $(cm/s)$, for $n$=0 and $n$=300, $U5$.

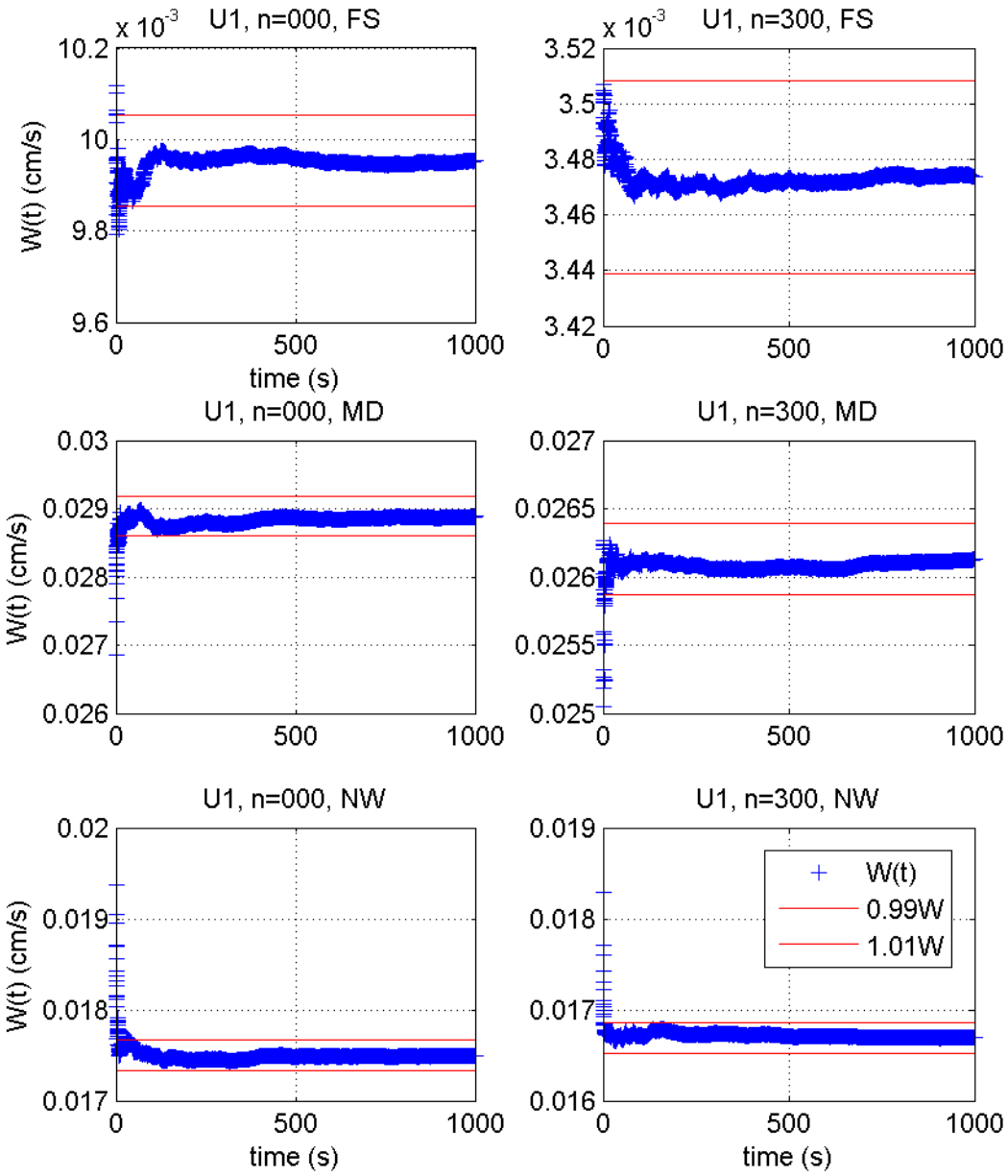


Figure 3.19: Convergence of $\langle \overline{w} \rangle$ $(cm/s)$, for $n$=0 and $n$=300, $U1$.

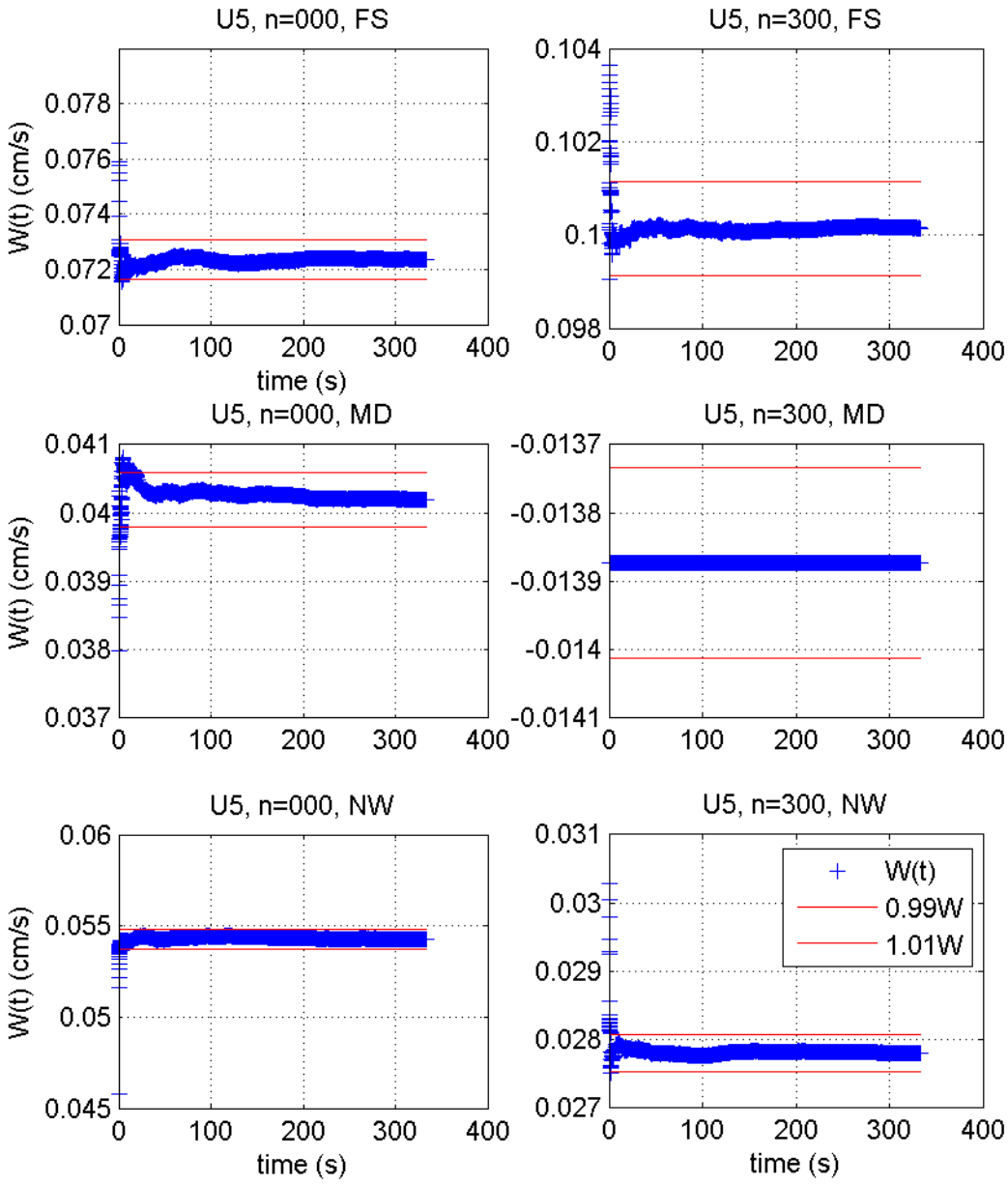


Figure 3.20: Convergence of $\langle \overline{w} \rangle$ $(cm/s)$, for $n$=0 and $n$=300, $U5$.

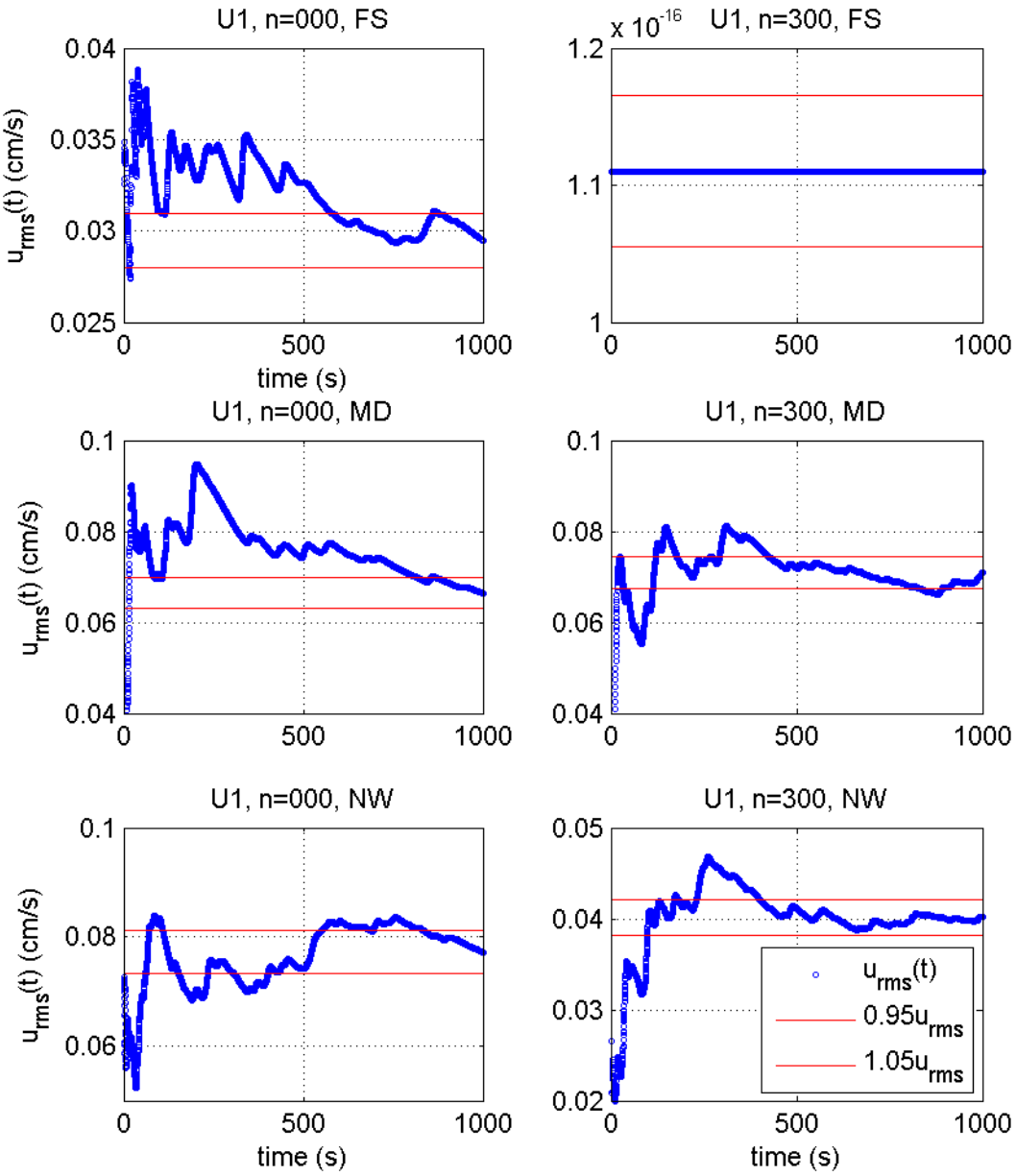


Figure 3.21: Convergence of $\langle\overline{u_{rms}}\rangle$ $(cm/s)$, for $n$=0 and $n$=300, $U1$.

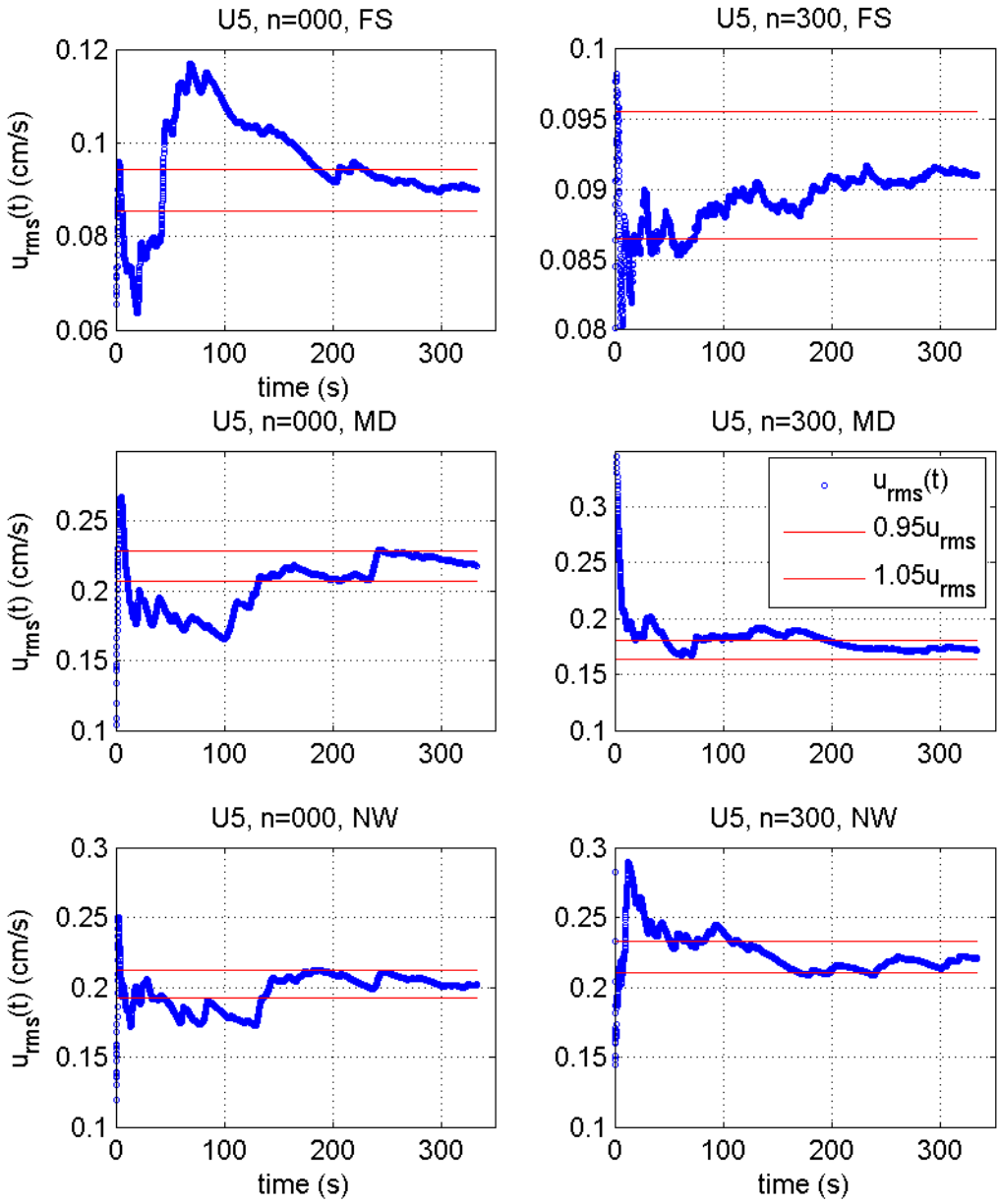


Figure 3.22: Convergence of $\langle\overline{u_{rms}}\rangle$ $(cm/s)$, for $n$=0 and $n$=300, $U5$.

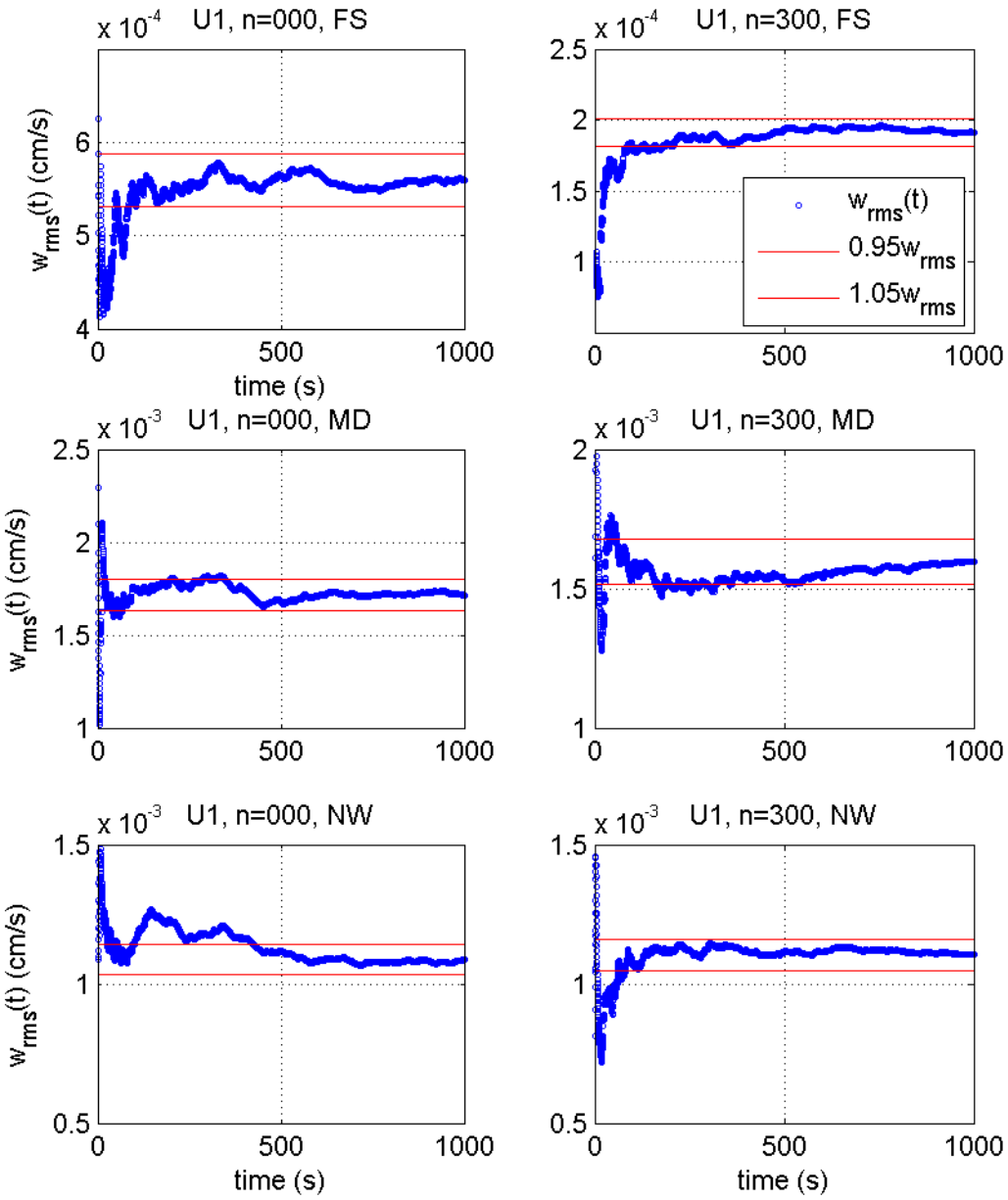


Figure 3.23: Convergence of $\langle\overline{w_{rms}}\rangle$ $(cm/s)$, for $n$=0 and $n$=300, $U1$.

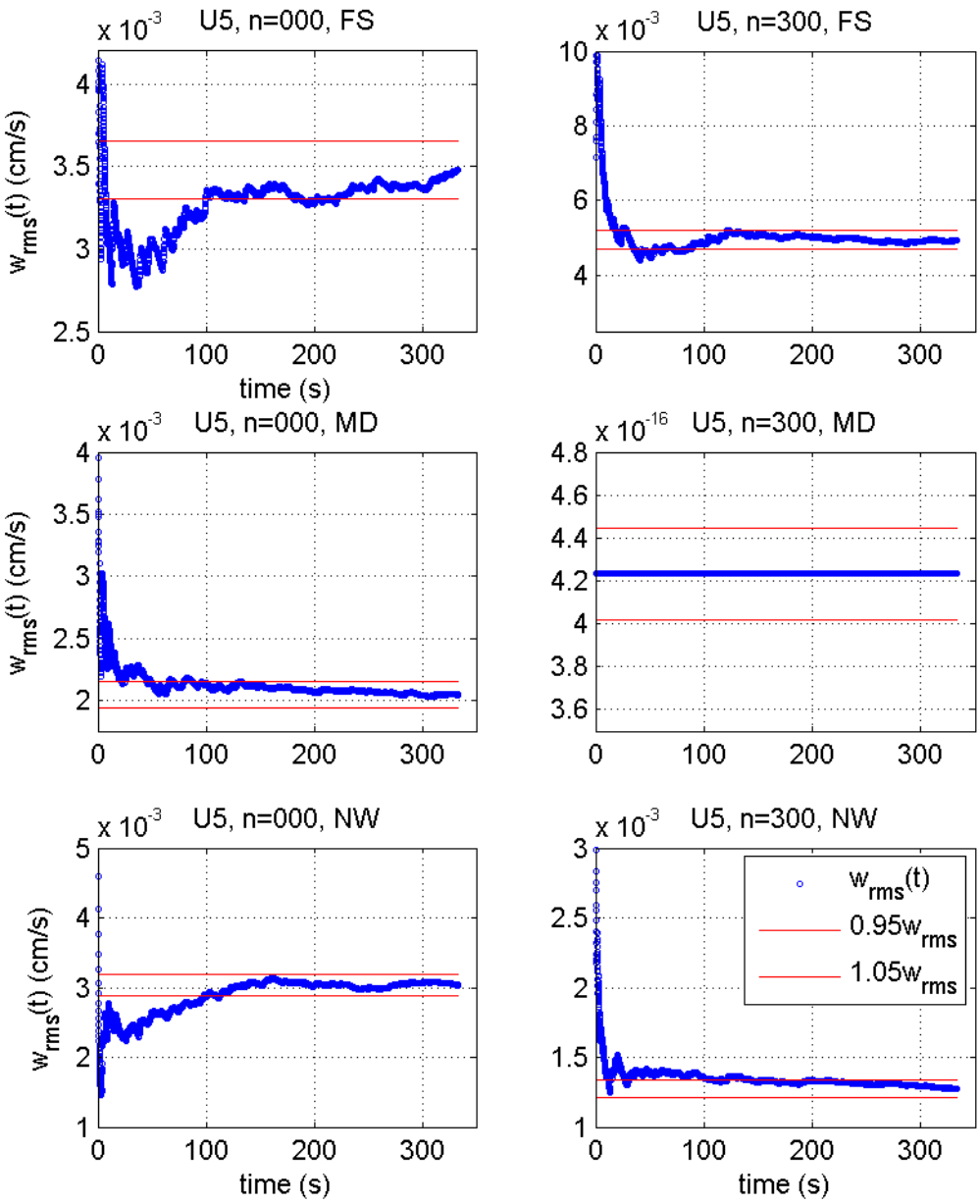


Figure 3.24: Convergence of $\langle\overline{w_{rms}}\rangle$ $(cm/s)$, for $n$=0 and $n$=300, $U5$.

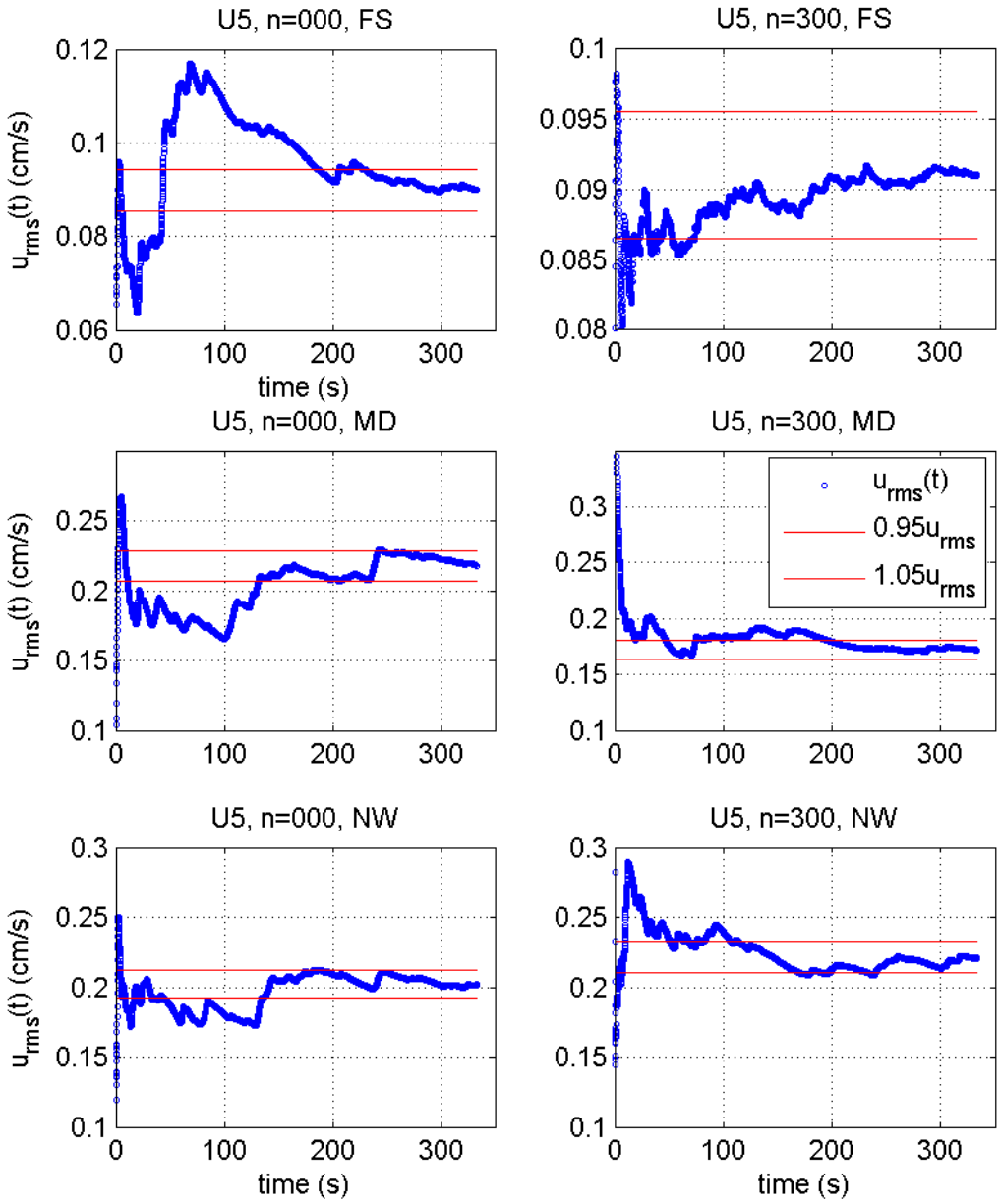


Figure 3.25: Convergence of $\langle\overline{u'w'}\rangle$ $(cm^2/s^2)$, for $n$=0 and $n$=300, $U1$.

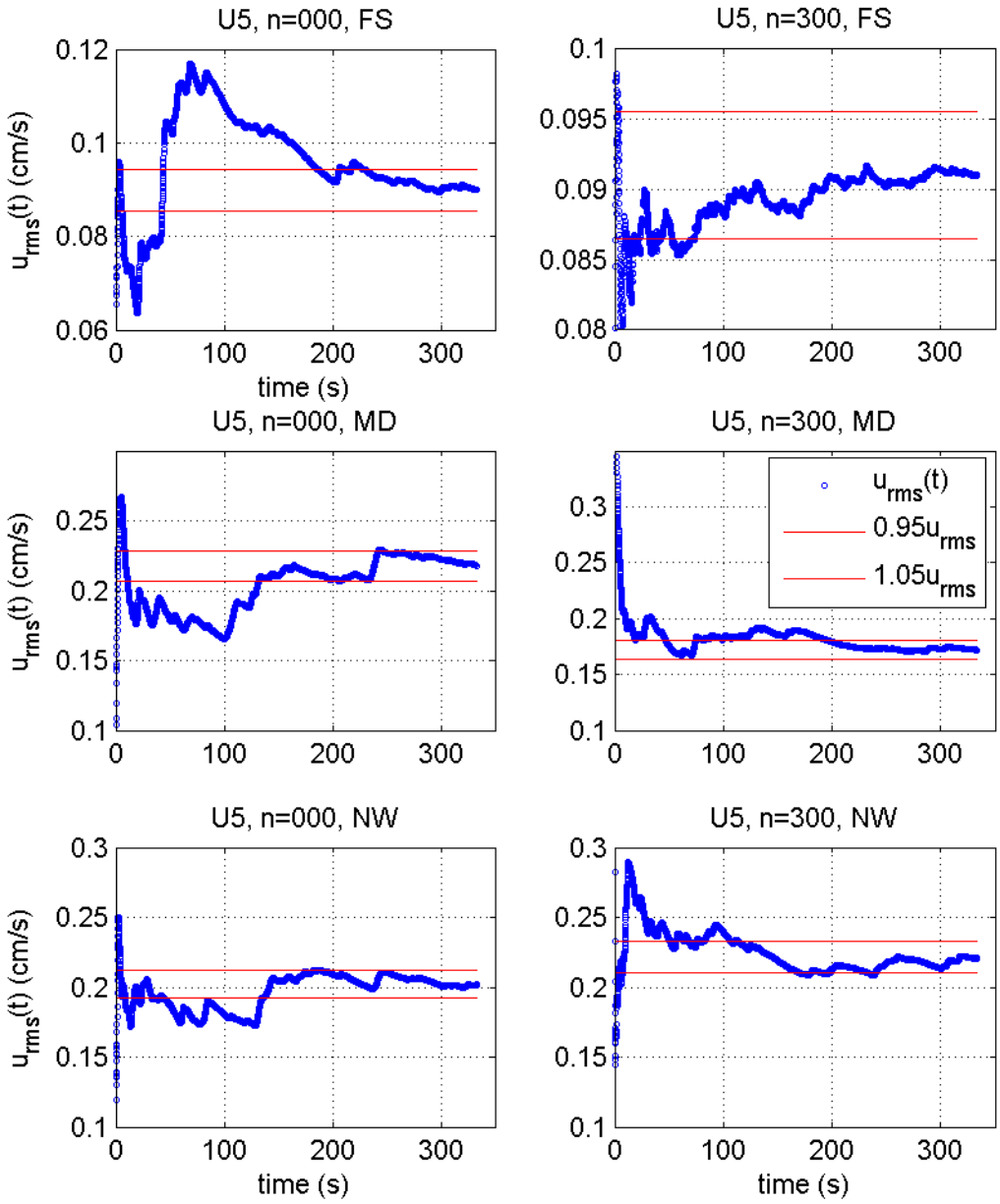


Figure 3.26: Convergence of $\langle\overline{u'w'}\rangle$ $(cm^2/s^2)$, for $n$=0 and $n$=300, $U5$.

From the convergence results is also noted that some of the calculated quantities result from round-off and computer accuracy issues, giving results of Reynolds numbers of the order $10^{-17}$, which is machine zero.

#### 3.2.1.3 Uncertainty analysis

An uncertainty analysis is necessary to evaluate the validity of the data presented. The need for such an analysis is accentuated given the low speed conditions of the experiments, the high frame rates, and the expected small displacements, conducive to statistics that might fall within the error bounds. For this analysis, the sources of uncertainty are categorized as bias and random errors.

The bias error is estimated using the root-sum-square (RSS) technique described by Kline and McClintock (1953). The random uncertainty is calculated using the bootstrap percentile technique as outlined by Diaconis and Efron (1983).

To estimate the bias in a particular result $R(X_1, X_2, ..., X_N)$, the error components $\delta_{Xi}$ for each variable $X_i$ are calculated as:

$$\delta R_{Xi} = \frac{\partial R}{\partial X_i}\delta X_i \tag{3.2}$$

And the total error is calculated by:

$$\delta R = \sqrt{\sum_{i=1}^{N}(\delta R_{X_i})} \tag{3.3}$$

Bias errors for $\langle\overline{u}\rangle$, $\langle\overline{w}\rangle$, $\langle\overline{u_{rms}}\rangle$, $\langle\overline{w_{rms}}\rangle$, and $\langle\overline{u'w'}\rangle$ at three vertical locations (FS, MD, and NW) are analyzed for $U1$ and $U5$, with $n$=0 and $n$=300. The results for 95% uncertainty interval from sets of 5000 image pairs analyzed are presented in Table 3.5.

Table 3.5: Bias error analysis.

| | Bias error for$U1$ | Bias error for $U5$ |
|---|---|---|
| $\langle\overline{u}\rangle$ $(cm/s)$ | $\pm$0.014 | $\pm$0.042 |
| $\langle\overline{w}\rangle$ $(cm/s)$ | $\pm$0.014 | $\pm$0.042 |
| $\langle\overline{u_{rms}}\rangle$ $(cm/s)$ | $\pm$0.020 | $\pm$0.059 |
| $\langle\overline{w_{rms}}\rangle$ $(cm/s)$ | $\pm$0.020 | $\pm$0.059 |
| $\langle\overline{u'w'}\rangle$ $(cm^2/s^2)$ | $\pm$0.0004 | $\pm$0.0035 |

To estimate random errors, the bootstrap technique is used to re-sample our data 1000 times, finding a 95% uncertainty interval for each analyzed quantity ($\langle\overline{u}\rangle$, $\langle\overline{w}\rangle$, $\langle\overline{u_{rms}}\rangle$, $\langle\overline{w_{rms}}\rangle$, and $\langle\overline{u'w'}\rangle$). The worst case bounds are presented in Table 3.6.

Special attention is paid to the dispersive fluxes $\langle\overline{u_i''u_i''}\rangle$, which results are presented in Table 3.7.

Table 3.6: Random error analysis.

| $n$=0, $U1$ | | | | | |
|---|---|---|---|---|---|
| | $\overline{u}$ $(cm/s)$ $\times 10^{-3}$ | $\overline{w}$ $(cm/s)$ $\times 10^{-3}$ | $\overline{u'^2}$ $(cm^2/s^2)$ $\times 10^{-3}$ | $\overline{w'^2}$ $(cm^2/s^2)$ $\times 10^{-6}$ | $\langle\overline{u'w'}\rangle$ $(cm^2/s^2)$ $\times 10^{-9}$ |
| FS | 759.7±0.824 | 9.953±0.017 | 0.869±0.041 | 0.313±0.022 | 0.280±0.042 |
| MD | 1159±1.822 | 28.89±0.046 | 4.415±0.201 | 2.942±0.180 | 11.09±1.713 |
| NW | 872.3±2.202 | 17.50±0.033 | 5.967±0.199 | 1.182±0.069 | 5.394±0.555 |
| $n$=300, $U1$ | | | | | |
| | $\overline{u}$ $(cm/s)$ $\times 10^{-3}$ | $\overline{w}$ $(cm/s)$ $\times 10^{-3}$ | $\overline{u'^2}$ $(cm^2/s^2)$ $\times 10^{-3}$ | $\overline{w'^2}$ $(cm^2/s^2)$ $\times 10^{-6}$ | $\langle\overline{u'w'}\rangle$ $(cm^2/s^2)$ $\times 10^{-9}$ |
| FS | 0.807±0.000 | 3.474±0.005 | 0.000±0.000 | 0.036±0.002 | 0.000±0.000 |
| MD | 955.4±2.064 | 26.13±0.043 | 5.044±0.165 | 2.552±0.171 | 12.46±1.408 |
| NW | 775.0±1.197 | 16.69±0.031 | 1.611±0.052 | 1.221±0.077 | 1.719±0.172 |
| $n$=0, $U5$ | | | | | |
| | $\overline{u}$ $(cm/s)$ $\times 10^{-3}$ | $\overline{w}$ $(cm/s)$ $\times 10^{-3}$ | $\overline{u'^2}$ $(cm^2/s^2)$ $\times 10^{-3}$ | $\overline{w'^2}$ $(cm^2/s^2)$ $\times 10^{-6}$ | $\langle\overline{u'w'}\rangle$ $(cm^2/s^2)$ $\times 10^{-9}$ |
| FS | 3703±2.585 | 72.34±0.100 | 8.087±0.335 | 12.09±0.881 | 80.63±9.933 |
| MD | 4196±6.140 | 40.20±0.058 | 47.43±1.844 | 4.180±0.371 | 228.3±30.38 |
| NW | 3465±5.999 | 54.28±0.088 | 40.80±1.694 | 9.205±0.683 | 372.9±48.09 |
| $n$=300, $U5$ | | | | | |
| | $\overline{u}$ $(cm/s)$ $\times 10^{-3}$ | $\overline{w}$ $(cm/s)$ $\times 10^{-3}$ | $\overline{u'^2}$ $(cm^2/s^2)$ $\times 10^{-3}$ | $\overline{w'^2}$ $(cm^2/s^2)$ $\times 10^{-6}$ | $\langle\overline{u'w'}\rangle$ $(cm^2/s^2)$ $\times 10^{-9}$ |
| FS | 1448±2.458 | 100.1±0.138 | 8.285±0.311 | 24.46±2.184 | 216.4±33.33 |
| MD | 5108±4.958 | 13.87±0.000 | 29.51±1.118 | 0.000±0.000 | 0.000±0.000 |
| NW | 5053±6.188 | 27.81±0.035 | 49.06±1.854 | 1.632±0.164 | 80.20±13.54 |

Table 3.7: Random error analysis for dispersive fluxes.

| $n$=0, $U1$ | | | |
|---|---|---|---|
| | $\langle\overline{u''u''}\rangle$ $(cm^2/s^2)$ | $\langle\overline{w''w''}\rangle$ $(cm^2/s^2)\times10^{-4}$ | $\langle\overline{u''w''}\rangle$ $(cm^2/s^2)$ |
| FS | 0.0256±0.0493 | 0.0867±0.0726 | -0.0003±0.0006 |
| MD | 0.0467±0.0902 | 0.5598±0.8194 | -0.0014±0.0027 |
| NW | 0.0412±0.0785 | 0.1805±0.0651 | -0.0003±0.0005 |
| $n$=300, $U1$ | | | |
| | $\langle\overline{u''u''}\rangle$ $(cm^2/s^2)$ | $\langle\overline{w''w''}\rangle$ $(cm^2/s^2)\times10^{-3}$ | $\langle\overline{u''w''}\rangle$ $(cm^2/s^2)$ |
| FS | 0 | 0.0015±0.0007 | 0 |
| MD | 0.0265±0.0474 | 0.0790±0.1100 | -0.0014±0.0023 |
| NW | 0.0270±0.0463 | 0.1578±0.0671 | -0.0010±0.0007 |
| $n$=0, $U5$ | | | |
| | $\langle\overline{u''u''}\rangle$ $(cm^2/s^2)$ | $\langle\overline{w''w''}\rangle$ $(cm^2/s^2)$ | $\langle\overline{u''w''}\rangle$ $(cm^2/s^2)$ |
| FS | 0.5007±0.9645 | 0.0001±0.0001 | -0.0035±0.0073 |
| MD | 0.7096±1.3670 | 0 | -0.0026±0.0052 |
| NW | 0.4882±0.9395 | 0.0071±0.0132 | 0.0572±0.1113 |
| $n$=300, $U5$ | | | |
| | $\langle\overline{u''u''}\rangle$ $(cm^2/s^2)$ | $\langle\overline{w''w''}\rangle$ $(cm^2/s^2)$ | $\langle\overline{u''w''}\rangle$ $(cm^2/s^2)$ |
| FS | 0.0665±0.0716 | 0.0022±0.0008 | -0.0081±0.0034 |
| MD | 0.9175±1.7487 | 0.0006±0.0004 | 0.0087±0.0200 |
| NW | 1.0154±1.9407 | 0.0001±0.0001 | 0.0058±0.0111 |

A reasonable range of uncertainties is seen for most values presented in Table 3.6. The values go from the 0.1% for mean velocities to a 15% for the Reynolds stress, acquiring more relevance due to the small magnitudes found for $\overline{u'w'}$. The scenario for dispersive fluxes is more critical, since most of the calculated values fall within the uncertainty range, indicating the possibility of not being measuring the actual physical process, but capturing a numerical error instead.

#### 3.2.1.4 Mean velocity and turbulence

The results for the mean horizontal velocity for all the cases considered are shown in Figure 3.27. Turbulent intensity ($u_{rms}$) and Reynolds stress $\langle\overline{u'v'}\rangle$ are shown in Figures 3.28 and 3.29, respectively.

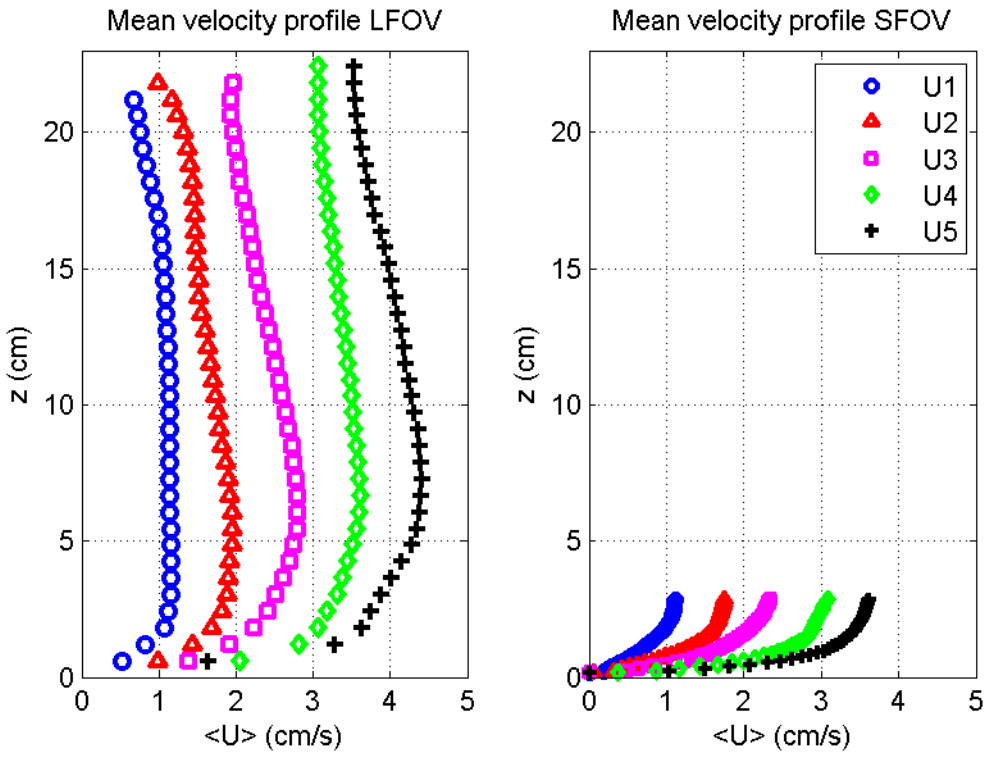


Figure 3.27: Base flow. Velocity profile $\langle\bar{u}\rangle$ (cm/s).

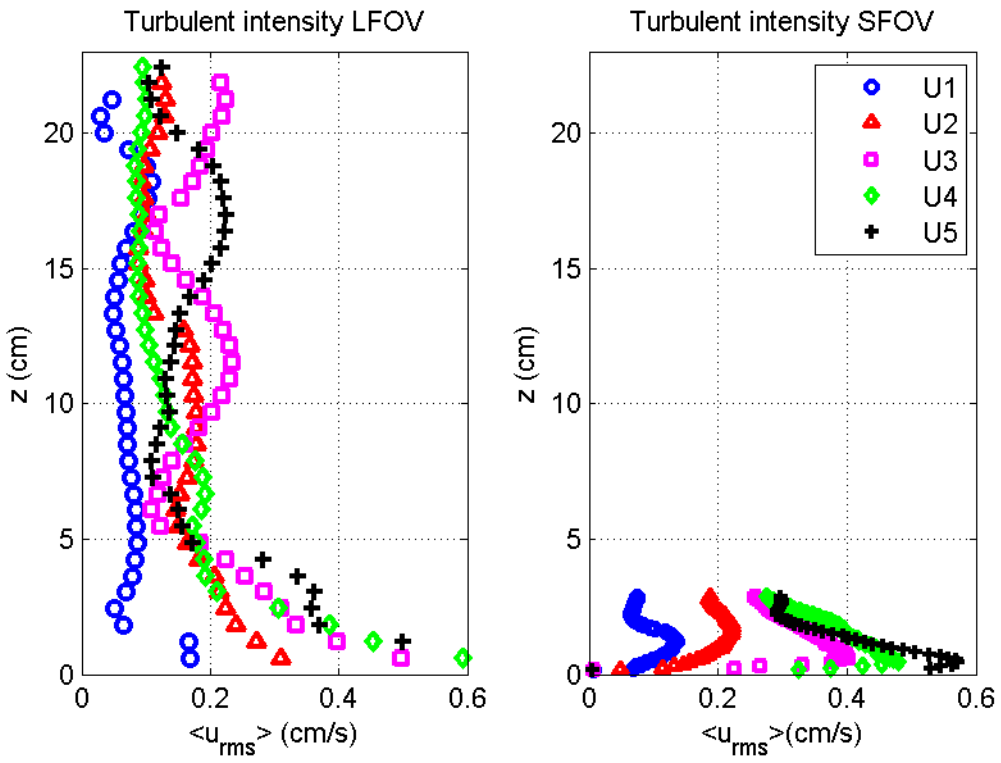


Figure 3.28: Base flow. Turbulence intensity $\langle \bar{u}_{rms} \rangle$ (cm/s).

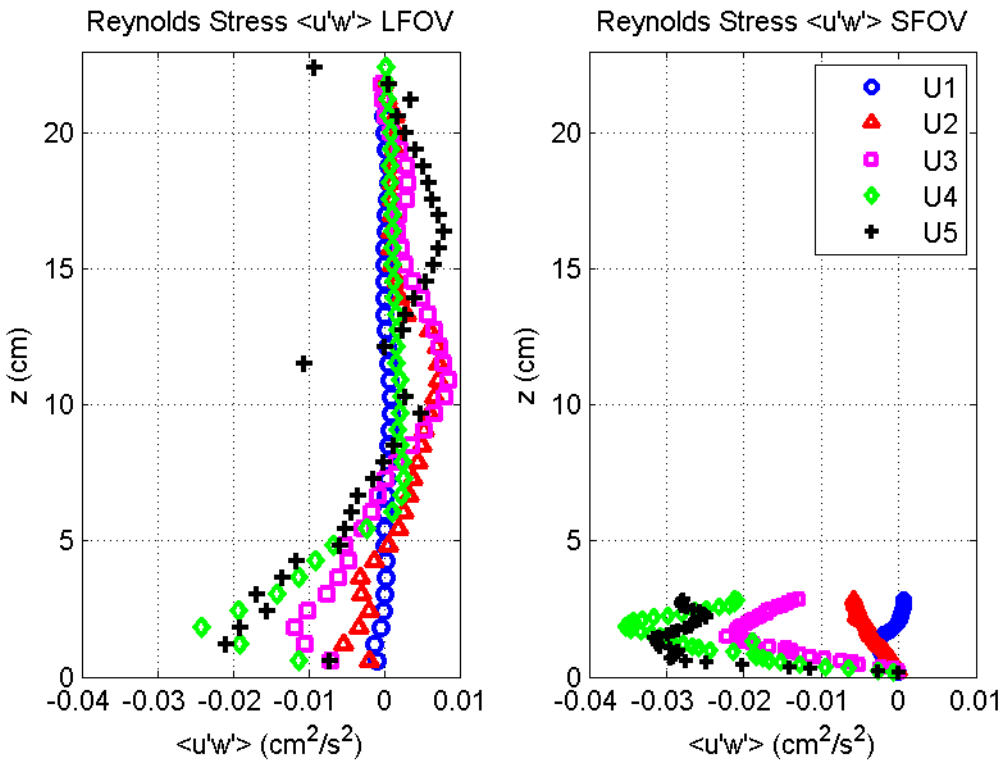


Figure 3.29: Base flow. Reynolds stress $\langle\overline{u'w'}\rangle$ $(cm^2/s^2)$.

As pointed out by Burke and Stolzenbach (1983), a model for vegetated flows should consider the differences in the near-wall variations of mean and turbulent quantities with respect to the non-vegetated flows. To compare against the vegetated case, a classical boundary layer approach is taken to obtain the values for the turbulent velocity $u_*$, by fitting the parametrized profiles $u^+$ vs $z^+$ , and considering a logarithmic law of the wall $u^+ = \frac{1}{K}\ln z^+ + B$ with values for the constants $K = 0.41$ and $B = 5.2$ (Pope 2000). An example of this method is shown in Figure 3.30 for the nominal velocity U1.

Figure 3.31 shows the calculated $u_*$ using the same procedure for each nominal velocity. It is noticed that if plotted against the maximum velocity reached within the SFOV region considered for the analysis, the five calculated values fall within a straight line. Using a linear regression it is found that for this range of velocities in this particular experiment, the turbulent velocity can be found roughly as:

$$u_* \quad = \quad 0.06\langle\overline{u}\rangle_{max} + 0.02 \quad (cm/s) \tag{3.4}$$

Following the near-wall analysis, it is possible to focus on the wall stress. The total shear stress in a wall boundary layer is the sum of the viscous stress $\mu\frac{d\langle\overline{U}\rangle}{dz}$ and the Reynolds stress $-\rho\left\langle\overline{u'w'}\right\rangle$, i.e.:

$$\tau(z) \quad = \quad \mu\frac{d\left\langle\overline{U}\right\rangle}{dz} - \rho\left\langle\overline{u'w'}\right\rangle \tag{3.5}$$

so that their respective contributions can be calculated from the experimental data as shown in Figure 3.32.

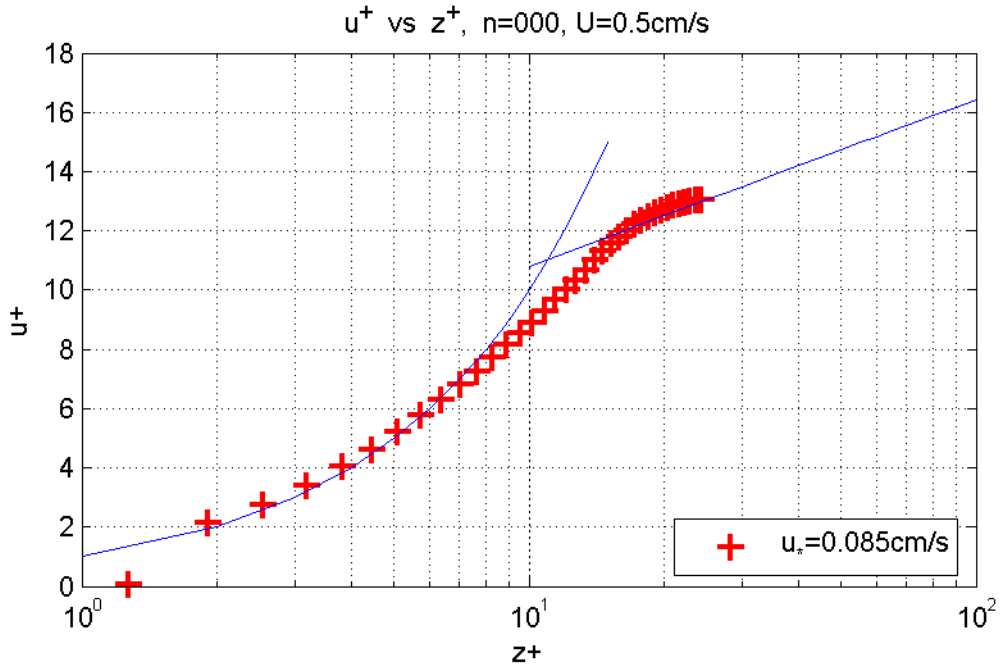


Figure 3.30: Base flow. Log-law for case U1, $n = 0$ to obtain $u_*$.

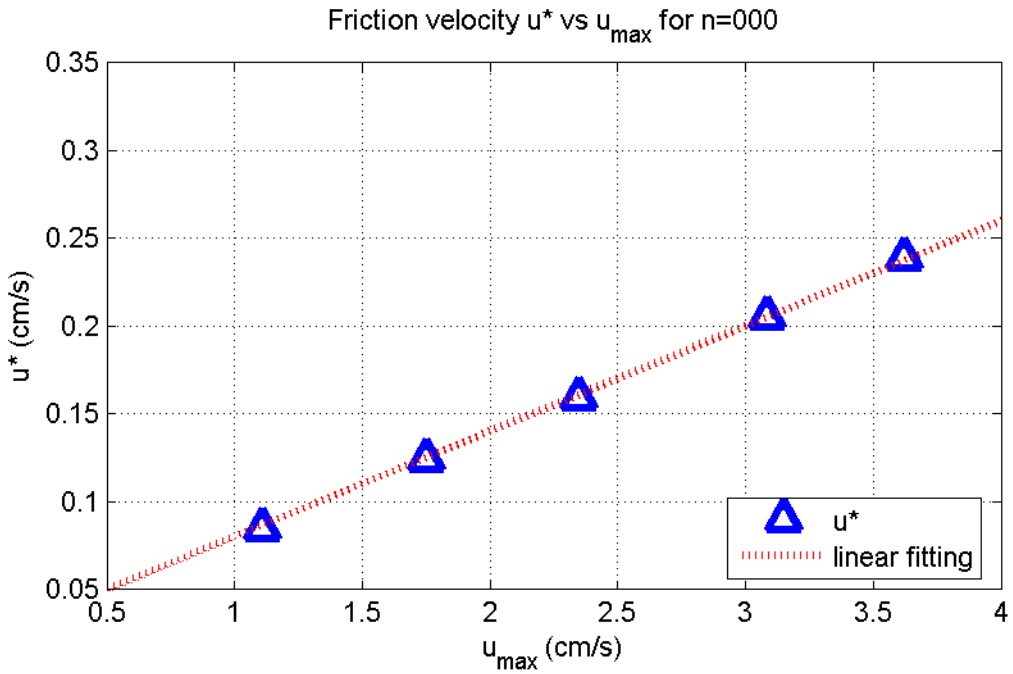


Figure 3.31: Base flow. Turbulent velocities $u_*$ $(cm/s)$.

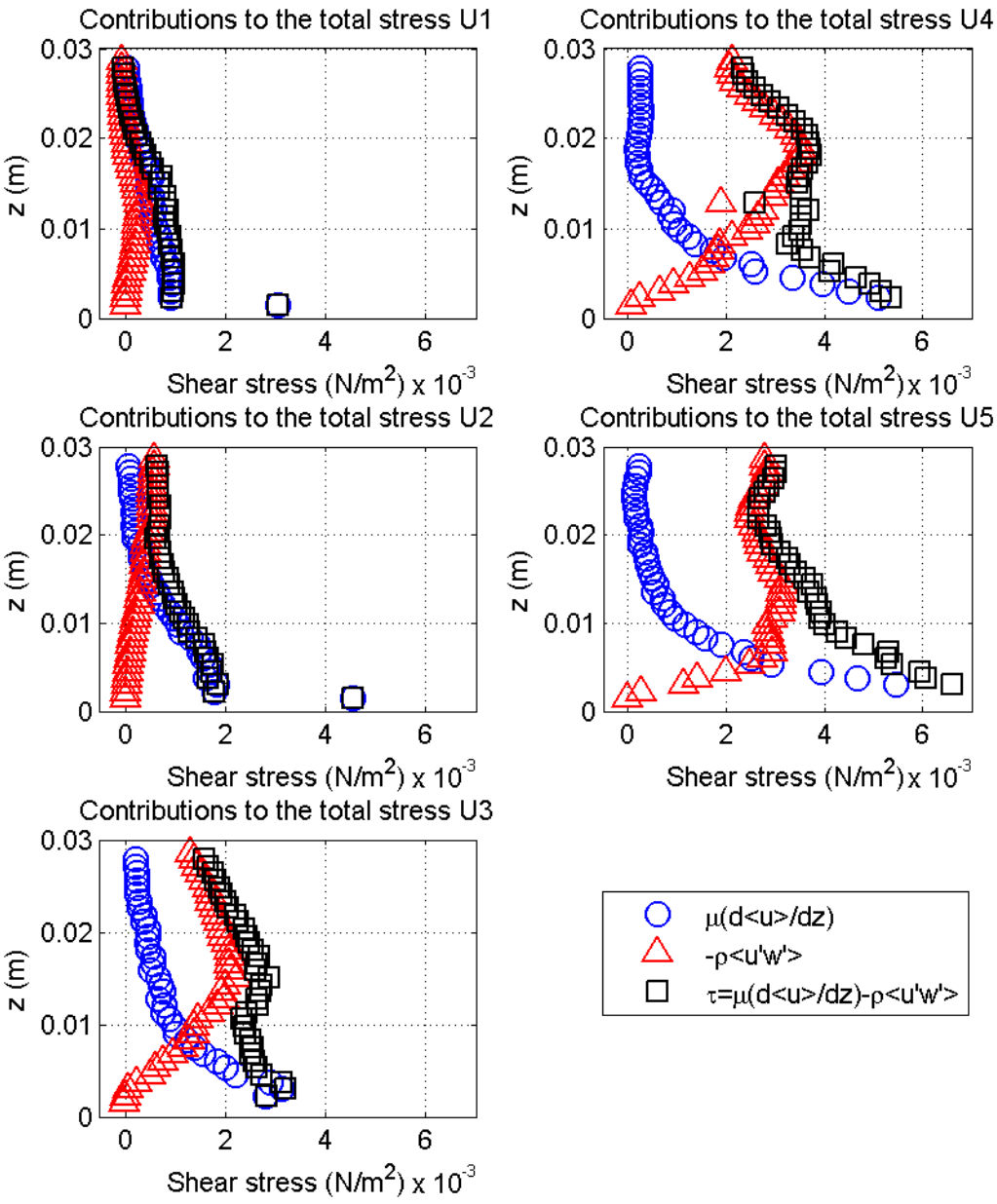


Figure 3.32: Base Flow. Total shear stress $\tau$ $(N/m^2)$.

The friction velocity, $u_*$, can be calculated by estimating a value for $u_*^2$ as the value of the total stress $\tau$ in the constant stress region normalized by $\rho$.With these results, it is now possible to analyze the vegetated case, allowing direct comparisons against a null set (n=0) to determine the actual influence of vegetation in the flow characteristics. Such analysis is done step-by-step in the following section, using a similar approach including the new contributions from vegetation drag.

### 3.2.2 Flow through emergent, flexible vegetation

#### 3.2.2.1 Mean velocity and turbulence

One of the main concerns in this kind of study is the validity of the one-dimensional flow assumption, on which several previous works are based (Nepf 1999, Wilson et. al. 2003, Ghisalberti and Nepf 2004). A first test of this assumption is mass conservation. Since the velocity profiles for sections up- and downstream of the canopy are available, the mass fluxes can be calculated and must be equal in order to satisfy the 1D assumption ($\dot{m}_{US} = \dot{m}_{DS}$). These fluxes (per unit width) are defined as follows:

$$\dot{m_{US}} = \int_0^h \langle \bar{u} \rangle_{US} (\rho \langle \bar{u} \rangle_{US} dz) \tag{3.6}$$

$$\dot{m_{DS}} = \int_0^h \langle \bar{u} \rangle_{DS} (\rho \langle \bar{u} \rangle_{DS} dz) \tag{3.7}$$

And a ratio between the mass fluxes up and downstream of the canopy can be calculated as an indicator of the assumption's accuracy for each vegetation density $n(m^{-2})$. Such ratios are shown in Table 3.8.

For $n = 0$ and $n = 300$ there is a good agreement, presenting the worst case with less than a 10% difference. However, for the $n = 200$ case there are larger

Table 3.8: Mass conservation ratios.

| n ($m^{-2}$) | Exp. | $\frac{\dot{m}_{DS}}{\dot{m}_{US}}$ | n ($m^{-2}$) | Exp. | $\frac{\dot{m}_{DS}}{\dot{m}_{US}}$ | n ($m^{-2}$) | Exp. | $\frac{\dot{m}_{DS}}{\dot{m}_{US}}$ |
|---|---|---|---|---|---|---|---|---|
| 0 | U1 | 0.865 | 200 | U1 | 0.680 | 300 | U1 | 0.901 |
| 0 | U2 | 1.073 | 200 | U2 | 0.770 | 300 | U2 | 1.024 |
| 0 | U3 | 1.046 | 200 | U3 | 0.781 | 300 | U3 | 0.937 |
| 0 | U4 | 1.075 | 200 | U4 | 0.738 | 300 | U4 | 1.025 |
| 0 | U5 | 1.096 | 200 | U5 | 0.699 | 300 | U5 | 1.052 |

differences, implying a stronger 3D field than originally assumed.

A common exercise when dealing with submerged objects in a fluid is to calculate the drag exerted on them by applying conservation of momentum for a fixed control volume (Kundu and Cohen 2004). Assuming steady state this can be calculated as:

$$D = \dot{M}_{US} + \dot{M}_{DS} \tag{3.8}$$

Where

$$\dot{M}_{US} = -\int_0^h \langle \bar{u} \rangle_{US} (\rho \langle \bar{u} \rangle_{US} dz) \tag{3.9}$$

$$\dot{M}_{DS} = \int_0^h \langle \bar{u} \rangle_{DS} (\rho \langle \bar{u} \rangle_{DS} dz) \tag{3.10}$$

Considering a constant density $\rho$ we can calculate the drag per unit mass per unit width, as

$$D/\rho = (\dot{M}_{US} + \dot{M}_{DS})/\rho \tag{3.11}$$

Following such a procedure yields the results shown in Figure 3.33.

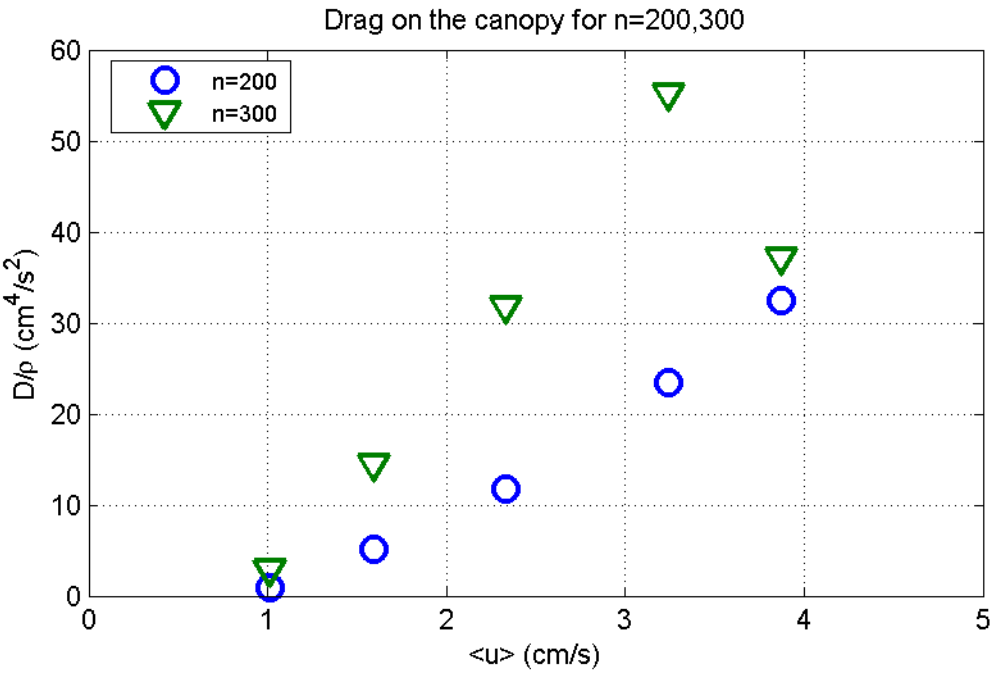


Figure 3.33: Bulk Vegetated Drag from momentum conservation $D/\rho$ $(cm^4/s^2)$.

The expected parabolic shape of the drag in terms of mean velocity will be useful to compare with a posterior more detailed analysis. While the $n$=200 case evidences the expected parabolic shape, it is noticeable the sudden fall in drag for the maximum velocity for the $n$=300 case, which could be explained by the bending of the plant's tops, creating a less obstructed area at the top of the canopy for the water to pass through. The reduction of the frontal area is noticed in Figures 3.12 and 3.13, and its effects are noted in the mean velocity profile presented in Figures 3.42 and 3.38.

Vertical profiles of mean longitudinal velocity $\langle \bar{u} \rangle$ were calculated for each section, density and flow rate, as shown in Figures 3.34 to 3.42.

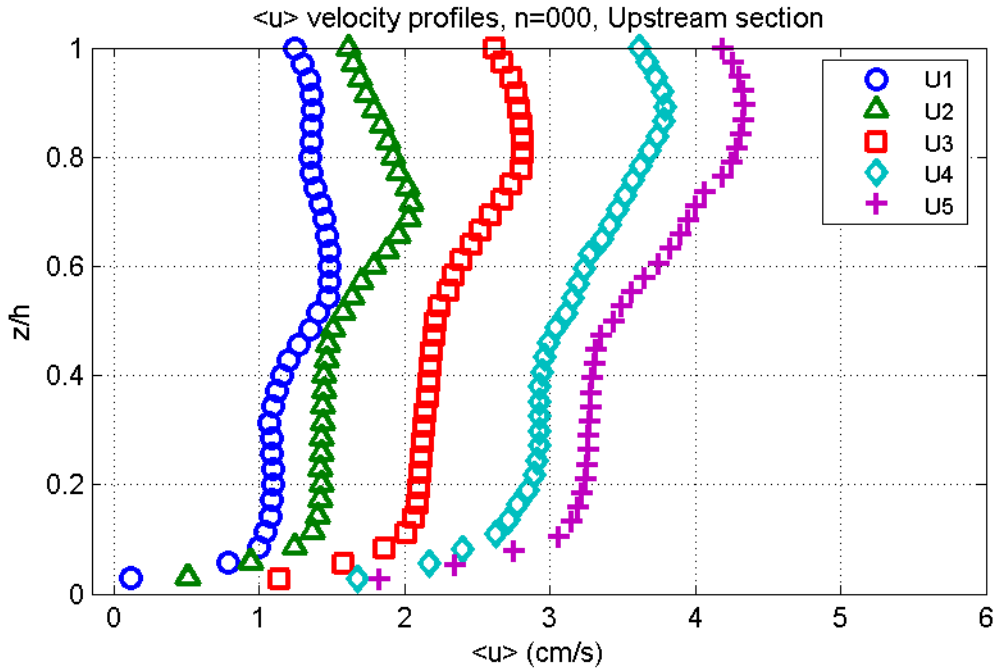


Figure 3.34: Longitudinal velocity $\langle \bar{u} \rangle$ , US, $n = 000$.

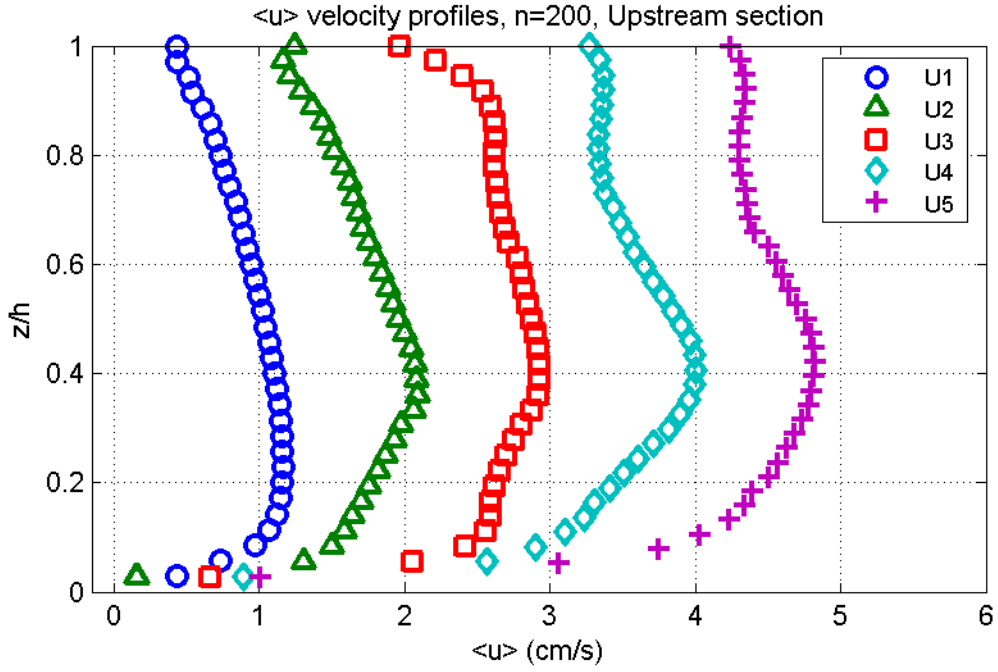


Figure 3.35: Longitudinal velocity $\langle \bar{u} \rangle$ , US, $n = 200$.

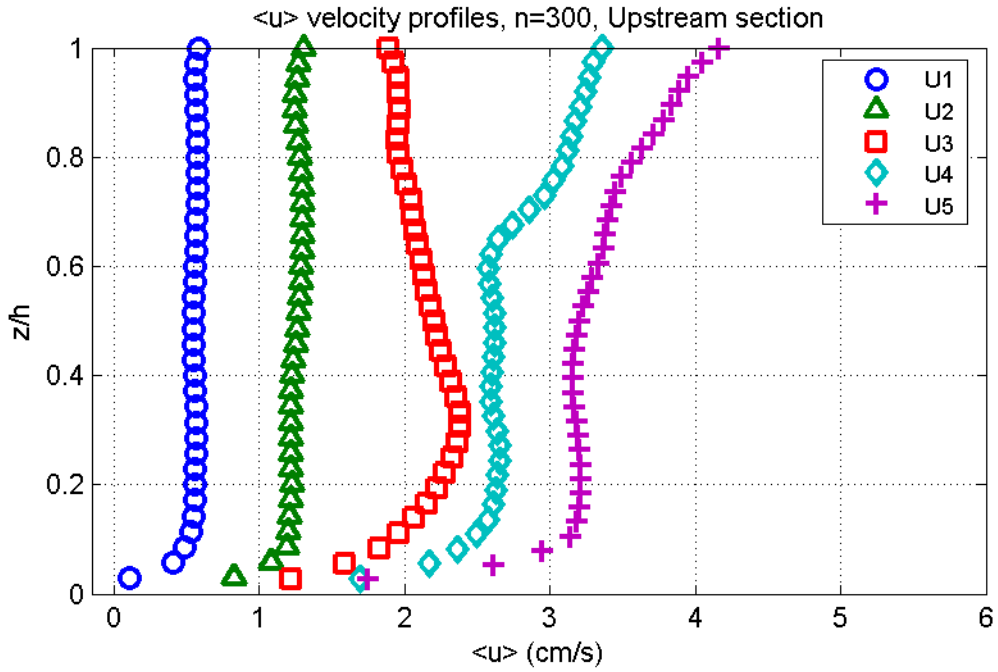


Figure 3.36: Longitudinal velocity $\langle \bar{u} \rangle$ , US, $n = 300$.

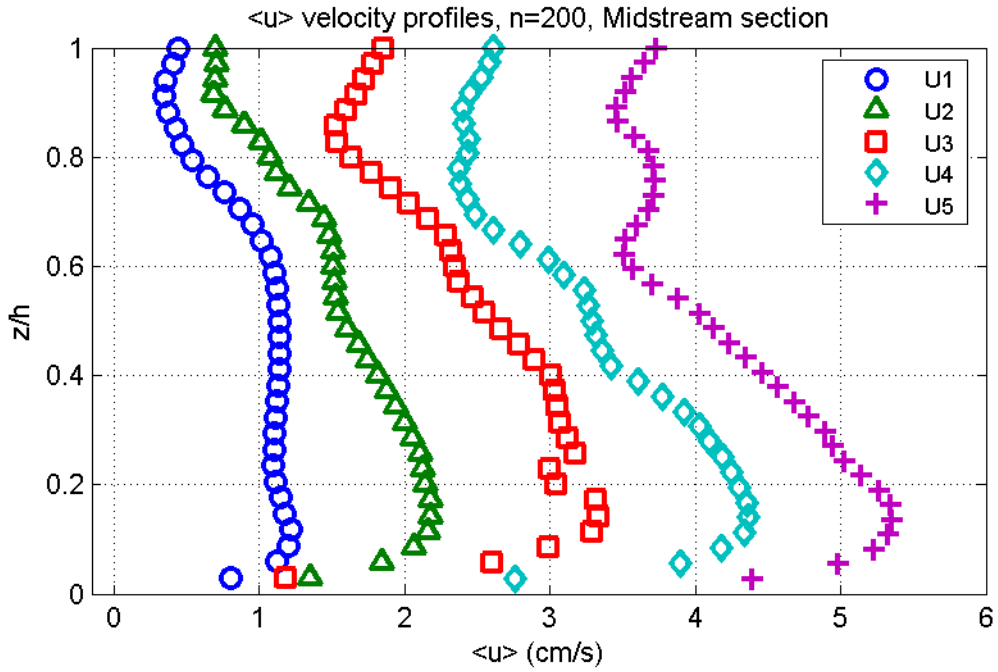


Figure 3.37: Longitudinal velocity $\langle \bar{u} \rangle$ , MS, $n = 200$.

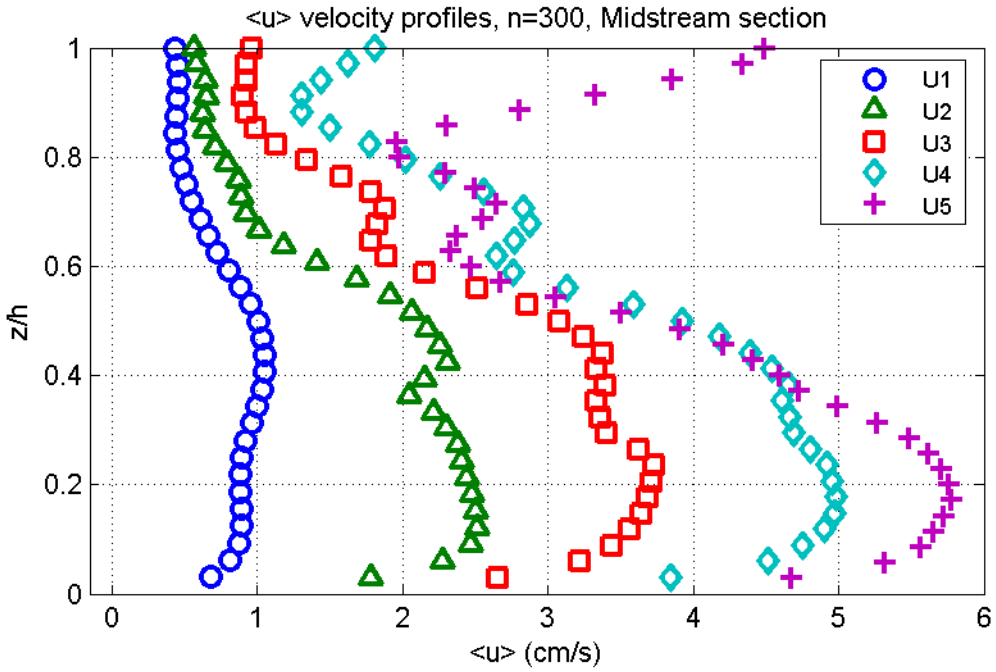


Figure 3.38: Longitudinal velocity $\langle \bar{u} \rangle$ , MS, $n = 300$.

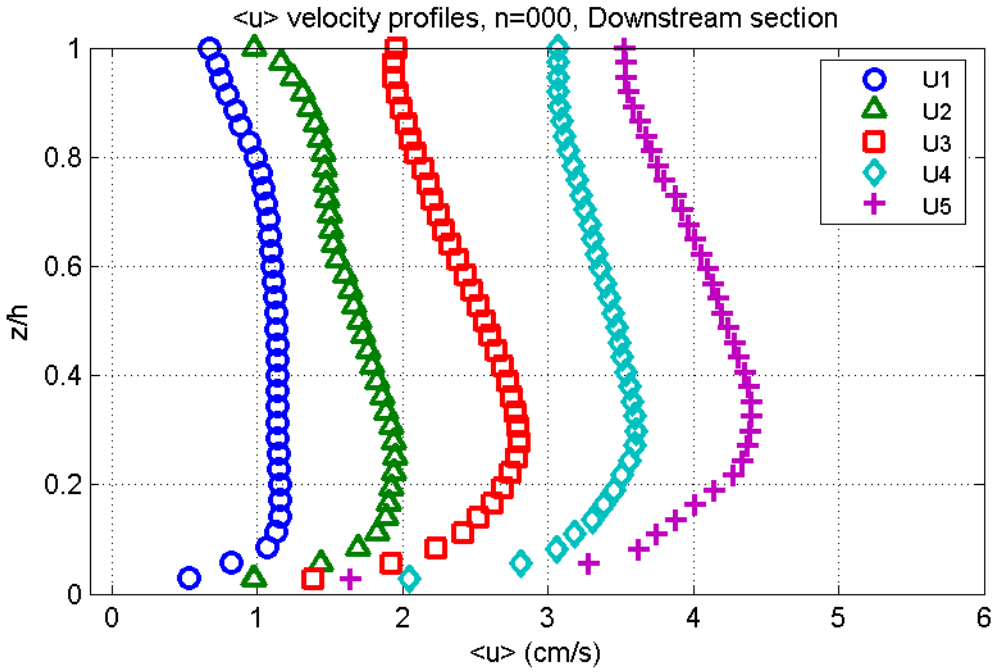


Figure 3.39: Longitudinal velocity $\langle \bar{u} \rangle$ , DS, $n = 000$.

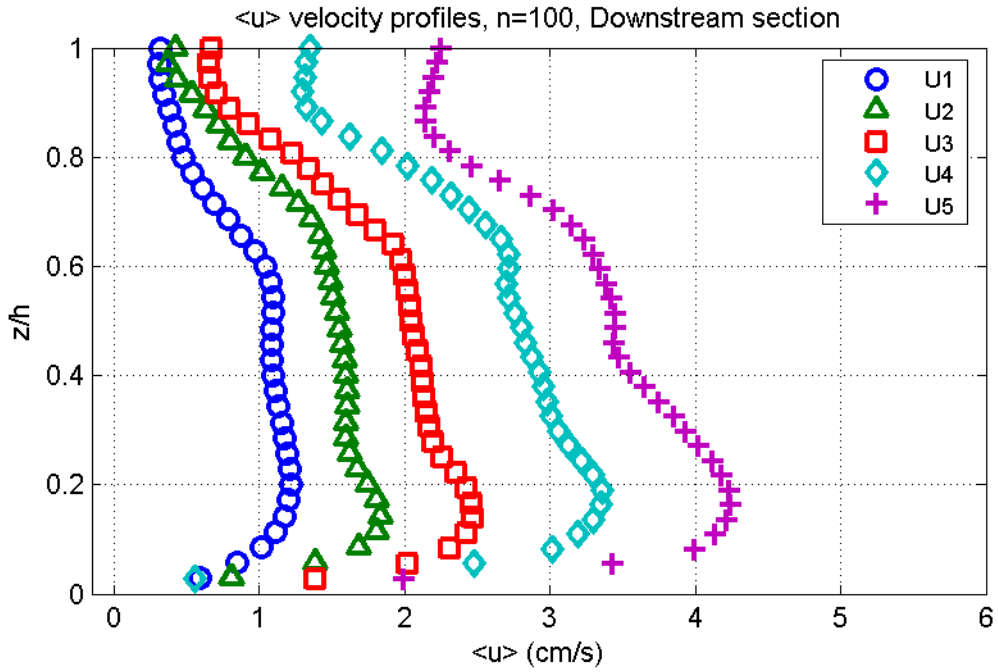


Figure 3.40: Longitudinal velocity $\langle \bar{u} \rangle$ , DS, $n = 100$.

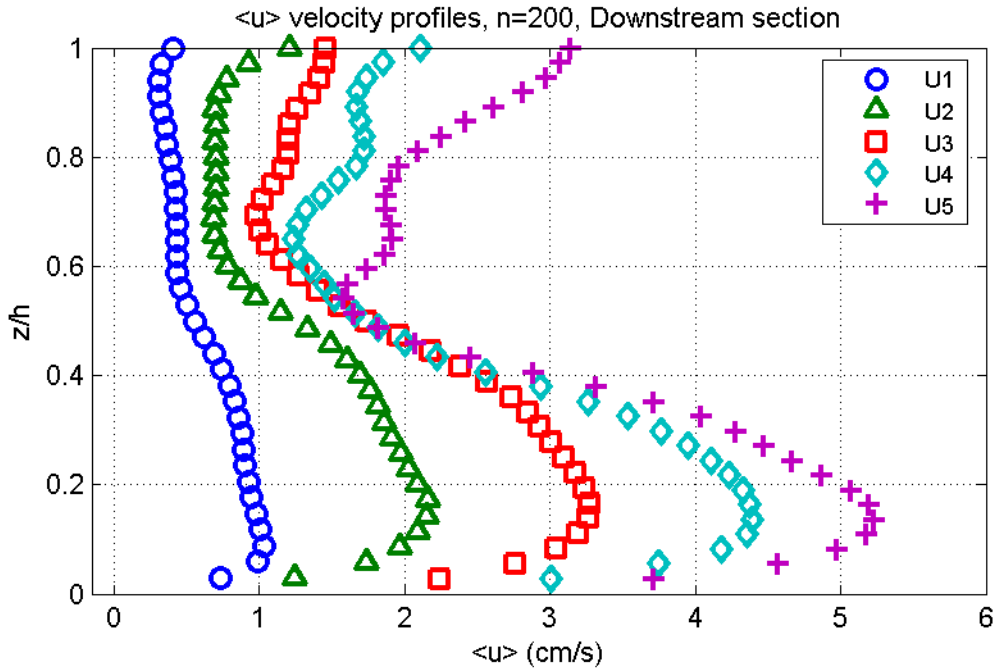


Figure 3.41: Longitudinal velocity $\langle \bar{u} \rangle$ , DS, $n = 200$.

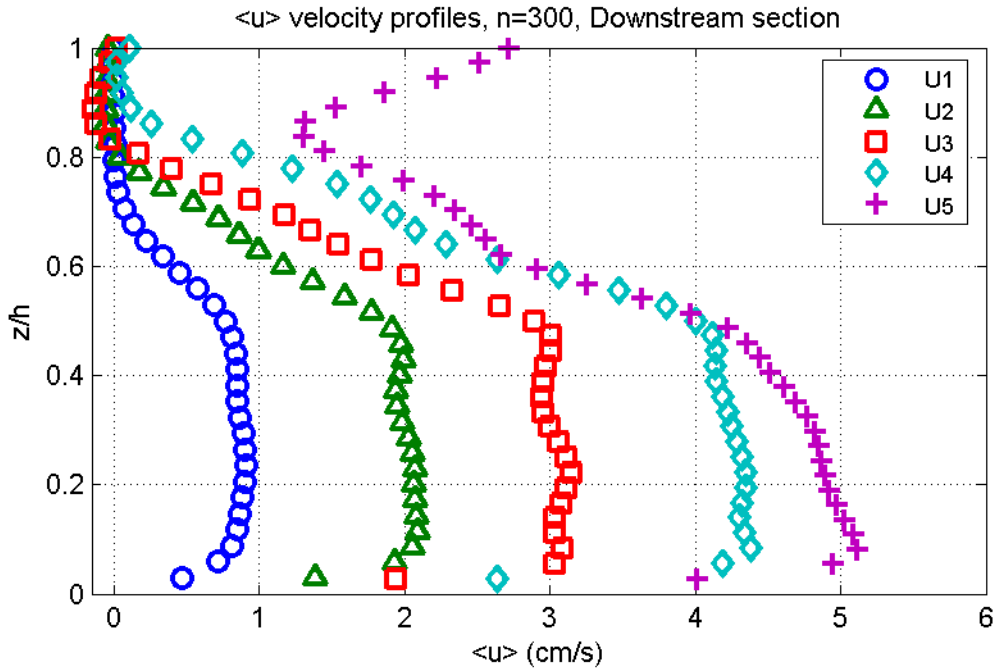


Figure 3.42: Longitudinal velocity $\langle \bar{u} \rangle$ , DS, $n = 300$.

There are noticeable differences between the obtained profiles immediately downstream of the canopy (DS) and the section within the canopy (MS). Some of the differences can be explained by the specific nature of the region selected for the MS analysis: being an area free of plants from the centerline to the wall closest to the camera, resulting in a stronger 3D flow and less spatial homogeneity. This leads to the selection of the DS section for most of the posterior analysis. In order to compare between the flow characteristics up- and downstream of the plants, longitudinal and vertical mean velocities ($\langle \bar{u} \rangle$ and $\langle \bar{w} \rangle$) are presented in Figures 3.43 and 3.44, as well as the turbulence intensity $\langle \bar{u}_{rms} \rangle$ and Reynolds stress $\langle \overline{u'w'} \rangle$ in Figures 3.45 and 3.46.

However, it is expected that the flow will relax after it passes through the canopy, leaving in doubt as to how long after the end of the patch measurements can be considered representative of the bulk characteristics of the flow within the plants. This problem is addressed by calculating vertical profiles at several

distances from the edge of the canopy, taking advantage of the field of view provided by using PIV. Two extreme situations are presented: the minimum velocity U1 for n=100 (Figures 3.47 to 3.50) and the maximum, U5 for n=300 (Figures 3.51 to 3.54). It can be seen that the changes exhibited by the flow after the first 15cm from the edge are quite small for all the variables analyzed, which allows us to consider the horizontal average from the DS section as representative of the flow within the patch.

Since the downstream profiles of the longitudinal velocity $\langle\overline{u}\rangle$ for each $UN$ look similar at each density $n$, these are normalized by the maximum velocity $\langle\overline{u}\rangle_{max}$ of each profile, yielding the non-dimensional profiles $\langle\overline{u}\rangle/\langle\overline{u}\rangle_{max}$ as shown in Figures 3.55 to 3.57 for densities n=100, 200, and 300, respectively. It is noticeable how the data collapse within a self-similar profile, indicating a possible independence of Reynolds number and depending only on the characteristics and morphology of the vegetation within the flow.

#### 3.2.2.2 Spectra

Another concern is the extent to which turbulence truly exists within this flow, since only low-speed flows are considered. Three vertical locations were selected for analysis: 1) near wall, 2) log-law region and 3) near free surface. Looking at the velocity time spectra for each set, the expected $-5/3$ region is found in all cases. The ensemble averaged spectra for the null ($n = 0$) and densest ($n = 300$) cases are shown in Figures 3.58 to 3.61 for the minimum and maximum velocities, using the results from 5000 pairs of images.

Such analysis yields a clear turbulence signature in most of the points selected, while also showing similarities in the structure for all cases.

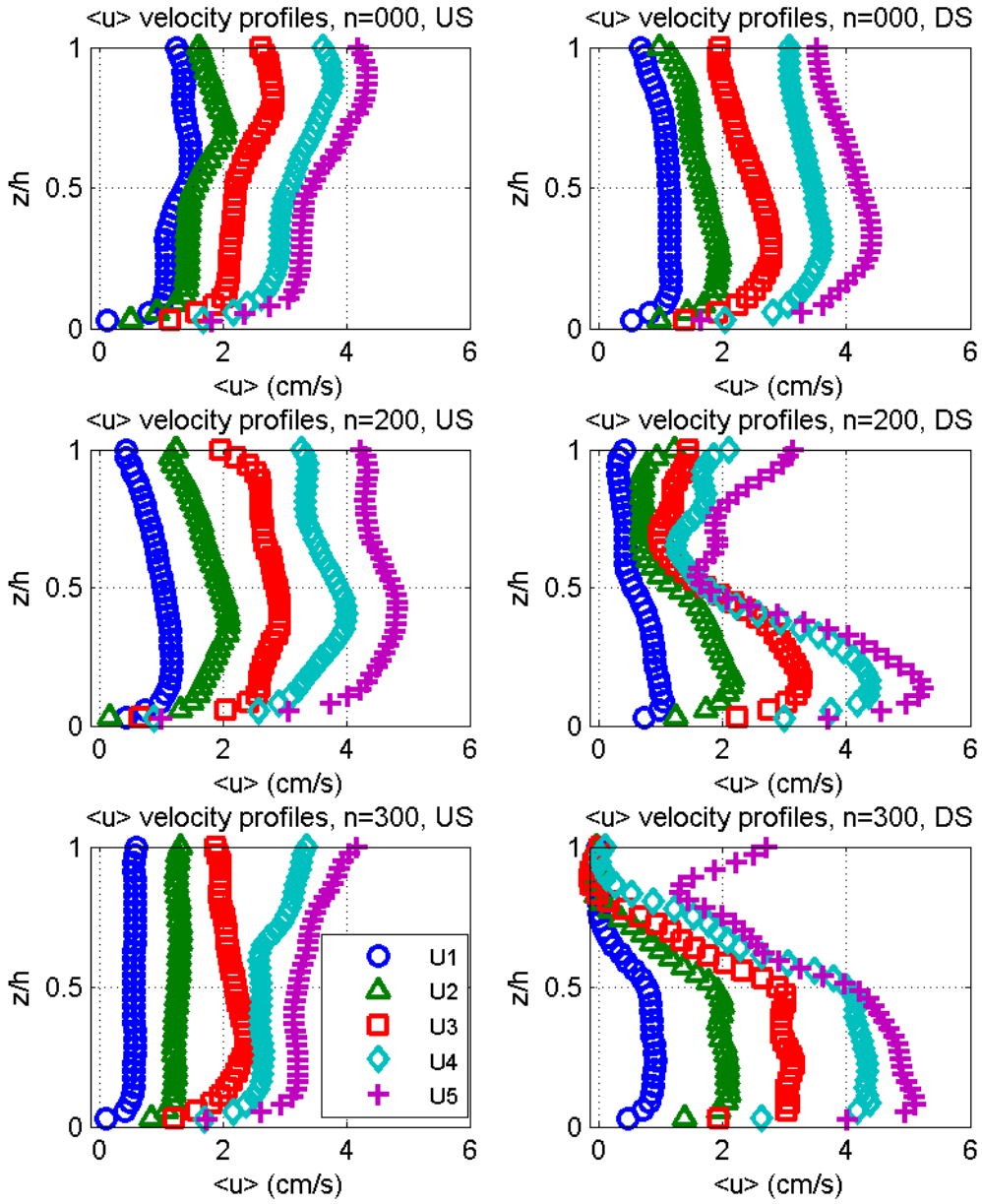


Figure 3.43: Longitudinal velocity $\langle \bar{u} \rangle$ $(cm/s)$.

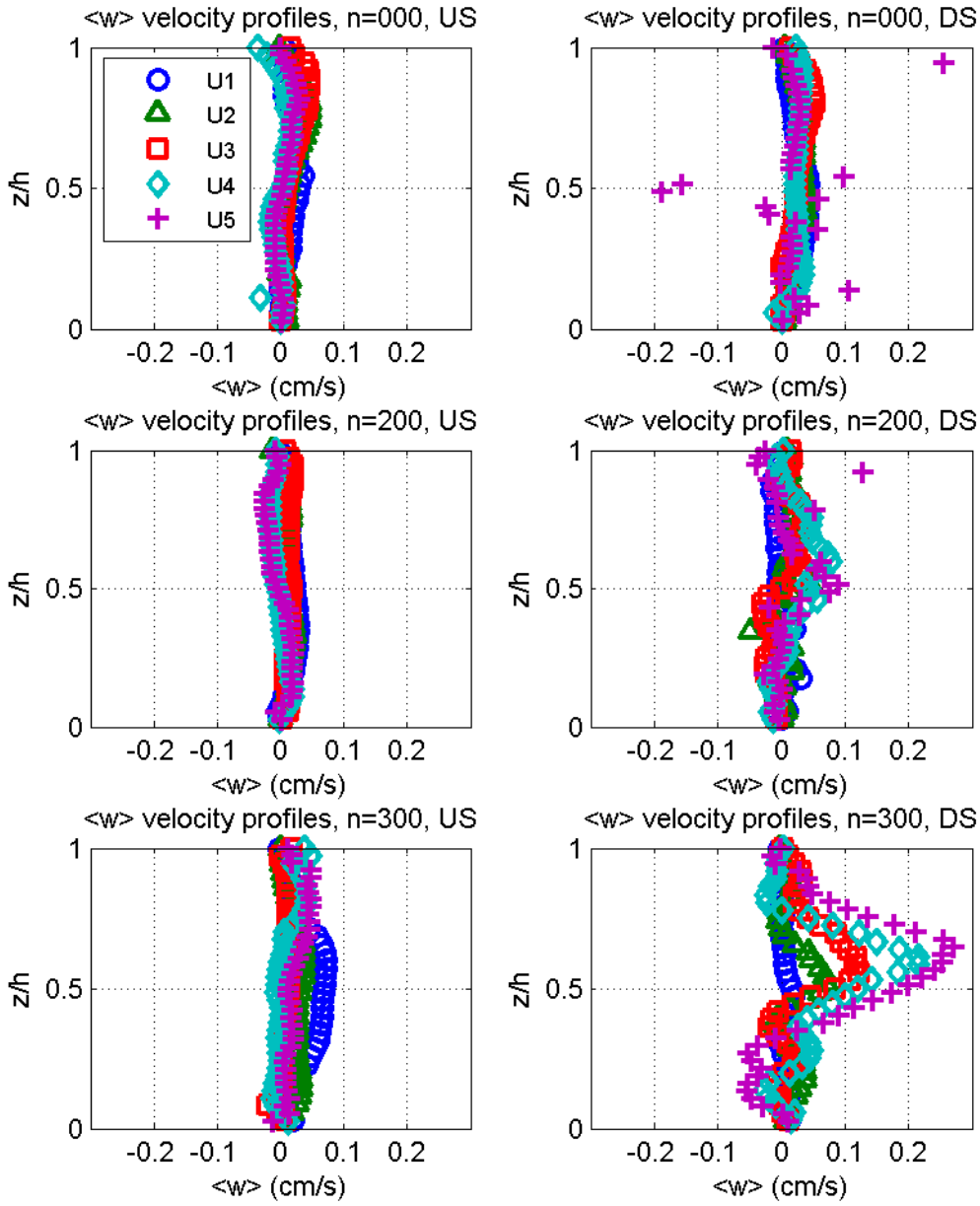


Figure 3.44: Vertical velocity $\langle \bar{w} \rangle$ $(cm/s)$.

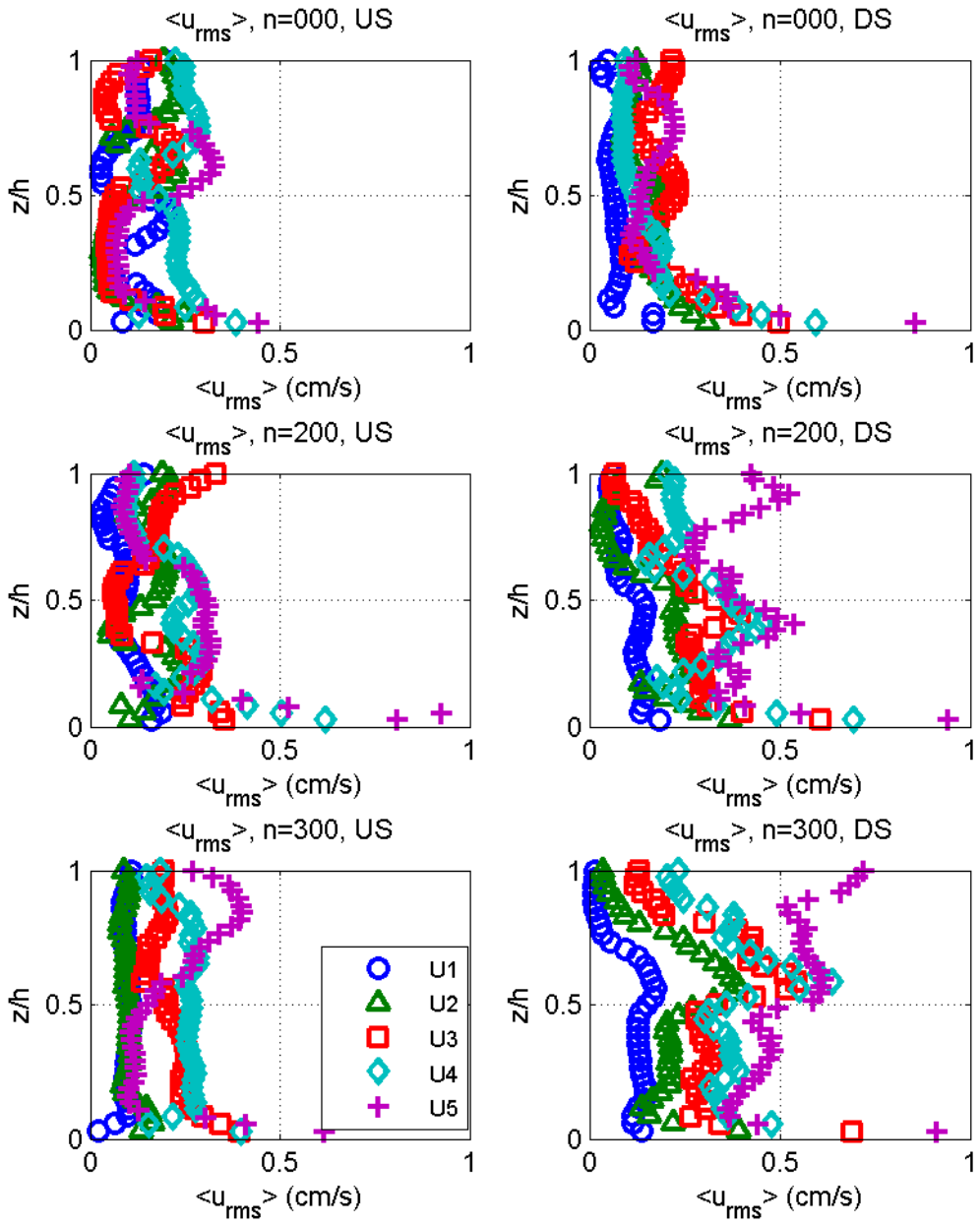


Figure 3.45: Turbulence intensity $\langle \bar{u}_{rms} \rangle$ $(cm/s)$.

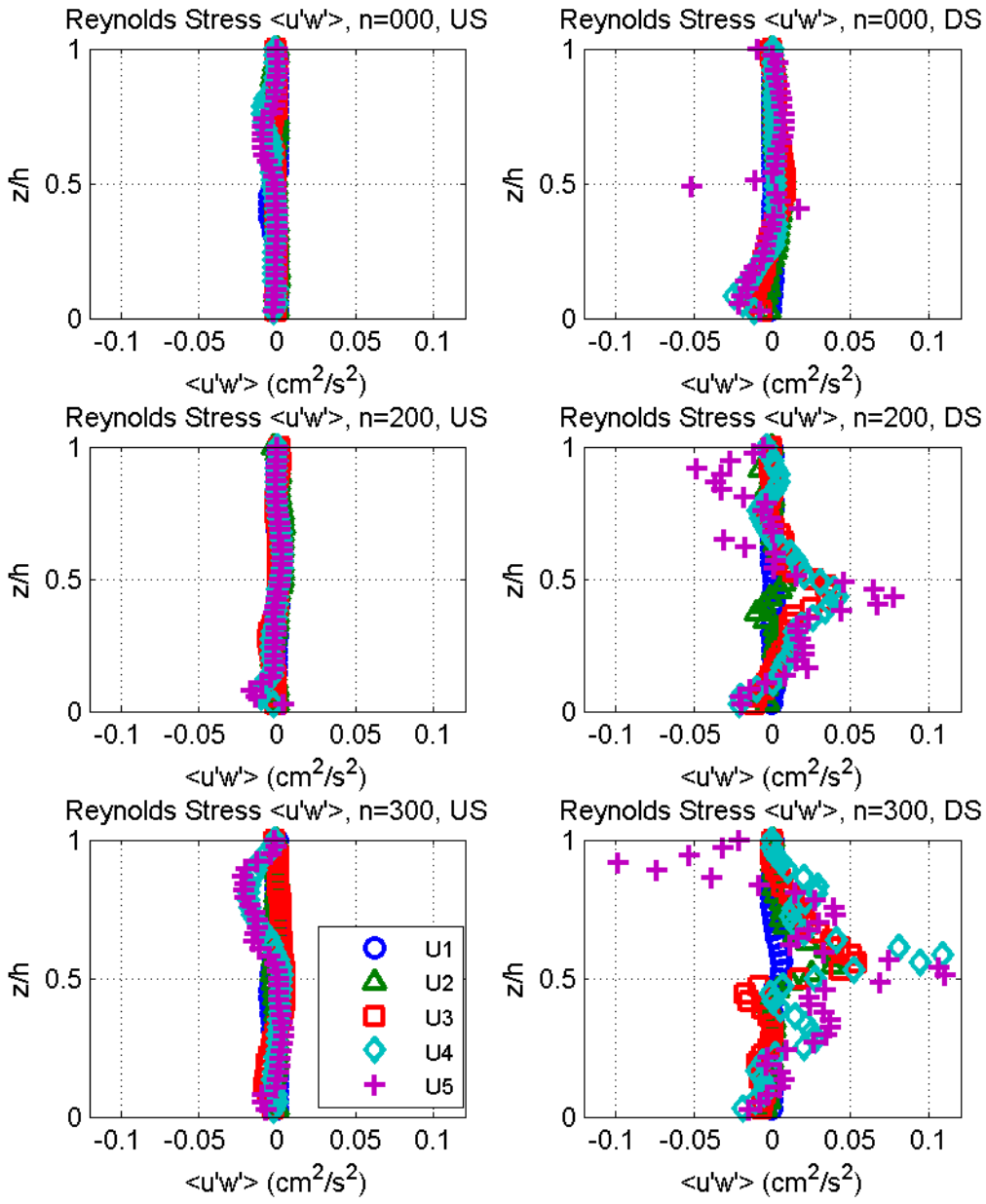


Figure 3.46: Reynolds Stress $\langle\overline{u'w'}\rangle$ $(cm^2/s^2)$.

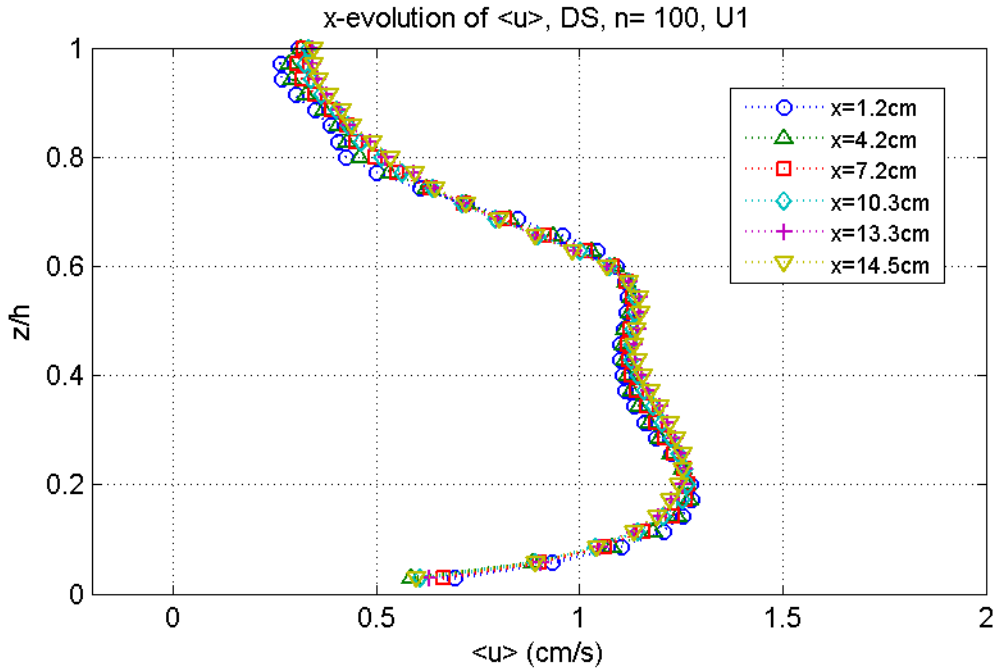


Figure 3.47: Streamwise evolution of longitudinal velocity $\langle \overline{u} \rangle$ $(cm/s)$, n=100, U1.

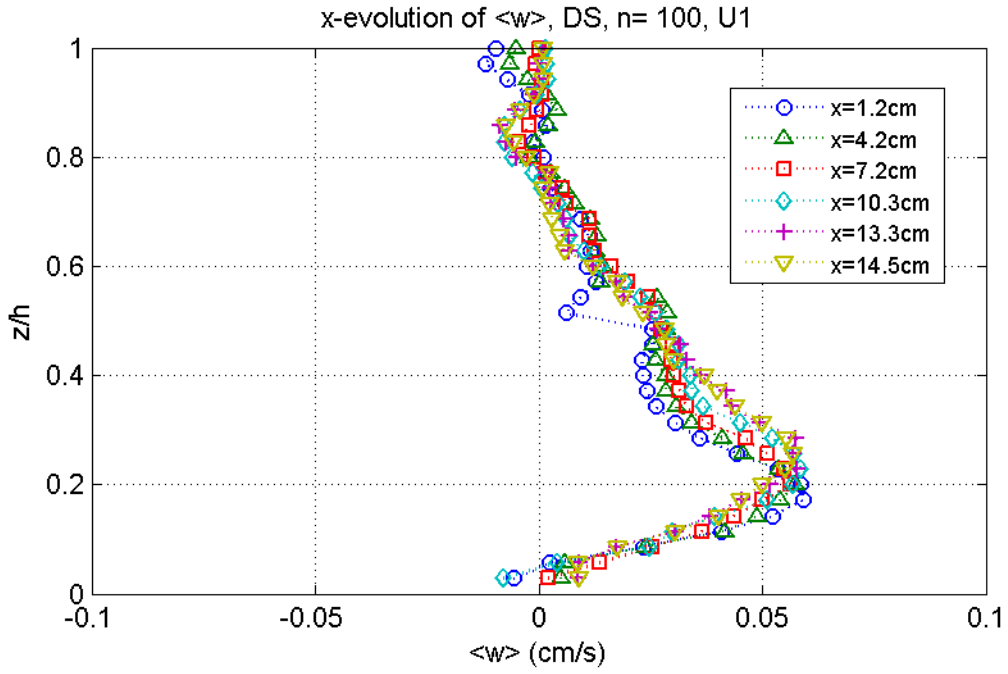


Figure 3.48: Streamwise evolution of vertical velocity $\langle \overline{w} \rangle$ $(cm/s)$, n=100, U1.

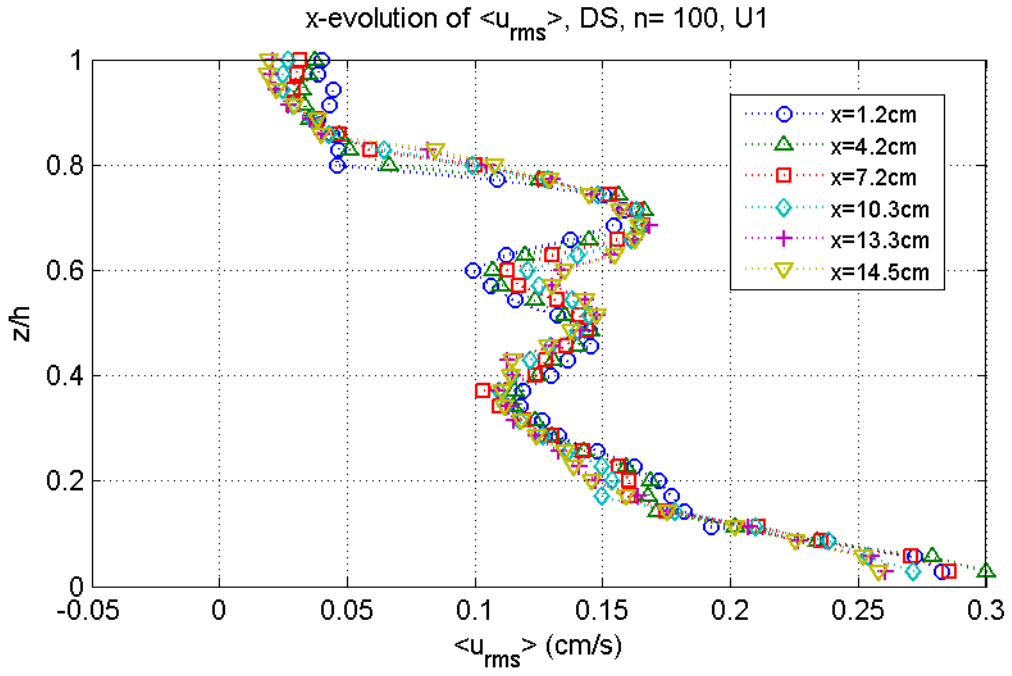


Figure 3.49: Streamwise evolution of turbulence intensity $\langle \overline{u}_{rms} \rangle$ $(cm/s)$, n=100, U1.

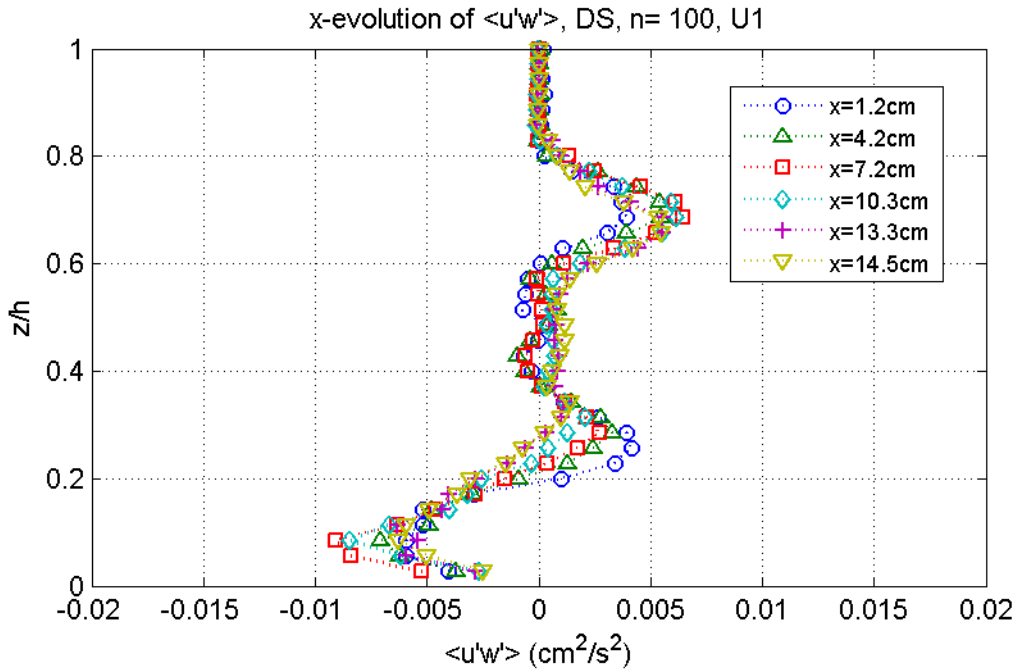


Figure 3.50: Streamwise evolution of Reynolds stress $\langle \overline{u'w'} \rangle$ $(cm^2/s^2)$, n=100, U1.

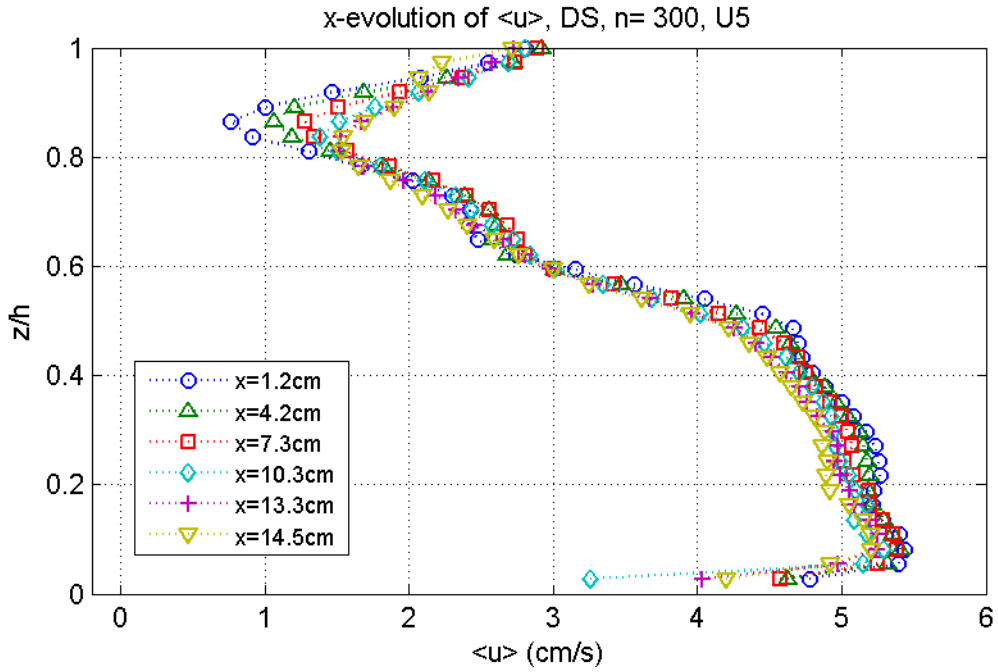


Figure 3.51: Streamwise evolution of longitudinal velocity $\langle \overline{u} \rangle$ $(cm/s)$, n=300, U5.

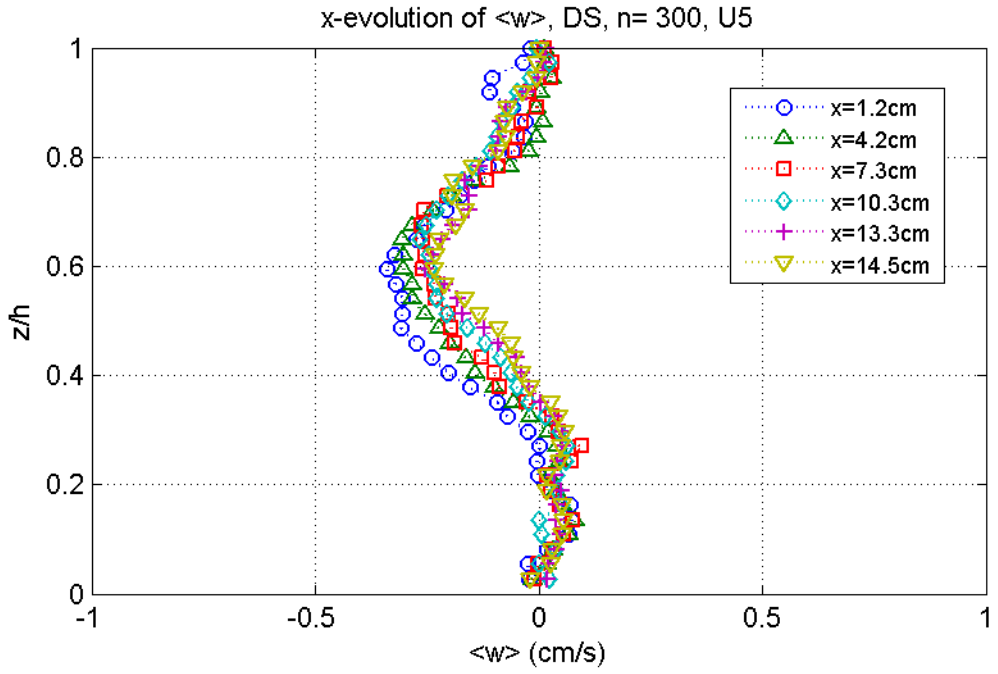


Figure 3.52: Streamwise evolution of vertical velocity $\langle \overline{w} \rangle$ $(cm/s)$, n=300, U5

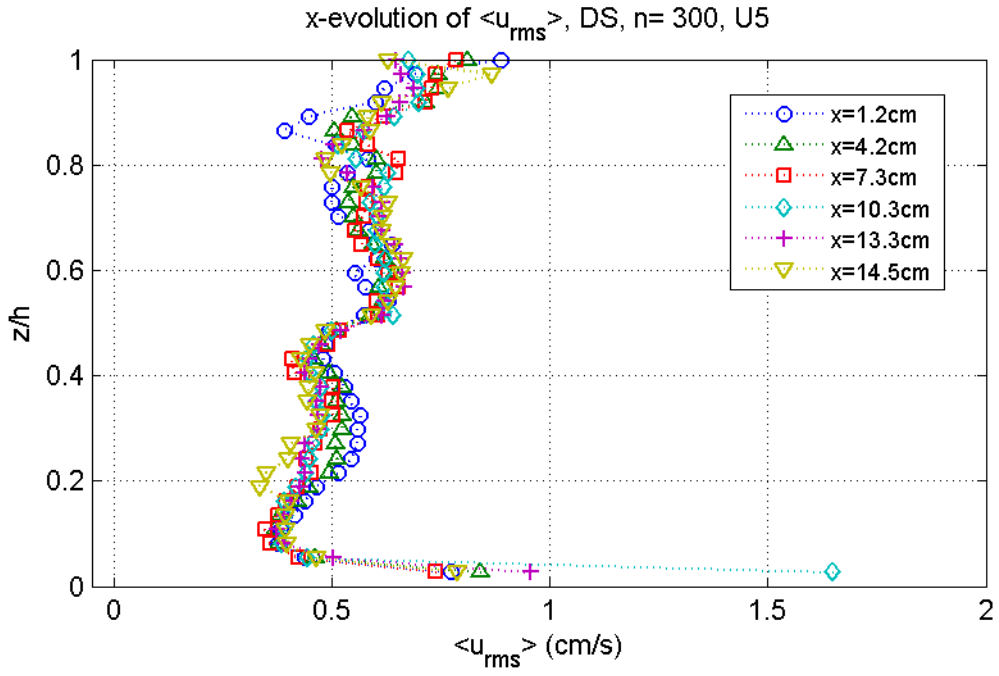


Figure 3.53: Streamwise evolution of turbulence intensity $\langle \overline{u}_{rms} \rangle$ $(cm/s)$, n=300, U5.

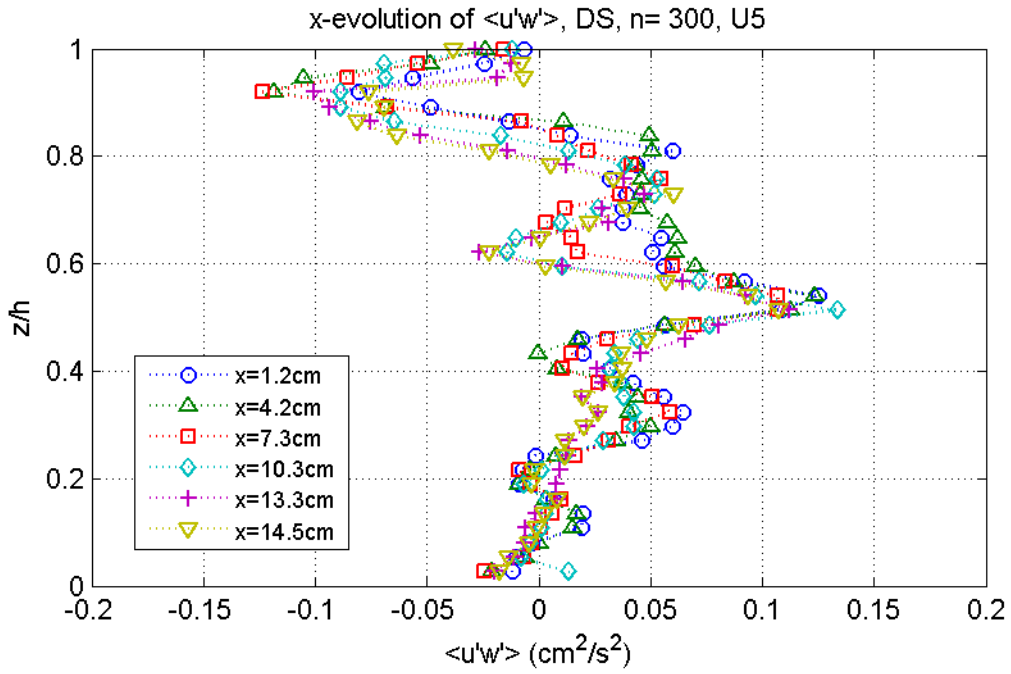


Figure 3.54: Streamwise evolution of Reynolds stress $\langle \overline{u'w'} \rangle$ $(cm^2/s^2)$, n=300, U5.

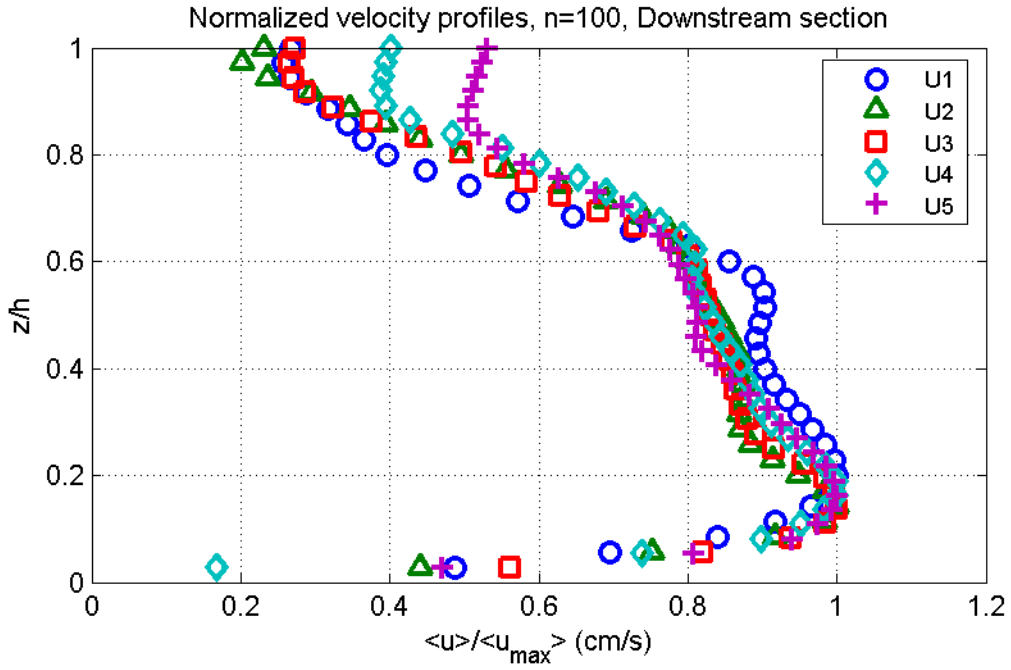


Figure 3.55: Normalized velocity $\langle\overline{u}\rangle/\langle\overline{u}\rangle_{max}$, n=100.

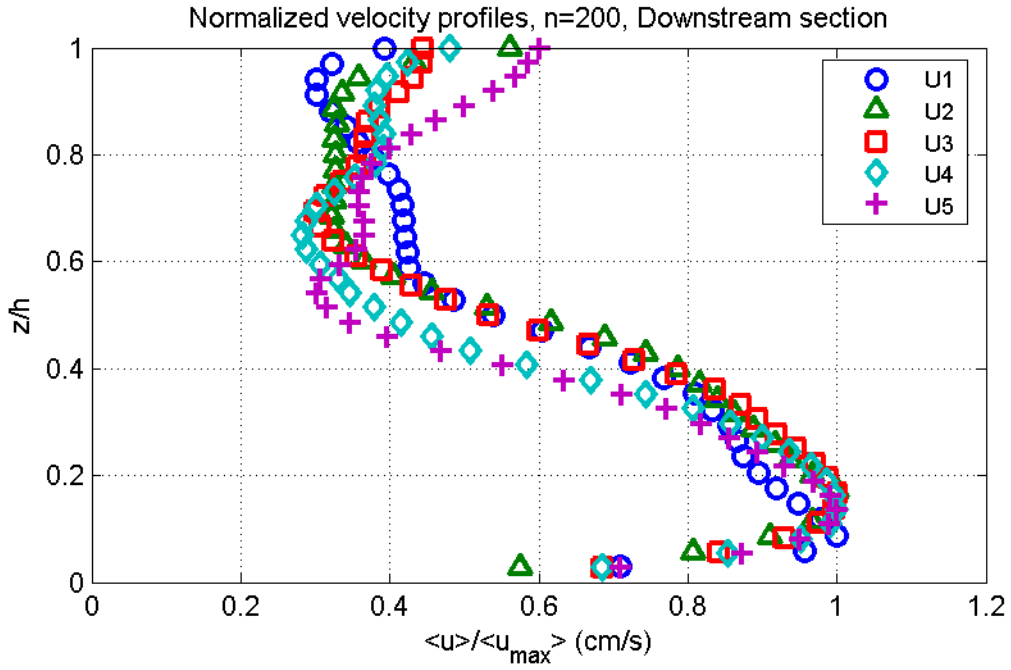


Figure 3.56: Normalized velocity $\langle\overline{u}\rangle/\langle\overline{u}\rangle_{max}$, n=200.

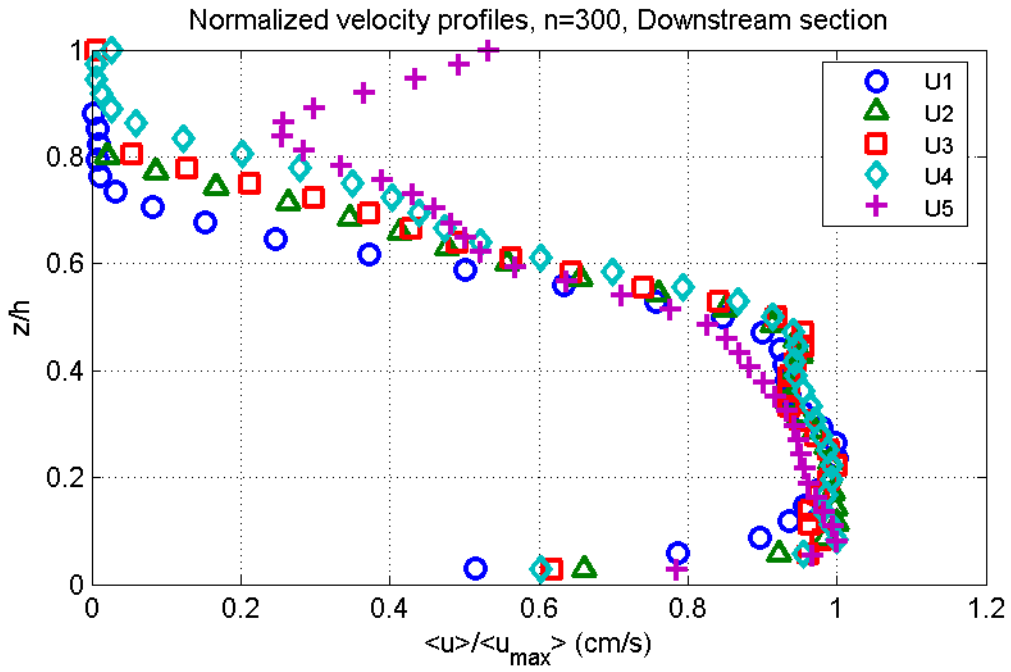


Figure 3.57: Normalized velocity $\langle\overline{u}\rangle/\langle\overline{u}\rangle_{max}$, n=300.

The spatial spectra are also calculated, following the procedure shown in Doron et. al. (2001). The spectral density at different $z$ transects is thus obtained as:

$$E_{ii}(k_1, z_j) = \frac{L}{2\pi N^2} \sum_n F_i(k_1, z_j) F_i^*(k_1, z_j)$$

Where $L$ is the domain length, $N$ is the number of data points in the horizontal FOV, $k_1$ is the wave number in the direction of the flow and $F$ and $F^*$ are the Fourier transform and its complex conjugate, respectively.

$$F_i(k_1, z_j) = \sum_n u_i(x_n, z_j) W(x_n, z_j) exp(-ik_1 x_n)$$

The results for the null ($n = 0$) and most populated ($n = 300$) experiments are shown in Figures 3.62 to 3.65, for nominal velocities $U1$ and $U5$, at three heights.

They show a clear range with the expected $-5/3$ slope, showing the dominance of turbulence in this regime.

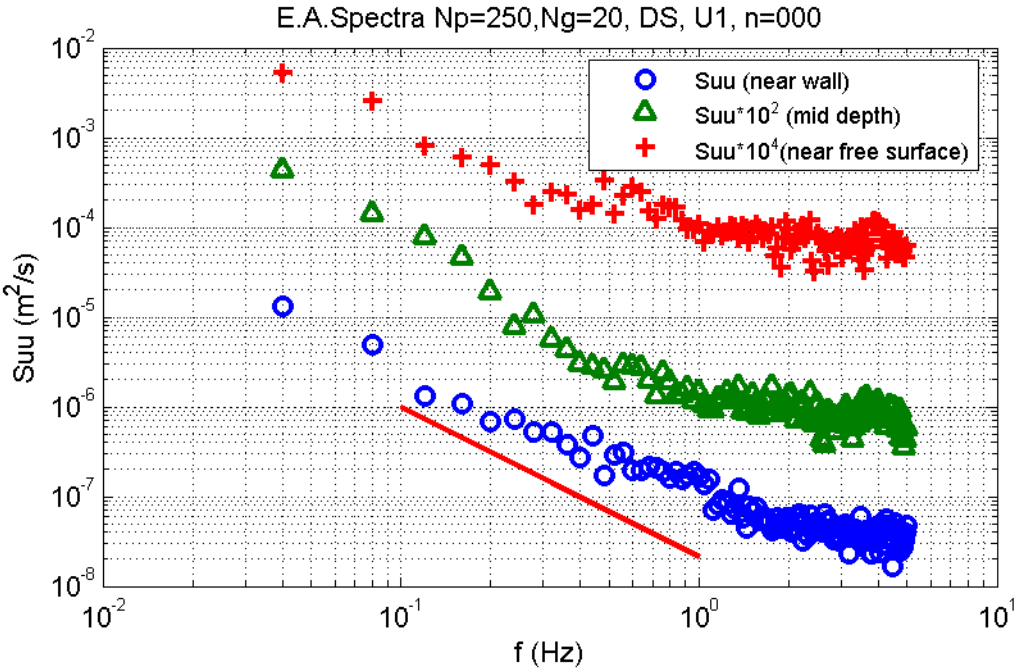


Figure 3.58: Ensemble averaged spectra $Suu$, n=000, U1.

The results shown in Figures 3.62 to 3.65 are obtained by ensemble averaging the spatial spectra of 5000 image pairs at three different heights. For reference purposes, the time history of horizontal velocity averaged over the x-direction at each height for the four extreme cases considered are shown in Figures 3.66 to 3.69.

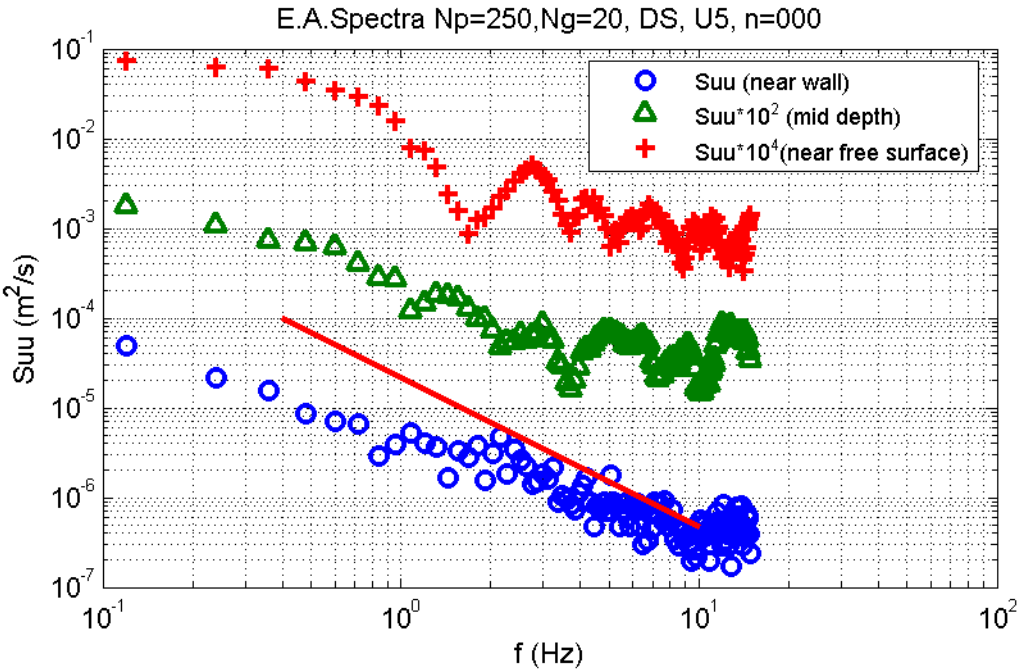


Figure 3.59: Ensemble averaged spectra $Suu$, n=000, U5.

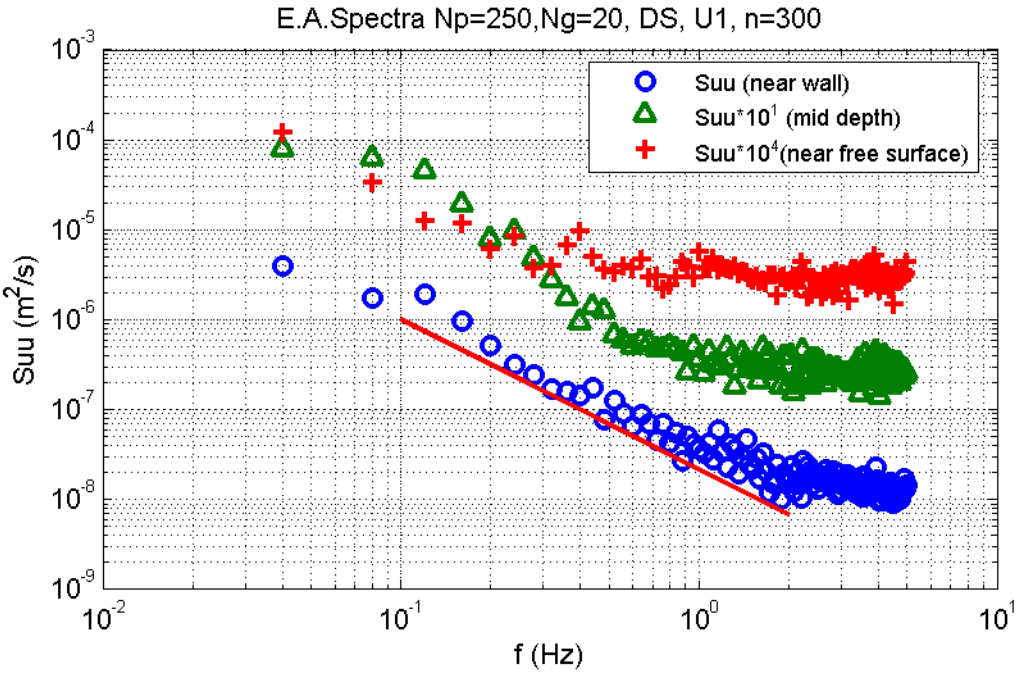


Figure 3.60: Ensemble averaged spectra $Suu$, n=300, U1.

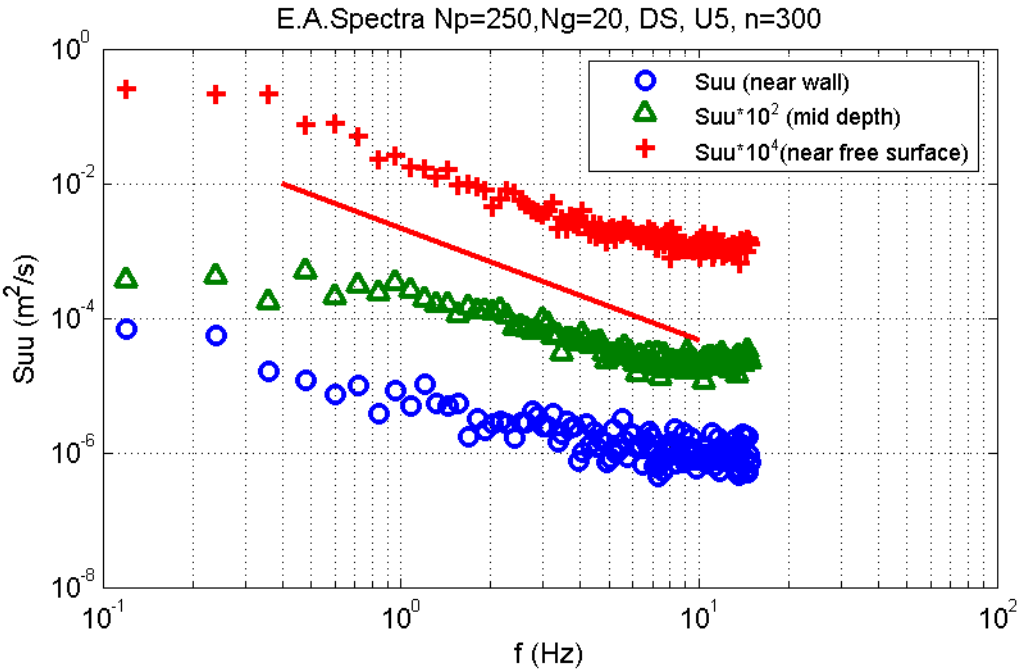


Figure 3.61: Ensemble averaged spectra $Suu$, n=300, U5.

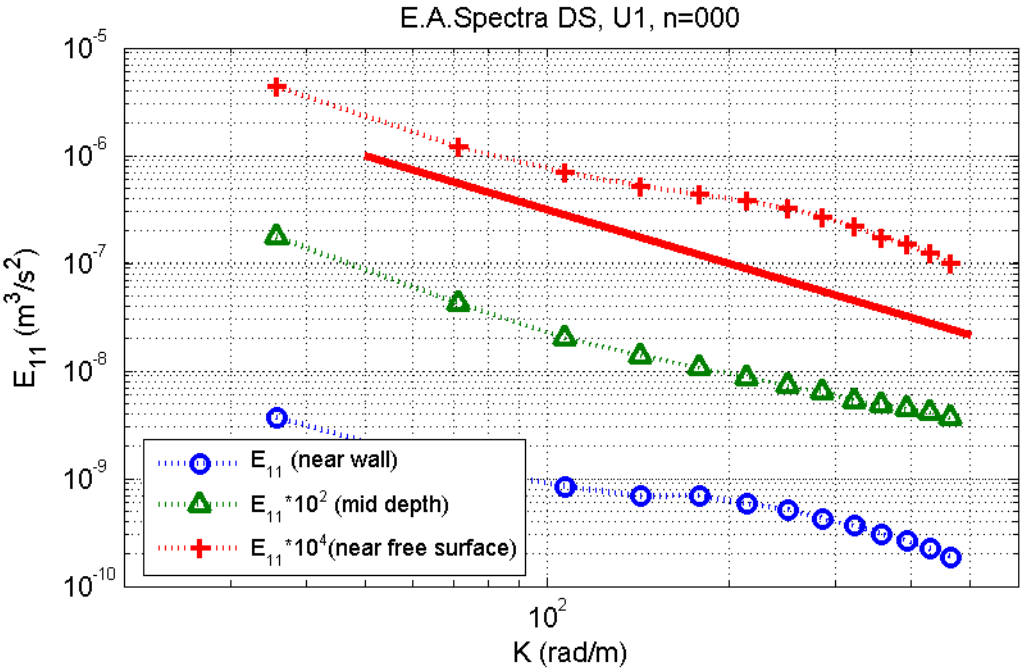


Figure 3.62: Power spectra $E_{11}$, n=000, U1.

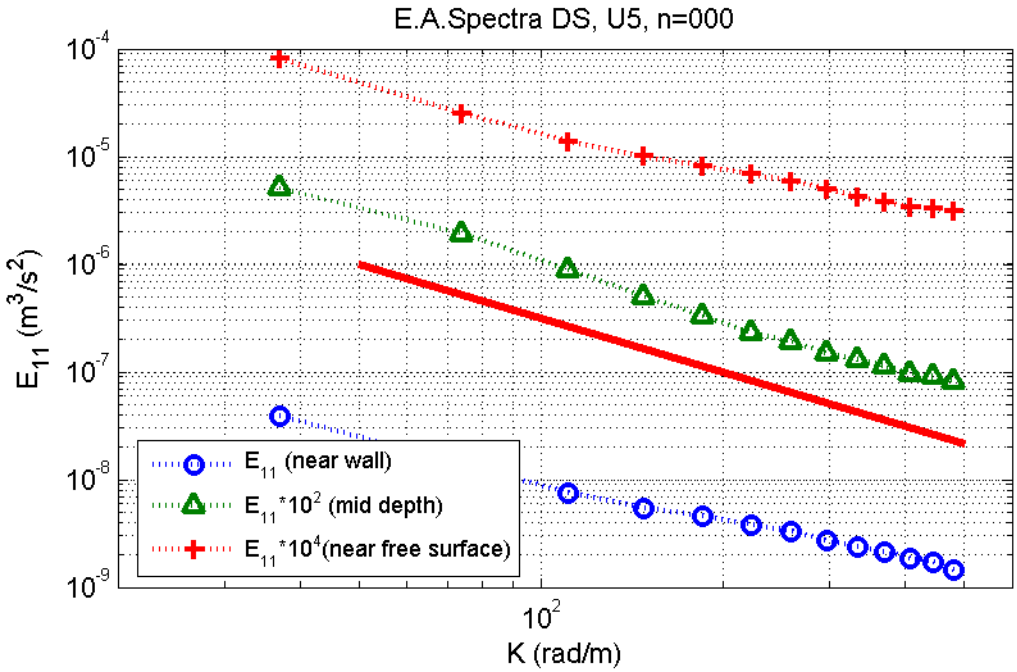


Figure 3.63: Power spectra $E_{11}$, n=000, U5.

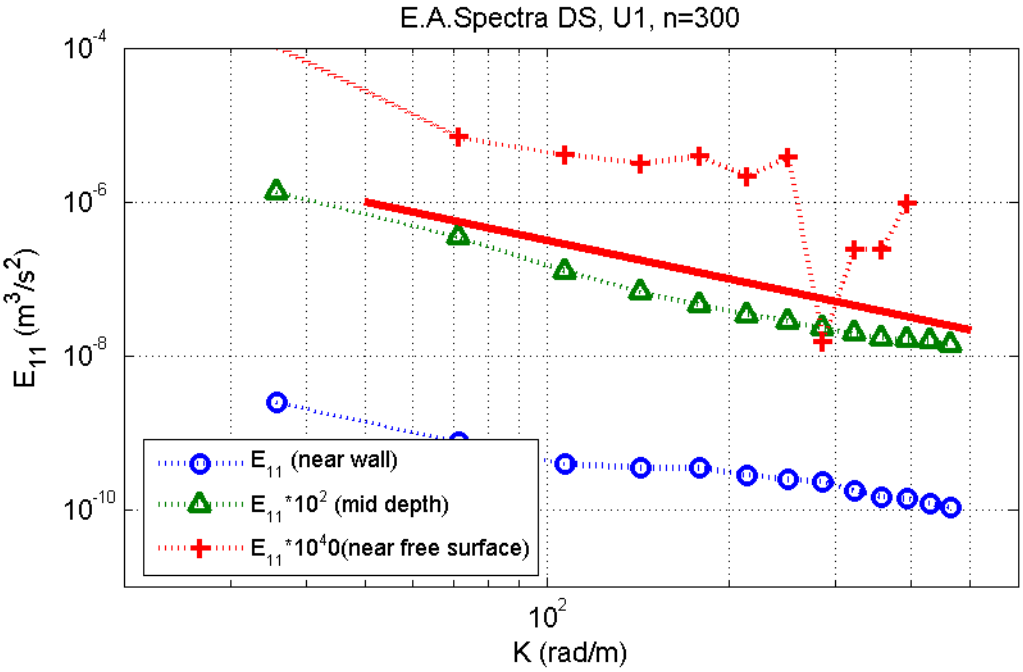


Figure 3.64: Power spectra $E_{11}$, n=300, U1.

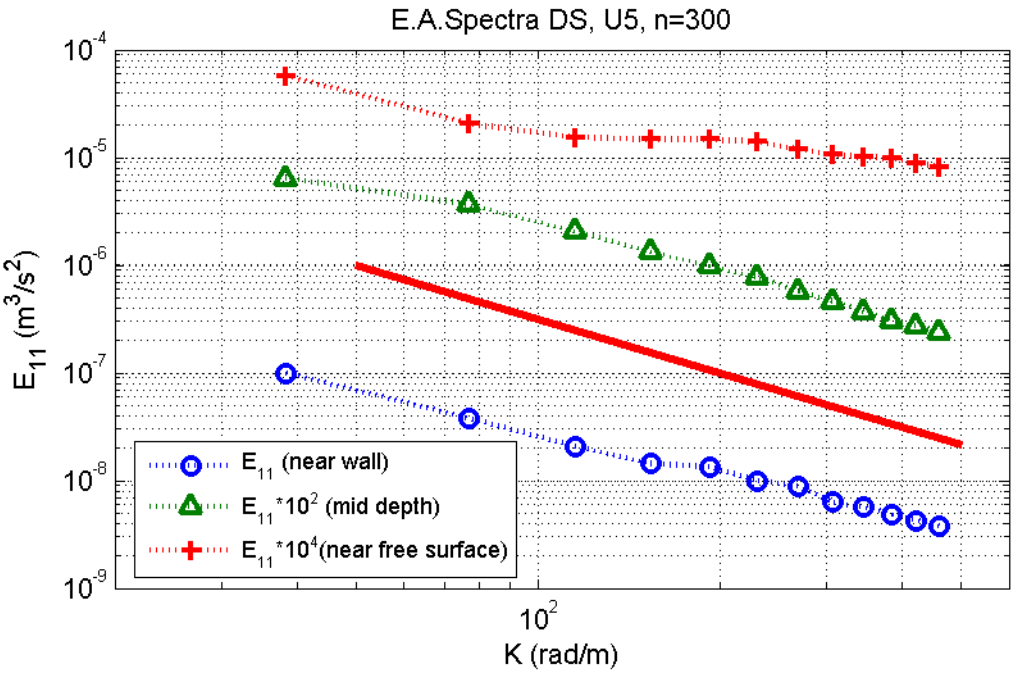


Figure 3.65: Power spectra $E_{11}$, n=300, U5.

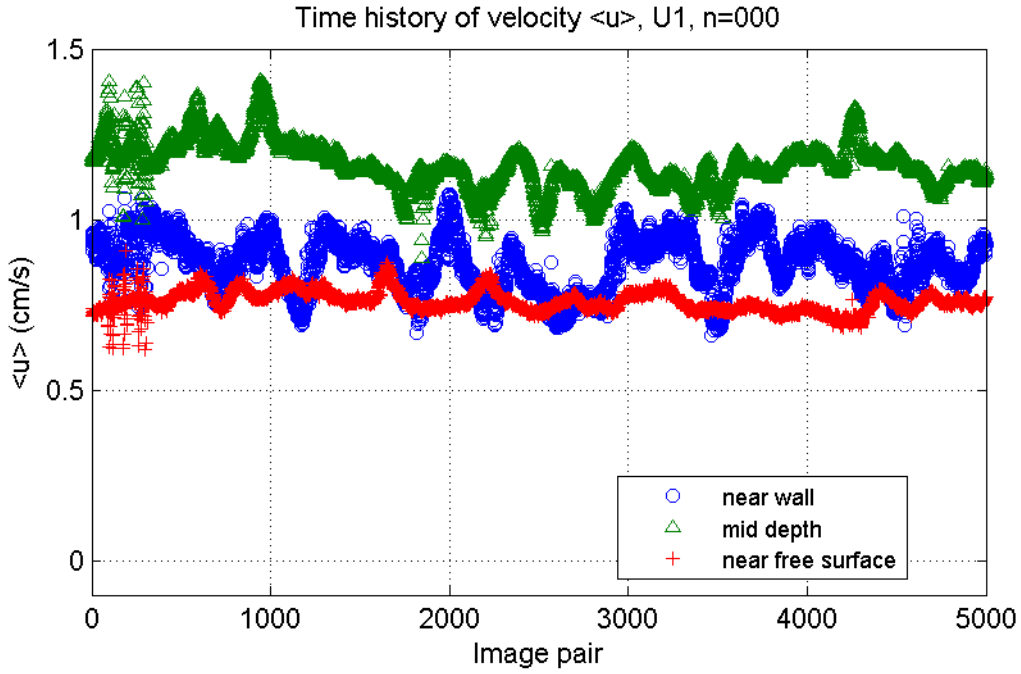


Figure 3.66: Time history of $\langle u \rangle$ $(cm/s)$ , n=000, U1.

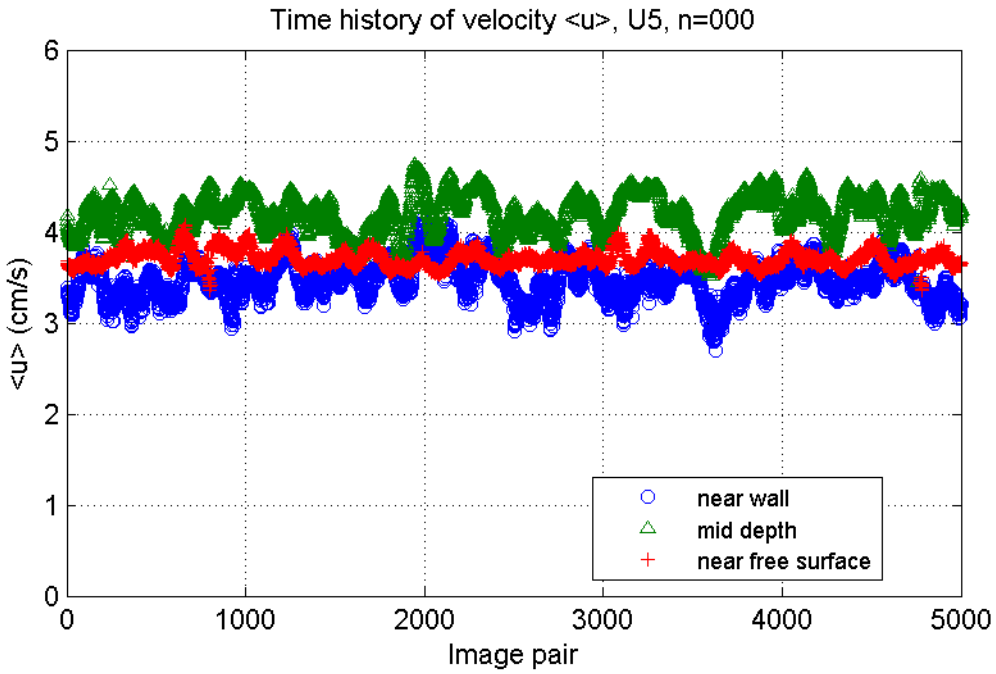


Figure 3.67: Time history of $\langle u \rangle$ $(cm/s)$ , n=000, U5.

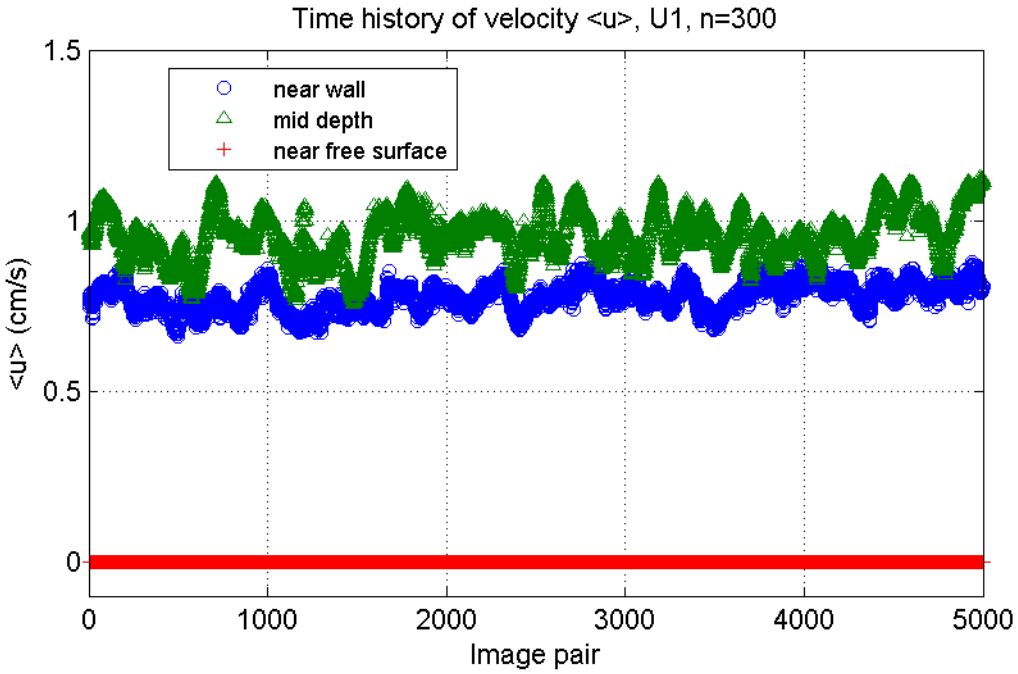


Figure 3.68: Time history of $\langle u \rangle$ $(cm/s)$ , n=300, U1.

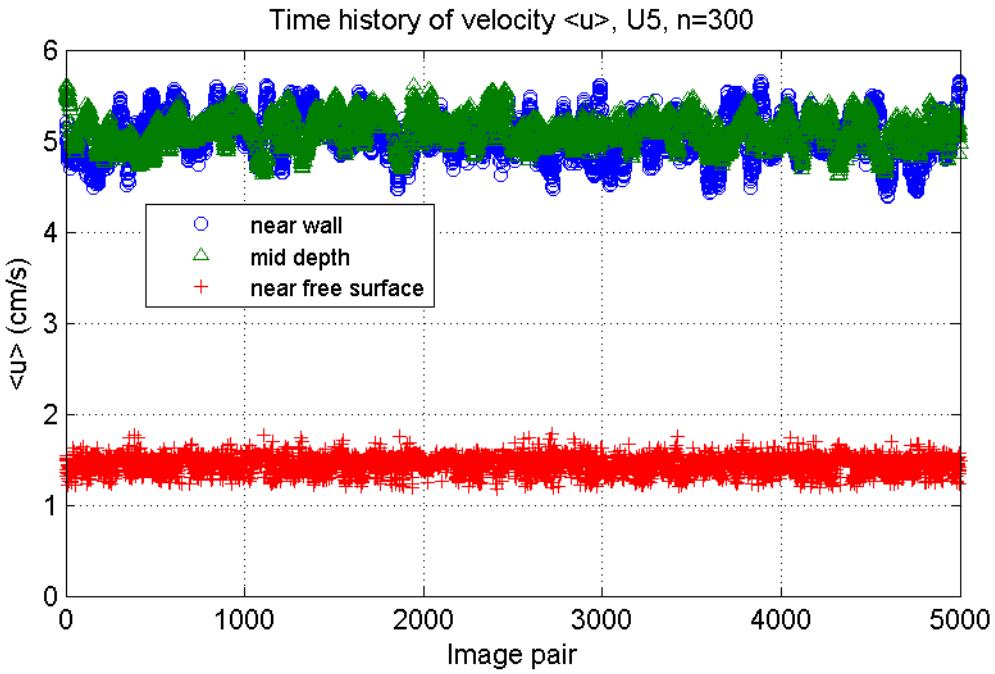


Figure 3.69: Time history of $\langle u \rangle$ $(cm/s)$ , n=300, U5.

There is no clear evidence of periodic low frequency fluctuations in the streamwise velocity, as it remains practically constant for the duration of the experiment.

#### 3.2.2.3 Near wall analysis

Using the SFOV images, it is possible to make an analysis similar to section 3.2.1., now for vegetated flow. Looking at a region 3cm from the bottom, for the DS section, the results for $\langle\overline{u}\rangle$, $\langle\overline{w}\rangle$, $\langle\overline{u}_{rms}\rangle$ and $\langle\overline{u'w'}\rangle$ are shown in Figures 3.70 to 3.73. This allows for a more detailed insight of the effects of the bottom combined with the vegetation.

In contrast to other studies, instead of being damped, the velocity and turbulence near the bottom increases with the presence of plants due to the morphology of the patch created. This is clearly observed in Figure 3.74, showing the maximum velocity against the respective density. To study the effects of vegetation on friction velocity ($u_*$) and bottom stress ($\tau_w$), the data is fitted to a log-law, thus obtaining the values for $u_*$ as shown in Figure 3.75.

There is a noticeable increase in $u_*$ as the densi ty increases. Comparing both parameters, by dividing the turbulent velocity by the maximum velocity, a clear trend is observed, as shown in Figure 3.76, where the normalized $u_*/\langle\overline{u}\rangle_{max}$ fall almost on the same point for all densities except for the slowest case U1. A similar trend is observed in Figure 3.77, by plotting the friction velocity against the maximum velocity of their respective profiles. All of the values seem to fall close to the same straight line as the results for the non-vegetated case (previously shown in Figure 3.31), still following closely the relation described in equation 3.2.

As previously done for the non-vegetated case, using equation 3.5 the experimental data allows the calculation of the total stress for each density and velocity. Such results are shown in Figures 3.78 to 3.81.

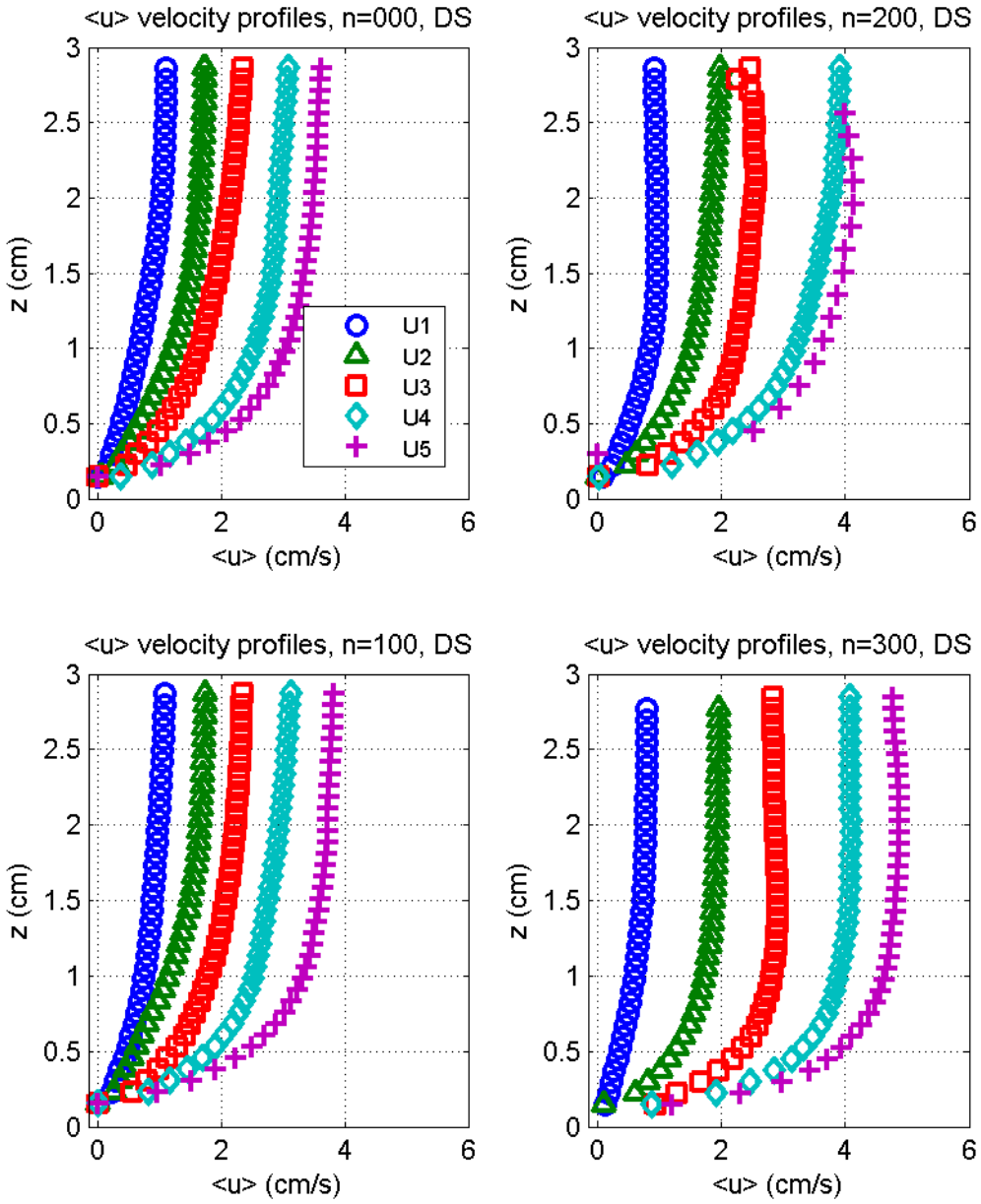


Figure 3.70: Longitudinal velocity $\langle \overline{u} \rangle$ $(cm/s)$, SFOV, all $n$.

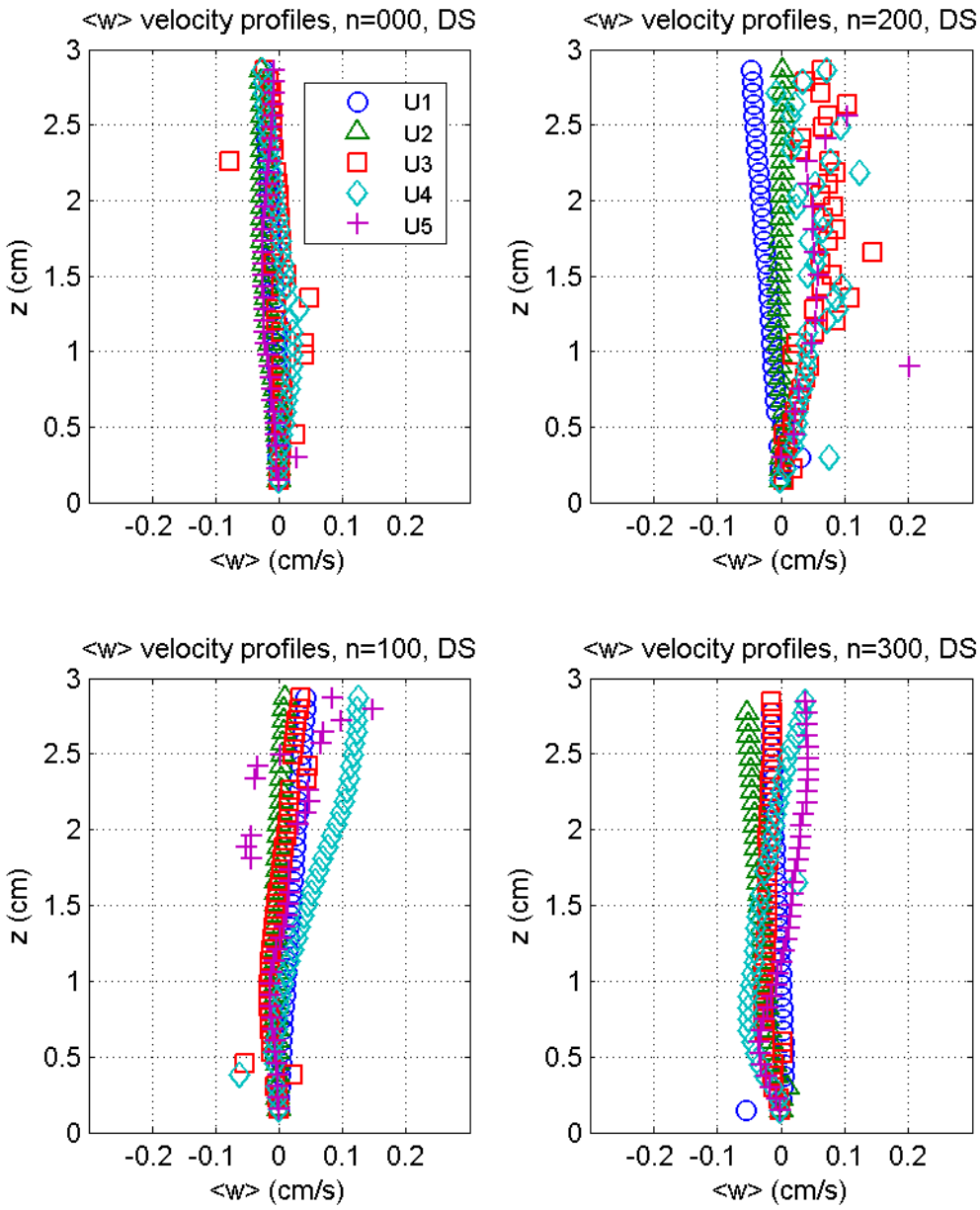


Figure 3.71: Vertical velocity $\langle \overline{w} \rangle$ $(cm/s)$, SFOV, all $n$.

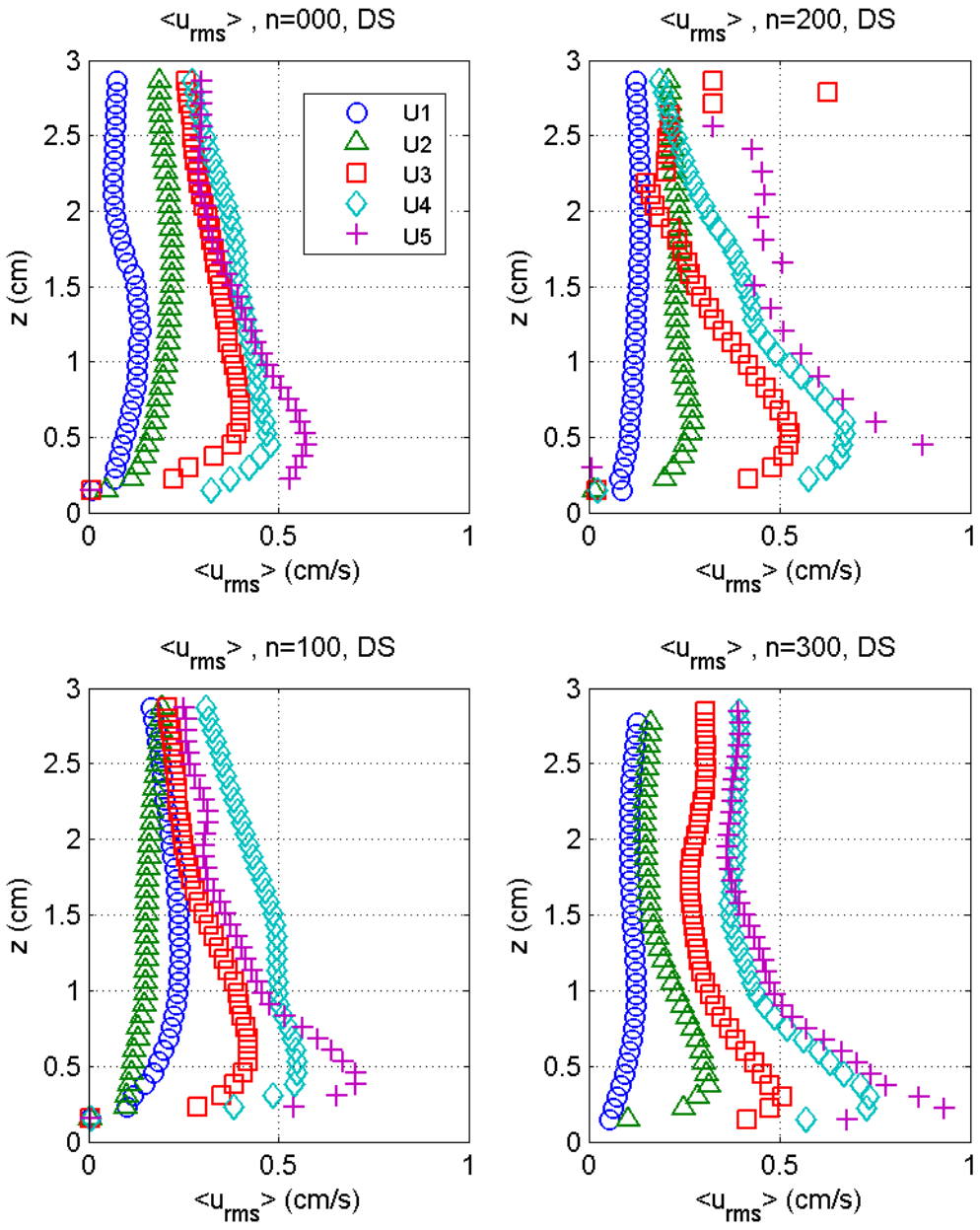


Figure 3.72: Turbulence intensity $\langle \overline{u}_{rms} \rangle$ $(cm/s)$, SFOV, all $n$.

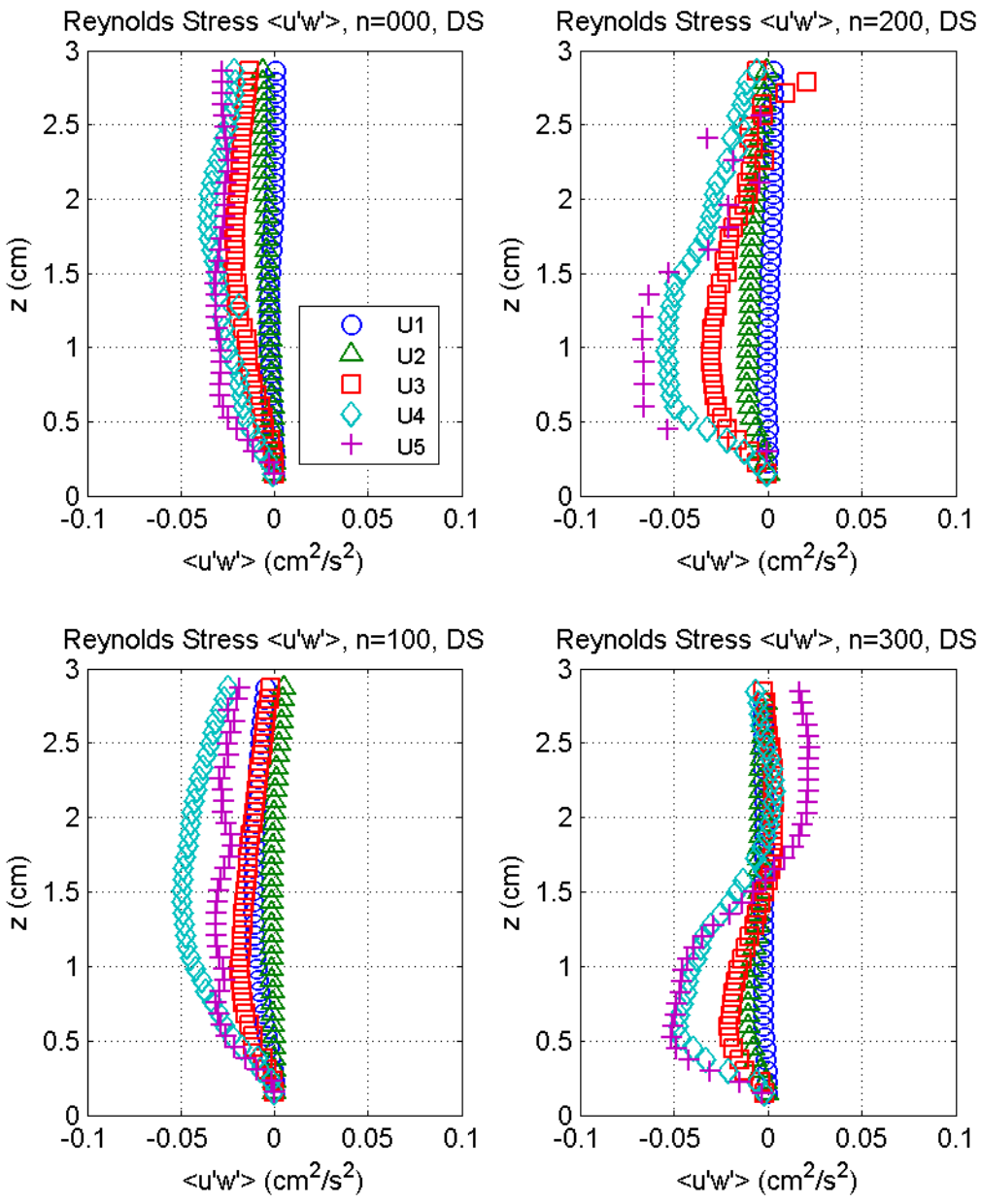


Figure 3.73: Reynolds stress $\langle\overline{u'w'}\rangle$ $(cm^2/s^2)$, SFOV, all $n$.

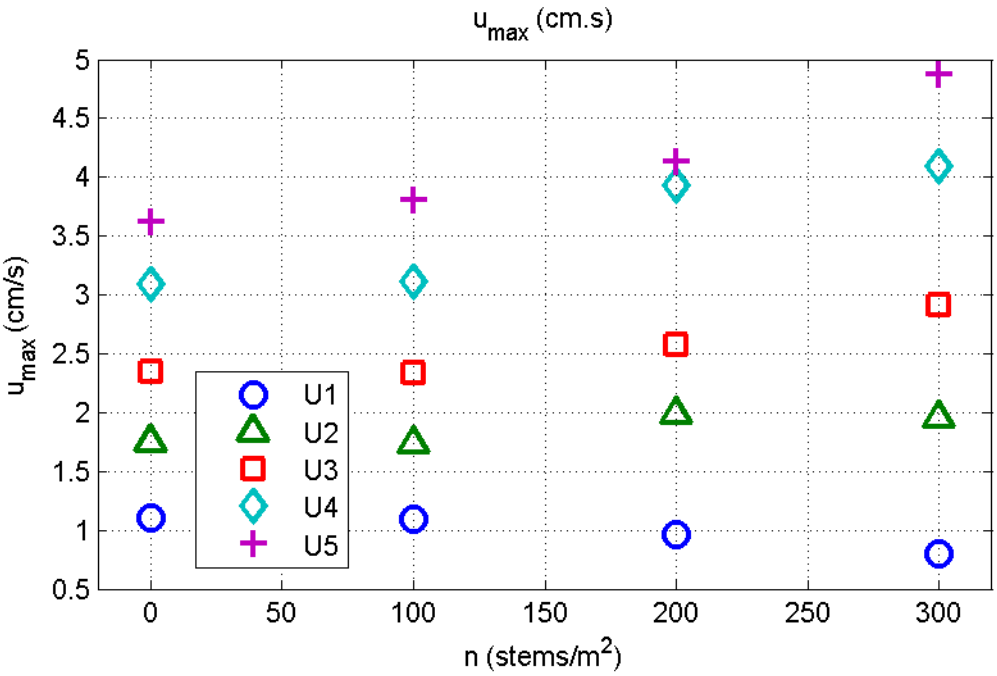


Figure 3.74: Maximum velocity $\langle \overline{u} \rangle_{max}$for each density $n$.

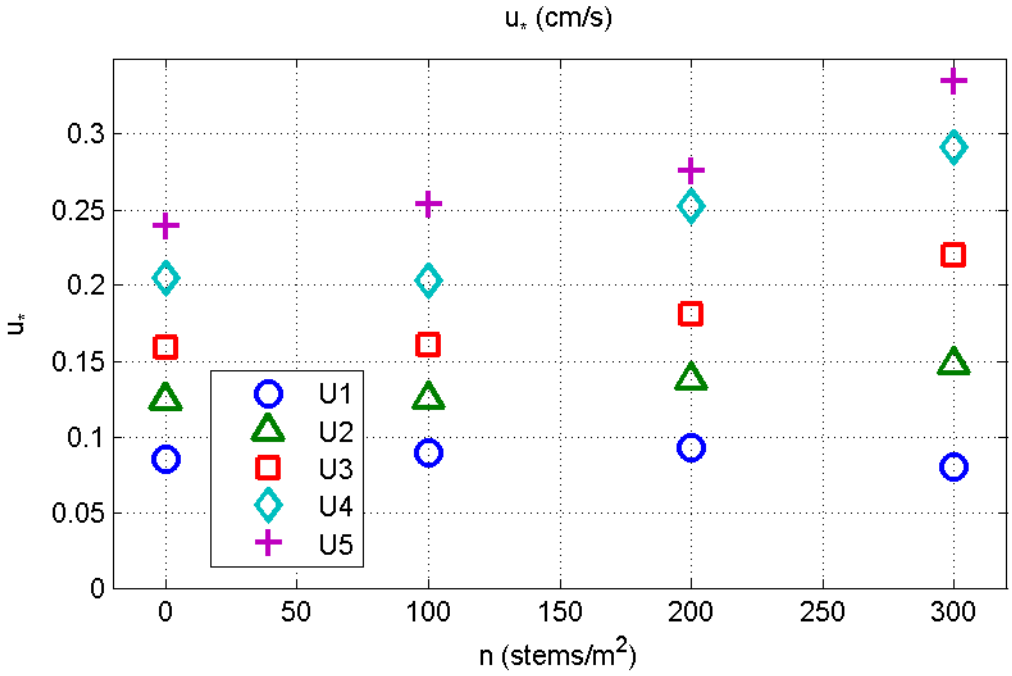


Figure 3.75: Turbulent velocity $u_*$ for each density $n$.

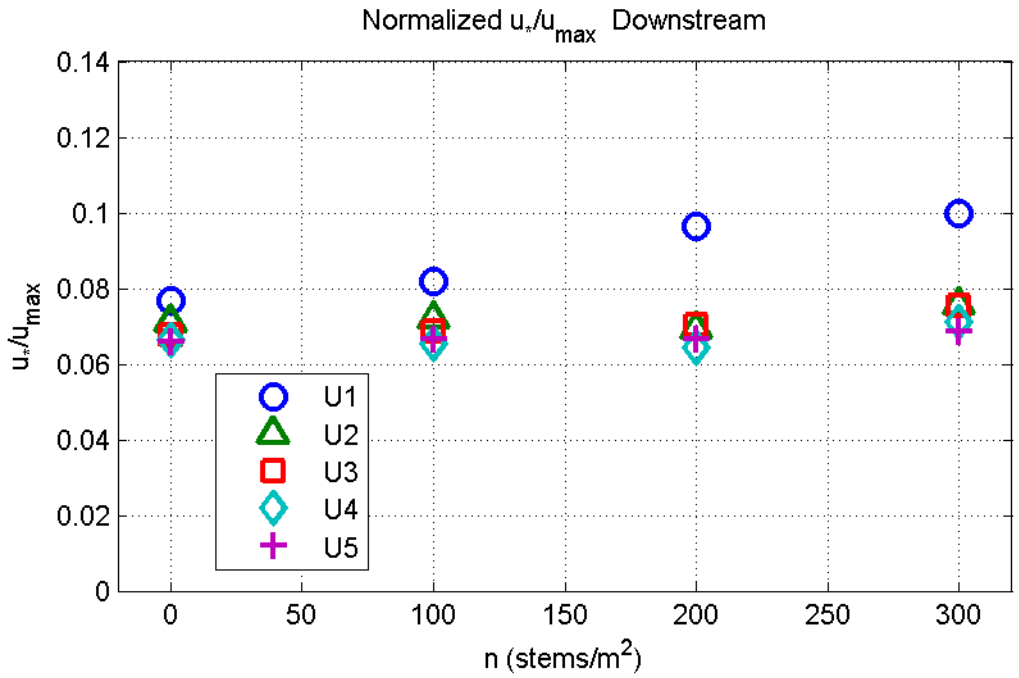


Figure 3.76: Normalized turbulent velocity $u_*/\langle\overline{u}\rangle_{max}$ for each density $n$.

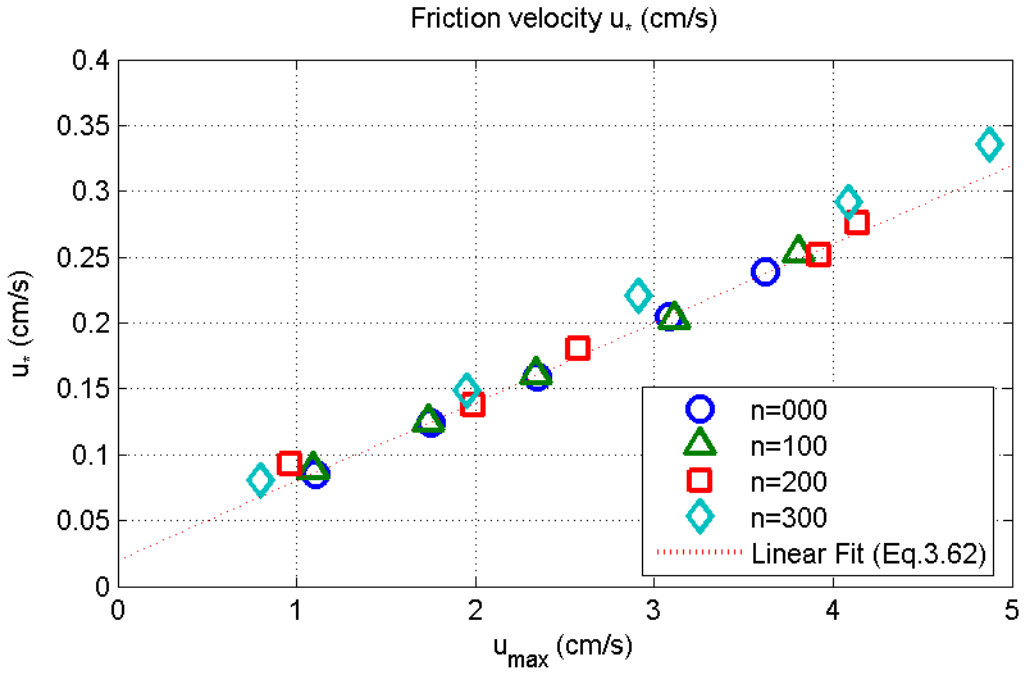


Figure 3.77: Turbulent velocity $u_*$ against its respective $\langle\overline{u_{max}}\rangle$.

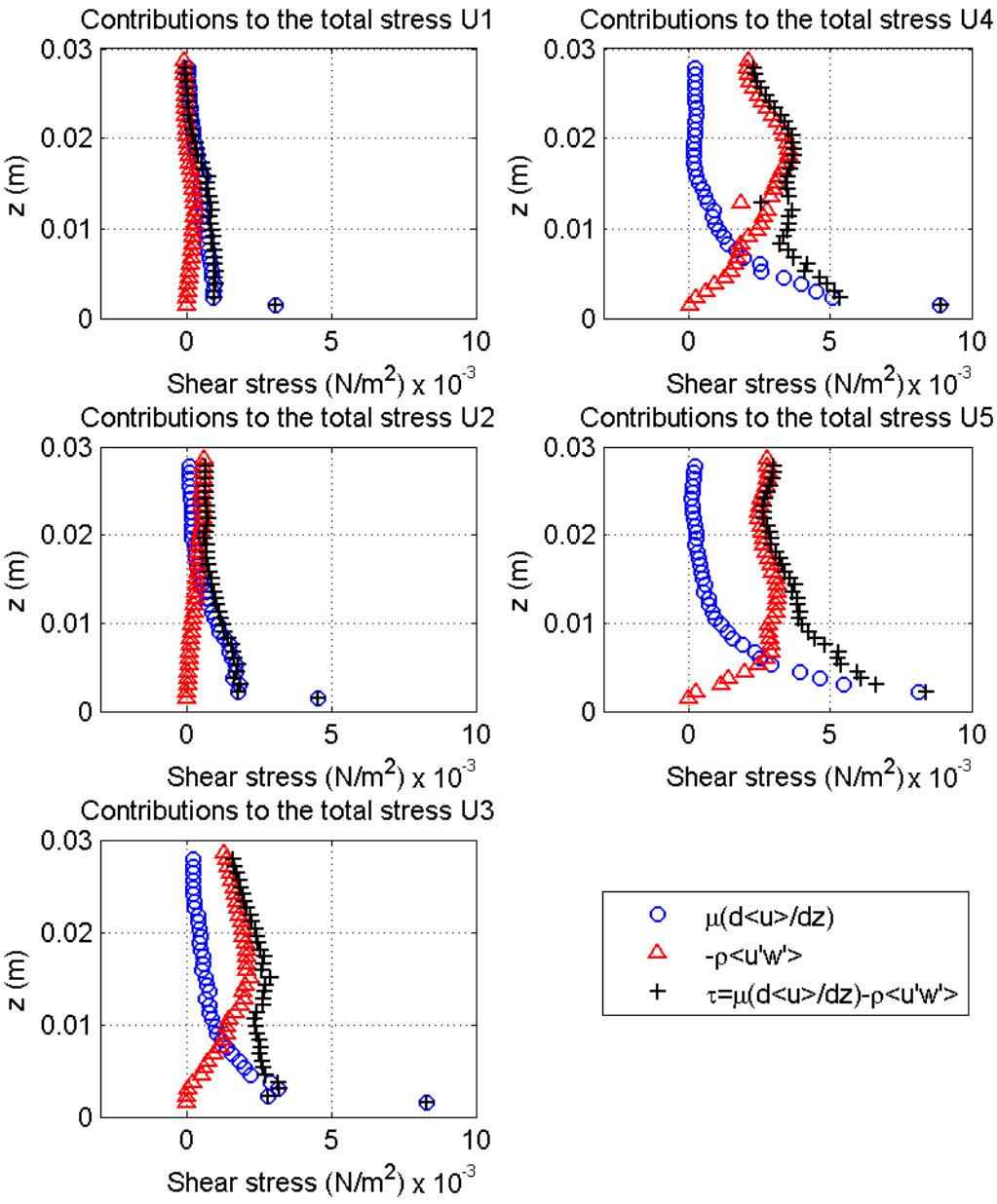


Figure 3.78: Vegetated flow, Total shear stress $\tau$ $(N/m^2)$, $n = 0$.

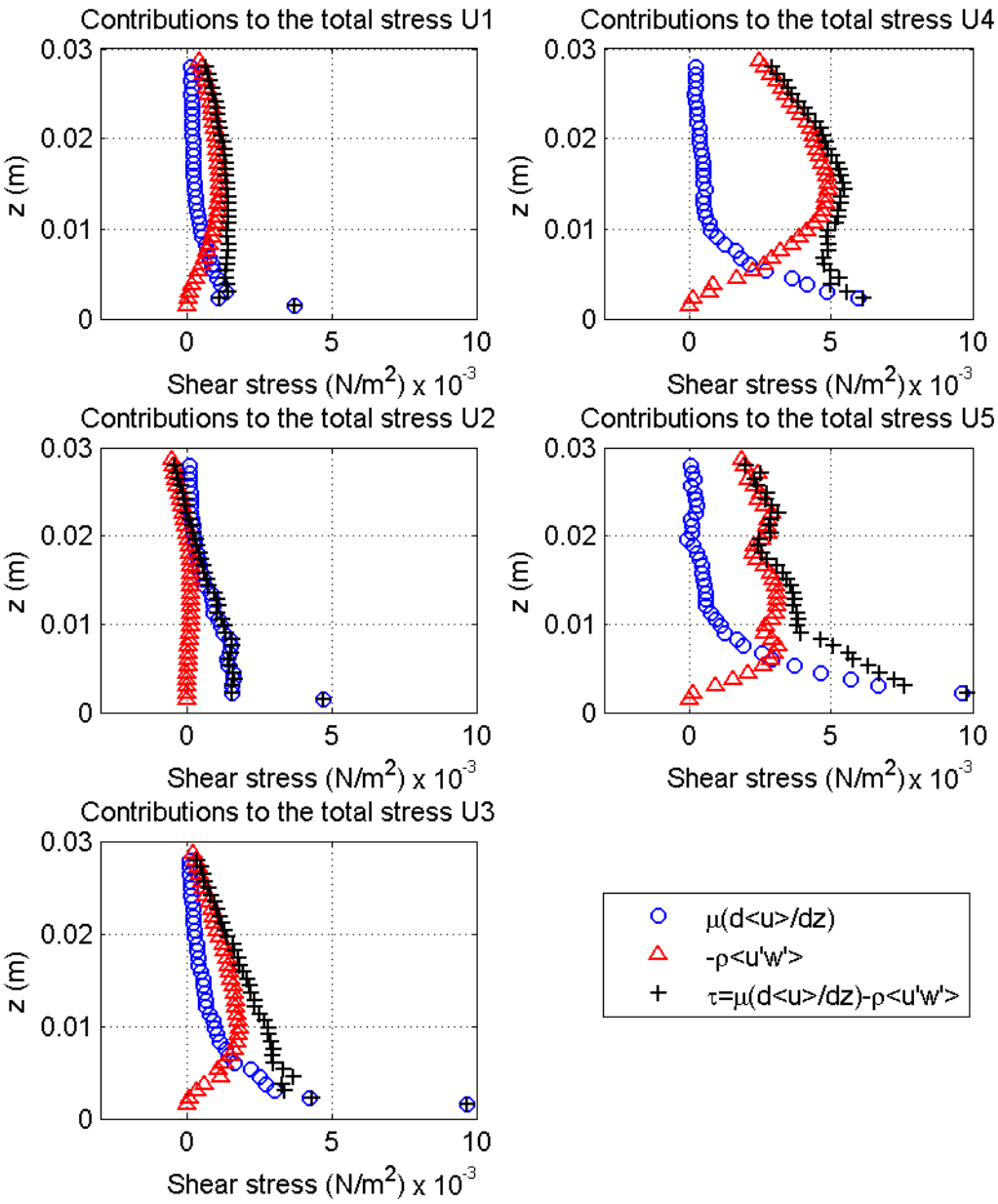


Figure 3.79: Vegetated flow, Total shear stress $\tau$ $(N/m^2)$, $n = 100$.

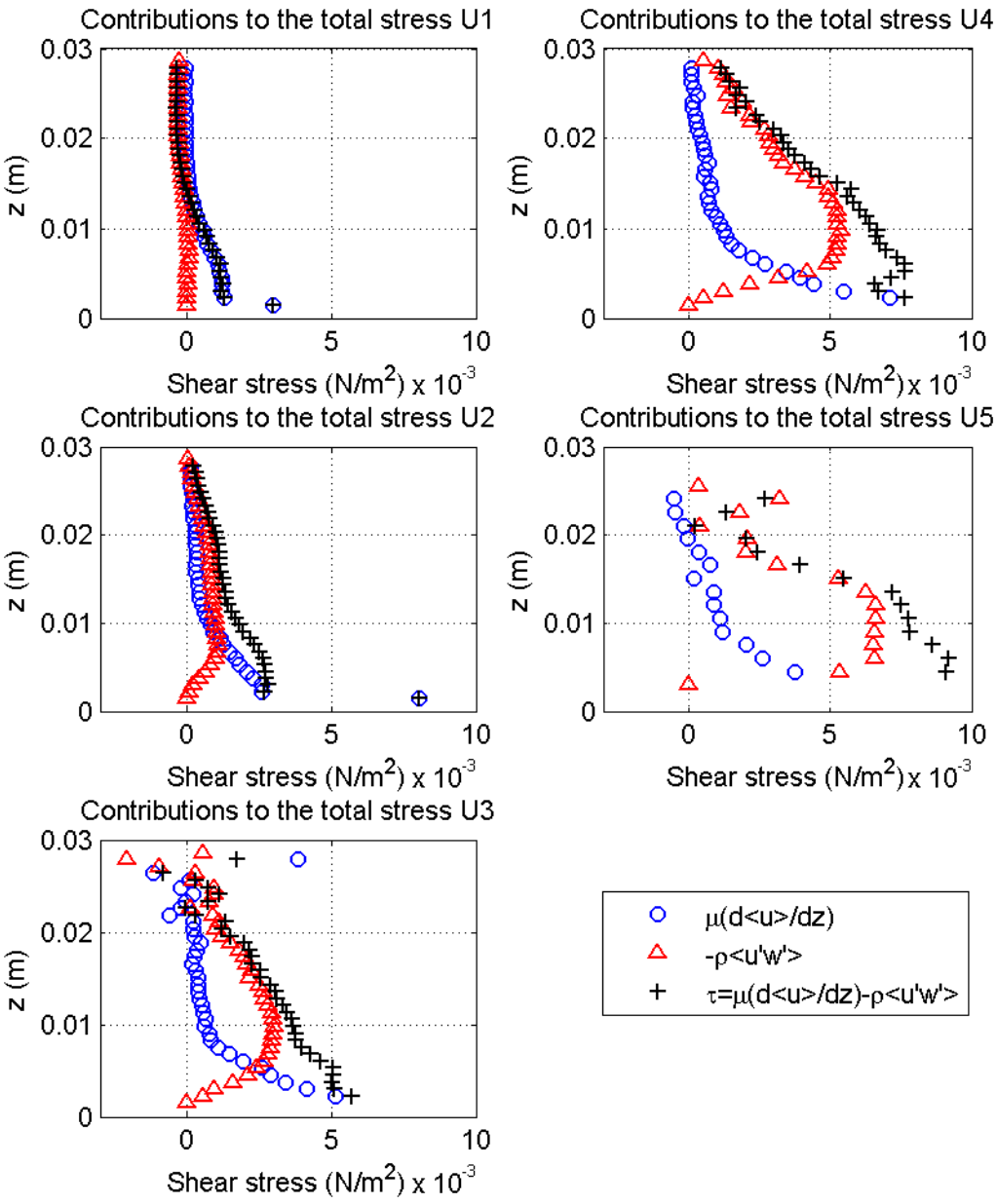


Figure 3.80: Vegetated flow, Total shear stress $\tau$ $(N/m^2)$, $n = 200$.

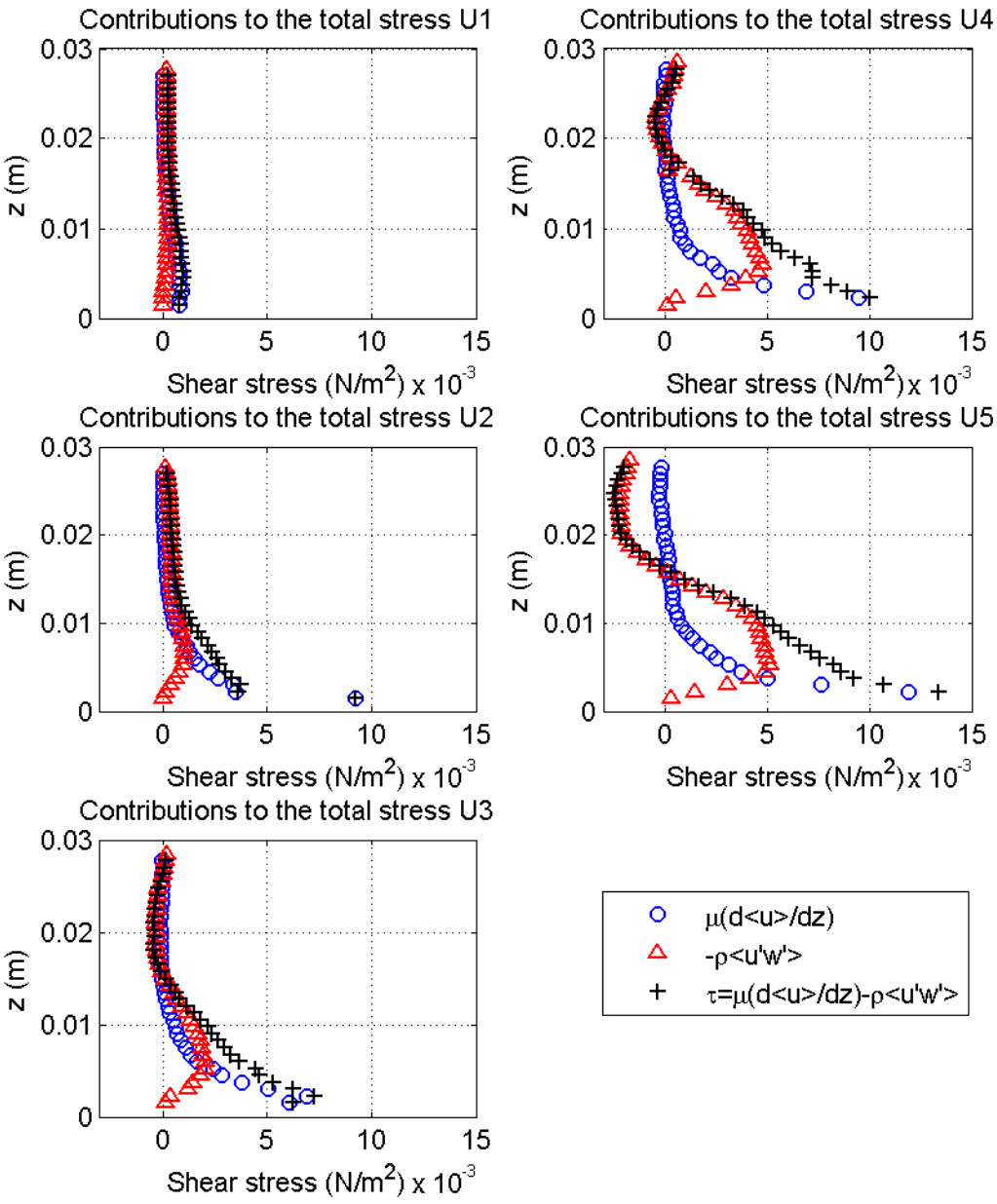


Figure 3.81: Vegetated flow, Total shear stress $\tau$ $(N/m^2)$, $n = 300$.

The results differ considerably from the null case ($n = 0$), and do not show a particular trend as the density increases.

The stress can be normalized by the wall stress $\tau_w$, which can be calculated as $\tau_w = \rho u_*^2$, thus depending on the friction velocity. There are different ways to calculate $u_*$ using the information available, by a) Obtaining the dimensional stress at the wall (from Figures 3.78 to 3.81) and using the definition $u_* = \sqrt{\frac{\tau_w}{\rho}}$, or b) Fitting a straight line to the region of constant $\langle\overline{u'w'}\rangle$, c) Fitting the experimental data using a logarithmic law, as mentioned in subsection 3.2.1.2, or d) Fitting the experimental data from the viscous sublayer where $u^+ = z^+$.

The results from such methods are shown in Tables 3.9 and 3.10, both with absolute values ($m/s$) and the ratios obtained by comparing against the first method mentioned.

There is a good agreement between the values obtained from the total stress and those from the log-law and viscous layer approaches, even when some values differ more than 30%, most of them fall within a $\pm 12\%$ range. The results from the total stress are taken as reference values hereafter.

If we normalize each component of the total stress by the bottom stress, $\tau_w$, obtained from the definition of the friction velocity, $u_* = \sqrt{\tau_w/\rho}$ , and plot it against a non-dimensional height $z^+ = \frac{u_* z}{\nu}$ we have the results shown in Figures 3.82 to 3.85.

Also, normalizing by $\tau(z)$ yields the results shown in Figures 3.86 to 3.89.

Table 3.9: Values for $u^*$ ($\times 10^{-3}(m/s)$) using different approaches.

| | | From total stress | From peak of $\langle\overline{u'w'}\rangle$ | From log-law (LFOV) | From log-law (SFOV) | From viscous layer $u^+ = z^+$ |
|---|---|---|---|---|---|---|
| n=0 | U1 | 0.975 | 0.975 | 0.900 | 0.850 | 0.860 |
| | U2 | 1.34 | 1.34 | 1.31 | 1.24 | 1.17 |
| | U3 | 1.64 | 1.64 | 1.70 | 1.59 | 1.47 |
| | U4 | 1.90 | 1.90 | 2.15 | 2.05 | 1.94 |
| | U5 | 1.98 | 1.98 | 2.48 | 2.39 | 2.18 |
| n=100 | U1 | 1.18 | 1.18 | 0.880 | 0.890 | 0.970 |
| | U2 | 1.25 | 1.25 | 1.30 | 1.25 | 1.09 |
| | U3 | 1.73 | 1.34 | 1.67 | 1.61 | 1.59 |
| | U4 | 2.32 | 2.19 | 2.13 | 2.03 | 1.93 |
| | U5 | 1.98 | 1.76 | 2.66 | 2.54 | 2.22 |
| n=200 | U1 | 1.10 | 1.10 | 0.890 | 0.930 | 1.01 |
| | U2 | 1.64 | 1.00 | 1.47 | 1.38 | 1.40 |
| | U3 | 1.92 | 1.73 | 2.15 | 1.81 | 1.89 |
| | U4 | 2.59 | 2.30 | 2.77 | 2.52 | 2.28 |
| | U5 | 2.78 | 2.57 | 3.23 | 2.76 | 2.40 |
| n=300 | U1 | 0.975 | 0.975 | 0.670 | 0.800 | 0.840 |
| | U2 | 1.73 | 1.00 | 1.53 | 1.48 | 1.62 |
| | U3 | 2.49 | 1.38 | 1.95 | 2.20 | 2.33 |
| | U4 | 2.70 | 2.15 | 2.92 | 2.91 | 2.85 |
| | U5 | 2.88 | 2.24 | 3.34 | 3.35 | 3.1 |

Table 3.10: Relative values for $u^*$ using different approaches.

| | | From total stress | From peak of $\langle\overline{u'w'}\rangle$ | From log-law (LFOV) | From log-law (SFOV) | From viscous layer $u^+ = z^+$ |
|---|---|---|---|---|---|---|
| n=0 | U1 | 1.0 | 1.0 | 0.92 | 0.87 | 0.88 |
| | U2 | 1.0 | 1.0 | 0.98 | 0.92 | 0.87 |
| | U3 | 1.0 | 1.0 | 1.03 | 0.97 | 0.89 |
| | U4 | 1.0 | 1.0 | 1.13 | 1.08 | 1.02 |
| | U5 | 1.0 | 1.0 | 1.26 | 1.21 | 1.10 |
| n=100 | U1 | 1.0 | 1.0 | 0.74 | 0.75 | 0.82 |
| | U2 | 1.0 | 1.0 | 1.04 | 1.00 | 0.88 |
| | U3 | 1.0 | 0.77 | 0.96 | 0.93 | 0.92 |
| | U4 | 1.0 | 0.94 | 0.92 | 0.87 | 0.83 |
| | U5 | 1.0 | 0.89 | 1.35 | 1.29 | 1.12 |
| n=200 | U1 | 1.0 | 1.0 | 0.81 | 0.85 | 0.92 |
| | U2 | 1.0 | 0.61 | 0.89 | 0.84 | 0.85 |
| | U3 | 1.0 | 0.90 | 1.12 | 0.94 | 0.98 |
| | U4 | 1.0 | 0.89 | 1.07 | 0.97 | 0.88 |
| | U5 | 1.0 | 0.93 | 1.16 | 0.99 | 0.86 |
| n=300 | U1 | 1.0 | 1.0 | 0.69 | 0.82 | 0.86 |
| | U2 | 1.0 | 0.58 | 0.88 | 0.85 | 0.94 |
| | U3 | 1.0 | 0.55 | 0.78 | 0.88 | 0.94 |
| | U4 | 1.0 | 0.79 | 1.08 | 1.08 | 1.05 |
| | U5 | 1.0 | 0.78 | 1.16 | 1.16 | 1.08 |

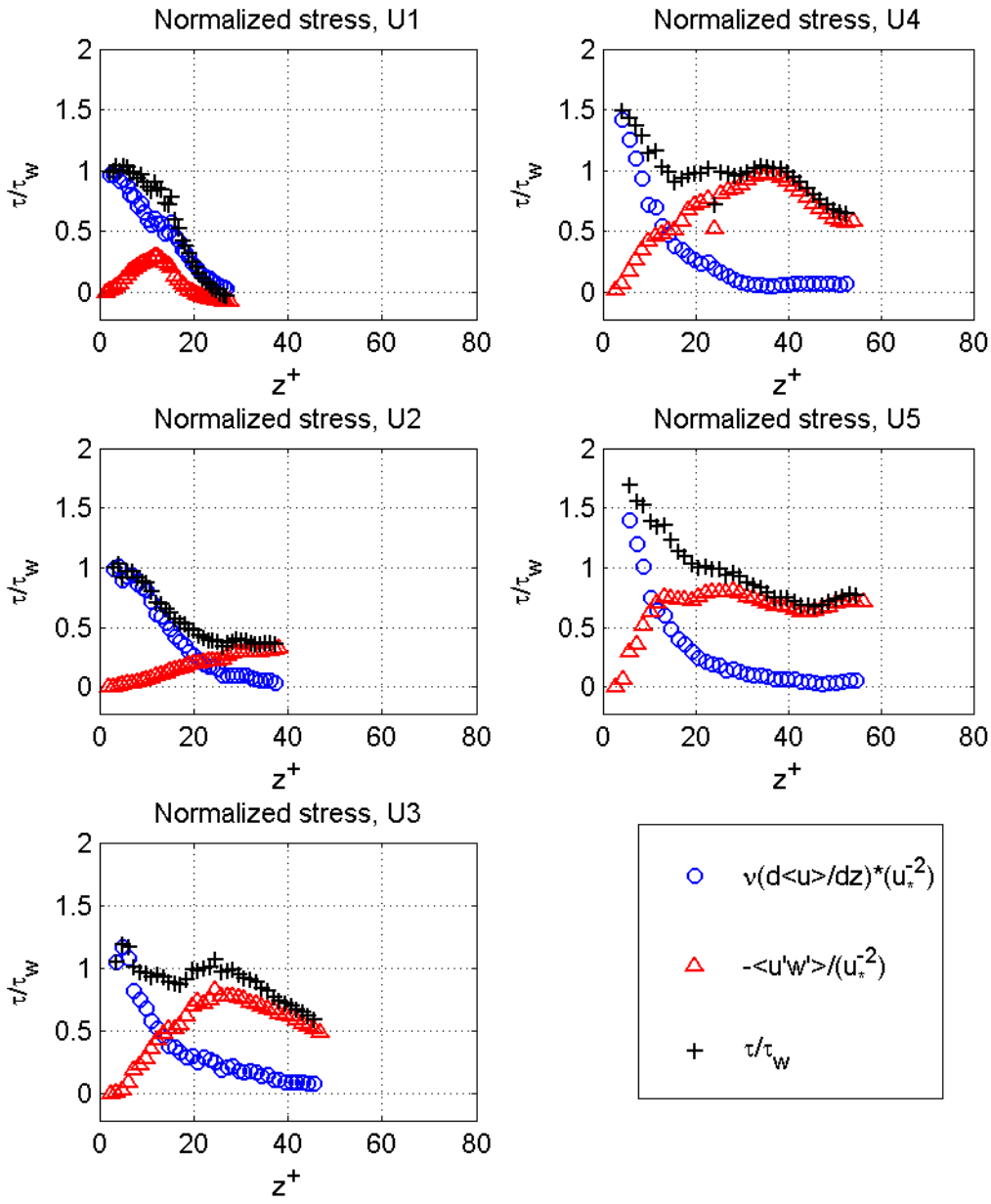


Figure 3.82: Non-dimensional stress $\tau(z)/\tau_w$, n=0.

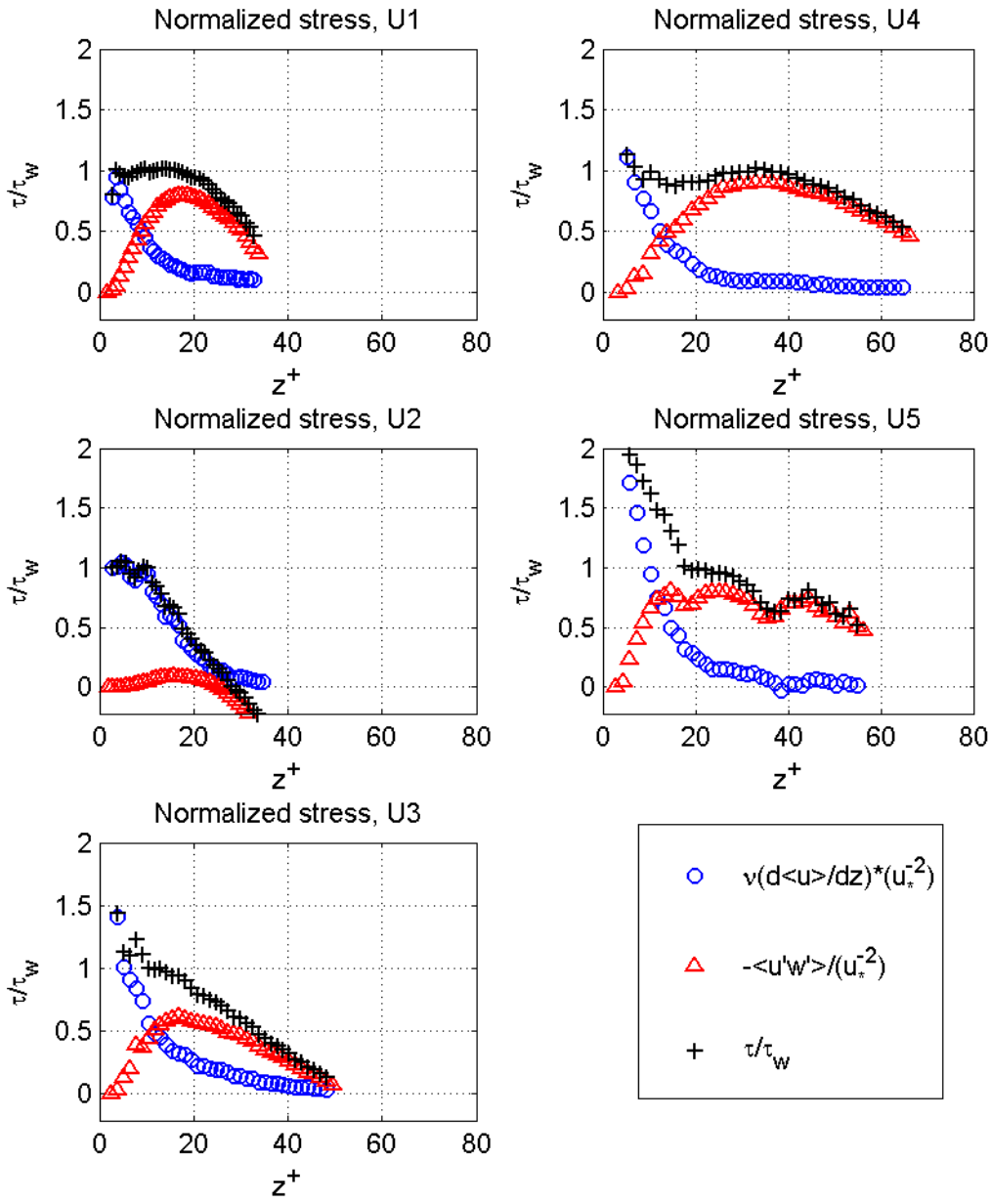


Figure 3.83: Non-dimensional stress $\tau(z)/\tau_w$, n=100.

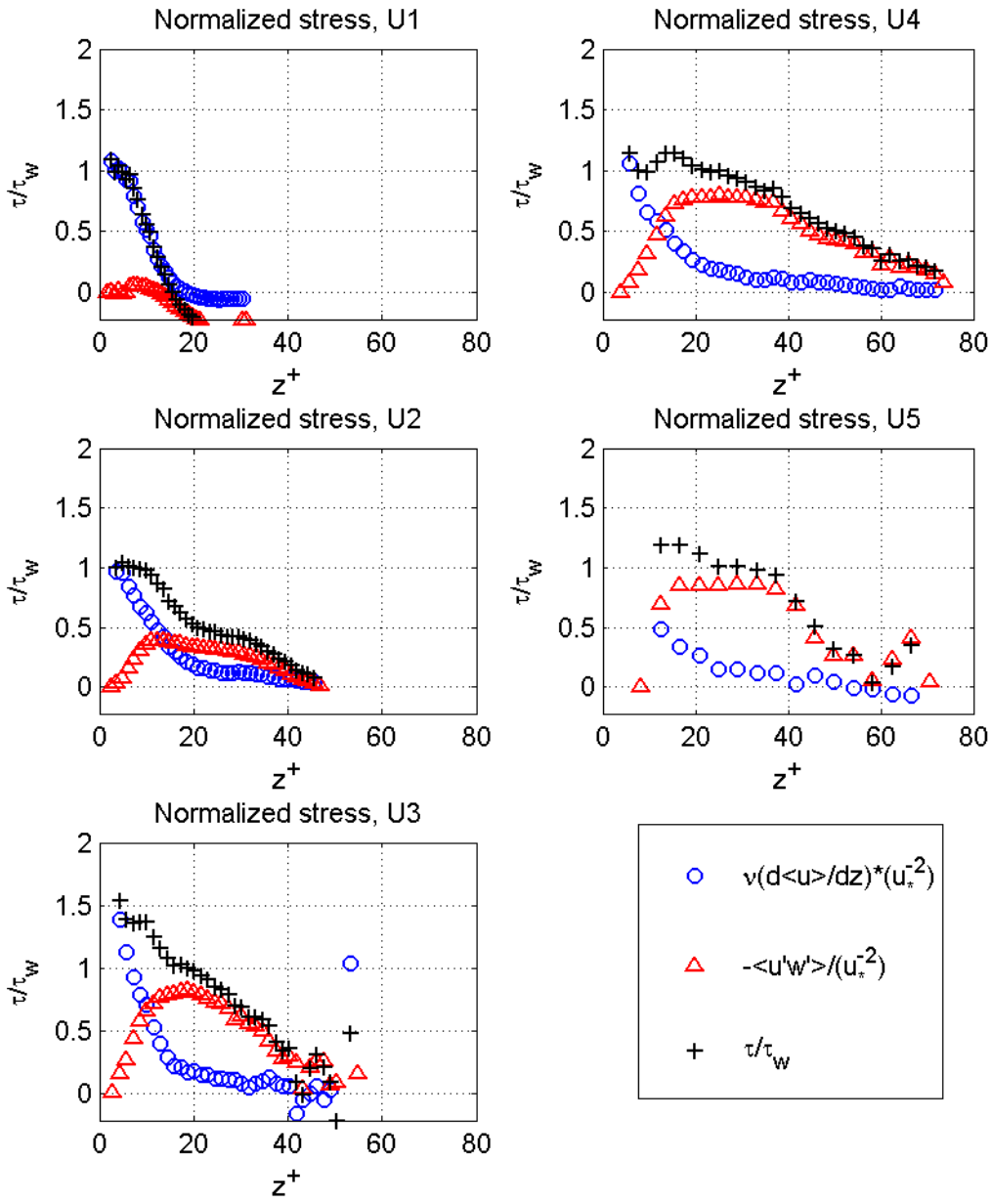


Figure 3.84: Non-dimensional stress $\tau(z)/\tau_w$, n=200.

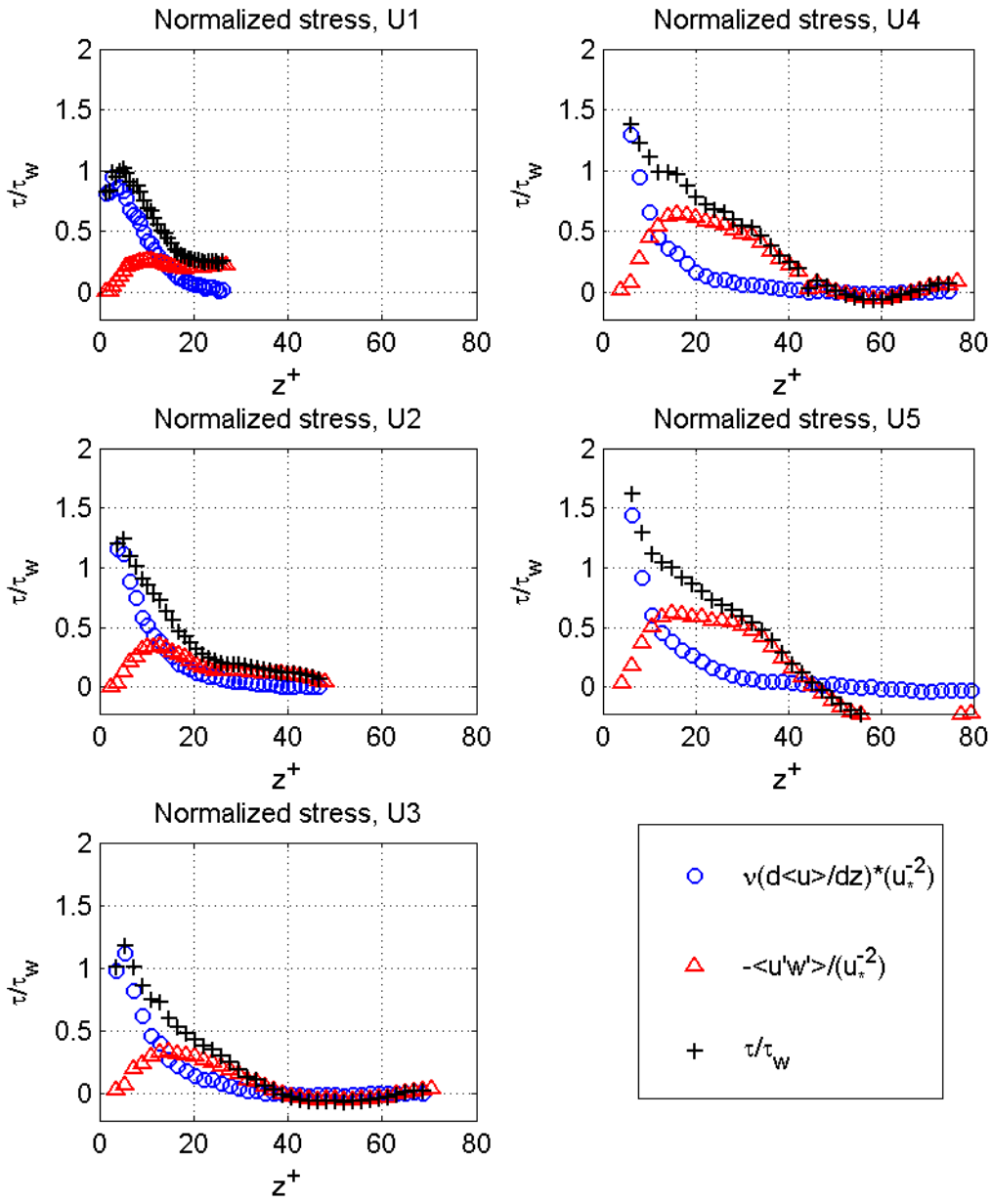


Figure 3.85: Non-dimensional stress $\tau(z)/\tau_w$, n=300.

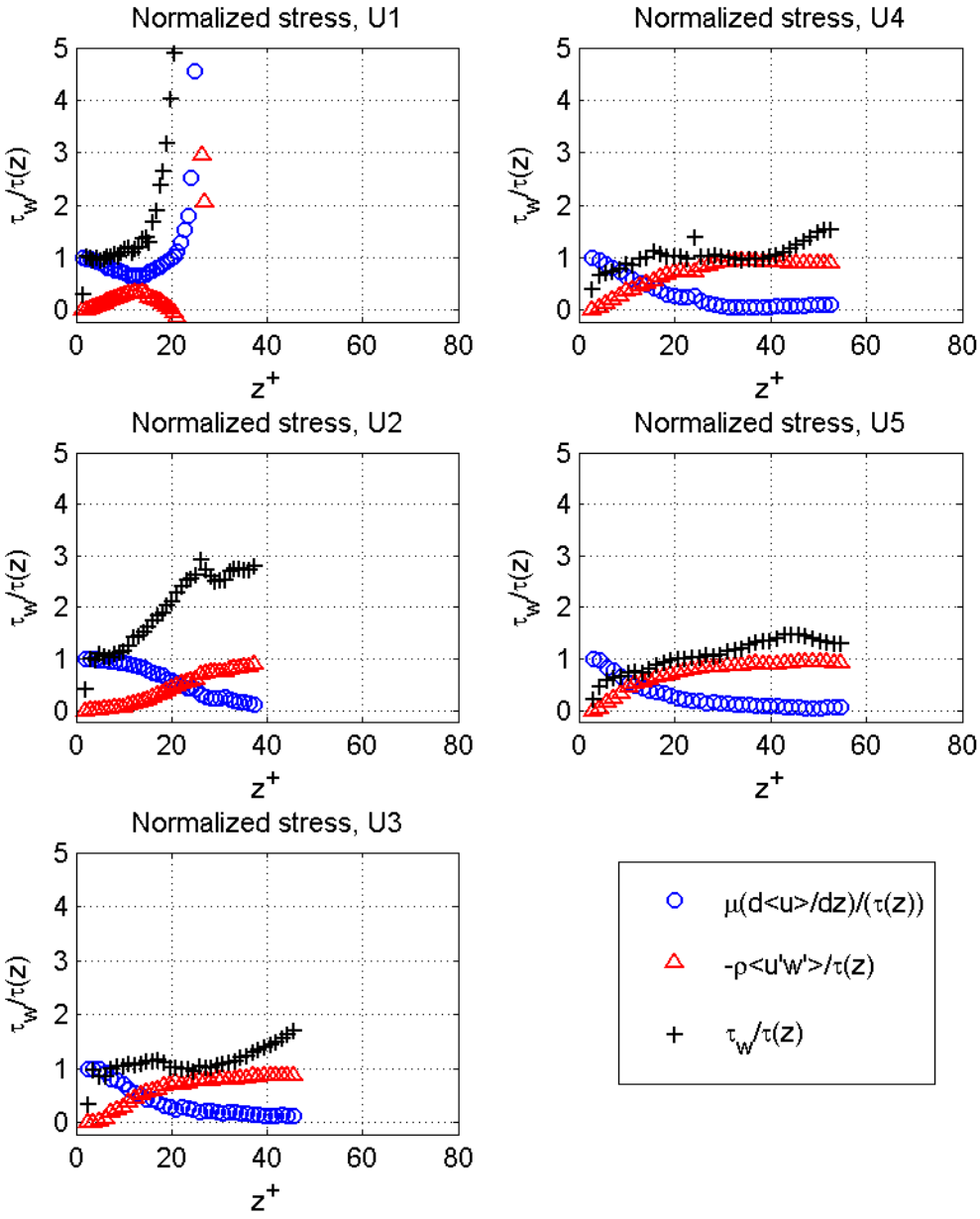


Figure 3.86: Non-dimensional stress $\tau/\tau(z)$, n=0.

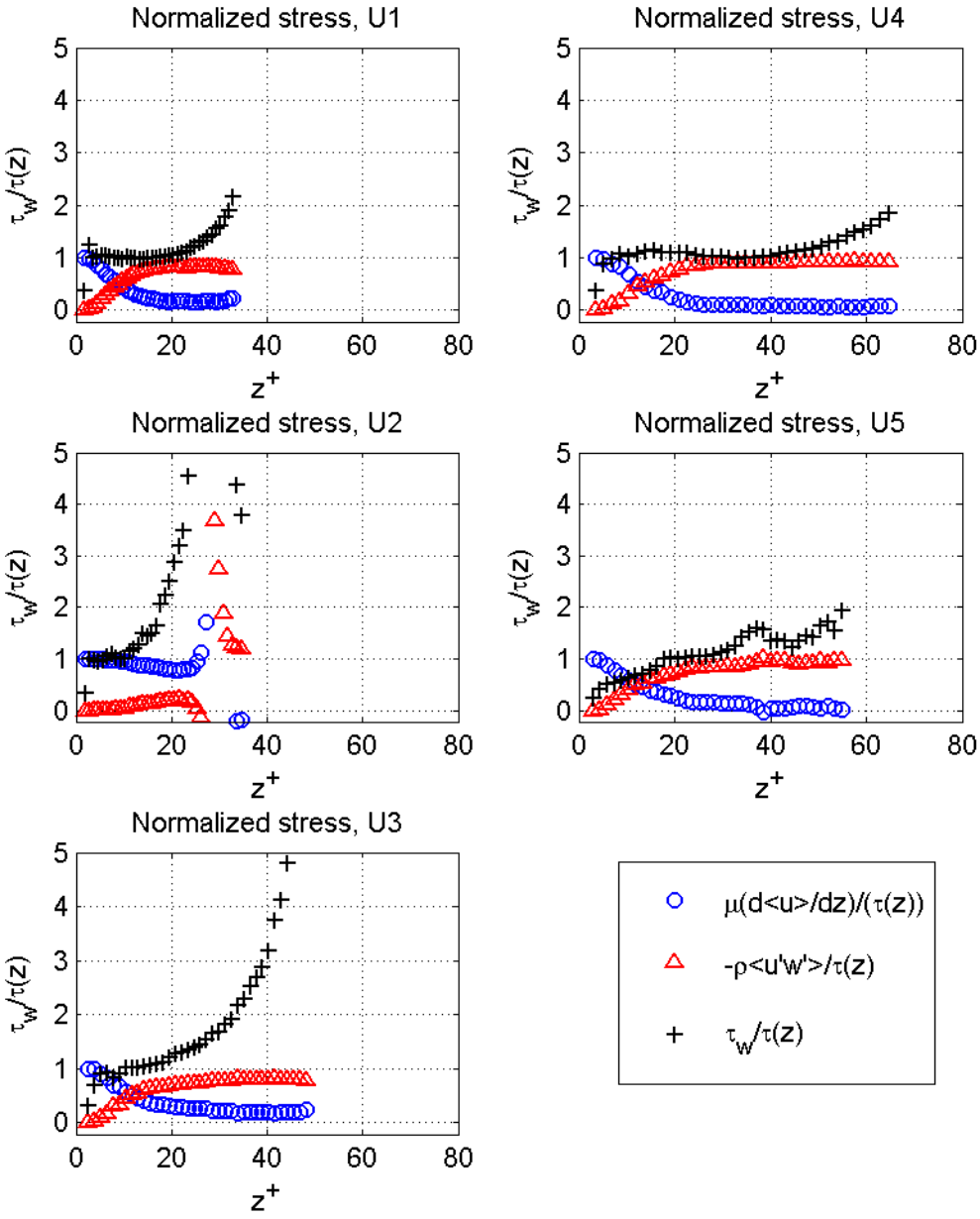


Figure 3.87: Non-dimensional stress $\tau/\tau(z)$, n=100.

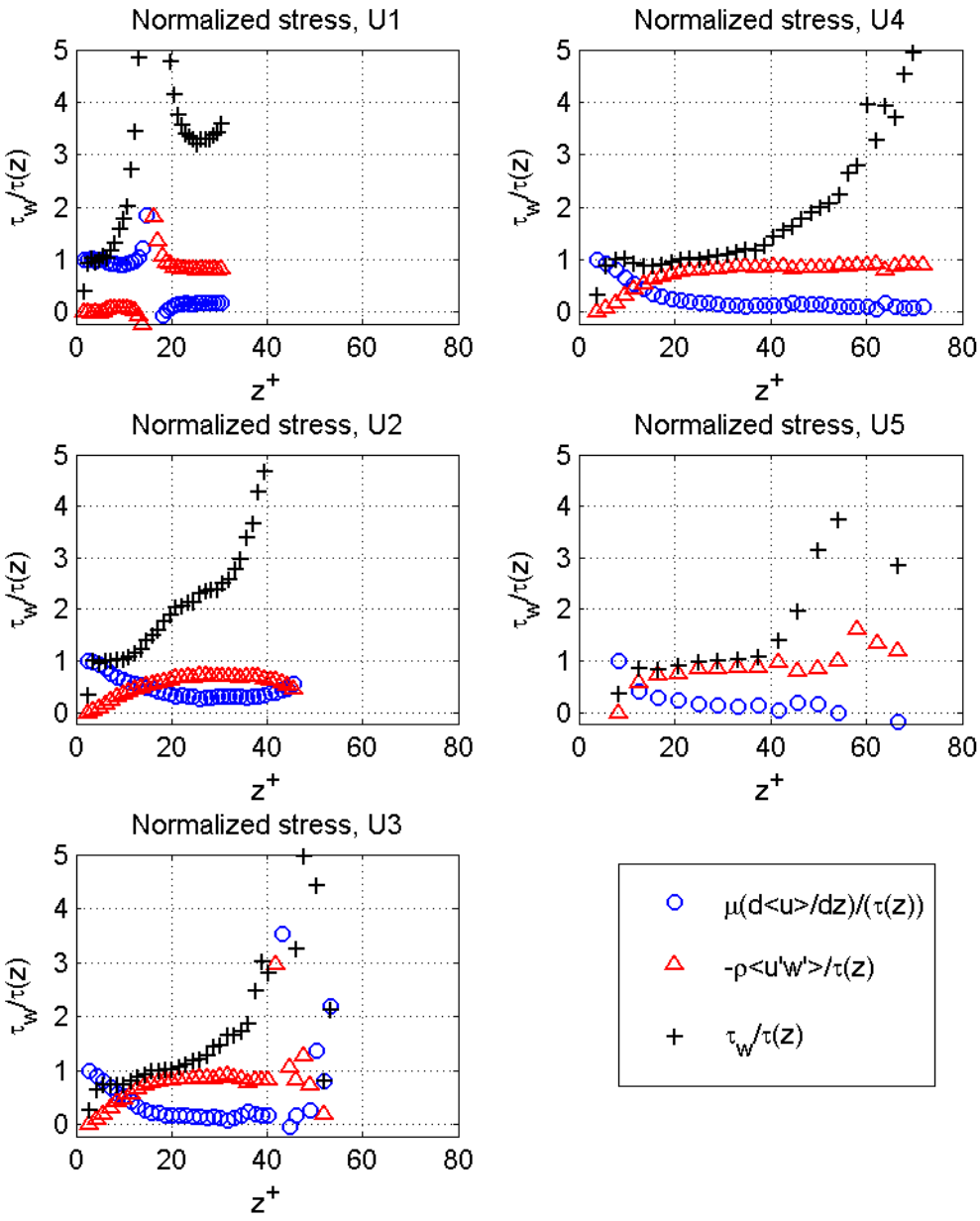


Figure 3.88: Non-dimensional stress $\tau/\tau(z)$, n=200.

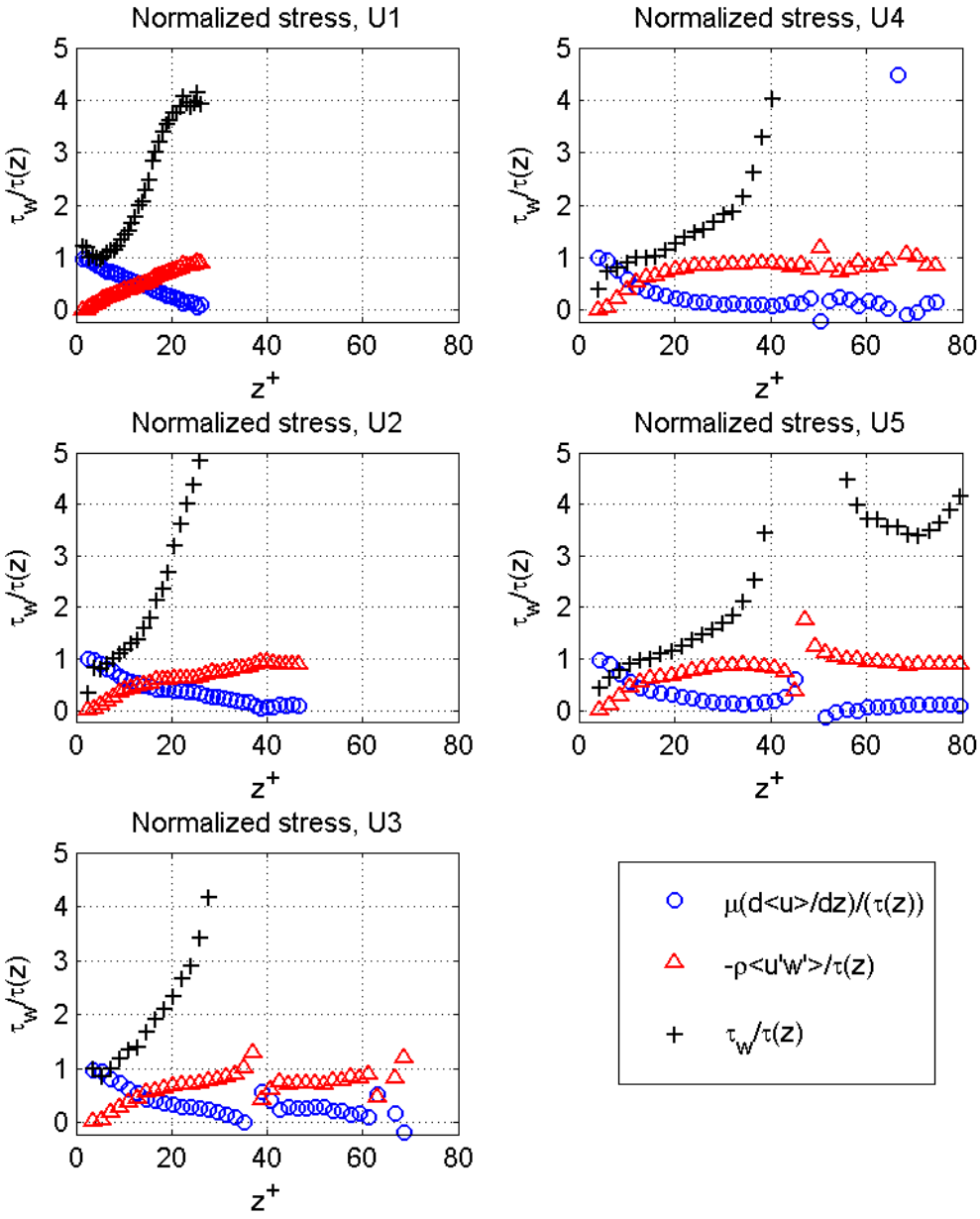


Figure 3.89: Non-dimensional stress $\tau/\tau(z)$, n=300.

The calculated ratios indicate a new component of drag that has not been considered. The results present some discontinuities, a product of the normalization, since in the regions of smaller stress, near-zero values are divided by near-zero quantities.

## 3.3 LIF Results

The effects of illumination and parallax must be evaluated from the calibration images. The mean intensity values from the calibration set is presented in Figure 3.90, where is clear the non-homogeneity of the intensity on the region of interest. For this purpose, the mean intensity for four known concentrations is plotted as a function of distance from the free surface, as well as the longitudinal position within the image, Figures 3.91 and 3.92.

The vertical dependence proves to be stronger than the horizontal, yielding a mean intensity approximately 20% smaller on the bottom than on the free surface. In the horizontal direction, the intensity manifests almost as constant, though it presents a slight decay at the right edge. This reinforces the importance of pixel by pixel calibration, since it is clear the differences in intensity with distance from the light source.

The results for both instantaneous and continuous releases are shown in Figures 3.93 and 3.94.

Time starts at $t_0 = 0$ when the dye release begins in order to capture how long it takes a) for the occurrence of the peak or b) reaching steady state, for the instantaneous and continuous releases respectively.

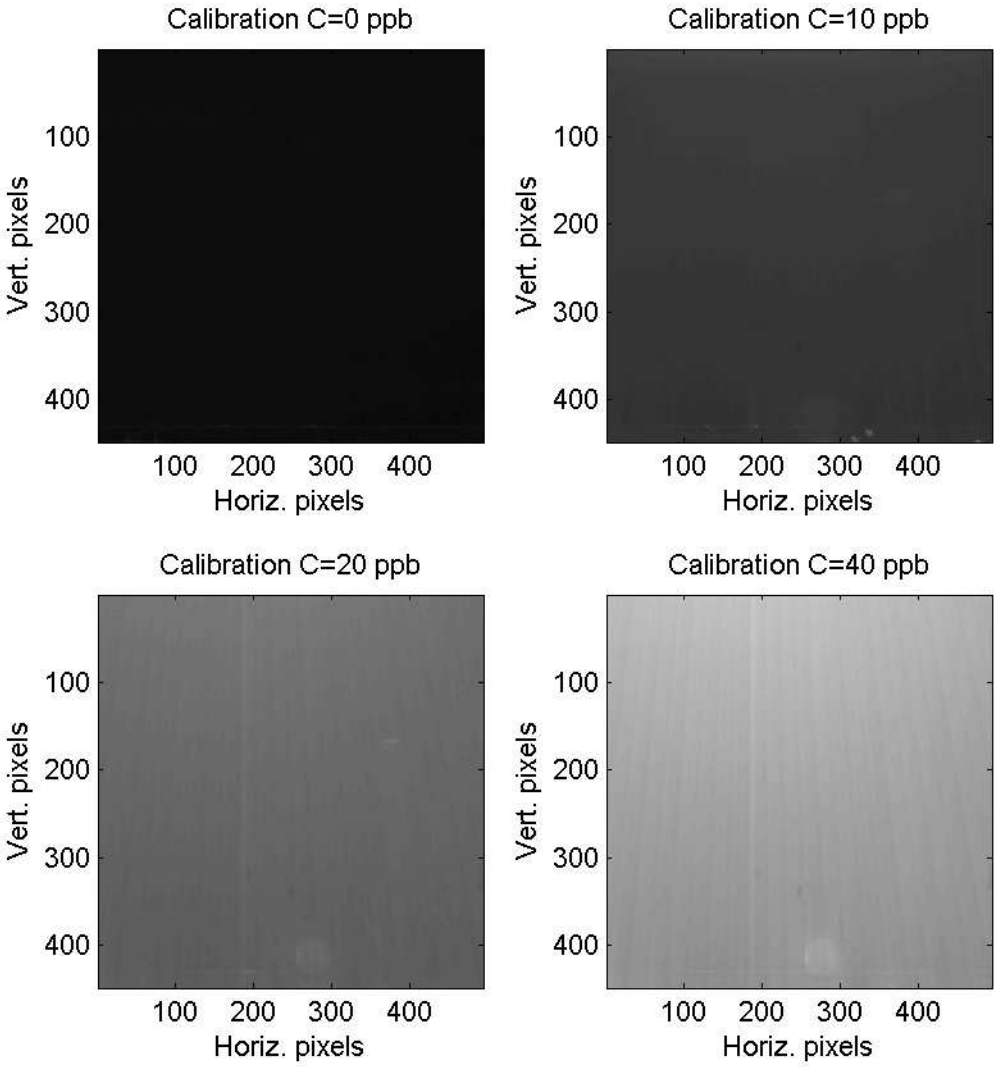


Figure 3.90: Calibration images for LIF.

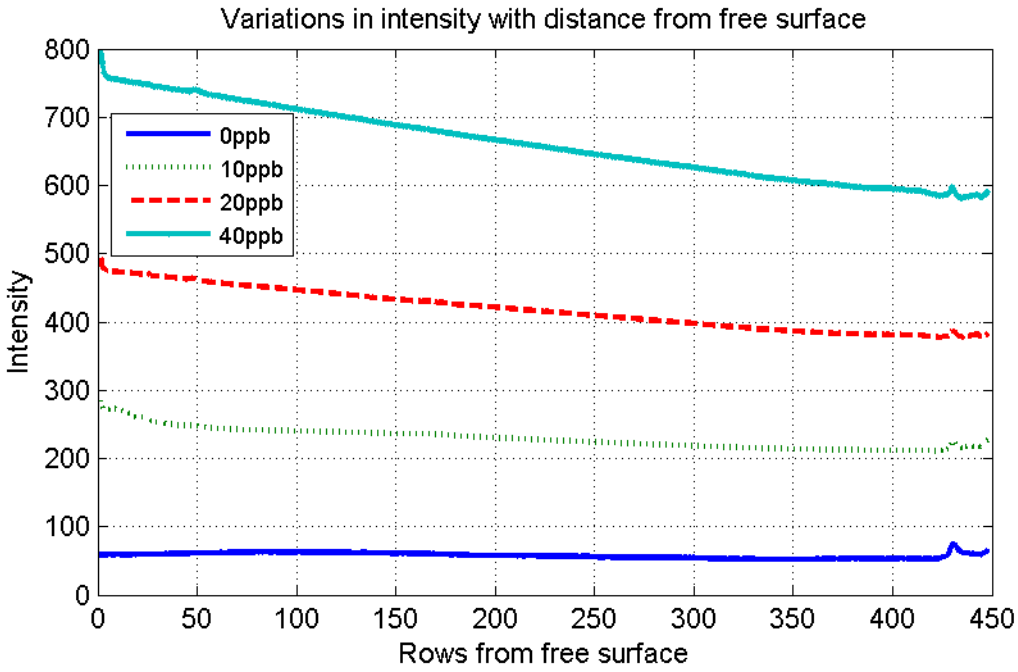


Figure 3.91: Intensity variations in vertical direction.

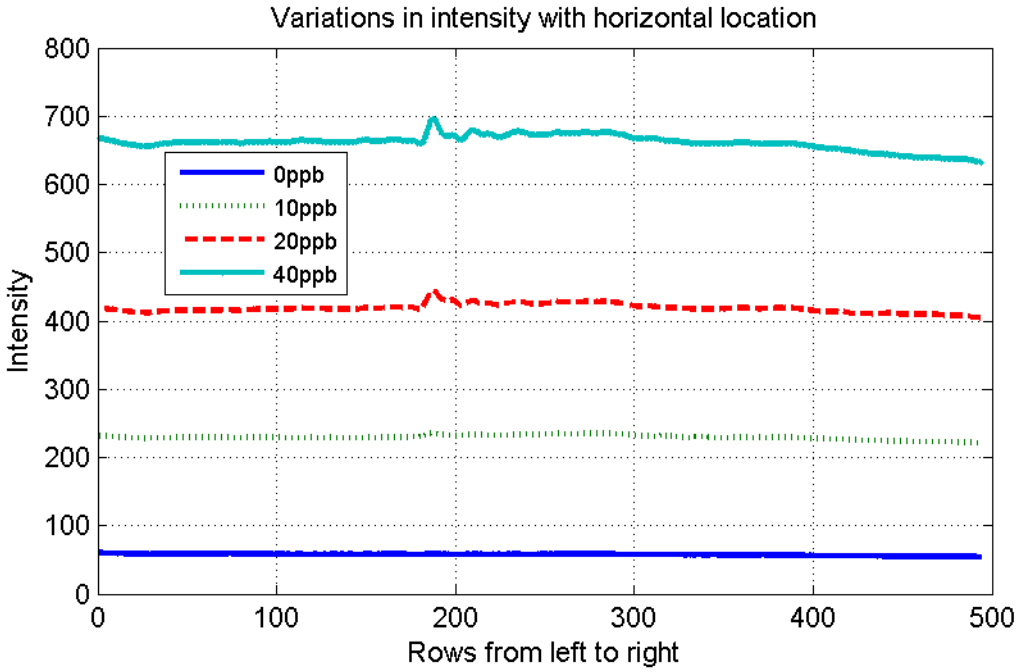


Figure 3.92: Intensity variations in horizontal direction.

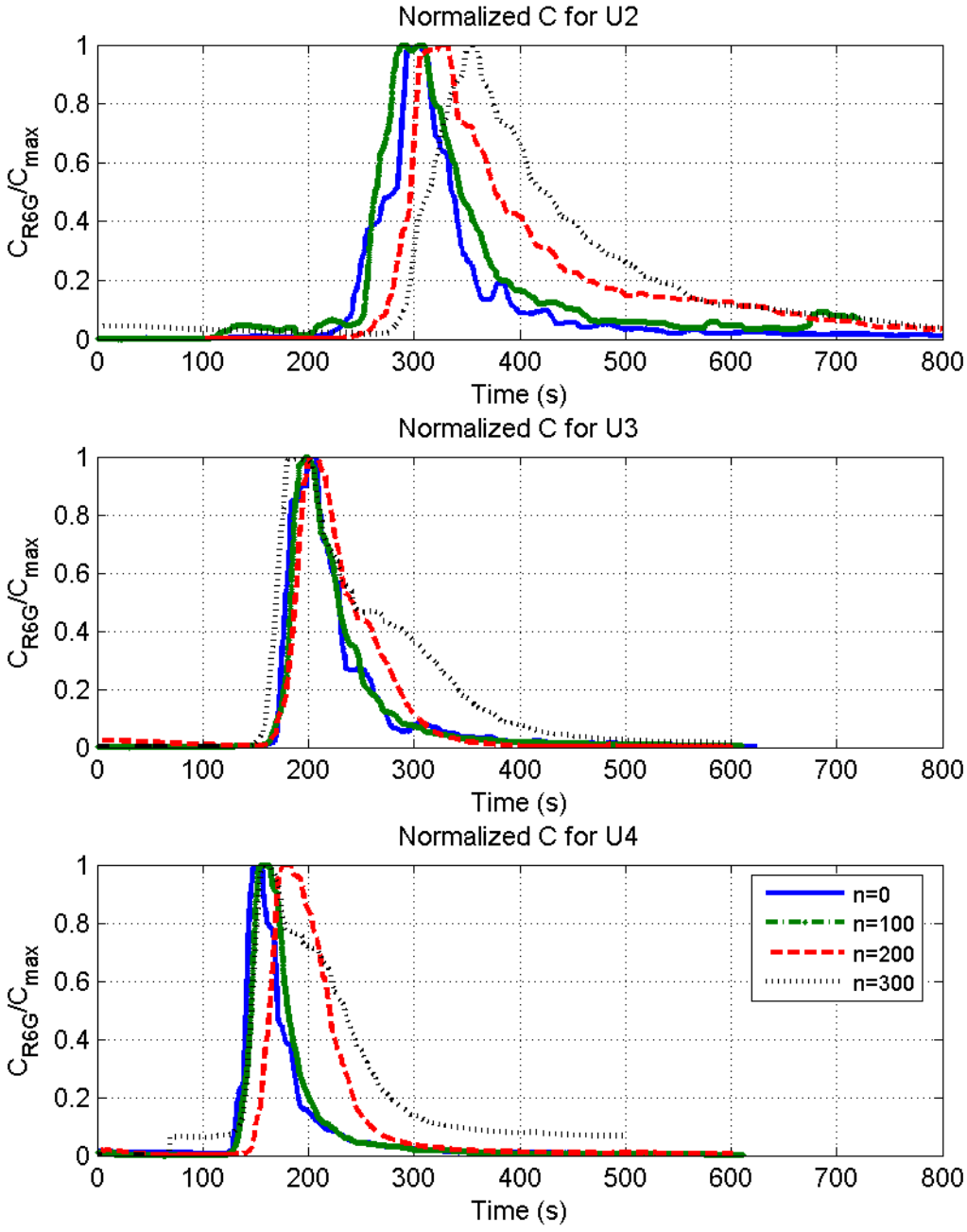


Figure 3.93: Concentration results from LIF. Instantaneous release.

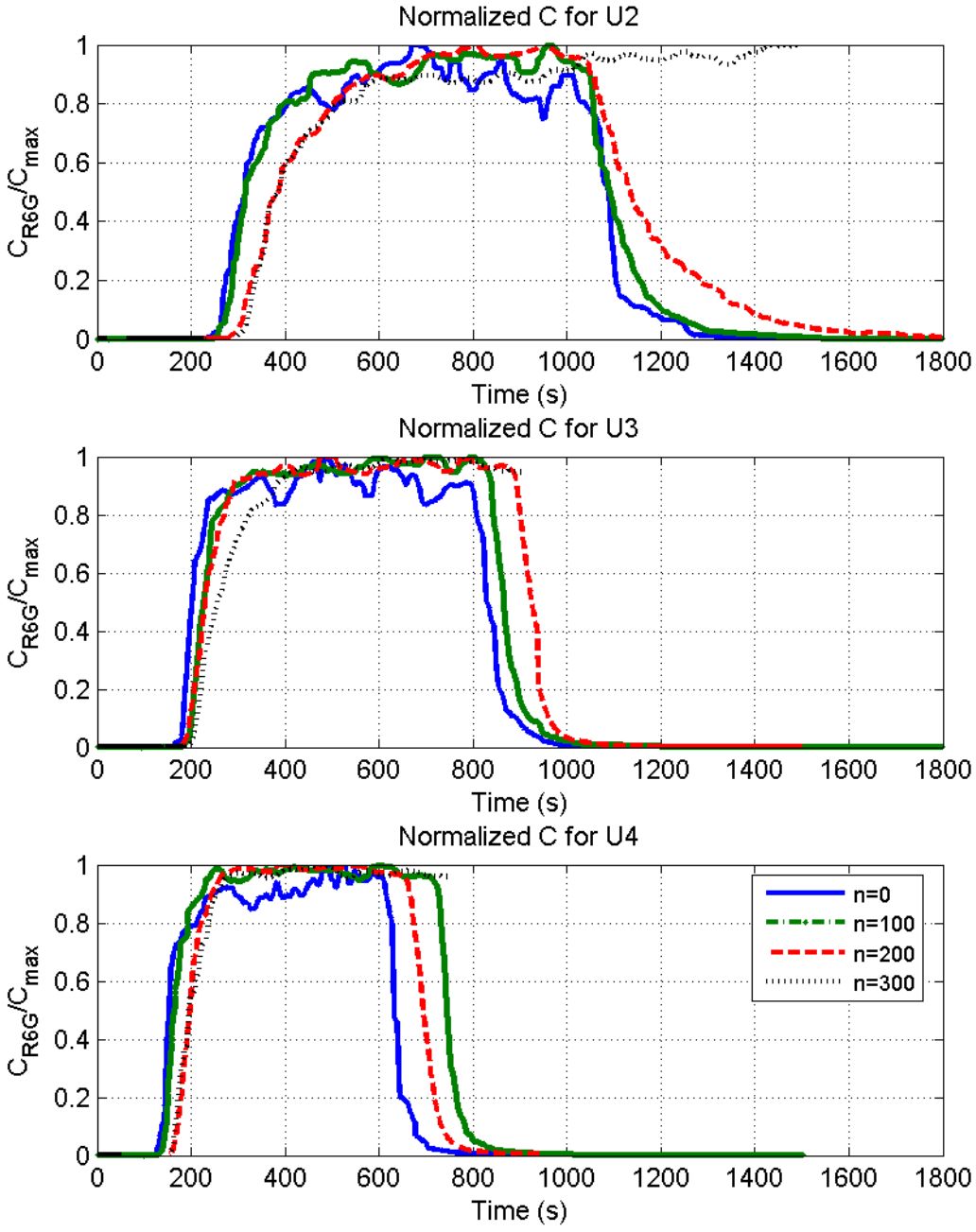


Figure 3.94: Concentration results from LIF. Continuous release.

With increased density, a longer time is needed for the front to appear. Higher densities imply longer times to reach a steady state, thus increasing the residence time in the patch, as can be noted by the lengthened tails in the concentration curve. However, this behavior is not clearly observed in all of these these results, due probably to the velocity distributions commented on in the previous section, a near-bottom region of small density and high velocity able to transport the scalar faster than expected, which suggests the use of different approaches to analyze the dispersion and diffusion in vegetated flows. With these factors in mind, the task to conduct a new series of experiments remains in order to capture more accurately the transport of passive scalars on flows with vertical dependence of vegetation density.

## 3.4 Analysis and discussion

### 3.4.1 Analysis of scales of turbulent motion

It is important to investigate the dominant scales in the flow under study. As mentioned briefly in section 3.2.1.1, the selection of the appropriate length and velocity scales is indispensable to characterize both mean and turbulent structure.

Working with turbulent flows it is common to use the friction velocity, $u_*$, the turbulence intensity, $u_{rms}$, or a characteristic eddy speed, $\sqrt{k}$, where $k$ is the turbulent kinetic energy (TKE), defined as $k = \frac{1}{2}(u'^2 + v'^2 + w'^2)$, as the velocity scale. From PIV data, it is possible to calculate $k$ by assuming horizontal isotropy, i.e. $u' = v'$, in order to estimate a 3D calculation using the available 2D data.

Common length scales are the longitudinal integral length scale $L_{11}$, obtained by integration of the auto correlation function, the Taylor microscale, $\lambda$, and an eddy characteristic length in terms of the TKE and the dissipation $\epsilon$, $L = k^{3/2}/\epsilon$.

As a first approach, it is possible to analyze the turbulent fluctuations $u'$ and $w'$ in their non-dimensional form using the now known $u^*$. A comparison for each density between the results from the small and large FOVs are presented in Figures 3.95 to 3.102.

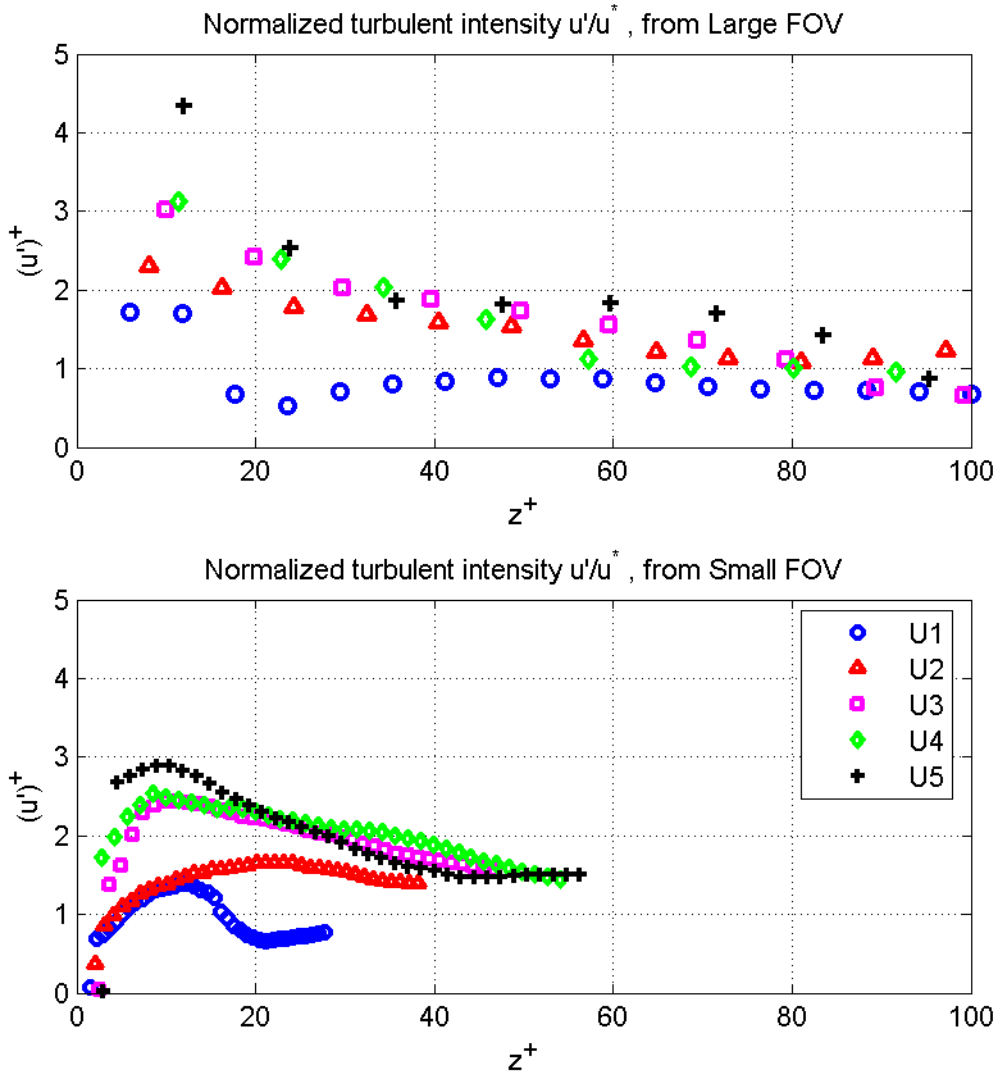


Figure 3.95: Non-dimensional turbulent fluctuation $u'^+$, n=0.

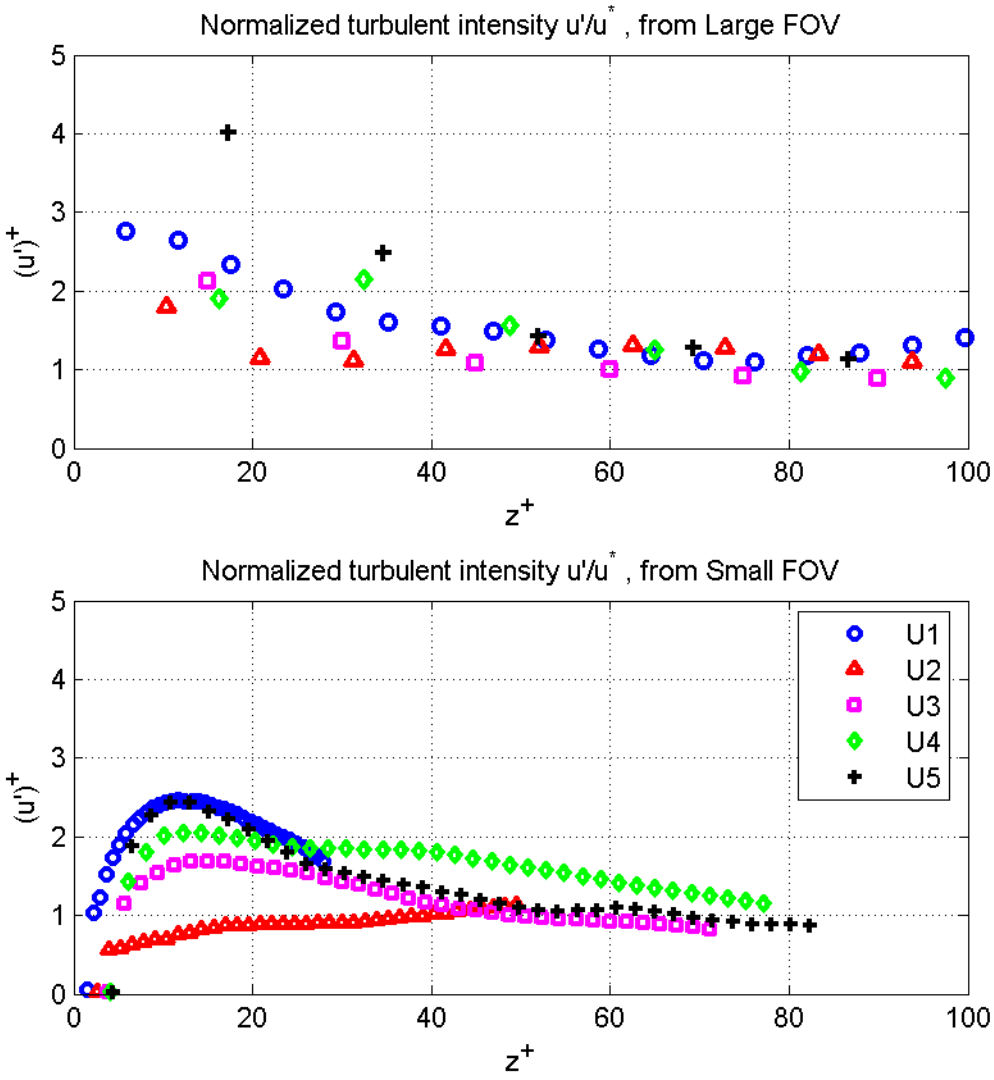


Figure 3.96: Non-dimensional turbulent fluctuation $u'^{+}$, n=100.

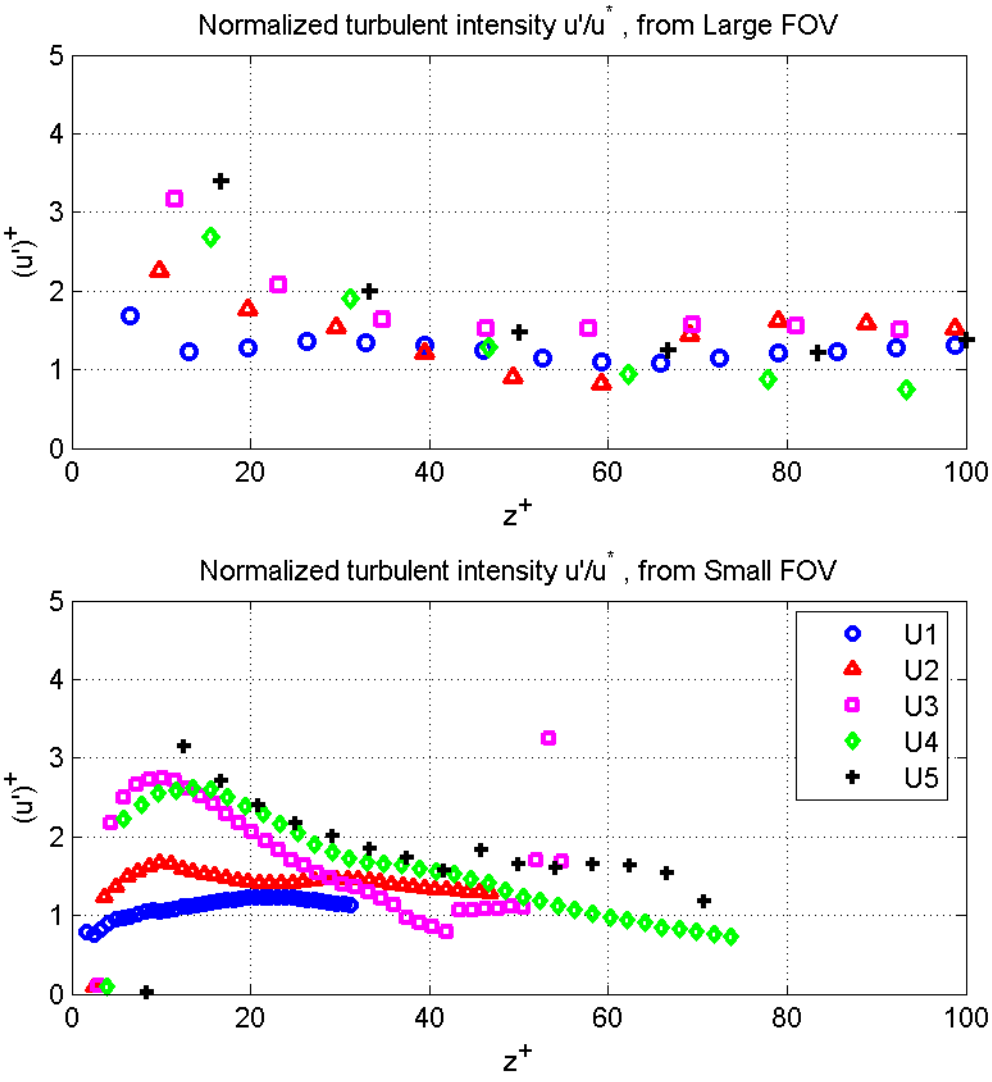


Figure 3.97: Non-dimensional turbulent fluctuation $u'^{+}$, n=200.

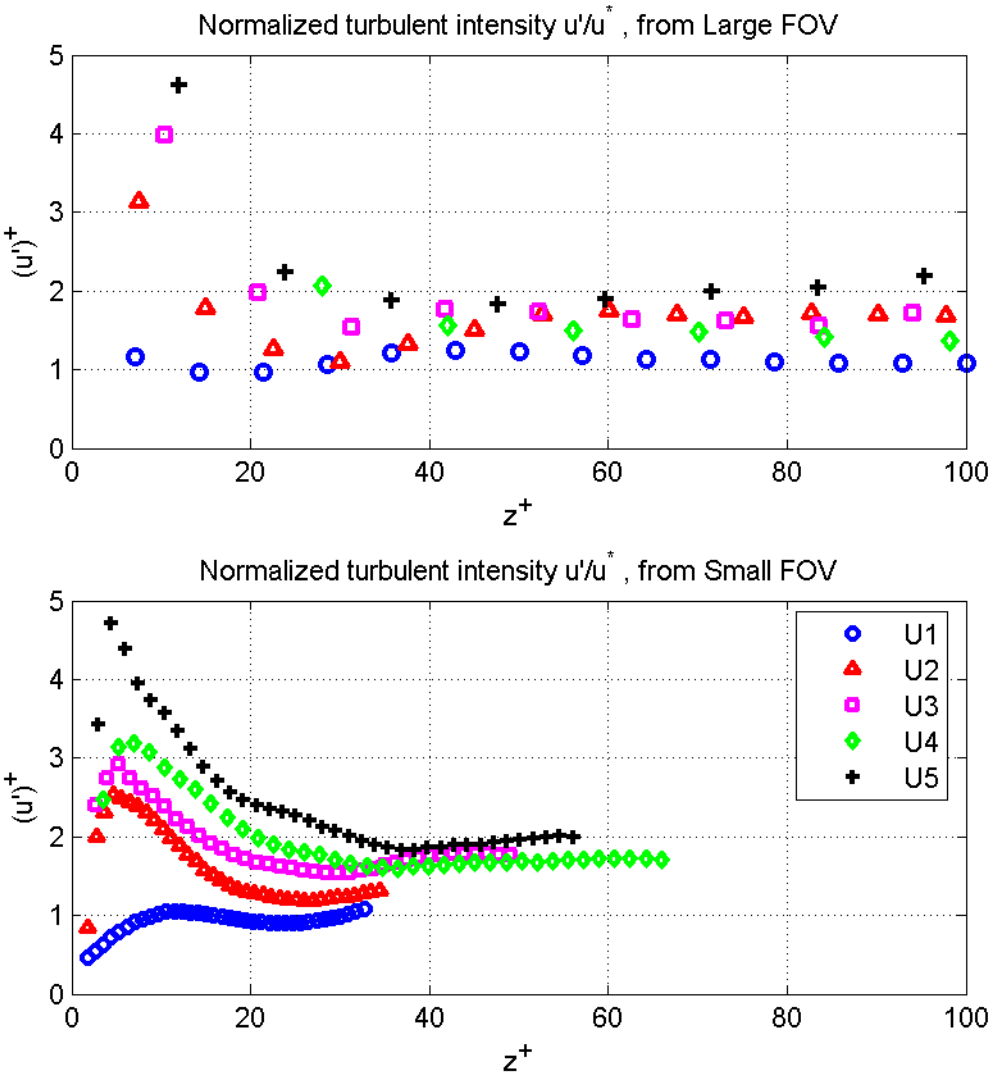


Figure 3.98: Non-dimensional turbulent fluctuation $u'^{+}$, n=300.

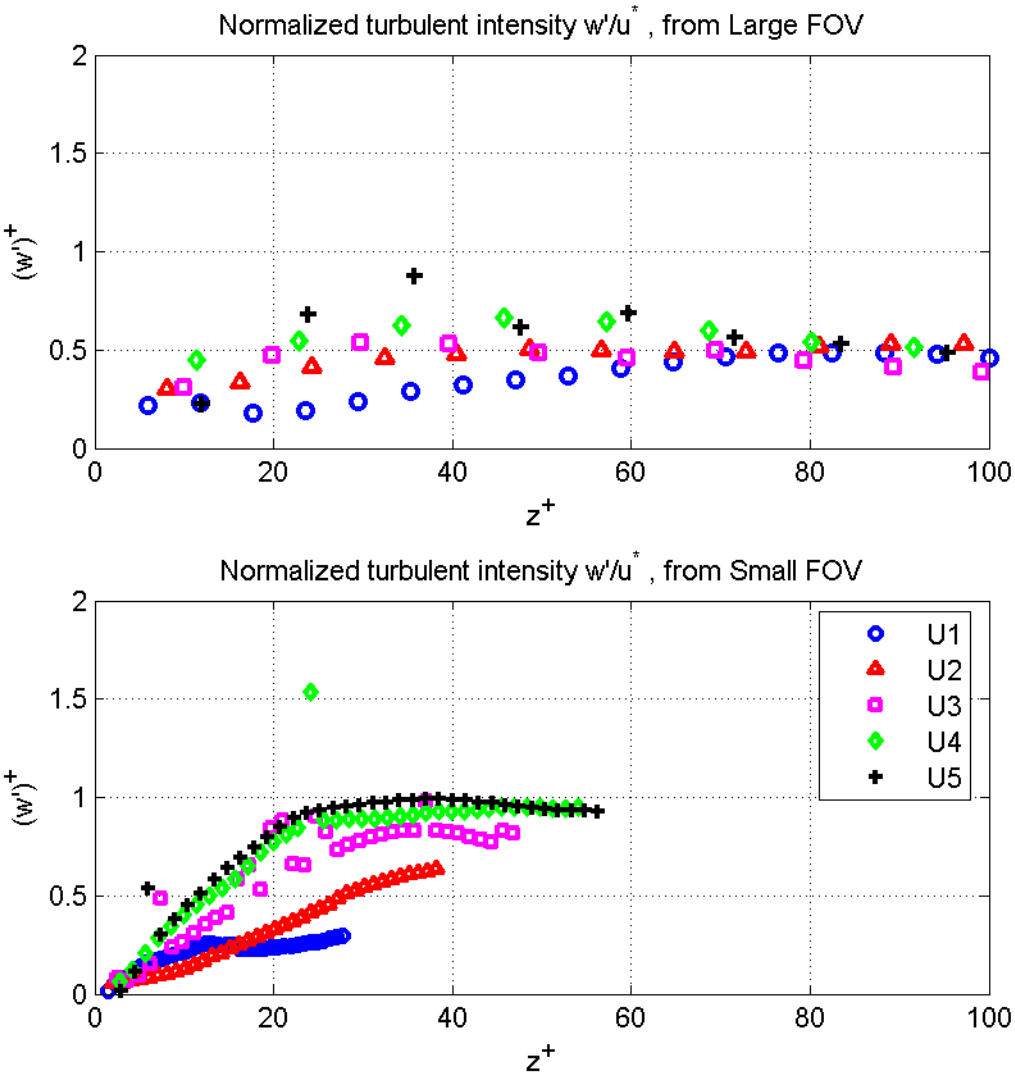


Figure 3.99: Non-dimensional turbulent fluctuation $w'^{+}$, n=0.

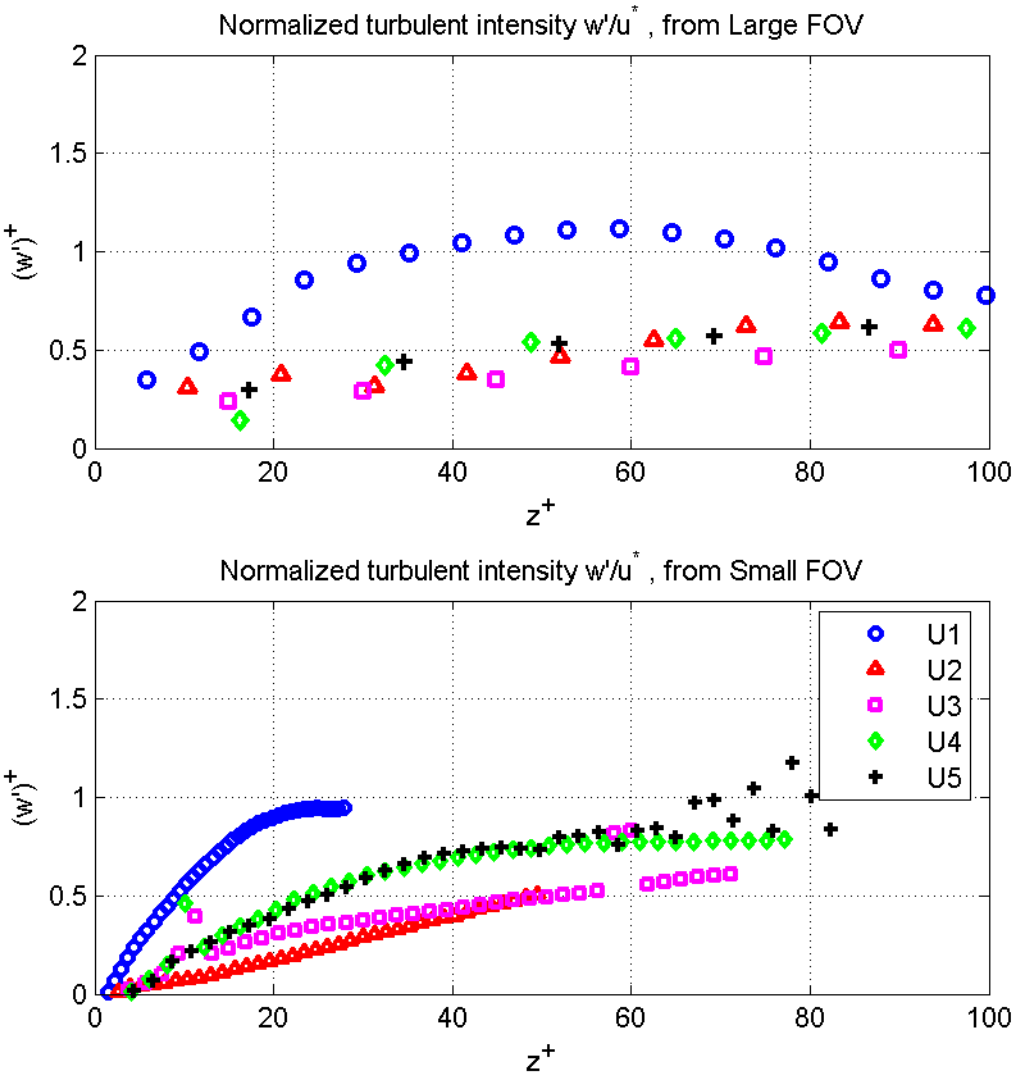


Figure 3.100: Non-dimensional turbulent fluctuation $w'^{+}$, n=100.

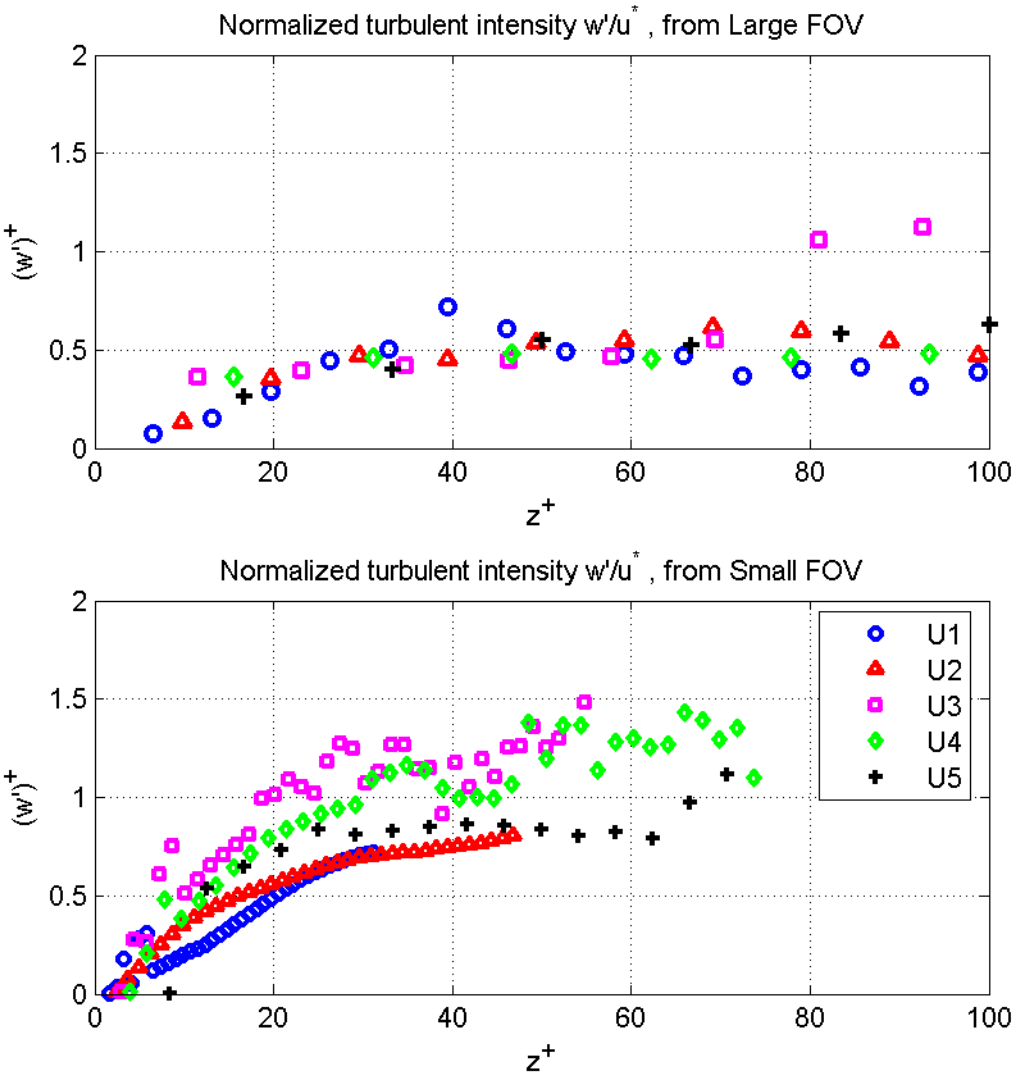


Figure 3.101: Non-dimensional turbulent fluctuation $w'^{+}$, n=200.

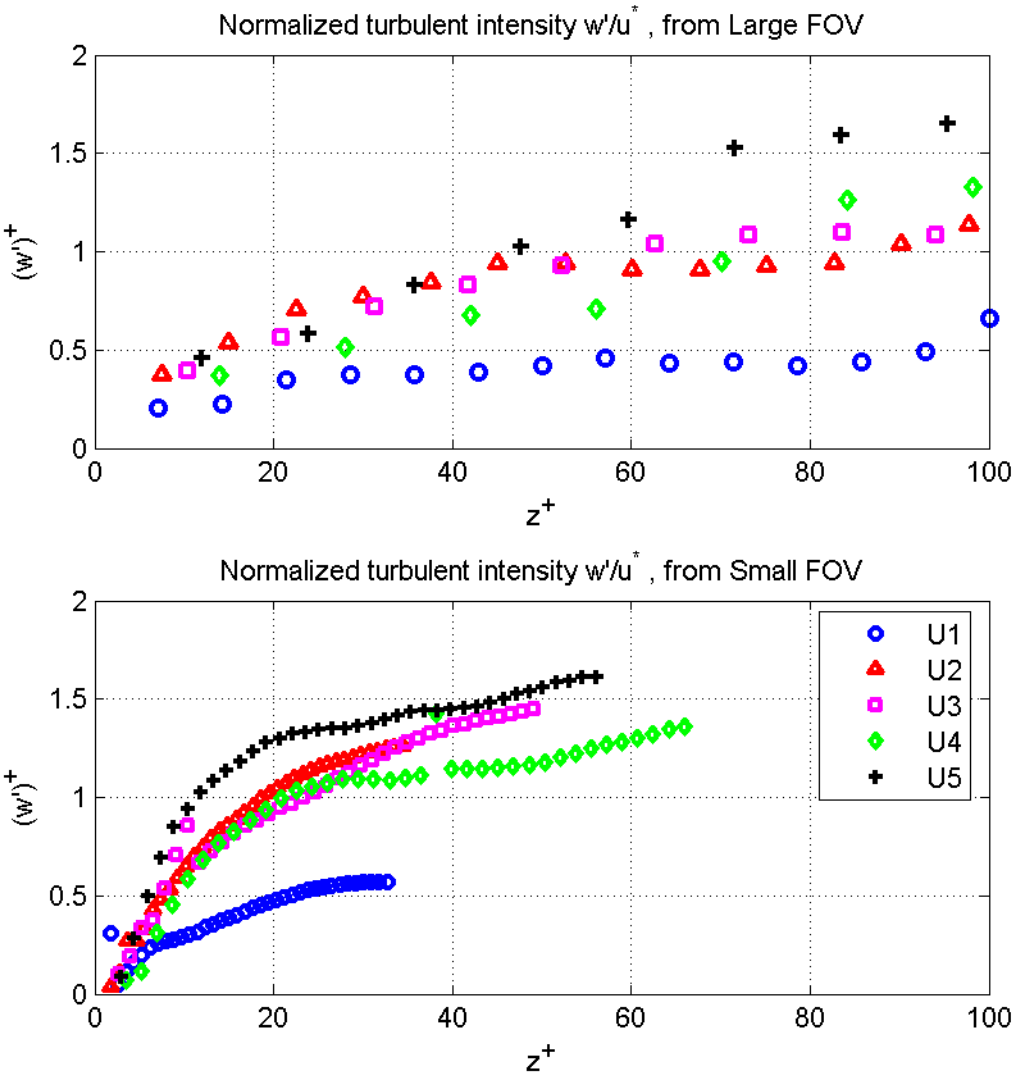


Figure 3.102: Non-dimensional turbulent fluctuation $w'^{+}$, n=300.

Even when the data presents similar trends, the results don't collapse into a single curve, which indicates a $Re$ dependence on each set, and that the friction velocity $u_*$, might not be the most characteristic velocity in this process, so that another normalization has yet to be found.

From the available data, the calculation of the TKE, $k = \frac{1}{2}(2u'^2 + w'^2)$, yields the results shown in their non dimensional form in Figures 3.103 to 3.106.

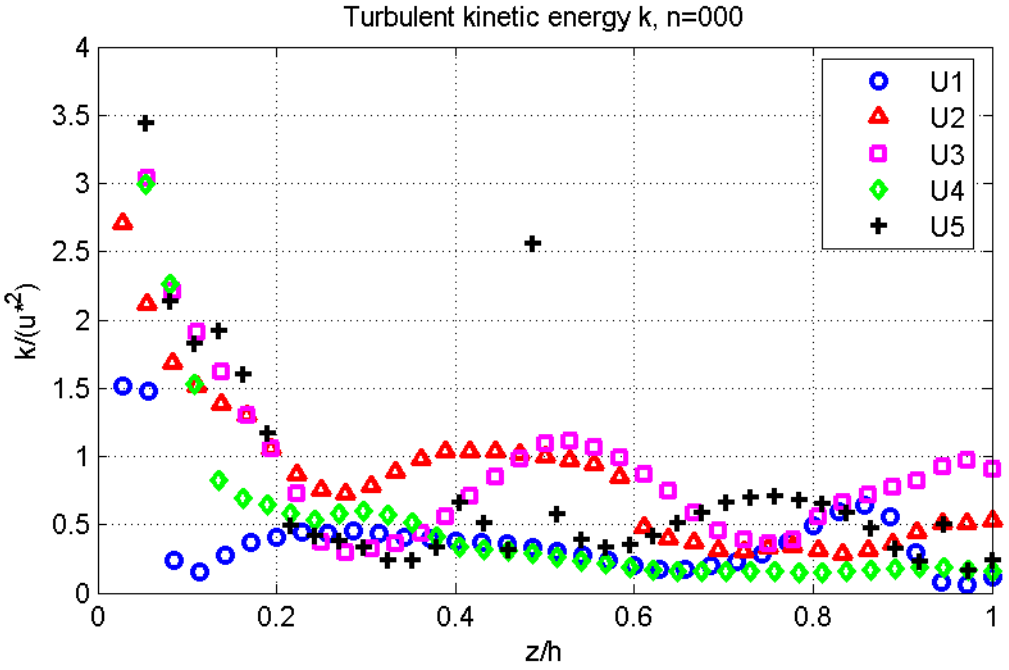


Figure 3.103: Non-dimensional TKE, n=0.

There is a noticeable increase in TKE as the plant density increases. For non-vegetated flow, the maximum occurs at the wall as expected, and it moves toward the most populated regions as we introduce vegetation within the flow.

Since the kinetic energy is already known, the Reynold stresses can be normalized using $\sqrt{k}$ as a characteristic velocity, which is presented in Figures 3.107 to 3.110.

It is noticed the expected similar behavior for $\langle\overline{u'^2}\rangle$ and $\langle\overline{w'^2}\rangle$, but it is the $\langle\overline{u'w'}\rangle$ component which provides more information, collapsing to a good agreement for all

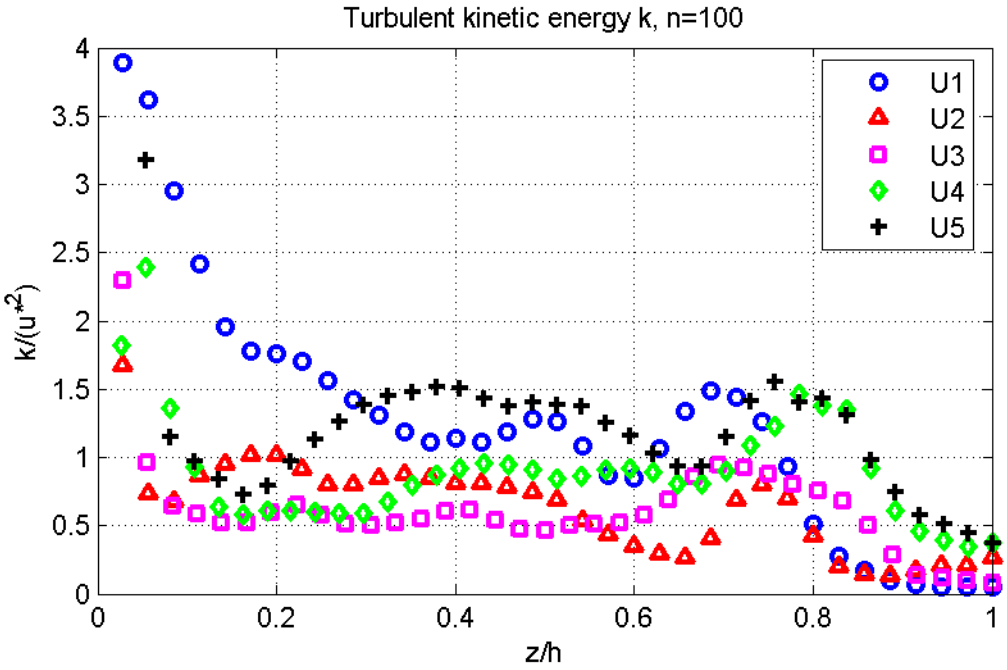


Figure 3.104: Non-dimensional TKE, n=100.

velocities considered, showing the passing from a bed stress dominated flow with no vegetation to a vegetated drag dominated flow as the plant density increases. Another noticeable finding is the collapse of the curves in a single slope when reaching the region of faster increase in vegetation, indicating a higher production due to the plant wakes.

In order to analyze the kinetic energy budget, is necessary to evaluate the production, $P$, and the dissipation, $\epsilon$. According to the 1D characteristics of this flow, the production can be calculated as $P = -\langle\overline{u'w'}\rangle\frac{\partial\langle\overline{u}\rangle}{\partial z}$, which is presented in its non-dimensional form in Figures 3.111 to 3.114.

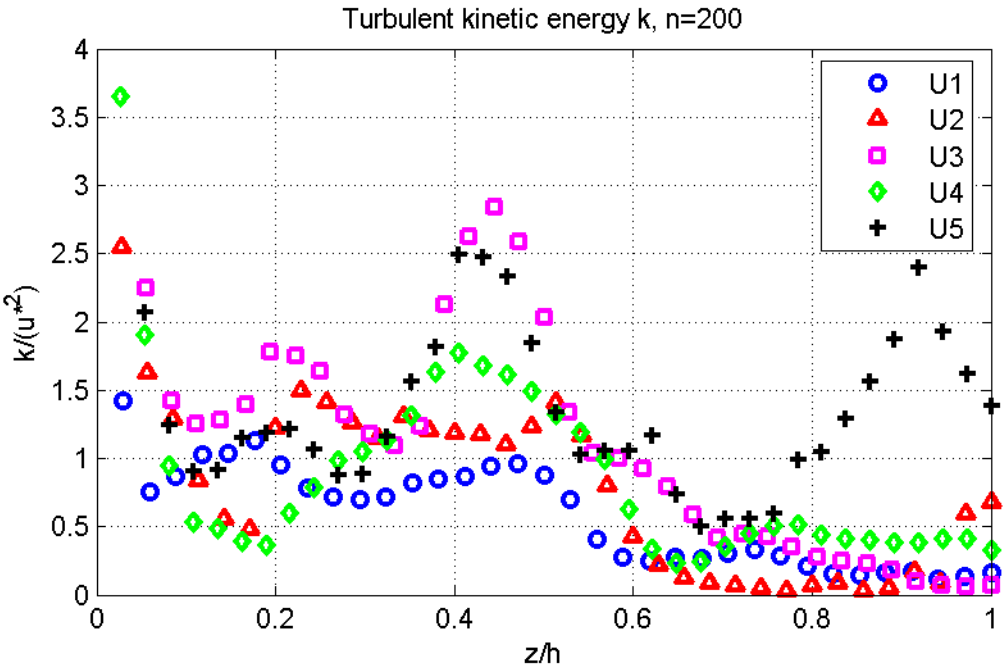


Figure 3.105: Non-dimensional TKE, n=200.

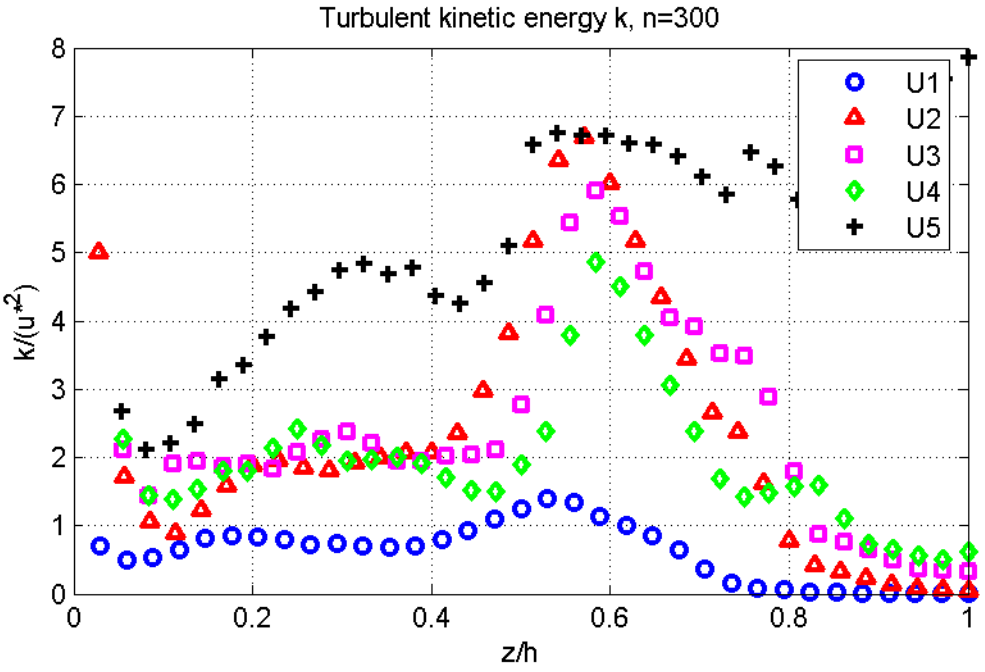


Figure 3.106: Non-dimensional TKE, n=300.

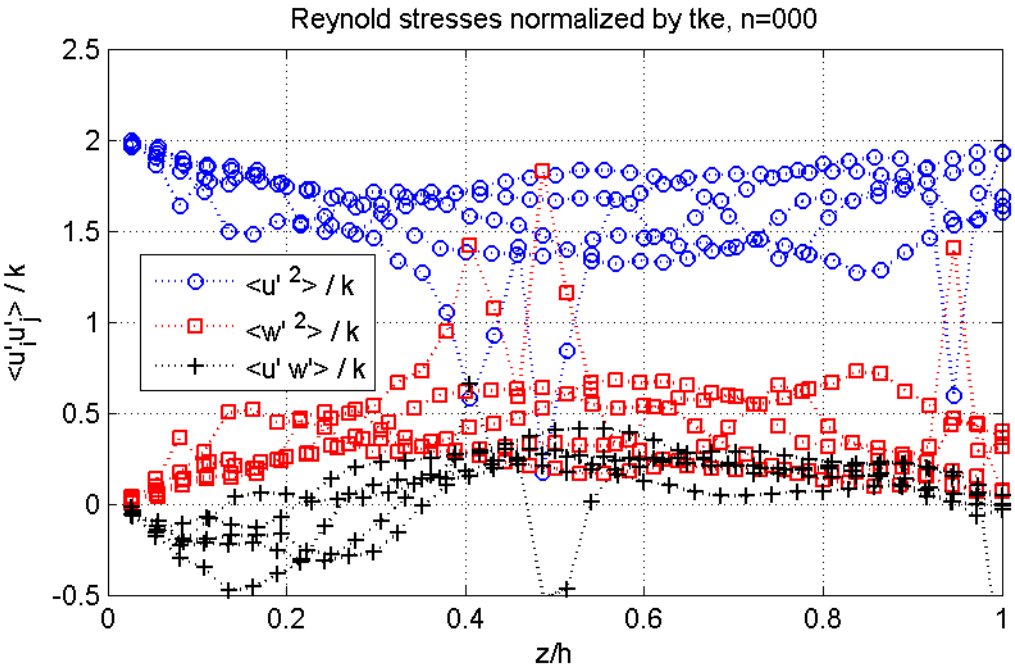


Figure 3.107: Non-dimensional Reynolds stresses, $\frac{\overline{\langle u_i' u_j' \rangle}}{k}$, n=0.

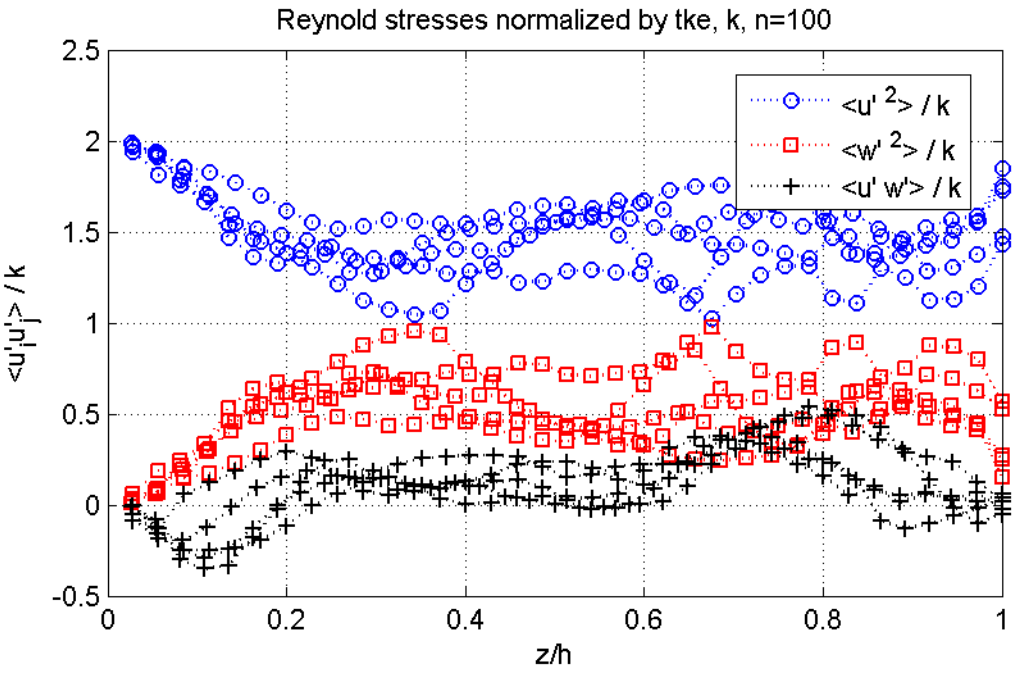


Figure 3.108: Non-dimensional Reynolds stresses, $\frac{\overline{\langle u_i' u_j' \rangle}}{k}$, n=100.

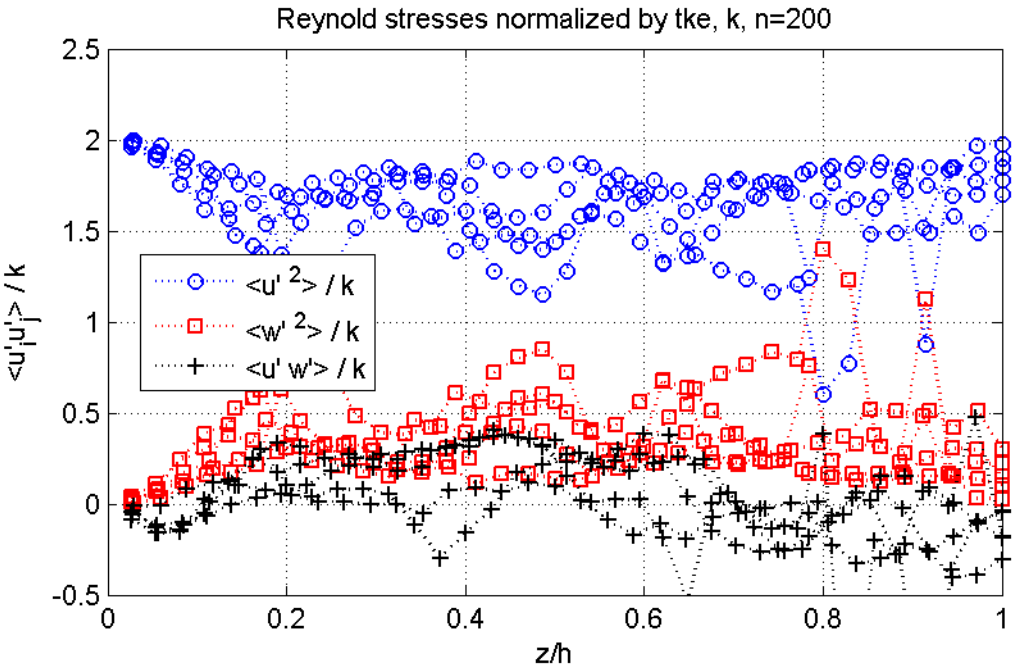


Figure 3.109: Non-dimensional Reynolds stresses, $\frac{\overline{\langle u_i' u_j' \rangle}}{k}$, n=200.

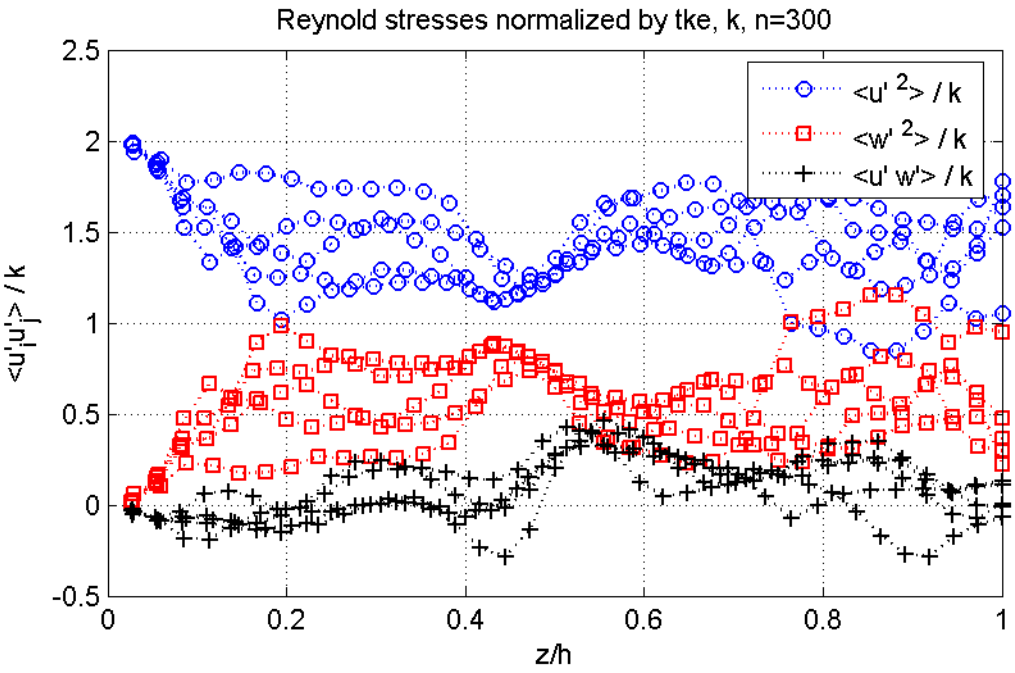


Figure 3.110: Non-dimensional Reynolds stresses, $\frac{\overline{\langle u_i' u_j' \rangle}}{k}$, n=300.

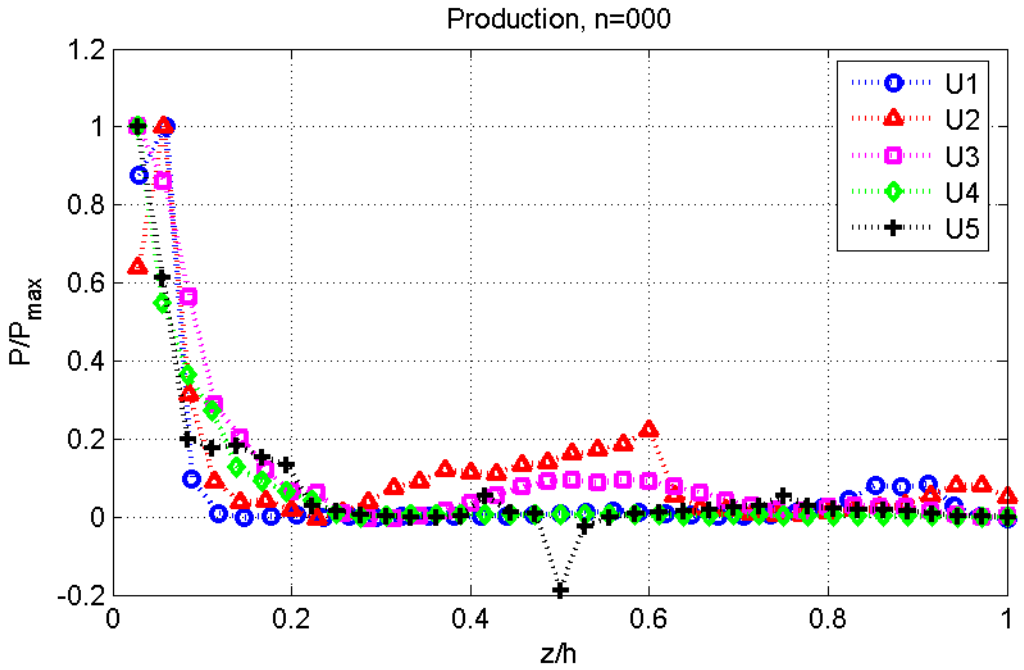


Figure 3.111: Non-dimensional production $P$, n=0.

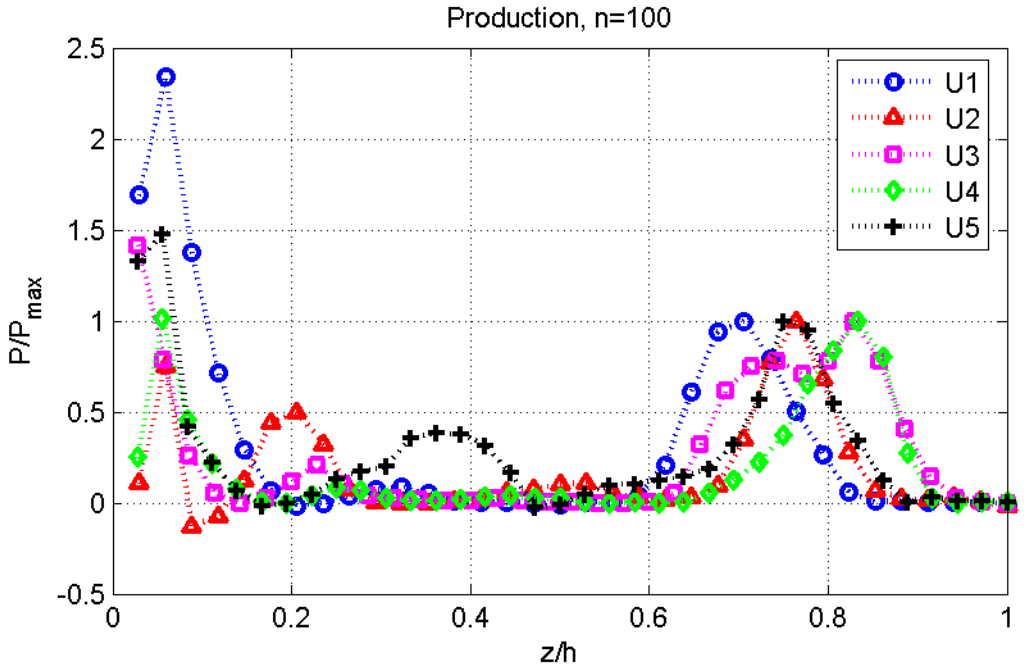


Figure 3.112: Non-dimensional production $P$, n=100.

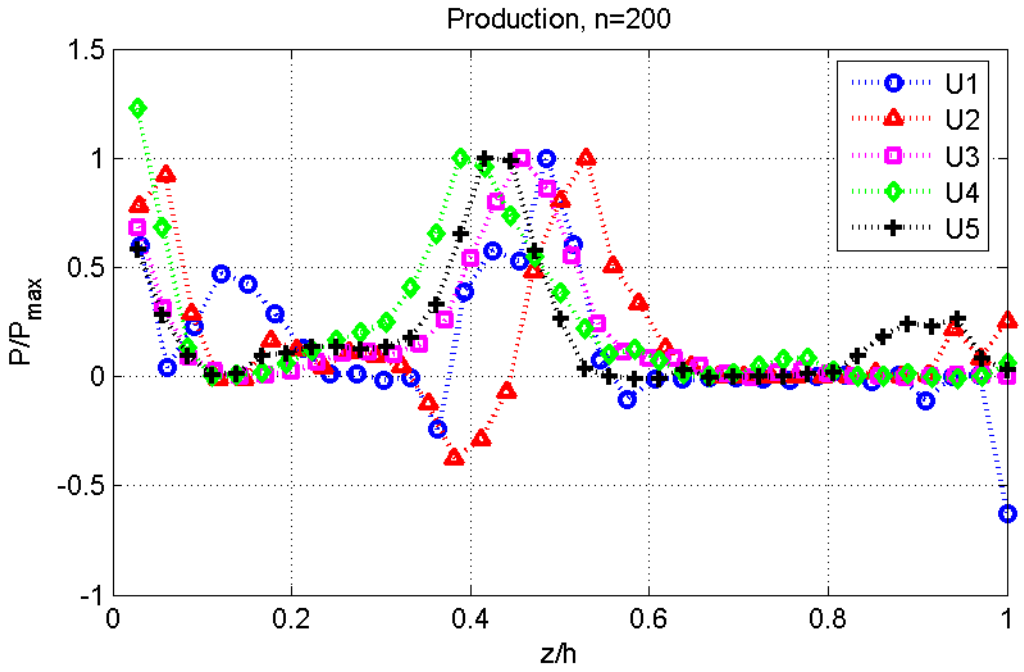


Figure 3.113: Non-dimensional production $P$, n=200.

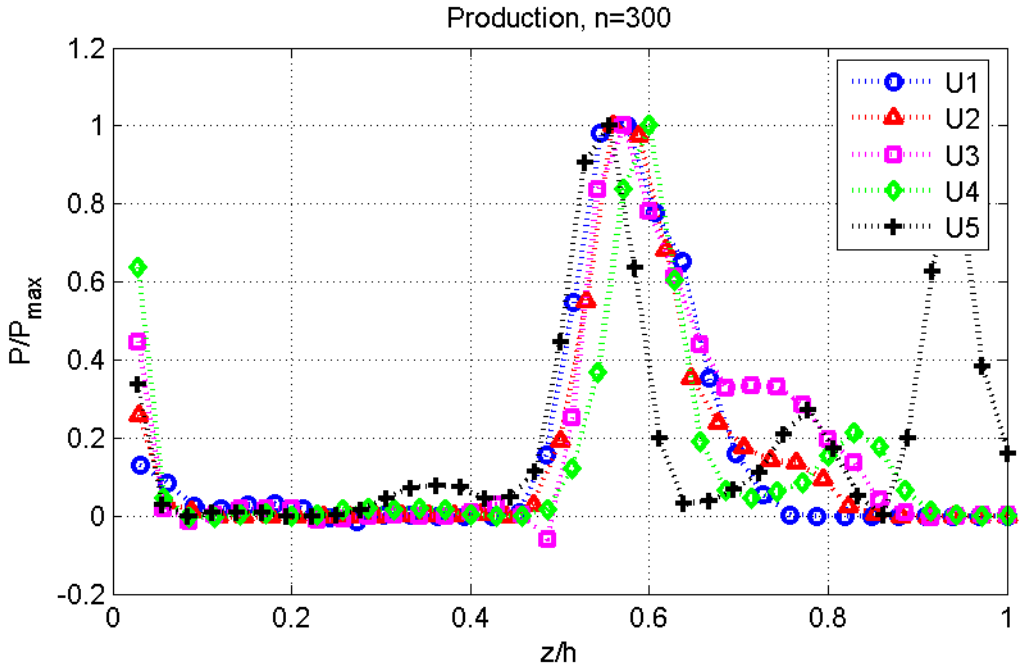


Figure 3.114: Non-dimensional production $P$, n=300.

The results for the production term show in a more evident way the dominance of the vegetation over the flow structure. A near-bed peak in production is observed from bed shear production, but as the plant population increases, the stem wake production falls close to 80% of that from the wall for n=100; becomes of the same magnitude at n=200, and clearly dominates at the maximum density of n=300, being almost twice the value at the wall.

To calculate the dissipation rate from the PIV data is not as straight forward as with previous turbulence metrics. There are some methods to obtain direct or indirect estimates depending on the information available. For this work, estimates of the dissipation were made based on scaling arguments and using the second order structure function.

From the definition of the eddie's length scale, $L = k^{3/2}/\epsilon$, for Reynolds numbers high enough, the dissipation can be calculated as $\epsilon = k^{3/2}/L$, and as a result from the energy cascade, it scales as $U_0^3/l_0$, where $U_0$ and $l_0$ are the characteristic velocity and length scales of the energy containing eddies. Using the scales available, if $U_0 = \sqrt{k}$ and $l_0 = L_{11}$, the dissipation can then be calculated as (Pope 2000):

$$\epsilon = \frac{k^{3/2}}{L} = \frac{k^{3/2}}{L_{11}} \left( \frac{L_{11}}{L} \right) \tag{3.12}$$

With this relationship, it would be easy to calculate the dissipation following the procedure explained by Pope (2000), using the fact that at high Reynolds numbers the ratio $L_{11}/L$ tends asymptotically to 0.43. However, the low-Reynolds number nature of the flows studied in this work don't allow us to use this relationship directly to find the actual values for dissipation, but it still can be used to get a quantitative idea of the order of magnitude expected for the dissipation rate.

At this point it is useful to define the turbulent Reynolds numbers used in the literature, since their values determine the approach we need to follow hereafter.

There are at least three main turbulent Reynolds numbers that can be evaluated from the PIV data:

$$\begin{aligned} Re_T &= \frac{u_{rms} L_{11}}{\nu} \\ Re_L &= \frac{k^{1/2} L}{\nu} \\ R_\lambda &= \frac{u_{rms} \lambda}{\nu} \end{aligned}$$

To calculate $Re_T$, it is necessary to find the longitudinal integral length scale, $L_{11}$. This is achieved by integrating the auto correlation function, i.e. $L_{11}(t) = \int_0^\infty f(r,t)dr$. The results for all plant densities are shown in Figure 3.115. Once this scale is obtained, the calculation of $Re_T$ yields the results shown in Figure 3.116.

As observed in Figure 3.115, between the minimum and maximum velocity for all vegetation densities, $L_{11}$ varies between 1 and 3cm, decreasing further for the most densely populated case where it drops as low as 0.3cm. Looking at the $Re_T$ values, these increase with larger $n$, but still remain at very low values of $Re_T = 0 - 130$.

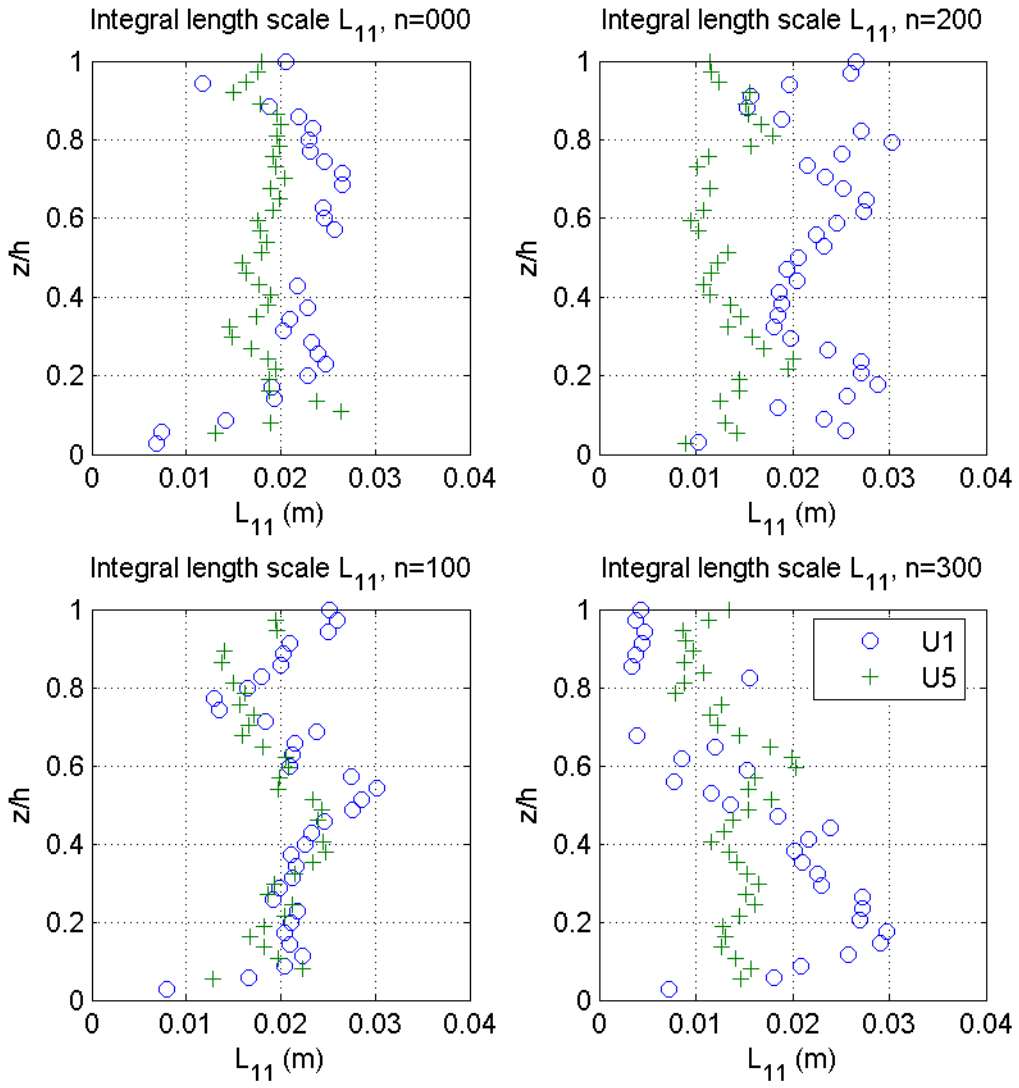


Figure 3.115: Longitudinal integral length scale $L_{11}$.

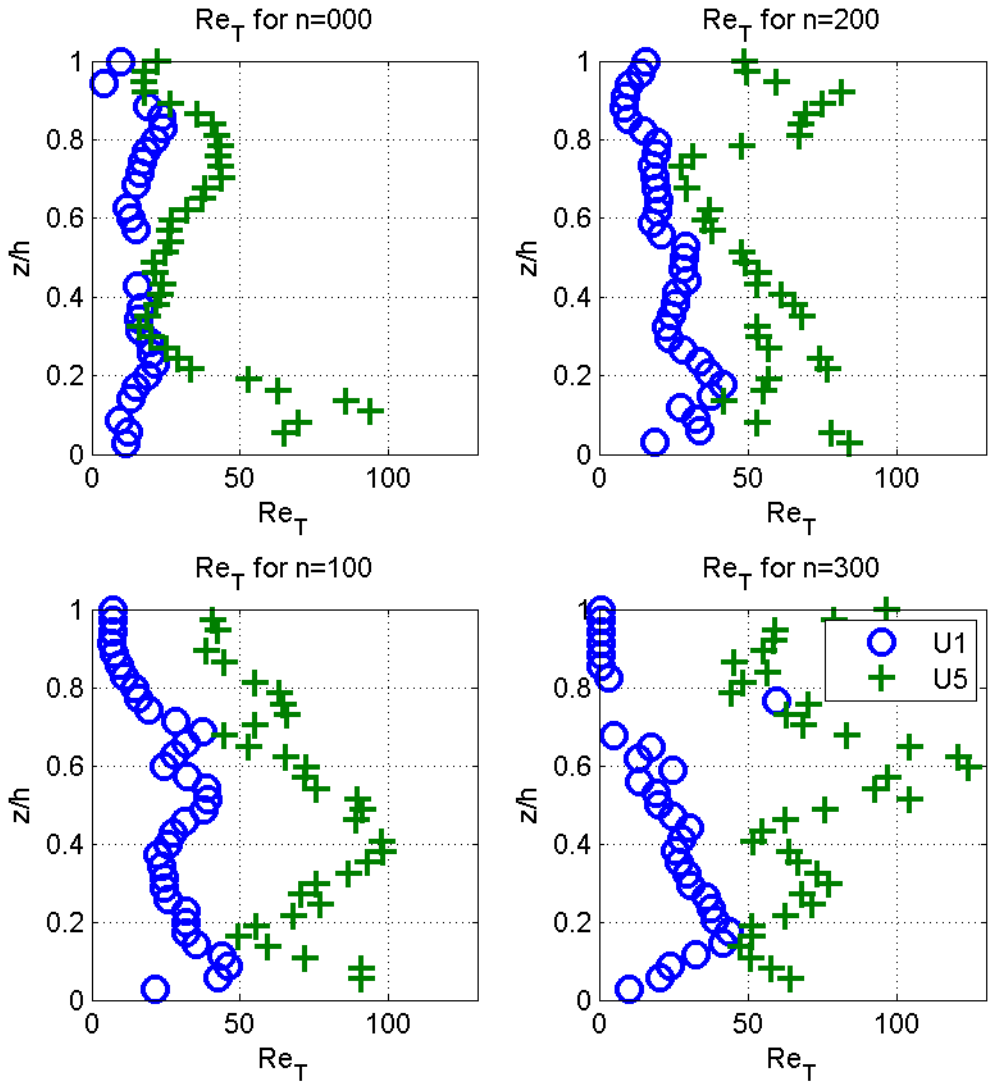


Figure 3.116: Turbulent Reynolds numbers $Re_T$.

Using the relationship between the different turbulent Reynolds numbers, as given by Pope (2000), makes it possible to find both $Re_L$ and $R_\lambda$ from the now evaluated $Re_T$.

$$Re_T = \frac{u_{rms} L_{11}}{\nu} = \sqrt{\frac{2}{3}} \frac{L_{11}}{L} Re_L \tag{3.13}$$

$$Re_L = \frac{k^{1/2} L}{\nu} = \frac{k^2}{\epsilon \nu} = \frac{3}{20} R_\lambda^2 \tag{3.14}$$

The relationships only hold for high Reynolds numbers, namely $Re_T > 100$, thus making it suspect to use them with our lower values. However, they allow us to find the Reynolds number range of our experiments, by using the highest calculated value $Re_T = 130$ to find the upper bound for $Re_L$ and $R_\lambda$. Using equations 3.13 and 3.14, as well as Figures 6.24 and 6.25 from Pope (2000), the values for $Re_L = 0 - 215$ and $R_\lambda = 0 - 38$ are calculated (Table 3.11).

Table 3.11: Turbulent Reynolds numbers.

| Reynolds number | Range |
|---|---|
| $Re_T$ | 0-130 |
| $Re_L$ | 0-215 |
| $R_\lambda$ | 0-38 |

Such low Reynolds numbers preclude the use of equation 3.12 to find an accurate dissipation rate. However, it can still be used for an order of magnitude estimation. The results for the minimum and maximum flow speed ($U1$ and $U5$) are shown in Figures 3.117 and 3.118.

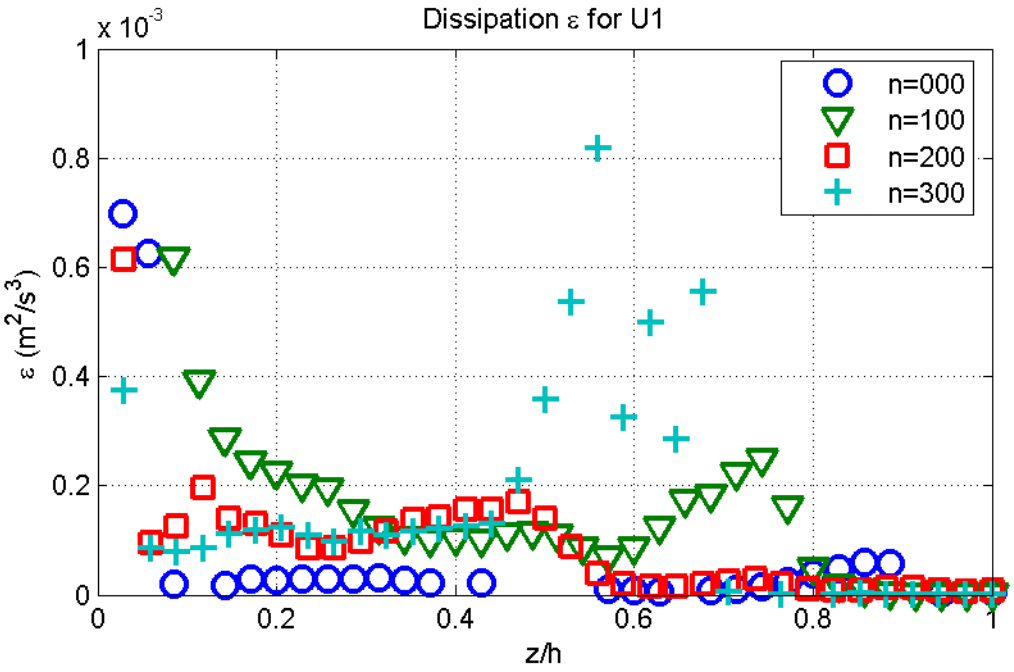


Figure 3.117: Dissipation estimates, $\epsilon = \frac{k^{3/2}}{L_{11}}$ for $U1$.

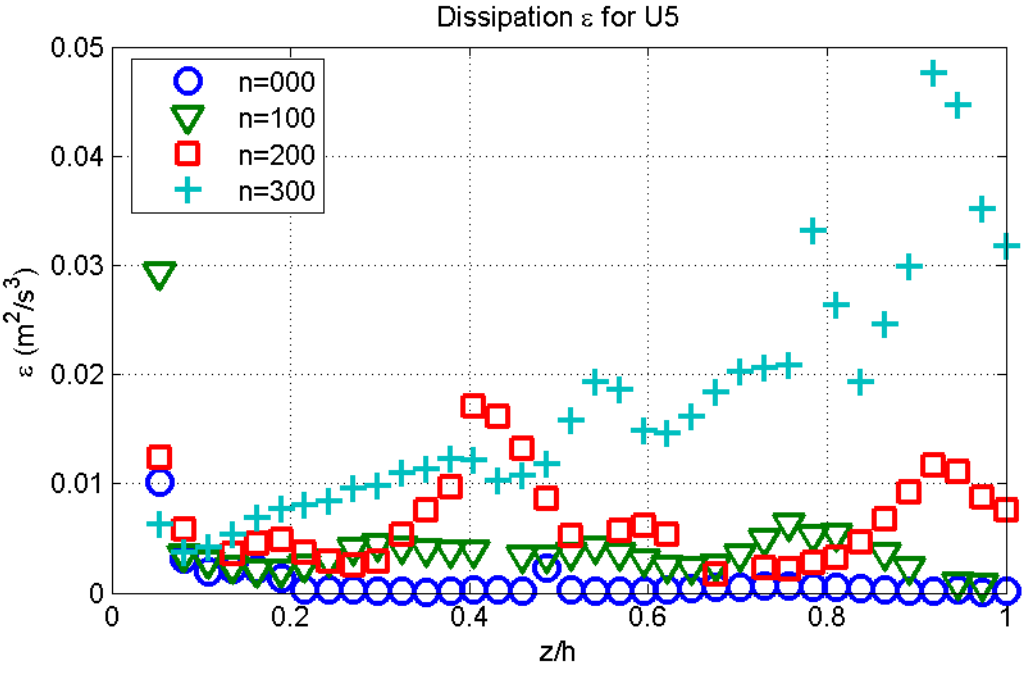


Figure 3.118: Dissipation estimates, $\epsilon = \frac{k^{3/2}}{L_{11}}$ for $U5$.

The analysis yields values of $\epsilon = 0.1 \times 10^{-3} m^2/s^3$ with near wall peaks close to six times higher, for the $U1$ case, whereas for $U5$ the values vary between $\epsilon = 0.002$ to $\epsilon = 0.05 m^2/s^3$. This lets us calculate estimates of the Kolmogorov scales, given as:

$$\begin{aligned} \eta &= \left(\frac{\nu^3}{\epsilon}\right)^{1/4} = (0.15 - 0.067) \times 10^{-3} m \\ \tau_\eta &= \left(\frac{\nu}{\epsilon}\right)^{1/2} = (0.0224 - 0.0045) s \\ u_\eta &= (\nu\epsilon)^{1/4} = (0.0067 - 0.015) m/s \end{aligned}$$

A second approach to find the dissipation involves the second order structure function, $D_{LL} = \langle [u(x+r,t) - u(x,t)][u(x+r,t) - u(x,t)] \rangle$, and the second Kolmogorov similarity hypothesis, namely that in the inertial subrange ($L >> r >> \eta$), $D_{LL}$ can be calculated as:

$$D_{LL}(r,t) = C_2(\epsilon r)^{2/3} \tag{3.15}$$

Where $C_2$ is a universal constant (taken as $C_2 = 2.1$). So that it is possible to calculate a compensated structure function:

$$\frac{1}{r}\left(\frac{D_{LL}}{C_2}\right)^{3/2} = \epsilon \tag{3.16}$$

This should allow us to find the dissipation rate by fitting a horizontal line in the inertial range. The normalized results are shown in Figures 3.119 to 3.122.

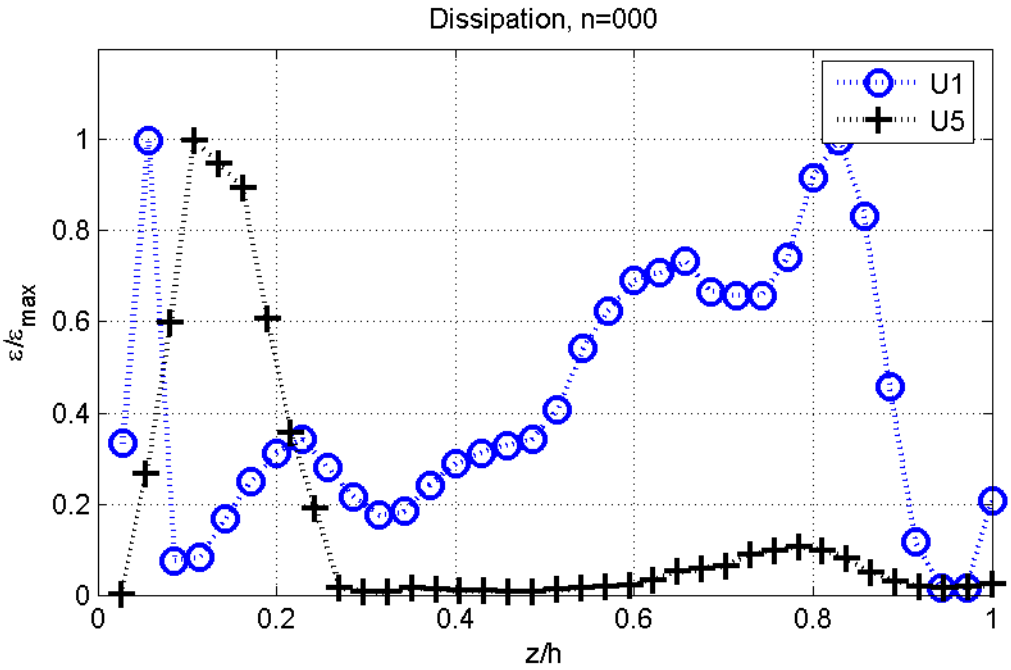


Figure 3.119: Dissipation estimates, fitting $D_{LL}$ for $n = 0$.

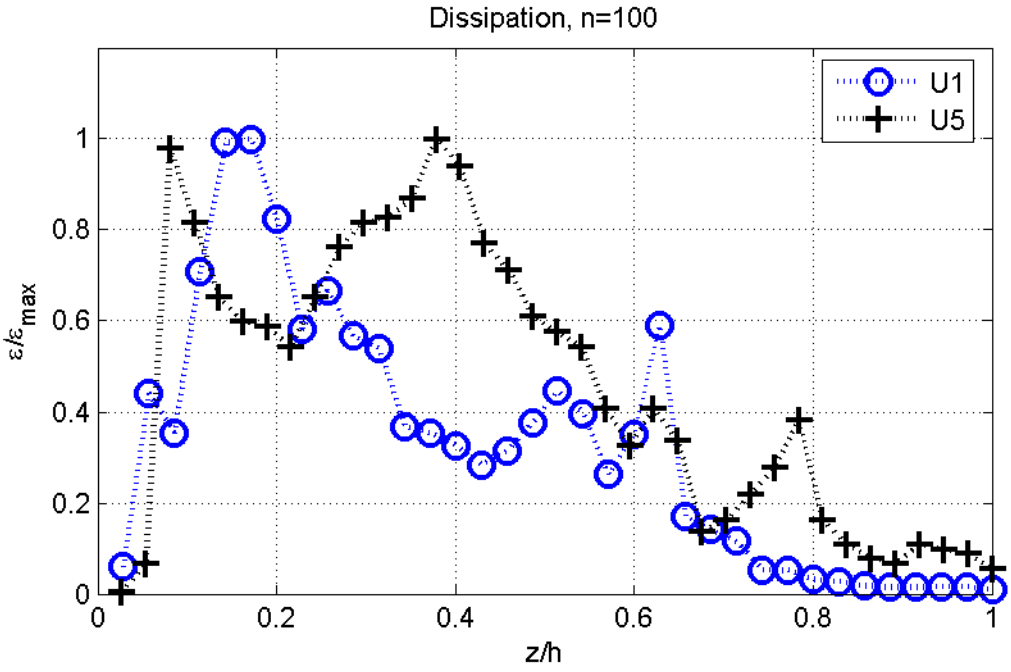


Figure 3.120: Dissipation estimates, fitting $D_{LL}$ for $n = 100$.

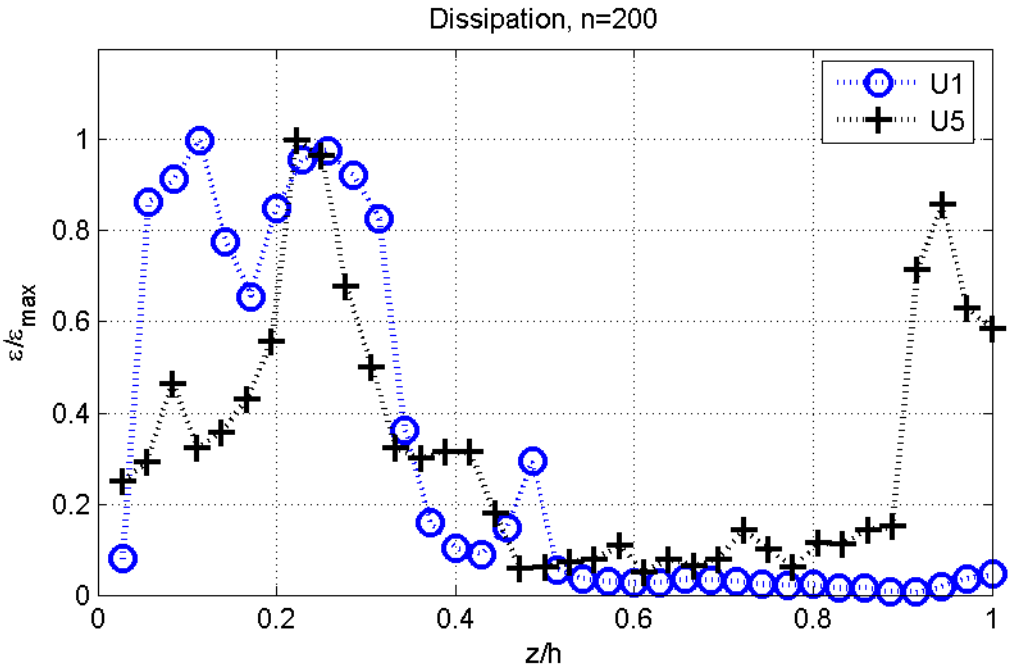


Figure 3.121: Dissipation estimates, fitting $D_{LL}$ for $n = 200$.

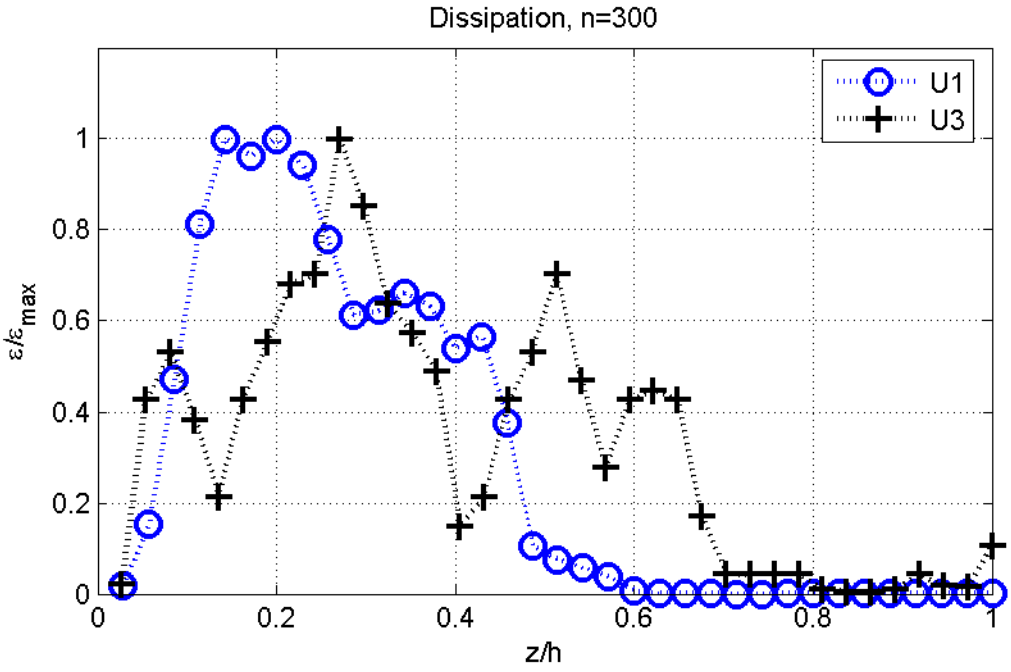


Figure 3.122: Dissipation estimates, fitting $D_{LL}$ for $n = 300$.

It is noticeable the increase in dissipation away from the wall as the vegetation density increases, damping out when the frontal area $a$ reaches its maximum, as well as a good agreement between the minimum and maximum flow speeds. However, the results qualitatively differ from the previous estimates, which may be due to the known inconsistencies by using the scaling approach $\epsilon = k^{3/2}/L_{11}$ with very low Reynolds numbers, but might also indicate high uncertainties in the calculated dissipation values. This ia clearly seen for the $n$=0 case (Figure 3.119), where $\epsilon$ increases away from the wall, which is more likely noise.

### 3.4.2 Models for prediction of longitudinal velocity

As mentioned in section 1.3, several studies have been made to model flow through aquatic vegetation. Since the conditions for this study are similar to those of Lightbody and Nepf (2006), their model is tested against the experimental data to investigate the applicability of such a model at the density ranges accounted for during the present study. Using equation 1.27, which is rewritten below as equation 3.17.

$$\frac{\langle\overline{u(z)}\rangle}{\langle\overline{u(z_0)}\rangle} = \sqrt{\frac{C_d(z_0)a(z_0)}{C_d(z)a(z)}} \tag{3.17}$$

Assuming a near constant drag coefficient, it is possible to predict normalized velocity profiles using the frontal area profiles shown in Figure 3.11. Such predicted velocity profiles $\langle\overline{u(z)}\rangle/\langle\overline{u(z_0)}\rangle$ are shown in Figures 3.123 to 3.125.

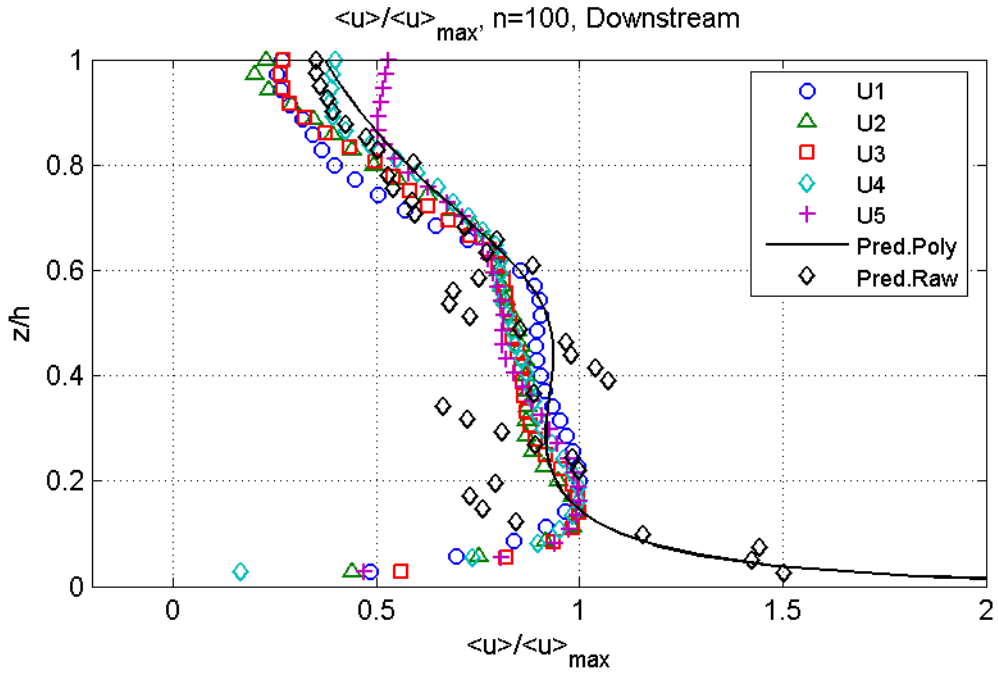


Figure 3.123: Predicted velocity $\langle\bar{u}\rangle/\langle\bar{u}\rangle_{max}$ for n=100.

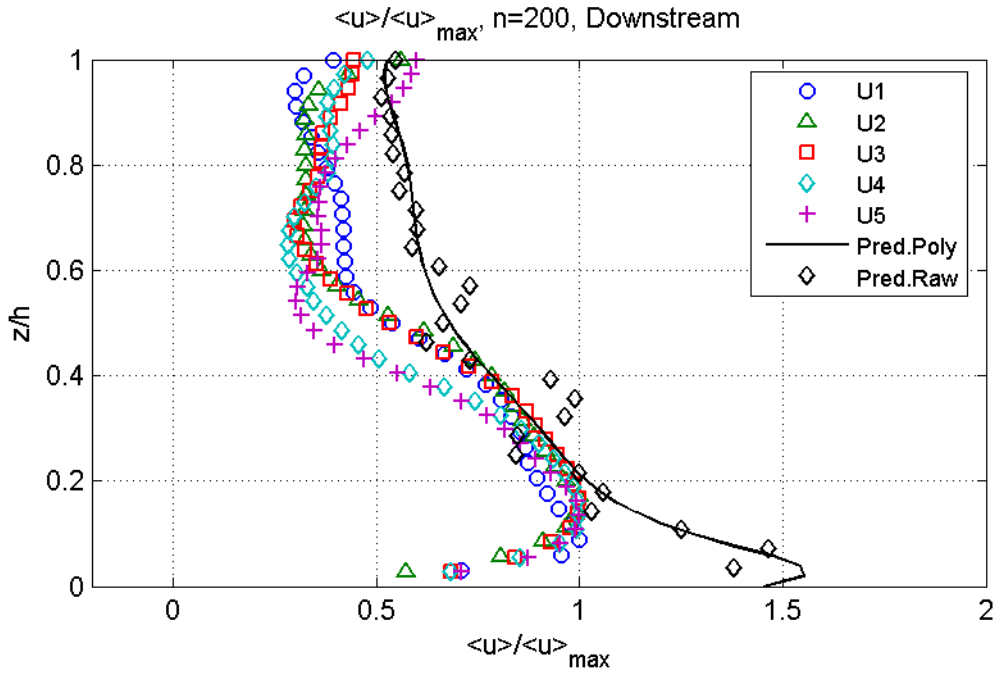


Figure 3.124: Predicted velocity $\langle\bar{u}\rangle/\langle\bar{u}\rangle_{max}$ for n=200.

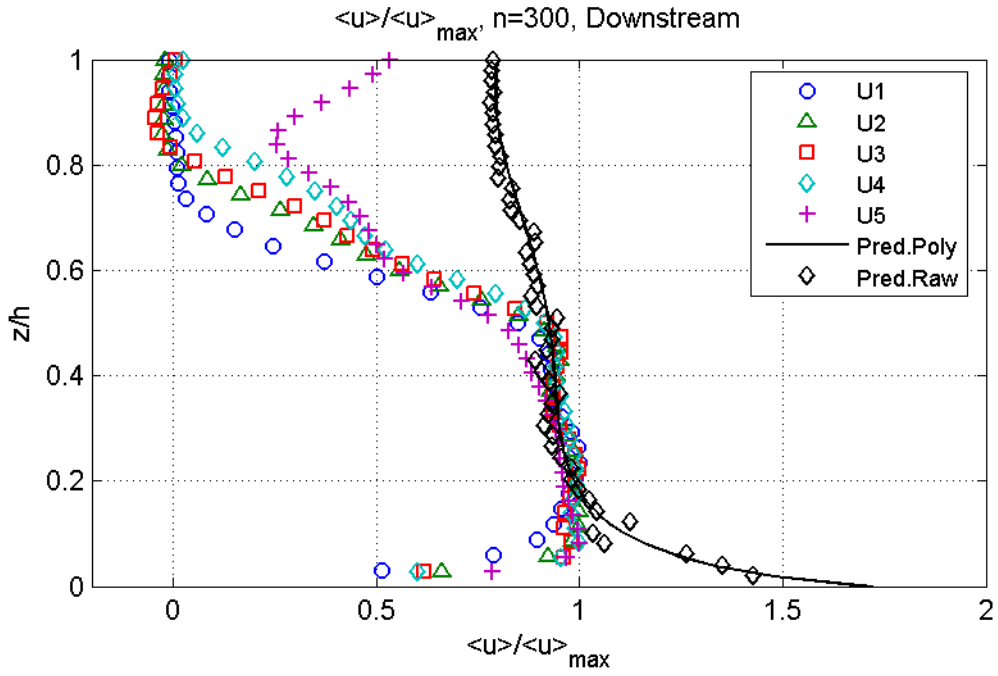


Figure 3.125: Predicted velocity $\langle\bar{u}\rangle/\langle\bar{u}\rangle_{max}$ for n=300.

While working quite well for the $n$=100 case (away from the wall), this model clearly overpredicts the momentum for larger densities. To gain a better understanding of this phenomena, every term previously neglected is calculated and compared to determine their importance.

### 3.4.3 Analysis of common assumptions

#### 3.4.3.1 Drag Coefficient

Since equation 3.17 overpredicts horizontal velocities for the present set, the assumptions and simplifications made for the model need to be evaluated. Using the same equation, it is possible to calculate a normalized drag coefficient using the experimental data for the actual velocities. The results for the calculated drag coefficients $C_d/C_d(z_0)$ are shown in Figures 3.126 to 3.128.

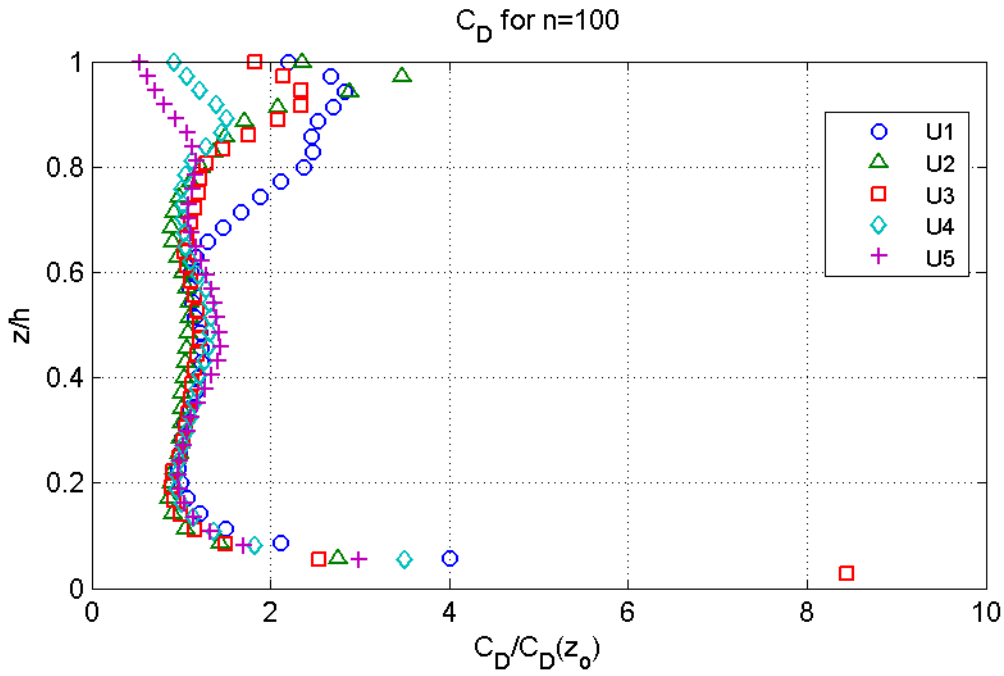


Figure 3.126: Calculated drag coefficient $C_d/C_d(z_0)$ for n=100.

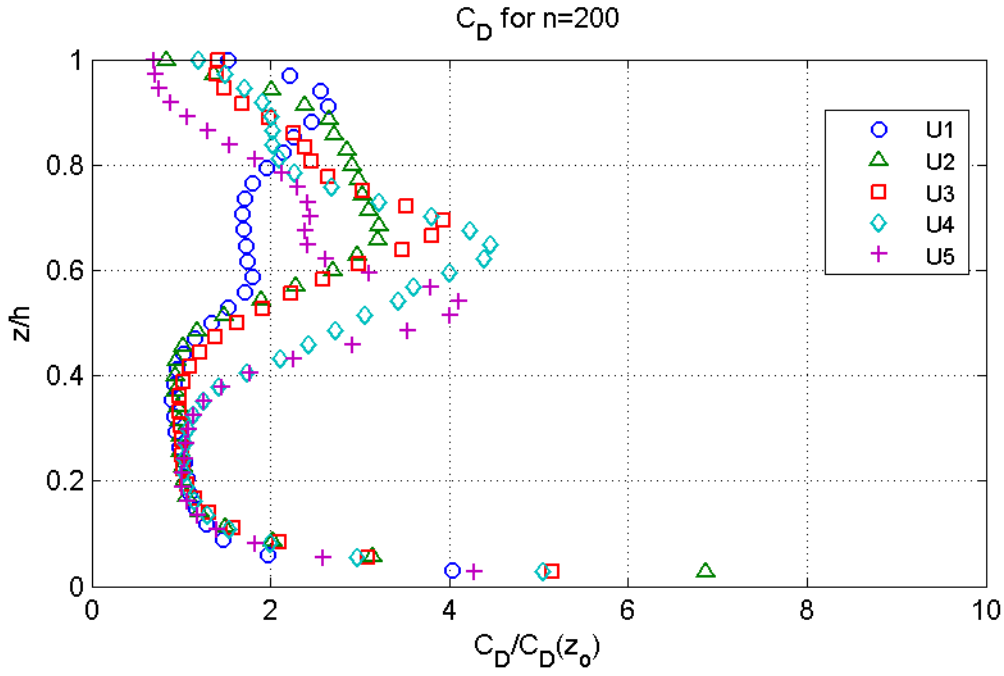


Figure 3.127: Calculated drag coefficient $C_d/C_d(z_0)$ for n=200.

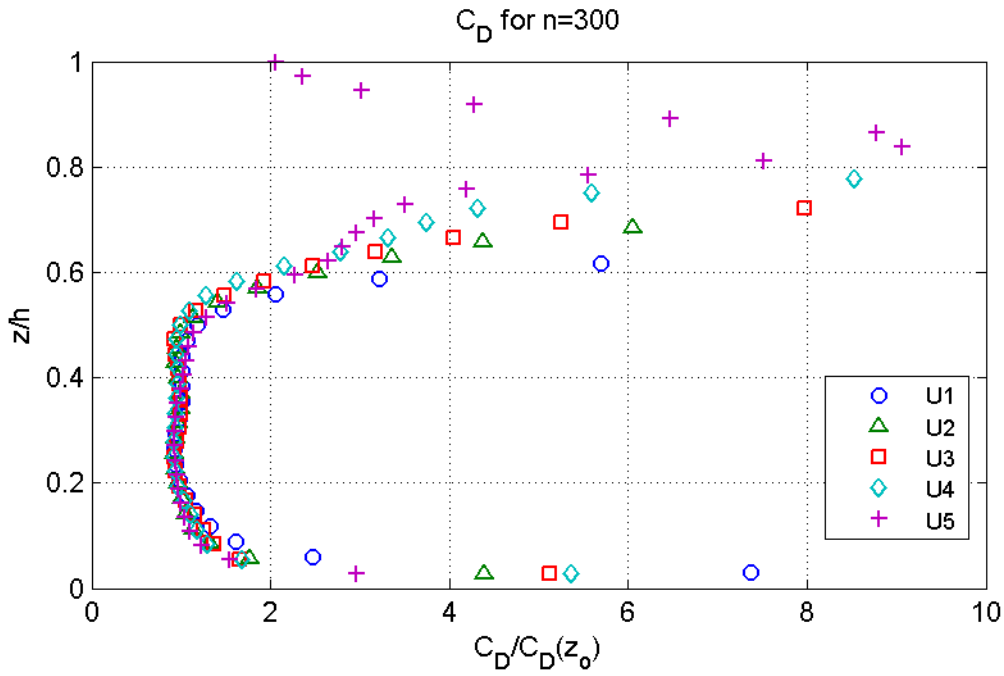


Figure 3.128: Calculated drag coefficient $C_d/C_d(z_0)$ for n=300.

Especially for n=100 and n=300 there is a clear region where $C_d$ remains constant. The dominance of wall stress at the bottom is clear, as well as the effects of denser vegetation when approaching the free surface. Plotting all the calculated $C_d$ values for all densities in the same Figure (Figure 3.129) this region becomes more evident.

However, even when the relation between $C_d$ and $z$ seems consistent, it is necessary to compare it against the frontal area profiles acquired for each density, $a(z)$, as this is a more representative parameter of the local vegetation density. Such comparison is presented in Figure 3.130. In this case, the region of constant $C_d$ does not appear as clear as before, but still gives us a better idea of the magnitude of the variations even with all the assumptions and terms neglected, and provides an idea of the ranges of $a$ $(m^{-1})$ in which such assumptions are valid.

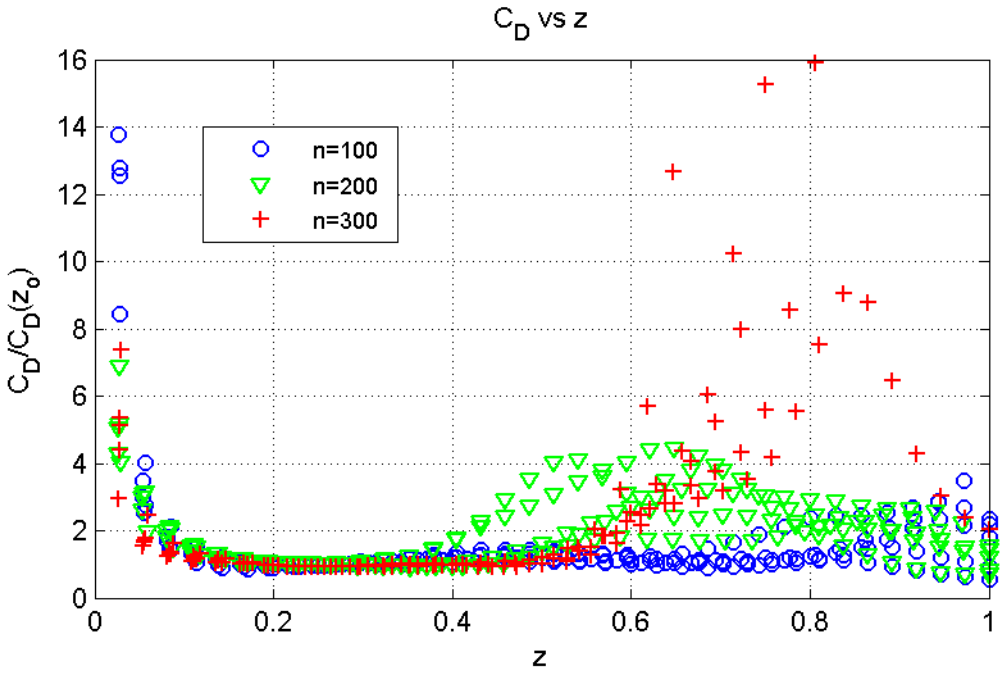


Figure 3.129: Calculated drag coefficient $C_d/C_d(z_0)$ for all densities.

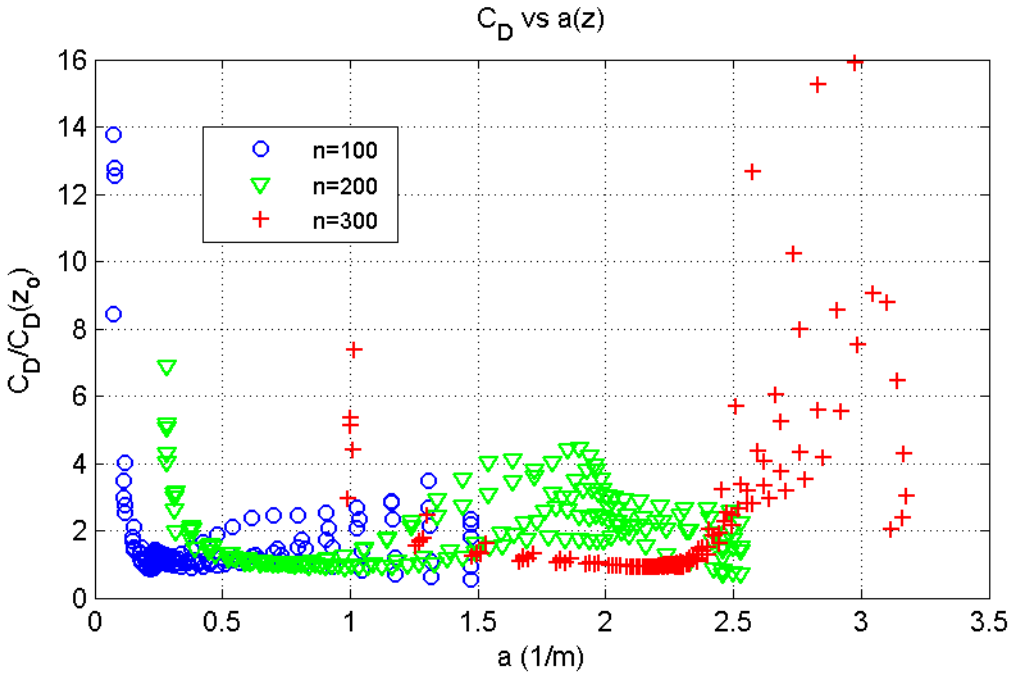


Figure 3.130: Calculated drag coefficient $C_d/C_d(z_0)$ vs $a$ $(m^{-1})$.

A similar comparison is made using the gradient of $a$, $\frac{da}{dz}$, as well as its inverse $\frac{dz}{da}$, to investigate if is not the actual frontal area, but the local gradient which dominates the drag. The results presented in Figures 3.131 and 3.132 show a similar trend as the comparisons against $a$. In this case, a constant $C_d$ holds for values of $\frac{da}{dz} > 0.25$, and increases rapidly as the gradient decreases.

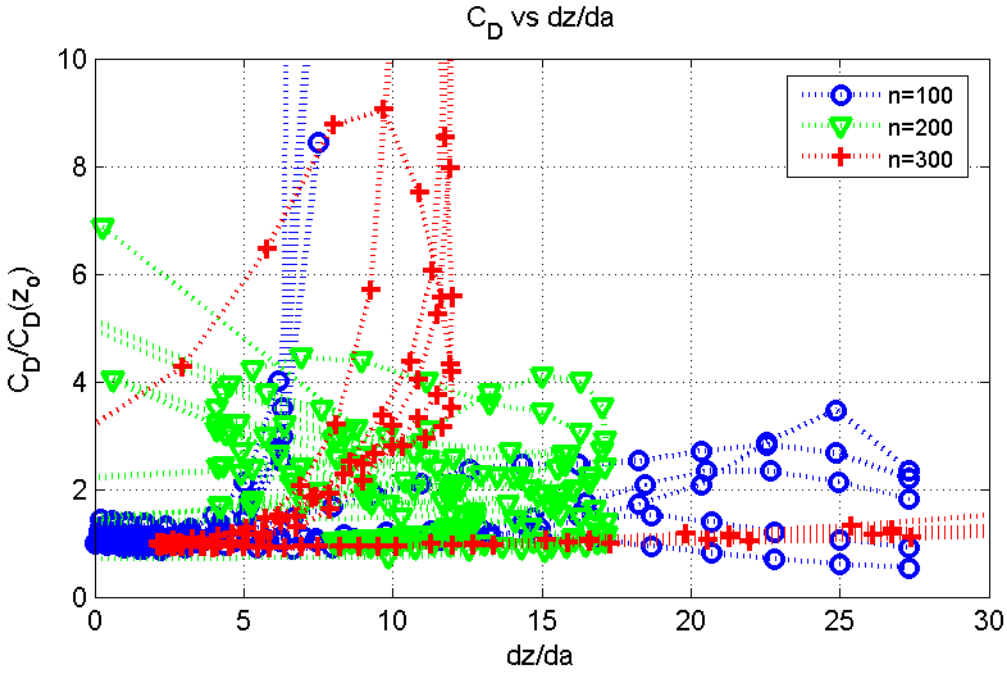


Figure 3.131: Calculated drag coefficient $C_d/C_d(z_0)$ vs $dz/da$

At this point, it is important to recall the first assumptions made from the momentum equation:

$$\langle u\rangle\frac{d\langle\overline{u}\rangle}{dx} + \langle\overline{w}\rangle\frac{d\langle\overline{u}\rangle}{dz} = -g\frac{\partial h}{\partial x} - \left(\frac{\partial}{\partial x}\langle\overline{u'u'}\rangle + \frac{\partial}{\partial z}\langle\overline{u'w'}\rangle\right) + \nu\frac{\partial^2\langle\overline{u}\rangle}{\partial z^2} - \left(\frac{\partial}{\partial x}\langle\overline{u''u''}\rangle + \frac{\partial}{\partial z}\langle\overline{u''w''}\rangle\right) - f_x \tag{3.18}$$

Assuming steady state, fully developed flow ($\frac{d\langle\overline{u}\rangle}{dx} = \frac{\partial}{\partial x}\langle\overline{u'u'}\rangle = 0$), and neglecting the dispersive terms $\frac{\partial}{\partial x}\langle\overline{u''u''}\rangle = \frac{\partial}{\partial z}\langle\overline{u''w''}\rangle = 0$, the rest of the terms can be

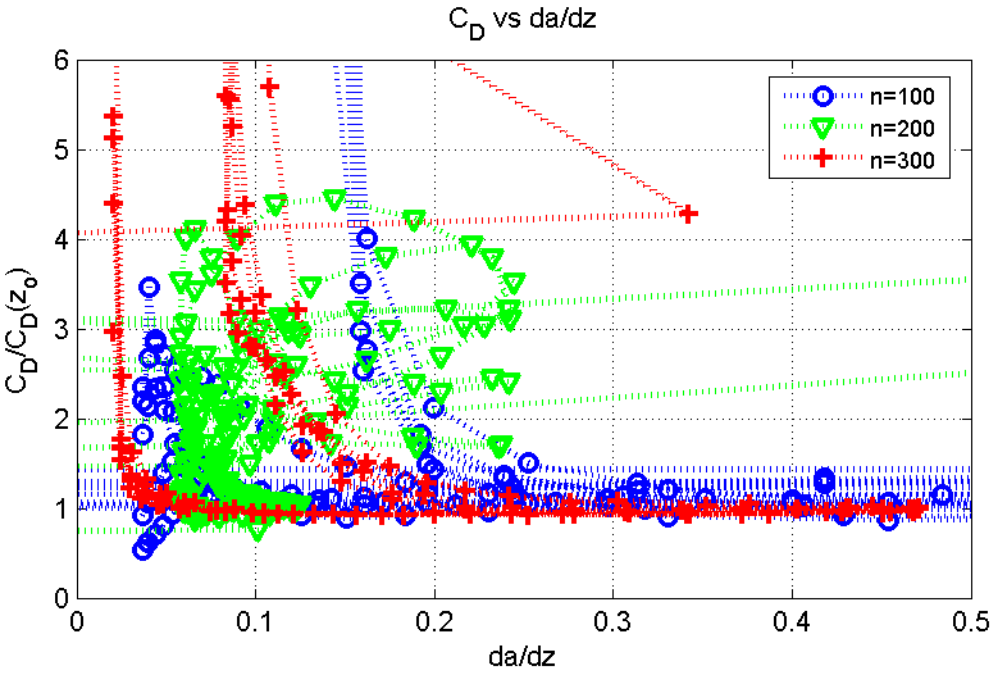


Figure 3.132: Calculated drag coefficient $C_d/C_d(z_0)$ vs $da/dz$

calculated from the data, using a quadratic expression for $f_x$ as:

$$f_x(z) = \frac{1}{2}C_d(z)a(z)\langle\overline{u(z)}\rangle^2 \tag{3.19}$$

It is necessary at this point to assume a value for the drag coefficient. Using the value from Dunn et. al. (1996) of $C_d = 1.13$ independent of $z$, yields the results shown in Figure 3.133.

This allows us to compare the contributions from each term in equation 3.18 with the experimental data, as shown in Figures 3.134 to 3.136.

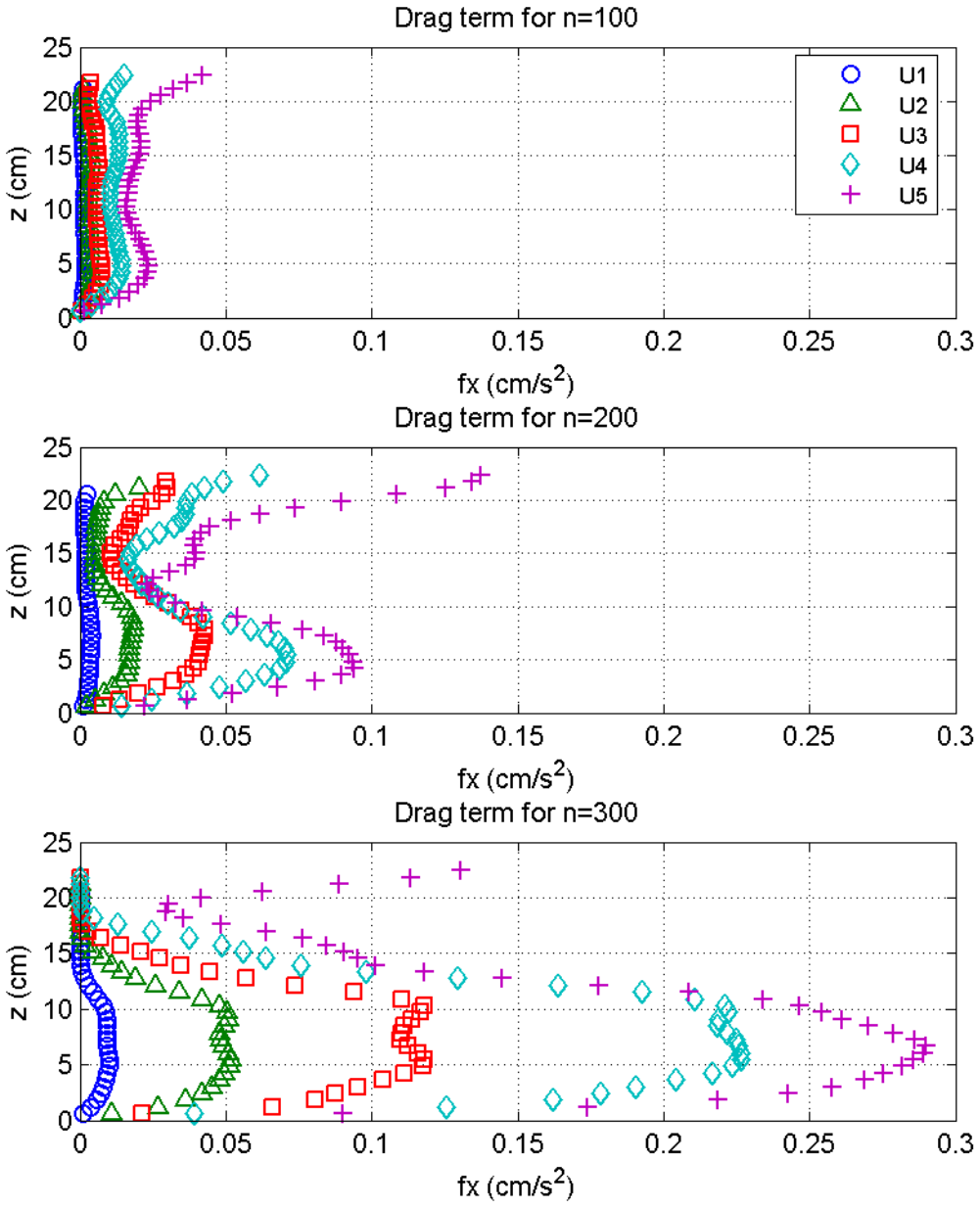


Figure 3.133: Calculated drag term $f_x$ $(cm/s^2)$.

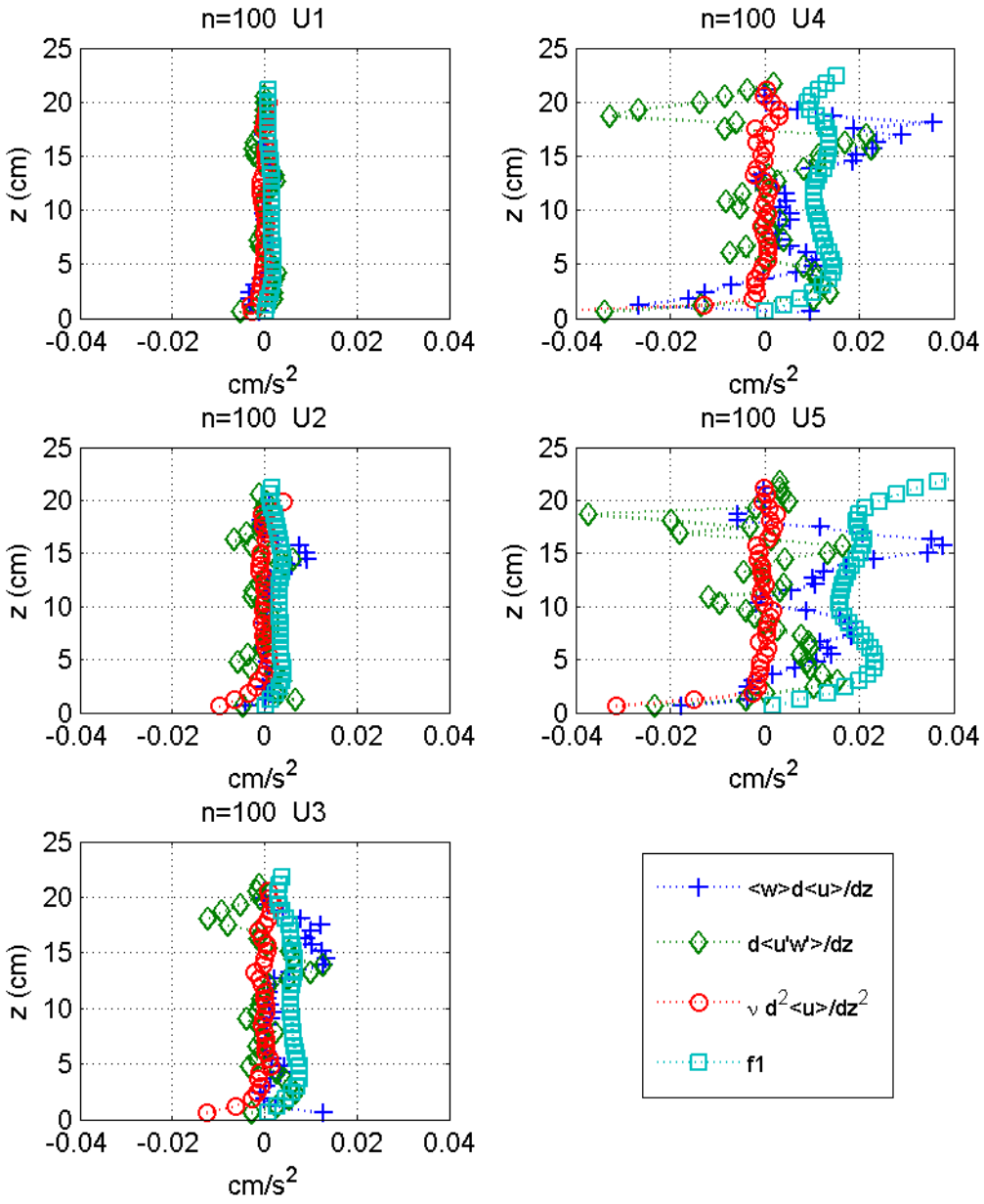


Figure 3.134: Momentum equation, term by term, n=100.

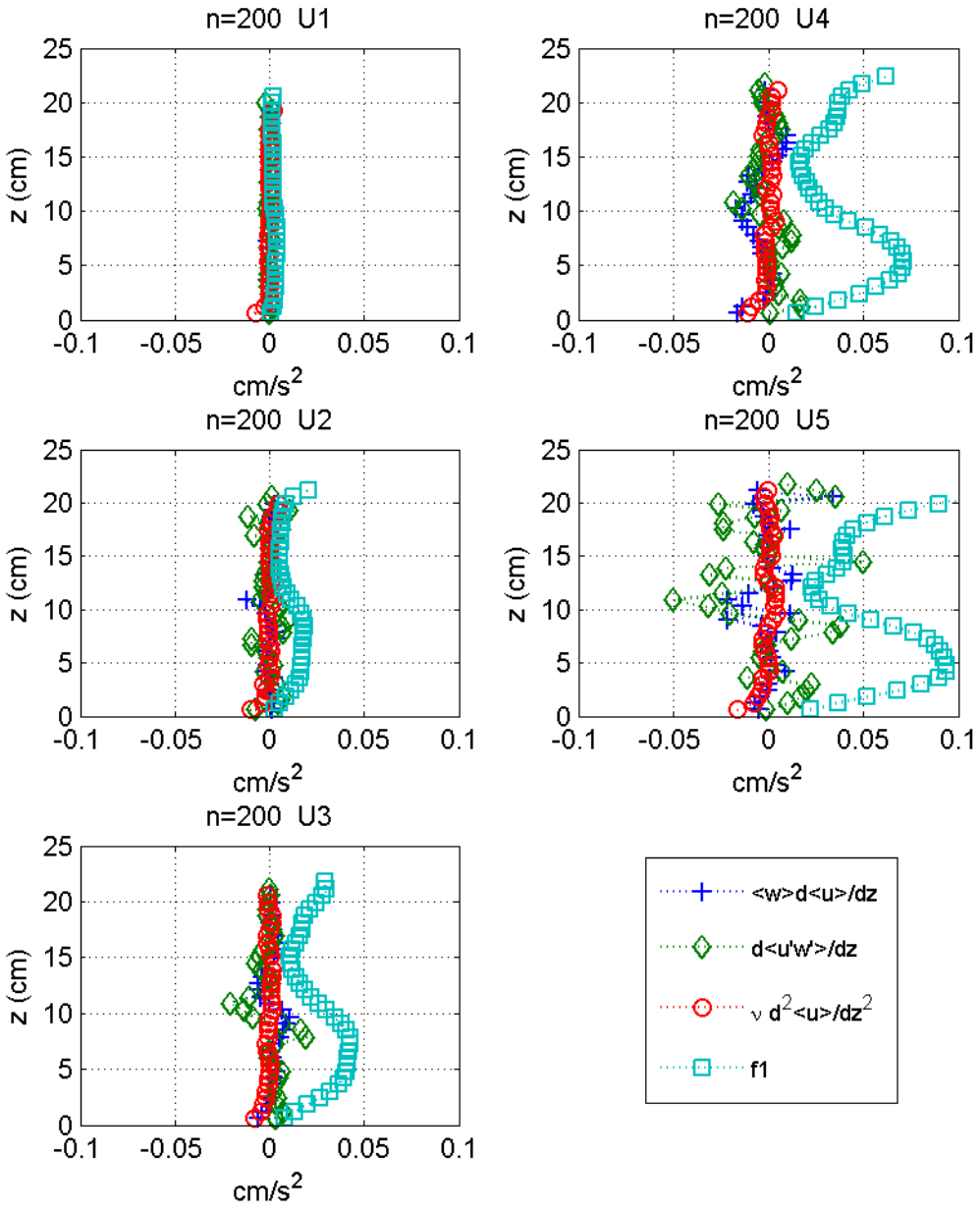


Figure 3.135: Momentum equation, term by term, n=200.

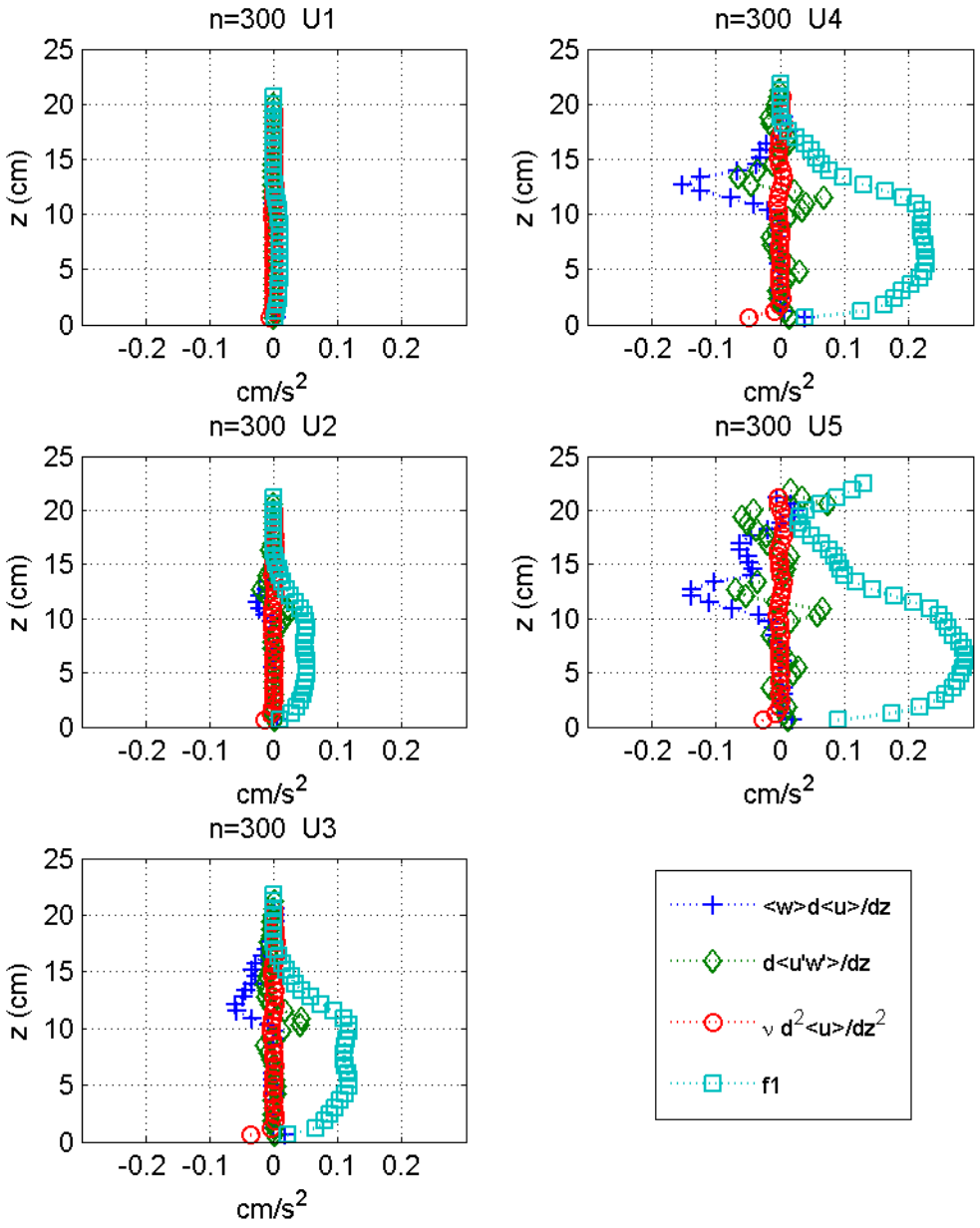


Figure 3.136: Momentum equation, term by term, n=300.

It is noticed that the drag term $f_x$ dominates for all cases, with significant contributions from $\langle\overline{w}\rangle\frac{d\langle\bar{u}\rangle}{dz}$ and $\frac{d\langle\overline{u'w'}\rangle}{dz}$ , and a negligible viscous term $\nu\frac{d^2\langle\bar{u}\rangle}{dz^2}$.

#### 3.4.3.2 Turbulent Viscosity

Another approach is based on turbulent viscosity models. Modeling the Reynolds stress in a simple shear flow as:

$$\langle\overline{u'w'}\rangle = -\nu_T\frac{\partial\langle\overline{u}\rangle}{\partial z}$$

It is possible to calculate the turbulent viscosity profiles, as shown in Figure 3.137.

Usually, this turbulent viscosity is written as the product of a velocity $u^*$ and a length $l^*$, such that $\nu_T = u^*l^*$, leading to either mixing-length models by specifying $l^*$ or two equation models as the $k-\epsilon$ model, relating $u^*$ and $l^*$ to the kinetic energy ($k$) and dissipation ($\epsilon$).

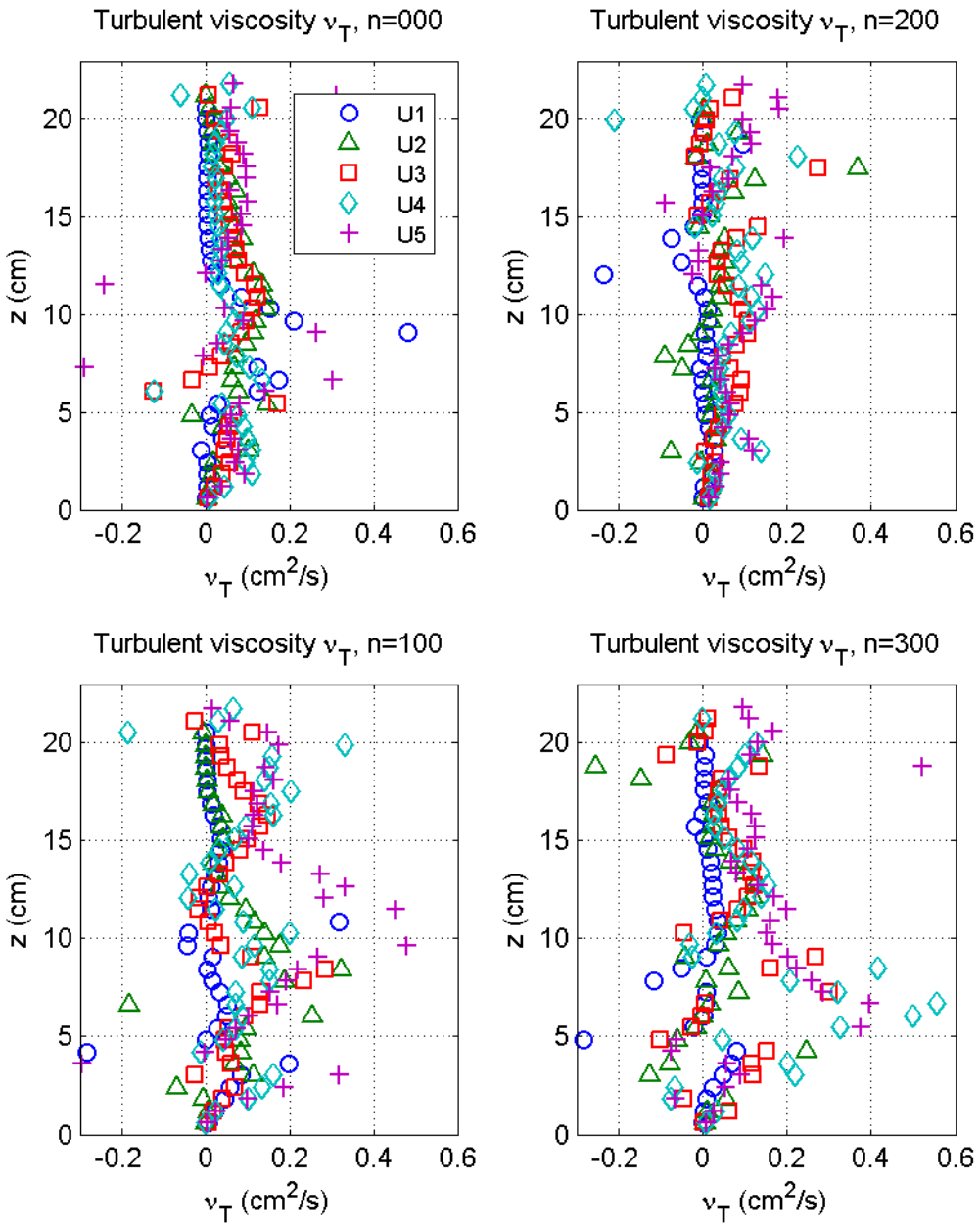


Figure 3.137: Turbulent viscosity $\nu_T$, for all $n$.

There is no clear visible trend on the z-dependence of the turbulent viscosity. It does not necessarily increase with more vegetation or higher velocities, although it peaks at approximately the same height in every case, at the region with the fastest increase in vegetation density, i.e. the maximum in the vertical gradient of $a$. The development of a mixing-layer approach model is not considered in the present work, but a follow-up of these results could lead to validation and calibration of existing models.

# Chapter 4

# Conclusions

## 4.1 Summary and conclusions

With the results presented through this work, several conclusions and recommendations can be produced for future experiments.

The 1D assumption as taken in the majority of laboratory experiments works quite well for the bulk mean velocities and provides at least the order of magnitude for turbulent fluctuations. The presence of vegetation creates a highly 3D flow, so that a more detailed spatial coverage and averaging, stream- and spanwise is required to better capture the flow structure.

The use of PIV proved to be accurate and able to capture a more robust set of information than other alternatives such as ADV or LDV. Besides its non-intrusive nature, it also provided more spatial information allowing the investigation of the dissipative fluxes originated from the spatial averaging, often neglected in previous works. Since the acquisition of PIV images requires a non-obstructed window to capture them, there is a concern about such data not being representative of the vegetated flow. However, it was shown that the data obtained from images just downstream of the patch presents the same structure as those taken in regions

with a smaller FOV within the plants. Besides, the analysis done to check for the x-evolution of velocity and turbulent fluctuations proved that the flow relaxation after leaving the canopy is not rapid enough as to invalidate the downstream data. It was also learned that at the densities considered it is possible to acquire images at different sections within the canopy, which will allow us to plan a new experimental set considering the downstream distance from the last group of stems or the presence of clumps at the sides of the FOV in order to account for the heterogeneity of the plant canopy.

Assuming a constant drag coefficient independent of Reynolds number and frontal area works only for a specific density range. Models created for submerged vegetation, often adapted from terrestrial canopy flow studies, that account for the vegetation effects using a Manning coefficient or skin friction approach are not universally appropriate for flow through vegetation, since they require evaluation of their own constants. A similar problem is shared by most of the current models for vegetated flow, requiring a priori knowledge of the drag and other coefficients, which are often taken as a calibration parameter to fit the model to the experimental data, leading to further research to be able to calculate the drag as a function of a variable frontal area and Reynolds number. Even when several attempts have been made to model the drag coefficient, most of them are based on a volume fraction ($\phi$) calculated from the frontal area ($a$), which is a straightforward calculation when using arrays of elements of regular geometry, but represents a significant source of uncertainty when working with real plants, making difficult a direct comparison against such models.

The vegetated drag proved to be the dominant factor in determining the flow structure, but the near wall interactions can not be neglected, particularly in shallower flows. By knowing the frontal area profile it is possible to estimate the maximum velocity, which provides a good estimate for the friction velocity $u*$ and

therefore the wall stress $\tau_w$, which still dominates in the near wall region despite the vegetation. When working with deeper flows, bed effects can be considered less important, as they represent less of the total bulk drag, but the study of the near wall region is necessary to investigate relevant processes such as the bed stress, sediment transport, and resuspension.

Laboratory studies on rigid and flexible mock vegetation have provided a better understanding of the processes within the canopy, and their resulting models have proved to work for several examples in nature. However, their conclusions can not be taken as universal, since plant morphology and distribution are the dominant factors and both can vary substantially from case to case. It is common to assume that higher densities will damp velocities, reduce bottom stress, increase mixing and residence time, but all of this depends on the type of vegetation immersed in the flow. In 1D flows, if the canopy presents a tree-like structure, with a trunk-like low frontal area at the bottom, branching out and spreading as it reaches towards the free surface, as in the present work, it creates a two-region flow, contradicting the statements from the previous sentence: higher densities slow down the flow at the upper part of the water column creating a higher speed region close to the bottom therefore increasing the friction velocity and bottom stress, affecting also the mixing and transportation through the canopy in different ways as expected.

# BIBLIOGRAPHY


[1] J. Ackerman. Submarine pollination in thre marine angiosperm zostera marina (zosteraceae). i. the influence of floral morphology on fluid flow. *American Journal of Botany*, 84(8):1099–110911, 1997.

[2] J. Ackerman. Diffusivity in a marine macrophyte canopy: implications for submarine pollination and dispersal. *American Journal of Botany*, 89(7):1119–1127, 2002.

[3] J. Ackerman and A. Okubo. Reduced mixing in a marine macrophyte canopy. *Functional Ecology*, 7:305–309, 1993.

[4] F. Arega and B.F. Sanders. Dispersion model for tidal wetlands. *Journal of Hydraulic Engineering*, 8:739–754, 2004.

[5] T. Asaeda, V.K. Trung, J.M.anatunge, and T. Van Bon. Modelling macrophyte-nutrient-phytoplankton interactions in shallow eutrophic lakes and the evaluation of environmental impacts. *Ecological engineering*, 16:341–357, 2001.

[6] K.W. Ayotte, J.J. Finnigan, and M.R. Raupach. A second-order closure for neutrally stratified vegetative canopy flows. *Boundary Layer Meteorology*, 90:198–216, 1999.

[7] M.J. Baptist, V. Babovic, J. Rodriguez, M. Keijzer, R.E. Uittenbogaard, A. Mynett, and A. Verwey. On inducing equations for vegetation resistance. *Journal of Hydraulic Research*, 45(4):435–450, 2007.

[8] Sumner Barr. A modeling study of several aspects of canopy flow. *Monthly Weather Review*, 99(6):485–493, 1971.

[9] G.K. Batchelor. *An Introduction to Fluid Dynamics*. Cambridge University Press, 1967.

[10] S. Bennett, T. Pirim, and B. Barkdoll. Using simulated emergent vegetation to alter stream flow direction within a straight experimental channel. *Geomorphology*, 44:115–126, 2002.

[11] W. Brutsaert. Heat and mass transfer to and from surfaces with dense vegetation or similar permeable roughness. *Boundary Layer Meteorology*, 16:365–388, 1979.

[12] W. Brutsaert. *Hydrology: an introduction*. Cambridge University Press, 2005.

[13] R.W. Burke and K.D. Stolzenbach. Free surface flow through salt marsh grass. Technical report, MIT-Sea Grant Report MITSG 83-16, 1983.

[14] S.U. Choi and H. Kang. Reynolds stress modeling of vegetated open-channel flows. *Journal of Hydraulic Research*, 42(1):3–11, 2004.

[15] R.M. Cionco. A mathematical model for air flow in a vegetative canopy. *Journal off Applied Meteorology*, 4:517–522, 1965.

[16] E.A. Cowen, K.A. Chang, and Q. Liao. A single-camera coupled ptv-lif technique. *Experiments in Fluids*, 31:63–73, 2001.

[17] E.A. Cowen and S.G. Monismith. A hybrid digital particle tracking velocimetry technique. *Experiments in fluids*, 22:199–211, 1997.

[18] J. Cui and V.S. Neary. Les study of turbulent flows with submerged vegetation. *Journal of Hydraulic Research*, 46(3):307–316, 2008.

[19] M.W. Denny, B.P. Gaylord, and E.A. Cowen. Flow and flexibility ii. the roles of size and shape in determining wave forces on the bulk kelp nereocystis luetkeana. *The Journal of Experimental Biology*, 200:3165–3183, 1997.

[20] P. Diaconis and B. Efron. Computer-intensive methods in statistics. *Scientific American*, 248:116–130, 1983.

[21] P. Doron, L. Bertuccioli, J. Katz, and T.R. Osborn. Turbulence characteristics and dissipation estimates in the coastal ocean bottom boundary layer from piv data. *Journal of Physical Oceanography*, 31:2108–2134, 2001.

[22] C. Dunn, F. Lopez, and M. Garcia. Mean flow and turbulence in a laboratory channel with simulated vegetation. Technical report, Hydraulic Engineering Series No. 51, UILU-ENG-96-2009, 1996.

[23] M.J. Dwyer, E.G. Patton, and R.H. Shaw. Turbulent kinetic energy budgets from a large eddy simulation of airflow above and within a forest canopy. *Boundary Layer Metheorology*, 84:23–43, 1997.

[24] M. Fathi-Maghadam and N. Kouwen. Nonrigid, nonsubmerged, vegetative roughness on floodplains. *Journal of Hydraulic Engineering*, 123:51–57, 1997.

[25] C.M. Finelli. Velocity and concentration distributions in turbulent odor plumes in the presence of vegetation mimics: a flume study. *Marine Ecology Progress Series*, 207:297–309, 2000.

[26] J. Finnigan. Turbulence in plant canopies. *Annu. Rev. Fluid Mech.*, 32:519–571, 2000.

[27] H.B. Fischer, E.J. List, R.Koh, J. Imberger, and N.H. Brooks. *Mixing in inland and coastal waters.* Academic Press, 1979.

[28] M. Ghisalberti. *Momentum and scalar transport in vegetated shear flows.* PhD thesis, Massachusetts Institute of Technology, 2005.

[29] M. Ghisalberti and H. Nepf. Mass transport in vegetated shear flows. *Environmental Fluid Mechanics*, 5:527–551, 2005.

[30] M. Ghisalberti and H. Nepf. The structure of the shear layer in flows over rigid and flexible canopies. *Environmental Fluid Mechanics*, 6:277–301, 2006.

[31] M. Ghisalberti and H. M. Nepf. The limited growth of vegetated shear layers. *Water Resources Research*, 40:1–12, 2004.

[32] M. Ghisalberti and H.M. Nepf. Mixing layers and coherent structures in vegetated aquatic flows. *Journal of Geophysical Research*, 107, 2002.

[33] P.H. Gleick. *Water Resources. Encyclopedia of Climate and Weather.* Oxford University Press, 1996.

[34] T. Helmio. Unsteady 1d flow model of compound channel with vegetated floodplains. *Journal of Hydrology*, 269:89–99, 2002.

[35] R.S. Jadhav and S.G. Buchberger. Effects of vegetation on flow through free water surface wetlands. *Ecological Engineering*, 5:481–496, 1995.

[36] G. Janauer and M. Dokulil. *Macrophytes and algae in running waters.* John Wiley & Sons, Ltd, 2006.

[37] J. Jarvela. Flow resistance of flexible and stiff vegetation: a flume study with natural plants. *Journal of Hydrology*, 269:44–54, 2002.

[38] J. Jarvela. *Flow resistance in environmental channels: Focus on vegetation.* PhD thesis, Helsinky University of Technology, 2004.

[39] H. Kang and S. Choi. Turbulence model of compound open-channel flows with and without vegetation on the floodplain using the reynolds stress model. *Advances in Water Resources*, 29:1650–1664, 2006.

[40] G. Katul, C. Lai, K. Schafer, B. Vidakovic, J. Albertson, D. Ellsworth, and R. Oren. Multiscale analysis of vegetation surface fluxes: from seconds to years. *Advances in Water Resources*, 24:1119–1132, 2001.

[41] M. G. Khublaryan, A. P. Frolov, and V. N. Zyryanov. Modeling water flow in the presence of higher vegetation. *Water Resources*, 31(6):617–622, 2004.

[42] A. King. Field measurements of bulk flow and transport through a small coastal embayment having variable distributions of aquatic vegetation. Master's thesis, Cornell University, 2006.

[43] S.J. Kline. Describing uncertainties in single-sample experiments. *Mechanical Engineering*, 75, 1953.

[44] D.L. Koch and A. Ladd. Moderate reynolds number flows through periodic and random arrays of aligned cylinders. *J. Fluid. Mech.*, 349:31–66, 1997.

[45] P.K. Kundu and I.M. Cohen. *Fluid Mechanics*. Elsevier Academic Press, 2004.

[46] J.K. Lee, L.C. Roigh, H.L. Jenter, and H.M. Visser. Drag coefficients for modeling flow through emergent vegetation in the florida everglades. *Ecological Engineering*, 22:237–248, 2004.

[47] X. Lee. Air motion within and above forest vegetation in non-ideal conditions. *Forest Ecology and Management*, 135:3–18, 2000.

[48] L.A. Leonard and M.E. Luther. Flow hydrodynamics in tidal marsh canopies. *Limnology and Oceanography*, 40(8):1474–1484, 1995.

[49] A. Lightbody. *The physical role of transverse deep zones in improving constructed treatment wetland performance*. PhD thesis, Massachusetts Institute of Technology, 2007.

[50] A.F. Lightbody and H.M. Nepf. Prediction of velocity profiles and longitudinal dispersion in emergent salt marsh vegetation. *Limnology and Oceanography*, 51(1):218–228, 2006.

[51] S. Liu, H. Liu, M. Xu, M. Y. Leclerc, T. Zhu, C. Jin, Z. Hong, J. Li, and H. Liu. Turbulence spectra and dissipation rates above and within a forest canopy. *Boundary-Layer Meteorology*, 98:83–102, 2001.

[52] F. Lopez and M. Garcia. Open-channel flowthrough simulated vegetation: Turbulence modeling and sediment transport. Technical report, Wetlands Research Program Technical Report WRP-CP-10, 1997.

[53] F. Lopez and M. Garcia. Open-channel flow through simulated vegetation: Suspended sediment transport modeling. *Water Resources Research*, 34(9):2341–2352, 1998.

[54] F. Lopez and M.H. Garcia. Mean flow and turbulence structure of open channel flow through non-emergent vegetation. *Journal of Hydraulic Engineering*, 127:392–402, 2001.

[55] J.D. Madsen, J. W. Sutherland, J. A. Bloomfield, L. W. Eichler, and C. W. Boylen. The decline of native vegetation under dense eurasian watermilfoil canopies. *Journal of Aquatic Plant Manage*, 29:94–99, 1991.

[56] N.E. Monsen, J.E. Cloern, and L.V. Lucas. A comment on the use of flushing time, residence time, and age as transport time scales. *Limnology and Oceanography*, 47(5):1545–1553, 2002.

E. Murphy. Longitudinal dispersion in vegetated flow. Master's thesis, MIT, 2006.

[57] V. S. Neary. Numerical solution of fully developed flow with vegetative resistance. *Journal of Engineering Mechanics*, 129(5):558–563, 2003.

[58] H. M. Nepf. Drag, turbulence and diffusion in flow through emergent vegetation. *Water Resources Research*, 35(2):479–489, 1999.

[59] H. M. Nepf, C. G. Mugnier, and R. A. Zavistoski. The effects of vegetation on longitudinal dispersion. *Estuarine, Coastal and Shelf Science*, 44:675–684, 1997a.

[60] H. M. Nepf, J. A. Sullivan, and R. A. Zavistoski. A model for diffusion within emergent vegetation. *Limnology and Oceanography*, 42(8):1735–1745, 1997b.

[61] H. M. Nepf and E. R. Vivoni. Turbulence structure in depth-limited, vegetated flow: Transition between emergent and submerged regimes.

[62] H. M. Nepf and E. R. Vivoni. Flow structure in depth-limited, vegetated flow. *Journal of Geophysical Research*, 105:28547–28557, 2000.

[63] H.M. Nepf and E.W. Koch. Vertical secondary flows in submersed plant-like arrays. *Limnol. Oceanogr.*, 44(4):1072–1080, 1999.

[64] C.E. Oldham and J.J. Sturman. The effect of emergent vegetation on convective flushing in shallow wetlands: scaling and experiments. *Limnol. Oceanogr.*, 46(6):1486–1493, 2001.

[65] J. D. Pinard and J.D. Wilson. First and second order closure model for wind in a plant canopy. *Journal of Applied Meteorology*, 40:1762–1768, 2001.

[66] D. Poggi, G. G. Katul, and J. D. Albertson. Momentum transfer and turbulent kinetic energy budgets within a dense model canopy. *Boundary-Layer Meteorology*, 111:589–614, 2004.

[67] S.B. Pope. *Turbulent Flows*. Cambridge University Press, 2000.

[68] M. R. Raupach and A. S. Thom. Turbulence in and above plant canopies. *Ann. Rev. Fluid Mech.*, 13:97–129, 1981.

[69] M. Righetti and A. Armanini. Flow resistance in open channel; flows with sparsely distributed bushes. *Journal of Hydrology*, 269:55–64, 2002.

[70] P. M. Rowinski and J. Kubrak. Velocity profiles on vegetated flood plains. 2003.

[71] F.J. Rueda and E.A. Cowen. Residence time of a freshwater embayment connected to a large lake. *Limnology and Oceanography*, 50(5):1638–1653, 2005.

[72] F.J. Rueda, E.A. Cowen, A.R. Blake, and K.L. Kull. Circulation and exchange in a small subembayment of lake ontario. *HMEM2002*, 2002.

[73] M. Schulz, H. Kozerski, T. Pluntke, and K. Rinke. The influence of macrophytes on sedimentation and nutrient retention in the lower river spree (germany). *Water Research*, 37:569–578, 2003.

[74] R. Shaw and E.G. Patton. Canopy element influences on resolved- and subgrid-scale energy within a large-eddy simulation. *Agricultural and Forest Meteorology*, 115:5–17, 2003.

[75] P.R. Spalart. Direct simulation of a turbulent boundary layer up to re=1410. *NASA Technical memorandum 89407*, 1986.

[76] U. Stephan and D. Gutknecht. Hydraulic resistance of submerged flexible vegetation. *Journal of Hydrology*, 269:27–43, 2002.

[77] H.B. Su, K.T. Paw, and R.H. Shaw. Development of a coupled leaf and canopy model for the simulation of plant-atmosphere interaction. *Journal of Applied Meteorology*, 35:733–748, 1996.

[78] Stanislaw J. Tajchman. Comments on measuring turbulent exchange within and above forest canopy. *Bulletin American Meteorological Society*, 62(11):1550–1559, 1981.

[79] Y. Tanino and H.M. Nepf. Laboratory investigation of mean drag in a random array of rigid, emergent cylinders. *Journal of Hydraulic Engineering*, 134:34–41, 2008a.

[80] Y. Tanino and H.M. Nepf. Lateral dispersion in random cylinder arrays at high reynolds number. *J. Fluid Mech.*, 600:339–371, 2008b.

[81] A. Tuzet and J. D. Wilson. Wind and turbulence in a sparse but regular plant canopy. *Journal of Applied Metheorology*, 41:573–587, 2002.

[82] E.H. Van-Nes, M.S. Van Den Berg, J.S. Clayton, H.Coops, M. Scheffer, and E. Van Ierland. A simple model for evaluating the costs and benefits of aquatic macrophytes. *Hydrobiologia*, 415:335–339, 1999.

[83] B.L. White and H.M. Nepf. Scalar transport in random cylinder arrays at moderate reynolds number. *J. Fluid Mech.*, 487:43–79, 2003.

[84] C. A. M. E. Wilson, T. Stoesser, P. D. Bates, and A. Batemann Pinzen. Open channel flow through different forms of submerged flexible vegetation. *Journal of Hydraulic Engineering*, 129(11):847–863, 2003.

[85] J.L. Wright and K.W. Brown. Comparison of momentum and energy balance methods of computing vertical transfer within a crop. *Agronomy Journal*, 59:427–432, 1967.